A Frequency Agile approach to Air-Coupled Lamb wave Inspection

Robert Banks

Submitted in November 1999

for the degree of Doctor of Philosophy

Centre for Ultrasonic Engineering

Department of Electronic and Electrical Engineering

The University of Strathclyde

204 George Street, Glasgow, G1 1WX

Scotland

Table of contents

List of Symbols

This list comprises most of the main symbols used throughout this Thesis, where x commonly denotes an additional operand defined within the text.

Symbol	*Definition*	*Unit*
Z_x	Specific Acoustic Impedance	MRayl
h_{33}	Piezoelectric charge constant in the thickness direction	Vm^{-1} or NC^{-1}
k_t	Electro-mechanical thickness mode coupling coefficient	
ε_r	Permittivity relative to ε_0	Fm^{-1}
ε_0	Permittivity of free space	Fm^{-1}
f	Frequency	Hz
s	Laplace complex operator	
k_t	Thickness mode coupling coefficient	
ρ	Density	kgm^{-3}
f_e	Frequency of Electrical Resonance	Hz
f_m	Frequency of Mechanical Resonance	Hz
T	Temperature	K
T_t	Transit time for bulk (longitudinal) waves	seconds
Z_x	Impedance	Ohms
T_x	Transmission coefficient	
V	Voltage	Volts
I	Current	Amps
k	Boltzmann's constant	W-s/K
E_x	Noise Voltage	$v/\sqrt{Hz}$
C_o	Static Capacitance of Transducer	pF
τ	Time constant	seconds
λ	Wavelength	m
c_{33}	Elastic stiffness constant in the thickness direction	Pa or Nm^{-2}
e_{xy}	Piezoelectric stress constant in the thickness direction	Cm^{-1}

ABSTRACT

This Thesis describes the design, manufacture and evaluation of a single sided through-air Lamb wave scanner for Non-Destructive Evaluation (NDE). The new scanning system utilises novel wideband piezocomposite transducers and specialised receive electronics to detect and monitor the thickness of faults within the structure under investigation using a frequency agile approach. Based upon the superheterodyne principle, this frequency agility dispenses with the costly requirement for precision manipulation of the transducer alignment, by effectively tuning the system for the thickness of the sample. Several important applications are identified, including defect detection on samples with tapered thicknesses and defect depth characterisation on plates with thickness erosion, in addition to conventional defect evaluation.

Through the application of finite element modelling and practical analysis, a new range of wideband composite transducer have been developed which offer a considerable improvement in operational bandwidth in comparison to conventional piezocomposites. Moreover, a specialised ultra low noise heterodyning amplifier was designed and constructed to provide sufficient gain and selectivity to detect the Lamb waves generated in the various structures under examination. Experimental results obtained from the prototype system illustrate a capability to distinguish defects within test specimens of differing materials and determine the thickness of the given defect. The current system is capable of resolving defects down to less than 2mm in diameter or 20% thinning in a 1mm thick aluminium plate for a Lamb wave with a wavelength of 3mm. Moreover, the handheld nature of the scanning head employed within this system has facilitated the examination of practical NDE examples, such as disbonds between vehicle support structures and outer panelling over curved structures.

Acknowledgements

Special thanks go to my supervisor, Professor Gordon Hayward for all the help, support and guidance he has offered me over the period of my studies. Which has hopefully been repaid in part by my services towards the groups' football team and giving him the occasional respite from work in the skiing capitol of Europe (Glenshee!!).

Significant others that require thanks are:
Tommy McCunnie and Alec Ward for all the technical expertise and "know how" shown in the manufacture of the weird and wonderful composite designs and for mercilessly taking the piss out of my technical drawing attempts.

Tony Gachagan, the big daddy of the lab, for all his help on the composites and for keeping a calm head on the football field while marshalling those around him. Roger Farlow, the electronics guru and unfortunate first draft Thesis reader *and always being there!*. Stephen Kelly for introducing me to the fantastic art of Kelido® and electrostatics. Graham Benny and Walter Galbraith for the transducer calibration work and further electronics advice as well as winning the best beard awards. Both Jamie Hyslop and Paul Reynolds for providing many hours of entertainment as they bickered away and for teaching me the mystic arts for FEM. All the beer monster boys (Bishop, Oily and Ricky) for laughs at the Christmas parties and furtherance of my alcohol dependency, and Sandy Cochran for galvanising the group into one coherent unit.

Finally, special thanks to my family for all the help and understanding they've shown through my time here. Only reminding me occasionally that "it's time to get a real job". Sorry you didn't get to read this Dad, maybe later.

Th-th-that's all folks!

Chapter One

Introduction

1.1 Background

There is an increasing demand within industry for reliable and robust non-contact, air-coupled ultrasonic non-destructive testing (NDT) apparatus. Ultrasound has found considerable application in a variety of fields, such as NDT, biomedical (pre-natal scanning, lithotripsy) and underwater systems (SONAR). However, conventionally within the field of NDT, the propagation of ultrasound from the sensor (or transducer) into the material under inspection has been facilitated by the use of couplants, such as water or gel. It is commonly accepted that the removal of the need to employ this coupling layer would be extremely advantageous, particularly since the use of thin couplants reduces scanning speed, with the requirement to maintain good surface contact. Additionally, couplants can be potentially damaging to certain materials, such as paper and certain carbon fibre laminates due to absorption of the couplant.

Ideally, the ultrasonic transducers should be removed from the surface of the test piece, with the ultrasonic energy propagating across the intervening air gap and insonifying the material remotely. Such a system could then facilitate the scanning of considerably more complex surface geometries and be more portable than existing immersion testing facilities. While there are air-coupled ultrasonic inspection systems using lasers [1] to generate ultrasound, these systems tend to be restrictively expensive and can potentially damage the surface under inspection. The inherent problem with using traditional piezoceramic transducers to transmit sound through air is the insertion loss, typically -97dB for transmission from ceramic to air, due to the large acoustic impedance differential between the transducer/air and air/solid boundary and sound absorption in air. Developments in ultrasonic transducer technology for air-coupled applications in the past decade have been considerable, with most of the attention focussed upon the improvement and integration of transducers such as electrostatic, piezoceramic and piezopolymer devices.

Many tasks within the practical ultrasonic field are limited by the available signal to noise ratio (SNR). This is especially true of air-coupled imaging techniques, where the signals utilised are either of low magnitude, or the signal is subject to a variety of attenuative effects. It is therefore imperative to gain a comprehensive understanding of

the receiver system and the noise sources which influence the resultant SNR. All aspects of the receiver design must be considered, both the transducers employed within the system and the receive electronics itself, in order to optimise the design of the system. For example, consider the relatively straightforward air-coupled NDT system illustrated in Figure 1.01.

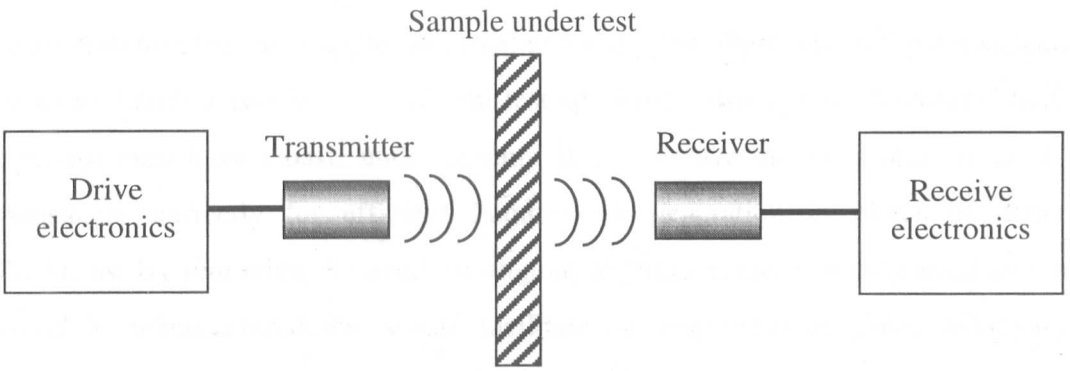

Figure 1.01 *Example of an air-coupled ultrasonic inspection system*

A previous investigation has been reported, detailing the noise mechanisms active within piezoelectric receivers [2] and the improvements required for a viable through-air Lamb wave scanner [3, 4]. Lamb wave scanning is facilitated by coupling the acoustic energy from the ultrasonic transducers into the plate under inspection, at a specified angle of incidence, in order to generate Lamb waves of a given mode. The advantages associated with this form of defect detection are that it allows for rapid in-situ scanning of thin platelet structures, in addition to the ability of Lamb waves to propagate over large distances (~10m) in bulk solids with very little signal degradation. Another important aspect of Lamb wave scanning [5] is the ability to detect disbonds and delaminations in aluminium and carbon-fibre plates.

The improvements necessary to implement such an air-coupled system are not restricted to a single aspect of the design, but rather to the system as a whole. On the transmission side, the drive frequency of the scanner must be optimised to the transmitter electrical resonance, while the receiver must be designed such that the mechanical resonance of the receiver matches the mechanical resonance of the transmitter. It has been shown that this procedure alone will increase the SNR four-fold [3] over conventional pulse-echo testing using a single transducer to both

transmit and receive. Additionally, improvements in SNR can be made in using piezocomposite technology rather than solid piezoceramic transducers and by utilising specialised low-noise receiver electronics.

Farlow [3] has described the application of piezocomposite transducers for the single-sided inspection of thin planar samples using Lamb wave methods. A significant restriction involves the requirement to alter the angular alignment of the transducers to generate Lamb waves within different test specimen. This approach requires that the operator must have a basic understanding of Lamb wave theory in order to align the transducer correctly for efficient Lamb wave generation in plates of differing thickness. By removing the need for angular alignment, one scanning head assembly could be manufactured that would facilitate the inspection of plates with varying thickness without the need for specialist knowledge. This work forms the background for the work covered in this Thesis.

This Thesis undertakes to solve this angular alignment problem by utilising the frequency-thickness (*fd*) product, associated with Lamb wave generation, to effectively beam-steer the acoustic energy by frequency manipulation. The *fd* product is associated with the Lamb wave dispersion characteristics of a given material and is commonly used to determine the phase velocity of a specific Lamb wave mode. This phase velocity then governs the angle of incidence required to efficiently generate Lamb waves in the plate by the simple coincidence principle. However, by tuning the system to generate a Lamb wave at a given *fd* product, the thickness of the plate can be altered as long as the frequency is also changed to keep the *fd* product constant. Hence, this variable frequency system does not change the angle of incidence, rather, retune the same Lamb wave mode within the plate at a different thickness. In order to achieve this, specialised receive electronics have had to be designed and manufactured to provide high gain (>90dB) and good selectivity. Additionally, considerable effort has been made in the design of a novel range of increased bandwidth piezocomposite transducers, which provide good sensitivity and are robust enough for industrial applications.

1.2 Aims and contributions of the Thesis

1.2.1 Aims of the Thesis

- In order to test samples of different thicknesses using Lamb wave techniques, it has been necessary to change the angle of the transducers. Reliability and ease of use would be greatly improved if it were possible to place the transducers in a head assembly that holds them in a fixed position for the lifetime of the equipment. This is particularly true if the equipment is to be used by an unskilled operator.

- More importantly, although it has been possible with earlier fixed frequency Lamb wave scanner to detect defects in a planar sample and to produce images with information on defect position and size, it has not been possible to accurately measure localised changes in thickness. Therefore, the new scanner design should allow the characterisation of defect depth in addition to simple detection.

- In order to implement such a scanning arrangement it is essential that robust wide bandwidth devices, which provide good acoustic impedance matching with air, are developed. Each device should have as wide a -3dB bandwidth as possible, compatible with other system constraints, such as sensitivity and intrinsic noise levels.

- To counteract the losses inherent within an air-coupled piezoelectric NDE system, a specialised electronics unit capable of modulating the received signal to the required frequency, filtering out the spurious and additional frequency components and interfacing with the computer acquisition hardware is necessary. Design and testing of a practical demonstration system, constituted a major goal of the Thesis.

1.2.2 Contributions of the Thesis to the field of air-coupled NDE/NDT

- A novel approach to the generation and detection of fundamental asymmetric Lamb waves within plate structures of varying thicknesses, from a fixed angle of incidence, is proposed. The scanning system incorporates improved piezocomposite transducer technology and specialised receiver electronics in order to counterbalance the influence of attenuation in air and difficulties with air/solid sound propagation.

- A new range of enhanced bandwidth piezocomposite transducers was designed for operation in air. These transducers incorporate modified structure geometry to distribute the thickness mode resonance of individual pillars laterally into surrounding pillars of differing thicknesses. The design process is described in detail, with theoretical and experimental measurements determined for surface displacements and output pressure patterns.

- Using a linear systems model approach, a greater understanding of the influence of noise bandwidth over the achievable signal to noise ratio is determined. This knowledge can then be used to determine the practical limits of filtering within ultrasonic receive systems.

- By theoretical analysis of the noise sources active in an ultrasonic receiver, a specialised amplifier arrangement was designed, capable of operating over a wide range of input frequencies, while still maintaining a narrowband filtering mechanism. This specialised heterodyne amplifier offers a system gain of over 90dB with an exceptional SNR performance of over 40dB.

- A 'frequency-agile' Lamb wave scanner was constructed that is capable of operation on plates of differing thickness from a fixed incident angle and without the need for couplant. This problem utilises the custom built transducers and electronics hardware described above, and is robust enough for industrial applications, e.g. scanning of transit vans panels, aerospace structures, etc.

1.3 Publications to date arising from the Thesis

R. Banks, R. Farlow, G. Hayward, "A Frequency Agile Ultrasonic Lamb Wave Scanner for NDE Systems", Proceedings Ultrasonics International Conference, Delft, Netherlands, 1997.

R. Banks, R. Farlow, G. Hayward, "A Non-Contact Frequency Agile Ultrasonic Lamb Wave Scanner for NDE Systems", Proceedings British Institute of Non-Destructive Testing Conference, Newcastle, UK, 1998.

R. Banks, "ANSYS® modelling as a design tool for Ultrasonic Engineering", Invited speaker at 1998 ANSYS® users conference, Droitwich Spa, UK, September, 1998.

G. Hayward, G. Benny, W. Galbraith, R. Banks, "The radiation field characteristics of piezopolymer membrane transducers when operating in air", Accepted for publication in IEEE transactions on Ultrasonics, Ferroelectrics and Frequency Control.

R. Banks, R. Farlow, G. Hayward, "A Frequency Agile Ultrasonic Lamb Wave Scanner for NDE Systems", Insight, Vol. 39, No. 11, November, pp.780-784, 1997.

Paper awarded The John Grimwade Medal for the best paper published in Insight in 1997.

1.4 Overview of Thesis

Chapter 2: Theoretical background and review of transducer technology

This Chapter introduces the theory associated with acoustic waves propagating between different media, covering boundary interactions of normal and oblique incidence. Using these boundary conditions, a mechanism to determine insertion losses for ultrasonic inspection systems is detailed. Additionally, theory pertaining to Lamb wave propagation in thin plates is described, highlighting the dependence of such waves on the thickness and frequency of the load medium. Subsequently, a review of available sensor technology is presented citing their applicability to air-coupled operation. Finally, system requirements are discussed for an air-coupled single-sided ultrasonic scanner capable of thickness gauging and defect detection in thin planar samples.

Chapter 3: Noise theory and receiver system design

This Chapter reviews some of the associated noise sources active within a typical ultrasonic receiver and illustrates their influence on the overall signal to noise ratio. A linear systems model [72] is used to theoretically describe this problem. Further to this, the need for tuneable bandpass filtering to reduce the noise bandwidth of the reception electronics is discussed, in which, the principles of modulation and heterodyne theory are introduced. The design of the receive system electronics is then described, detailing the different component sections and their performance is measured experimentally.

Chapter 4: Theoretical techniques for assessment of piezocomposite transducer system performance

This Chapter illustrates the design process and methodology associated with modelling an ultrasonic transducer. The finite element method utilised in this Thesis for the modelling of piezoelectric transducers was the commercial version of the ANSYS® [79] code, version 5.4 with no nodal or element restrictions. The design criteria concerning boundary limitations and reduction of computation time by symmetrical minimisation are discussed. In addition to ANSYS®, a brief review is presented of the theoretical beam profiling package developed within the Ultrasonic

laboratories in the University of Strathclyde, to characterise the output pressure field and surface displacements of ultrasonic transducers.

Chapter 5: Development of a new range of wideband piezocomposites

This Chapter details previous investigations on the enhancement of sensor bandwidth in the piezocomposite field and proposes an alternative method for transducer configuration and construction. Using ANSYS®, the new transducer configurations are evaluated and compared with results determined experimentally. Of greatest importance, is the surface displacement and output pressure field characteristics of the new transducers.

Chapter 6: Performance of the new Lamb wave scanner

This Chapter describes the progression of the scanner design from its original conceptual prototype, incorporating electrostatic transducers, in order to verify the feasibility of tuning for differing thickness by frequency manipulation, to the final design incorporating the enhanced bandwidth piezocomposites. Results are presented using both transducer configurations for plates of differing thicknesses and importantly, defect detection is demonstrated in both aluminium and carbon fibre. Additionally, defect detection and characterisation is described for non-planar practical examples.

Chapter 7: Conclusions and recommendations for further work

The resultant system is reviewed with respect to the initial stipulated guidelines and comments made on the overall performance of the system. Conclusions are drawn on the effectiveness of the new receiver electronics and the new transducer technology. Further to this, suggestions are made for future work on improving the system and improving the efficiency of the transducers.

Chapter 2

Theoretical background and a review of transducer technology

2.1 Introduction

The field of *ultrasonics*, is the study of sound outwith the frequency range of audible perception to the human ear, i.e. above approximately 18kHz. First discovered in 1883 by Galton [6] during studies to determine the acoustic bandwidth of the human ear and resulted in the first recognised ultrasonic transducer, the dog whistle (A transducer being described as a device which converts energy from one form to another). It was also around the time, that the first observations of the *piezoelectric effect* [7] in crystalline structures had been made by J. and P. Curie in 1880. The piezoelectric effect is the ability of the crystalline structure to develop an electric charge proportional to the mechanical stress placed upon the composition. Conversely, when an electrical field is exerted on the structure, the material will deform proportionally, this is referred to as the inverse piezoelectric effect.

However, it was not until the First World War, between 1914-1918, that the piezoelectric effect was utilised in a practical ultrasonic application. A Frenchman, Langevin [8] investigated the use of quartz transducers for both transmission and reception of ultrasound in water, which lead to a rapid growth in ultrasonic research in the years between the two world wars. During this time, research was carried out on the acoustic properties of liquids and gases, as well as the first documented work on ultrasonic flaw detection in solids by Sokolov [6,8] in 1934. Although the Second World War interrupted some public academic activities in ultrasonic applications research, further insights were made into materials research, with the discovery of a high dielectric ceramic composition of barium titanate, in 1941. Due to wartime restrictions, this knowledge did not reach the public domain until 1944, by which time several other publications had been made relating to the phenomenon. The most significant innovation of this time, was the discovery of the *poling process.* That is, the application of a sufficiently high voltage to realign the polarisation of the ceramic structure, such that all the dipoles are aligned parallel to the applied electric field. These advances in materials research in conjunction with other wartime discoveries, such as RADAR/SONAR, lead to the development of pulsed ultrasound techniques and thus to applications in non-destructive testing and biomedicine.

The 1960's brought the advent of another ceramic material, lead zirconate titanate (PZT) which has become the most dominant form of ceramic utilised in the ultrasonic industry to date. This form of ceramic has a very strong piezoelectric effect and through alteration of the zirconium/titanate ratio and the introduction of impurities, can be tailored to specific application needs.

2.2 Ultrasonic inspection

In recent years, the expansion of ultrasonics into both the industrial and biomedical environment has been vast, with ultrasound being utilised for various applications from range sensors and thickness gauge measurements [8], to paper roughness measurement [9] and non-contact inspection [3]. It is this latter topic of research which this Thesis is mainly concerned with, namely the inspection of planar structures without the need for coupling fluid. The rest of this Chapter deals with the theory governing the propagation of sound waves in differing layered media, highlighting some of the problems inherent with transferring acoustic energy between air and solid media. Additionally, a review of available transducer technology is presented citing examples of applications in both contact and non-contact operation

As stated previously, the earliest recorded flaw detector was tested in the 1930's and although this work was groundbreaking, it was of little value. It was not until the Second World War, with the introduction of pulsed techniques that the first true flaw detection in solids was completed by Sproule [8]. In pulse mode operation, the transducer emits a short burst of ultrasound consisting of a few wavelengths into the specimen under examination. The ultrasound then travels through the material and is reflected from any boundary with which the sound is incident. These reflections are then received either on the original transmitting device *(pulse-echo)* or on a second transducer *(pitch-catch)*, as illustrated in Figure 2.01.

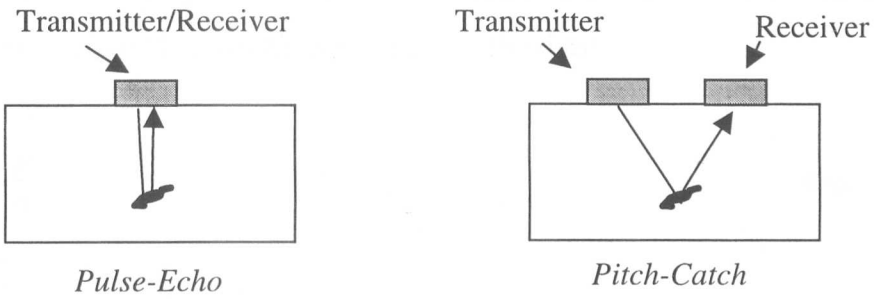

Figure 2.01 *Differing scanning configurations*

Traditionally, such ultrasonic systems are implemented through direct contact between the transducer and the material under examination. A significant problem with this arrangement is that in order to efficiently couple the sound between source and target the transducers must be bonded to the sample, or connected via a *coupling fluid.* This coupling fluid is required in the majority of ultrasonic inspection systems to overcome the large acoustic impedance mismatch between air and high acoustic impedance media, such as steel or aluminium.

2.2.1 Reflection and transmission at normal incidence

Consider a simple ultrasonic inspection system, with a single transducer located a distance, d, from the test piece, as illustrated in Figure 2.02. Assuming that the output of the transducer is planar and at a single frequency, the sound transmitted will be incident to the plane boundary of the test piece under investigation. Consequently, a proportion of the sound hitting the planar boundary will be reflected back towards the transducer and the remainder of the sound will be transmitted into the sample.

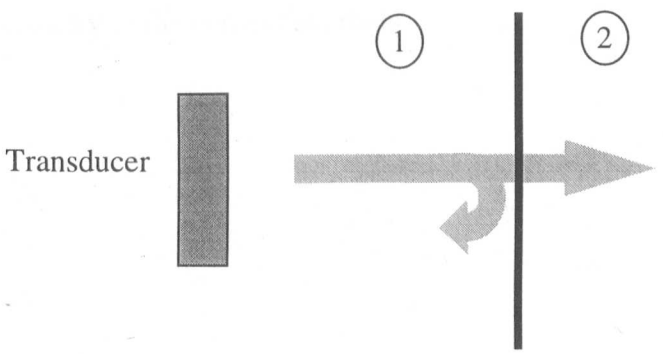

Figure 2.02 *Wave propagation between two planar coincident mediums*

Both the medium of propagation and the medium into which the sound is being transmitted have a *specific acoustic impedance*, defined as:

$$Z_a = \frac{p}{u} \qquad \textbf{Eqn. 2.01}$$

where,

p = the acoustic pressure (or stress) developed by the mechanical wave

u = the particle velocity of the mechanical wave

Impedance is, a complex quantity, but for plane waves propagating in an isotropic, lossless medium, this can be re-written as follows and is referred to as the *characteristic impedance* of the material:

$$R_a = \rho c \qquad \textbf{Eqn. 2.02}$$

where,

ρ = the density of the material

c = the velocity of the sound within the material

Now, consider again the case of the sound wave on the planar boundary. It assumed that the boundary is lossless in that all the pressure of the incident wave is converted to reflected or transmitted pressure. In addition, the particle velocities on both sides of the boundary must be balanced (i.e. the velocities of the reflected and transmitted wave must a product of incident wave). Figure 2.03 represents the wave incident upon the boundary in terms of acoustic pressure p_i, p_t and p_r which represent the contributions from the incident, transmitted and reflected wave respectively, while u_i, u_t and u_r define the particle velocity in the constituent parts.

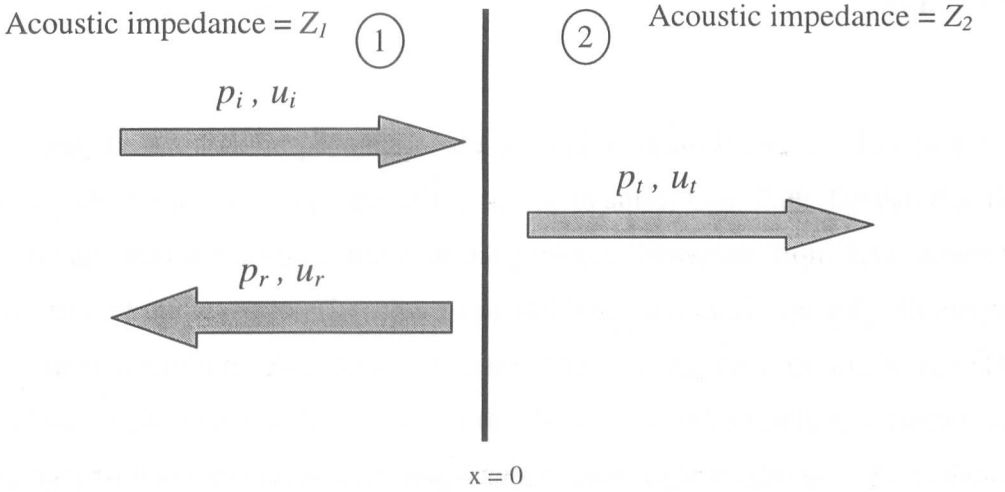

Figure 2.03 *Boundary conditions for normal incidence*

Hence,

$$p_i = A_i sin(\omega t - k_1 x) \quad = \quad u_i Z_1 \qquad \textbf{Eqn. 2.03}$$

$$p_r = A_r sin(\omega t + k_1 x) \quad = \quad -u_r Z_1 \qquad \textbf{Eqn. 2.04}$$

$$p_t = A_t sin(\omega t - k_2 x) \quad = \quad u_t Z_2 \qquad \textbf{Eqn. 2.05}$$

A_i, A_r and A_t represent the amplitudes of the respective waves and k_1 and k_2 the wave numbers. While x is positive in the direction of the incident beam. Hence putting $x = 0$ at the boundary and respecting the previous boundary conditions to preserve continuity.

$$A_t = A_i + A_r \qquad \textbf{Eqn. 2.06}$$

and:

$$Z_2 A_t = Z_1(A_i + A_r) \qquad \textbf{Eqn. 2.07}$$

thus:

$$\frac{p_t}{p_i} = \frac{A_t}{A_i} = \frac{2Z_2}{Z_1 + Z_2} \qquad \textbf{Eqn. 2.08}$$

and:

$$\frac{p_r}{p_i} = \frac{A_r}{A_i} = \frac{Z_2 - Z_1}{Z_1 + Z_2} \qquad \textbf{Eqn. 2.09}$$

Additionally,

$$\frac{u_t}{u_i} = \frac{A_t Z_1}{A_i Z_2} = \frac{2Z_1}{Z_1 + Z_2} \qquad \textbf{Eqn. 2.10}$$

and:

$$\frac{u_r}{u_i} = -\frac{A_r}{A_i} = \frac{Z_1 - Z_2}{Z_1 + Z_2} \qquad \textbf{Eqn. 2.11}$$

Hence, when the acoustic impedance of the second medium is greater than that of the medium in which the wave is propagating, i.e. air to solid, Eqn. **2.09** dictates that there will not be any phase change in the acoustic pressure. However, Eqn. **2.11** shows that there will be a phase inversion (i.e. change of 180°) in the particle velocity. Conversely, when the second medium, Z_2 is less than that of the first, Z_1, the opposite is true. Thus, the *amplitude reflection coefficient, R_a,* is the ratio of sound amplitude reflected from the boundary to that incident and the *amplitude transmission coefficient, T_a,* is the ratio of sound amplitude transmitted into the second medium from the incident wave.

$$R_a = \frac{Z_2 - Z_1}{Z_1 + Z_2} \qquad \textbf{Eqn. 2.12}$$

$$T_a = \frac{2Z_2}{Z_1 + Z_2} \qquad \textbf{Eqn. 2.13}$$

The ratio of energy reflected by the second medium at the boundary is defined as the *intensity reflection coefficient*, α_r, which is defined as the ratio of the intensity, reflected by the wave, I_r, to that of the wave incident at the boundary, I_i. Additionally the amount of energy transferred into the second medium is governed by the *intensity transmission coefficient*, α_t. With the ratio governed by the intensity of the transmitted wave, I_t, to that of the incident wave. Again, assuming a lossless boundary transfer. Thus,

$$I_i = I_t + I_r$$

Therefore,

$$\alpha_r + \alpha_t = 1 \qquad \textbf{Eqn. 2.14}$$

Furthermore, intensity is proportional to the source acoustic pressure.

$$I = \frac{\frac{1}{2}p^2}{\rho c} \qquad \textbf{Eqn. 2.15}$$

Hence by substitution of Eqn. **2.14** into Eqns. **2.09** and **2.11.**

$$\alpha_r = \frac{I_r}{I_i} = \frac{A_r^2}{A_i^2} = \left(\frac{Z_2 - Z_1}{Z_1 + Z_2}\right)^2 \qquad \textbf{Eqn. 2.16}$$

and from Eqn. **2.14**

$$\alpha_t = 1 - \alpha_r = \frac{4Z_1Z_2}{(Z_1 + Z_2)^2} \qquad \textbf{Eqn. 2.17}$$

It is apparent that as the acoustic impedance of the medium into which sound is being transmitted, Z_2, increases with respect to Z_1, the amount of sound reflected from the boundary will increase toward 100% reflection. Therefore considering a practical example, Figure 2.02, where ultrasound is being propagated between a piezoceramic transducer and a steel test plate, through a water medium. The system can be represented as a 4-layer boundary system, as illustrated in Figure 2.04.

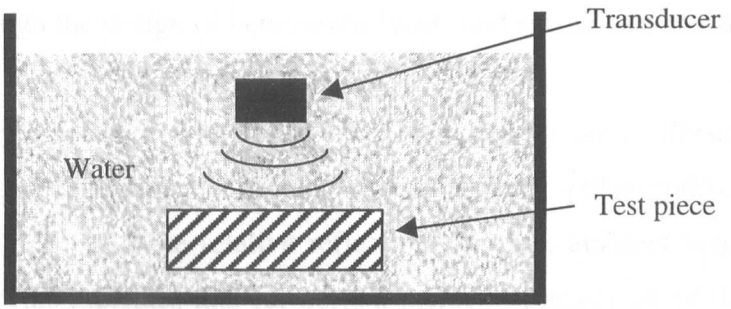

Figure 2.04 *Boundary conditions for pulse-echo system in water*

The specific acoustic impedance [10] of each medium is given below and the assumption is made that the materials are in direct contact:

Piezoceramic	-	33 MRayls
Water	-	1.5 MRayls
Steel	-	47 MRayls

Utilising Eqns. **2.12** and **2.13** the insertion loss of the acoustic signal travelling from the transducer to the rear face of the steel block and back again can be calculated. Note that a special case exists in the amplitude transmission coefficient from the ceramic transducer, as given in Eqn. **2.18**.

$$T_{transducer} = \frac{Z_2}{Z_1 + Z_2}$$ **Eqn. 2.18**

This is because the transducer radiates sound energy equally from both faces of the transducer, hence the amplitude transmission coefficient from one face will be half that normally described by the equation. In this example, the overall insertion loss within the pulse-echo arrangement for a signal reflected from the rear face of the block under inspection is 0.009 or -41dB. However, if the water medium is replaced by that of air, with a specific acoustic impedance of 0.000434 MRayls, then the insertion loss within the system now becomes 9.75×10^{-10} or –180dB. It is evident from these two calculations that the replacement of the water coupling by that of air leads to a significant degradation in system sensitivity of –139dB. Therefore, in order to design a viable air-coupled inspection system for non-destructive testing (NDT), these losses must be overcome through the design of better transducers and specialised electronics.

An additional problem associated with pulse-echo operation in air is illustrated by calculating the amplitude reflection coefficient for the acoustic pulse contacting the steel test piece. Using Eqn. **2.12** the relative reflection from the air/steel boundary is given as 0.99 or 99%. This indicates that for normal incidence, nearly all of the signal incident on the steel test piece is reflected. Therefore, due to the fact that the pre-amplifier circuitry will have to incorporate high levels of gain to overcome the insertion losses within the system, it is very likely that the initial reflection from the air/steel boundary would saturate the receiver electronics. One possible method to protect against this, is to include a electronic gating mechanism in the receive electronics which would deactivate the receiver until the initial reflection had passed. However, since the speed of sound in steel or other such metals is high, $>5000 ms^{-1}$, the wave travelling through the test specimen would arrive approximately 1μs after the front face reflection for a 2mm thick steel sample. Such a gating system is impractical, as it is not feasible to design a amplifier which will a) recover from saturation, or b) switch on in such a short period of time. Hence another solution must be investigated.

2.2.2 Reflection and transmission of sound at angles of incidence

Section 2.2.1 illustrated the practical problems associated with air-coupled, single sided pulse-echo inspection techniques. One possible solution is the introduction of a second transducer to act as a separate receiver, known as the pitch-catch technique. When configured as a single sided NDE system, both the transmitting and receiving ultrasonic transducers must be positioned at an angle off the normal. This is illustrated in Figure 2.05, where a longitudinal wave is incident with a planar boundary at an angle, θ_1.Here, a portion of the energy is reflected from the boundary and importantly, some of the energy is transferred into the sample and is partly confined due to internal reflection.

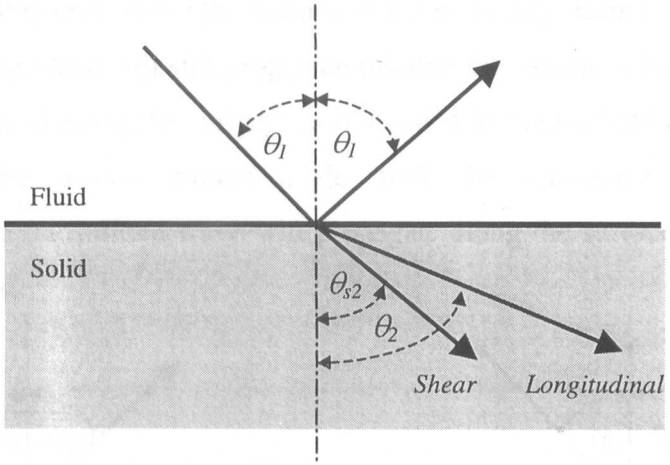

Figure 2.05 *Reflection and refraction of an angular incident beam on a planar boundary*

In the case of water/solid or air/solid boundaries, only the solid medium will support shear wave propagation in the refracted waves, meaning that mode conversion of the incident signal will take place at the boundary. This assumption is made to reduce the overall complexity of the system, although Poisson [6] suggests that a liquid may support such a shear stress for a very limited period of time. The acoustic pressure incident on the boundary is divided into two components, a shear and longitudinal (or compressive) stress. Both of which propagate with different speeds and directions within the solid medium governed by Snell's law [11] as follows:

$$\frac{c_1}{\sin\theta_1} = \frac{c_2}{\sin\theta_2} = \frac{c_{s2}}{\sin\theta_{s2}} \qquad \textbf{Eqn. 2.19}$$

Where, c_1 and c_2 are the longitudinal velocities in medium 1 and 2 and c_{s2} is the shear wave velocity in the solid medium 2. θ_1 represents the angle of incidence and reflection of the incident wave in the first medium, θ_2 is the angle of propagation of the longitudinal component of the wave in the solid medium and finally θ_{s2} is the angle of refraction for the shear wave within the solid media.

As illustrated in Figure 2.05, three waves are generated at the fluid/solid interface. However, as the angle of incidence is increased there are three *critical angles,* which influence the transmission of sound into the sample. These are the angles at which the longitudinal and transverse components of the incident wave are refracted to such a degree that they propagate along the surface of the boundary. Hence, at the first critical angle the transverse wave will still propagate through the sample, while the longitudinal wave will be directed along the surface, as illustrated in Figure 2.06(a). As the angle is increased past the second critical angle, both the transverse and longitudinal components of the transmitted wave will propagate along the surface of the boundary, see Figure 2.06(b).

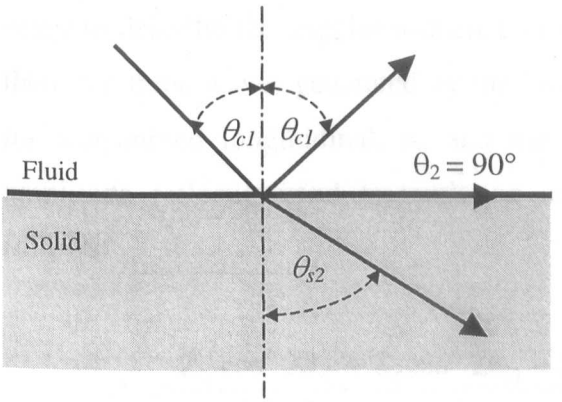

Figure 2.06(a) *First critical angle*

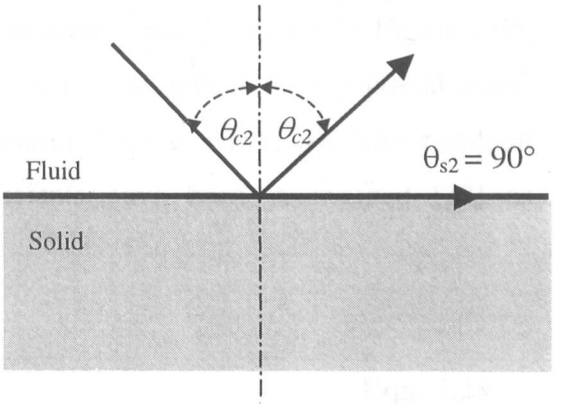

Figure 2.06(b) *Second critical angle*

Beyond the second critical angle, a third condition occurs where more of the energy is coupled into the solid in the form of surface waves. This is marked by a decrease in the intensity of the reflected wave and the waves propagating along the boundary are referred to as *Rayleigh waves.* The equations governing these critical angles are given by:

$$c_2 = \frac{c_1}{\sin\theta_{c1}} \qquad \textbf{Eqn. 2.20}$$

$$c_{s2} = \frac{c_2}{\sin\theta_{c2}} \qquad \textbf{Eqn. 2.21}$$

$$c_R = \frac{c_1}{\sin\theta_{c3}} \qquad \textbf{Eqn. 2.22}$$

Where, c_R is the Rayleigh wave velocity and θ_{c1}, θ_{c2} and θ_{c3} are the first to third critical angles respectively.

2.2.3 Calculation of insertion losses at oblique angles

In the case of a wave incident on a fluid/solid boundary at an oblique angle of incidence, as illustrated in Figure 2.05, the interaction of the waves within the system is considerably more complex than that of normal incidence. As a result, the equations governing the amplitude reflection and transmission coefficients are more complex in order to describe the angular influence of the incident wave. Referring to Figure 2.05, there are three waves generated by the incident wave, the reflected longitudinal wave, p_{rl}, transmitted longitudinal, p_{tl} and the transmitted shear wave, p_{ts}. The resultant amplitude reflection and transmission coefficients have been determined [12] as follows:

$$R_L = \frac{Z_2\cos^2 2\theta_{s2} + Z_T\sin^2 2\theta_{s2} - Z_1}{Z_2\cos^2 2\theta_{s2} + Z_T\sin^2 2\theta_{s2} + Z_1} \qquad \textbf{Eqn. 2.23}$$

$$T_L = \frac{2Z_2\cos 2\theta_{s2}}{Z_2\cos^2 2\theta_{s2} + Z_T\sin^2 2\theta_{s2} + Z_1} \qquad \textbf{Eqn. 2.24}$$

$$T_T = -\frac{2Z_T\sin 2\theta_{s2}}{Z_2\cos^2 2\theta_{s2} + Z_T\sin^2 2\theta_{s2} + Z_1} \qquad \textbf{Eqn. 2.25}$$

Where, R_L is the reflection coefficient for the longitudinal wave and T_L and T_T are the transmission coefficients for the longitudinal and shear components respectively. The impedance, Z_1, is defined as the mechanical impedance of the sound wave travelling in

the fluid, while Z_2 and Z_T, define the impedance of the longitudinal and shear wave propagating in the solid respectively.

Now consider the opposite conditions, with an acoustic wave propagating from a solid into a fluid medium, as illustrated in Figure 2.07.

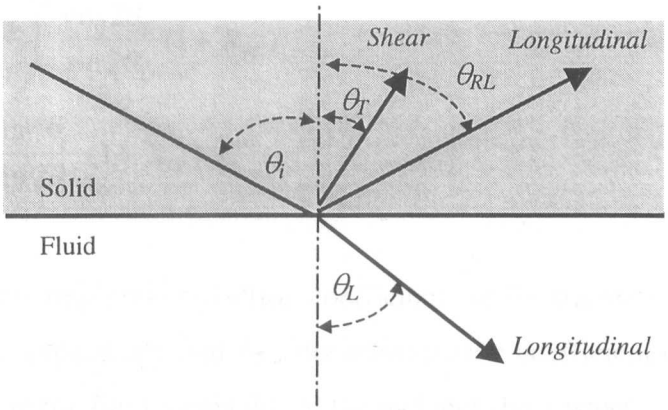

Figure 2.07 *Mode changing at a solid/fluid boundary*

In this case, the solid medium will support both longitudinal and shear waves propagating within its boundaries. Therefore, both wave situations must be considered in the analysis of a wave incident upon the solid/fluid boundary. Both result in three new waves being produced, these comprise the transmitted longitudinal wave into the fluid and the reflected longitudinal and shear components within the solid. Firstly, consider an incident longitudinal wave, where the relative coefficients are given as follows.

$$R_{LL} = \frac{Z_1 + Z_T \sin^2 2\theta_T - Z_1 \cos^2 2\theta_T}{Z_1 + Z_T \sin^2 2\theta_T + Z_1 \cos^2 2\theta_T} \qquad \textbf{Eqn. 2.26}$$

$$R_{LT} = \left(\frac{c_s}{c_2}\right)^2 \frac{\sin 2\theta_L}{\cos 2\theta_T}(1 - R_{LL}) \qquad \textbf{Eqn. 2.27}$$

$$T_{LL} = \frac{\rho_1}{\rho_2} \frac{c_1 \cos\theta_L}{c_2 \cos\theta_i \cos^2 2\theta_T}(1 - R_{LL}) \qquad \textbf{Eqn. 2.28}$$

Here, R_{LL} and T_{LL} are the amplitude reflection and transmission coefficients for the longitudinal wave and R_{LT} is the reflection coefficient of the transverse (or shear) wave

generated by the incident longitudinal wave. Secondly, consider the resultant coefficients for a shear wave within the solid, incident on the solid/fluid boundary.

$$R_{TT} = \frac{Z_1 + Z_2 \cos^2 2\theta_T - Z_T \sin^2 2\theta_T}{Z_1 + Z_2 \cos^2 2\theta_T + Z_T \sin^2 2\theta_T} \qquad \textbf{Eqn. 2.29}$$

$$R_{TL} = -\left(\frac{c_2}{c_T}\right)^2 \frac{\cos 2\theta_T}{\sin 2\theta_L}(1 + R_{TT}) \qquad \textbf{Eqn. 2.30}$$

$$T_{TL} = \frac{\rho_1}{\rho_2}\frac{\tan\theta_i}{\sin 2\theta_L}(1 + R_{TT}) \qquad \textbf{Eqn. 2.31}$$

R_{TT} and R_{TL}, are the amplitude reflection coefficients of the transverse and longitudinal wave components respectively and T_{TL}, the transmission coefficient of the longitudinal wave propagating in the fluid media due to the incident shear wave.

Thus, knowing the amplitude reflection and transmission coefficients for both fluid/solid and solid/fluid boundary conditions, the echo coefficients for longitudinal and shear wave propagation in the solid medium can be determined from an acoustic wave incident at an oblique angle. Whereby, E_L is the echo coefficient for the purely longitudinal wave and E_T the transverse propagating the solid media for a pitch-catch system operating at an oblique incidence.

$$E_L = T_L R_{LL} T_{LL} \qquad \textbf{Eqn. 2.32}$$

$$E_T = T_T R_{TT} T_{TL} \qquad \textbf{Eqn. 2.33}$$

Using a mathematical software package developed by R. Farlow [13], the echo coefficients for the transverse propagated wave (Eqn. **2.33**) can be plotted as a function of angle of incidence as illustrated in Figures 2.08 and 2.09 for a water/steel and air/steel boundary respectively.

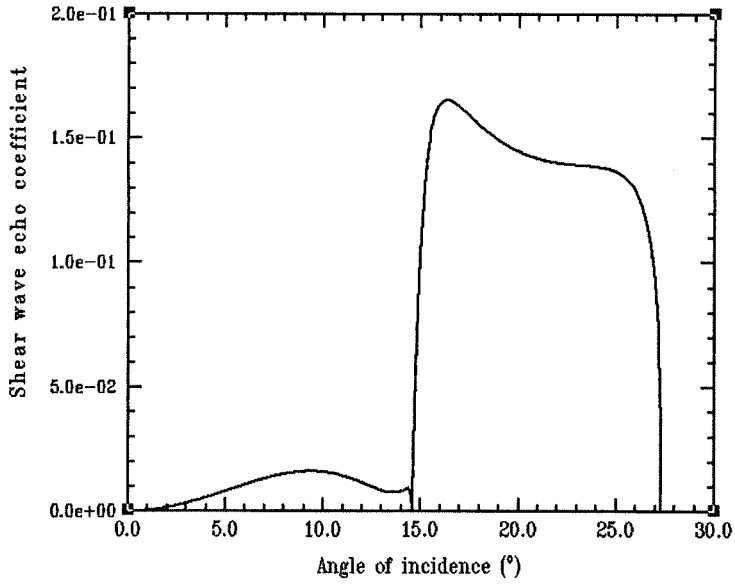

Figure 2.08 *Shear wave echo coefficient (E_T) for water/steel boundary*

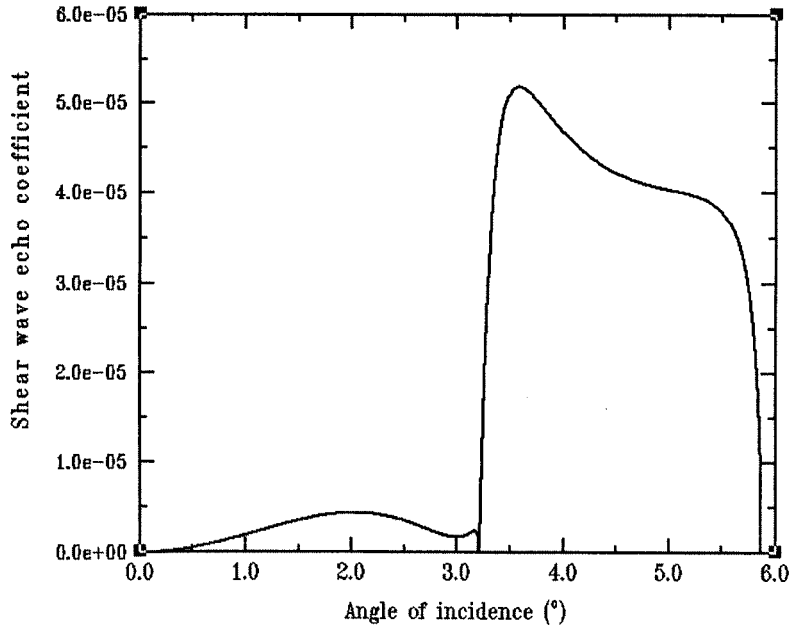

Figure 2.09 *Shear wave echo coefficient (E_T) for air/steel boundary*

By examination of the Figures 2.08 and 2.09 it is apparent that the losses involved in air coupled operation compared to water coupling are considerably higher, as the maximum echo coefficient for the air boundary condition is substantially reduced. Moreover, the critical angle for operation in air is notably smaller than that of the critical angle for the water coupled example.

Hence, the '2-way' loss for the longitudinal and shear waves propagating in an air-coupled system with a single reflection from the rear face of the sample, see Figure 2.10, can be determined.

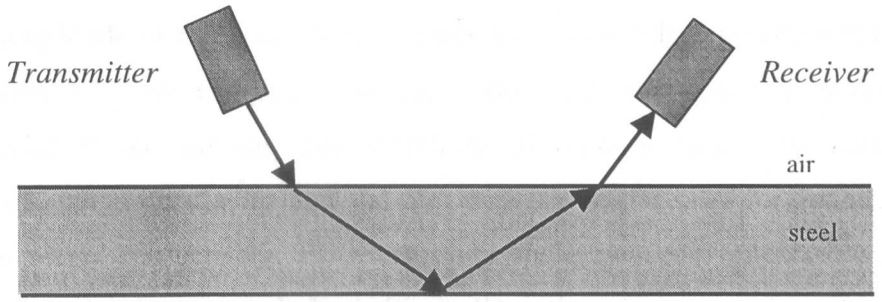

Figure 2.10 *Arrangement for simple air-coupled pitch–catch system*

In this example, the total '2-way' loss for a pitch-catch inspection system operating at an angle off normal incidence, with only a single reflection from the rear face of the solid sample can be calculated by combining Eqns. **2.13, 2.18, 2.32** and **2.33**.

$$(\text{2-way loss})_{\text{Longitudinal}} = T_{\text{Transducer}} E_L T_a \quad \text{(Longitudinal wave in sample)} \qquad \textbf{Eqn. 2.34}$$

$$(\text{2-way loss})_{\text{Shear}} = T_{\text{Transducer}} E_T T_a \quad \text{(Transverse wave in sample)} \qquad \textbf{Eqn. 2.35}$$

Therefore, the total '2-way' loss for a pitch-catch air-coupled system generating shear waves within a steel plate sample at the peak echo coefficient of $5.0\text{x}10^{-5}$ at 3.5° can be calculated from Eqn. **2.35** as $1.42\text{x}10^{-9}$ or -176dB. In comparison, a similar system operating in water has an overall insertion loss of 0.0139 or -37dB from the peak echo coefficient of 0.168 at an angle of 16°. It is thus apparent that the total insertion loss suffered by a system operating in pitch-catch mode at oblique angle incidence (-176dB) is comparable with that of pulse-echo normal incidence (-180dB). Moreover, as a substantial portion of the wave propagating in the steel plate is reflected (in the case of the air/steel boundary), there will be very little increase in insertion loss for a signal detected after 100 internal reflections in comparison to after just one reflection. This allows the transducers to be spaced further apart and therefore allows for the possibility of scanning larger areas.

2.3 Rayleigh and Lamb waves

Rayleigh waves [14], named after the English scientist Lord Rayleigh, are waves that propagate across the surface of a solid material. The vibrations are extremely localised, with the amplitude of the wave decaying rapidly with depth, typically not penetrating greater than two wavelengths into the solid, and their particle polarisation is perpendicular to the surface. The vibrations of these particles are split into two components, perpendicular to and parallel with the surface, as for longitudinal and transverse waves respectively. However, since these two components have differing velocities the vibrations are polarised elliptically with a continuous change in phase and shape in a cyclic manner.

However, when the thickness of the test piece is reduced such that the surface wave can penetrate to the opposite side, Rayleigh waves degenerate into *Lamb* or *plate* waves [14]. As a rule of thumb, Rayleigh waves only penetrate into the thickness of a plate by less than two wavelengths. Thus, Lamb wave displacement occurs in the direction of wave propagation and perpendicularly to the plane of the plate. Lamb waves are two-dimensional propagating vibrations of which there are two fundamental types, *symmetrical* (or stress) waves and *anti-symmetrical* (or bending) waves which can exist in theory at an unlimited number of modes. Figure 2.11 illustrates the particle displacement associated with both of these Lamb waves classes, noting that particles in the middle of the plate vibrate purely transversally for the asymmetrical wave and as a pure longitudinal wave for the case of the symmetrical mode, while all other particles vibrate elliptically.

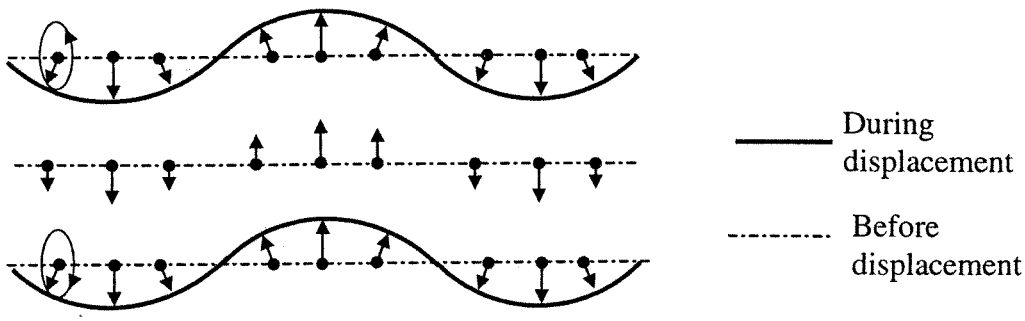

Figure 2.11(a) *Anti-symmetrical Lamb wave*

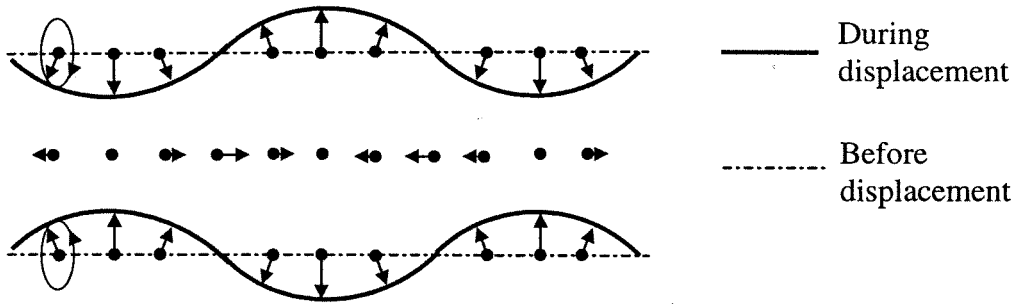

Figure 2.11(b) *Symmetrical Lamb wave*

In order to understand how Lamb waves are produced, it is convenient to refer to Figure 2.12. As the plate thickness is reduced and the fluid/solid boundaries move closer together, a point is reached where it becomes impossible for the fundamental longitudinal and shear waves to propagate independently along the plate. When this occurs, energy will propagate most efficiently along the plate at those frequencies for which the various reflected components combine in or out of phase at regular intervals along the length of the plate. For a given frequency of operation and a given plate thickness this is possible for a finite number of Lamb wave modes.

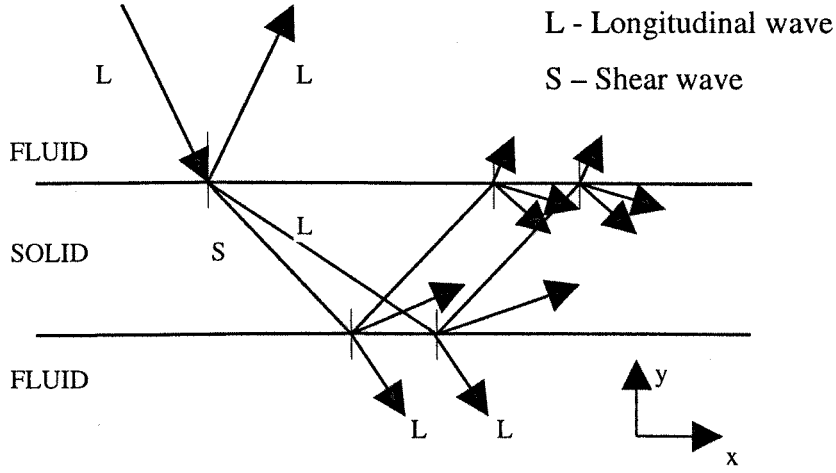

Figure 2.12 *Longitudinal and shear wave propagation in solids*

For a plate of given thickness, 2d, at a particular frequency, f, a finite number of symmetrical and anti-symmetrical Lamb wave modes can exist, differing from one another by their phase and group velocities and displacement distribution. The phase velocities for these modes can be determined by solving the transcendental equations derived by Viktorov [14] for the frequency-thickness product.

Symmetrical modes

$$\frac{\tanh \pi fd}{\tanh \pi fd} \frac{\sqrt{\frac{v_S^2 - v^2}{v_S^2 v^2}}}{\sqrt{\frac{v_L^2 - v^2}{v_L^2 v^2}}} = \frac{4\sqrt{\left(1 - \frac{v^2}{v_L^2}\right)\left(1 - \frac{v^2}{v_S^2}\right)}}{\left(2 - \frac{v^2}{v_S^2}\right)} \qquad \textbf{Eqn. 2.36}$$

Anti-Symmetrical modes

$$\frac{\tanh \pi fd}{\tanh \pi fd} \frac{\sqrt{\frac{v_S^2 - v^2}{v_S^2 v^2}}}{\sqrt{\frac{v_L^2 - v^2}{v_L^2 v^2}}} = \frac{\left(2 - \frac{v^2}{v_S^2}\right)}{4\sqrt{\left(1 - \frac{v^2}{v_L^2}\right)\left(1 - \frac{v^2}{v_S^2}\right)}} \qquad \textbf{Eqn. 2.37}$$

Where, v_L and v_S are longitudinal and shear wave velocities, respectively, in the plate and v is the phase velocity of the Lamb wave. Thus, utilising software, such as Disperse [15] developed at Imperial College, London, the frequency-thickness product can be utilised to produce phase velocity dispersion curves for both symmetrical and anti-symmetrical modes in for example steel, as illustrated in Figure 2.13.

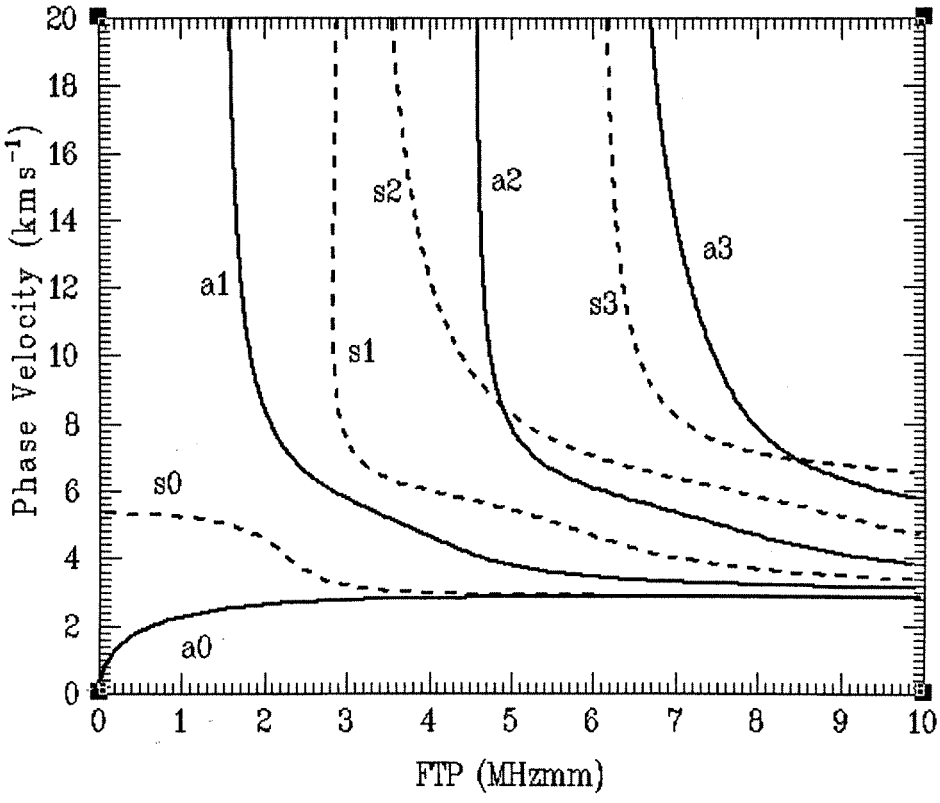

Figure 2.13 *Dispersion curves for Lamb waves in steel*

Note, that for brevity, symmetrical and anti-symmetrical waves are referred to as s_n *and* a_n waves, where n denotes the wave number. Hence the fundamental modes for both are s_0 and a_0 respectively.

Therefore having determined the phase velocity of the Lamb wave, it is possible to calculate the angle of incidence required using the coincidence principle, where θ_i, is the angle of incidence, v_i, is the velocity of sound in the surrounding media and v, is the phase velocity in the plate.

$$\sin(\theta_i) = \frac{v_i}{v} \qquad \textbf{Eqn. 2.38}$$

The use of Rayleigh and Lamb waves has broadened the scope available for ultrasonic inspection, from the original methods that exclusively utilised longitudinal and transverse wave propagation. The inherent problem with the original methods was that the object under test generally had to have greater dimensions than the wavelength of the ultrasound that was used to test the sample. This effectively limited the types of material that could be examined and thin-walled structures and surfaces had to be tested by other means such as X-rays or magnetic means. However, the application of Rayleigh and Lamb waves greatly facilitates such inspection without recourse to prohibitively high frequencies.

2.4 Ultrasonic sensor technology

As a result of the advances in material science, there are a wide range of devices for the generation and reception of ultrasonic energy. These are commonly referred to as ultrasonic transducers and are divided into various categories.

- Optical methods
- Electromagnetic
- Piezoelectric
- Electrostatic

These different categories of transducer are now explained, citing references to promote the understanding of the mode of operation and applications of the sensor in the ultrasonics industry. Although this Thesis deals primarily with non-contact inspection, transducer technology pertaining to both contact and non-contact scanning methods are examined, with the advantages and disadvantages both highlighted.

2.4.1 Laser generated ultrasound

The application of laser generated through-air ultrasound has been of great interest in the non-destructive testing and evaluation (NDT/NDE) fields over the past decade, due to the non-contact nature and potential for rapid scanning. Optically generated ultrasound should also, theoretically, provide better defect resolution due to the smaller transmitted wavelength and focussed nature of the transmitter. There are several methods by which a pulsed laser can generate ultrasonic waves in both solids and liquids [16]. The two most common methods are *thermoelastic* generation and *ablation*. Thermoelastic generation is facilitated by the heating of the specimen under examination through absorbed energy from the pulsed laser, until thermal expansion occurs. This form of generation favours the formation of shear wave stresses [17] within the test piece. Alternatively, ablation is the systematic evaporation of a previously applied coating upon the substrate, a coating that can in turn alter the acoustic characteristics of the material under inspection. Moreover, the ablative generation method produces a more dominant longitudinal signal.

Optical detection of ultrasound is achieved through a number of methods [18], including *interferometry,* where the mechanical displacement of the surface is transferred into electrical energy and *non-interferometric* methods such as surface-grating or knife-edge techniques which sense beam deviation in the reflected signal. The sensitivity of this form of ultrasonic generation and detection is dependent on a number of factors such as light absorption and scattering in the transmission media and the quantity of light reflected from the inspected surface. However, as concluded by Wagner [19], conventional piezoceramic transducers are still more sensitive than optical detection from a highly reflective surface. Moreover, the ideal conditions for laser generated ultrasound include a highly absorptive material surface with is contradictive of the good reflective properties required for detection.

Although laser generated ultrasonic systems have not found the *widespread* implementation that was originally perceived, primarily due to the problems indicated, much work has been done in the NDT field using this technology. Hoyes et al. [1] describe a non-contact laser defect imaging system capable of ultrasonic generation and detection of a 4mm drill hole with 0.5mm resolution. In this system, the laser system itself was stationary with the sample under inspection mounted on an X-Y positional table for manipulation. Similarly, Dewhurst et al. [20] presented a system for detection and characterisation of defects in carbon fibre composites. Defects were simulated by the inclusion of PTFE sections during the manufacture of the multi-layer carbon structure between 1-20mm thick, defect sizes ranged from 6mm x 6mm to 3mm x 3mm. Although the defects were visualised, the scanner only had a resolution of 1mm and the overall scanning time was an hour for a 40 by 46 pixel image. As with the previous example, the disadvantage of such a system is the need for the scanning head to be fixed with the sample being manipulated by a secondary positional assembly. This effectively restricts the number of applications suitable for this system as well as substantially increasing the cost requirements. An alternative approach by McKie et al. [21] describes an automated optical scanner with a mirrored scanning head, which allows the photon beam to be directed over non-uniform samples and a higher rate of scanning. In addition to this, using a second reference signal allows the scanner to eliminate reflective variations and reduce other coherent noise factors.

2.4.2 Electromagnetic acoustic transducer

The electromagnetic acoustic transducer or EMAT [22] is restricted in its use within NDT applications since the material under inspection must be electrically conductive. The ultrasonic energy is generated within the EMAT by passing a current transient through an induction coil. Eddy currents are then induced between the transducer and the material under inspection, causing a static magnetic field to form and establishing a Lorentz force. This in turn converts the electrical currents into mechanical forces. Conversely, when used as a receiver the mechanical displacements under the transducer will cause the reverse to be true.

One advantage with this form of transducer is that it is capable of generating and detection a large variety of elastic modes, depending upon the coil design. Additionally, due to their simple robust design, EMAT's are ideal for use at elevated temperatures and have been used at contact temperatures up to 2000°F. The main drawbacks are the need for the sample under test to be conductive and the low sensitivity of the device. Applications suggested [23] for this type of transducer include thickness gauging and defect detection, primarily at elevated temperatures

2.4.3 Piezoelectric transducers

2.4.3.1 Piezoceramics

The bulk of the applications carried out within the ultrasonic NDT industry utilise piezoceramic transducers for the generation and detection of ultrasound. Traditionally such systems employ coupling methods such as thin coupling gels, or immersion of the test piece in water baths or 'water-jet' arrangements [24], where the ultrasound is propagated along a narrow jet of water onto the test subject for increased sensitivity through direct coupling. Jansen and Hutchins [25] describe such an arrangement, using piezoceramic transducers in the imaging of defects within thin aluminium plates using Lamb waves. However, this method of inspection is prohibitive in large-scale evaluation of in-situ samples such as airframes. Additionally, the use of such couplant is not possible in certain industrial applications, where the water will be absorbed into the test piece thereby altering the acoustic properties, i.e. wood, paper and carbon fibre composites and causing damage. Alternatively, the transducer can be coupled directly

to the specimen [26] using only a small amount of liquid coupling. Although this incurs the problems mentioned previously, this technique is more versatile for in-situ scanning of large structures. The typical arrangement has the transducer coupled directly to the sample in the case of thickness testing or with an angled *shoe,* which is used to propagate the sound into the sample at an angle and hence generate shear waves. Both of these methods rely on a good degree of coupling between transducer and target, which must in turn be monitored separately. This method has found considerable use in the aerospace sector for on site inspection of airframes [27]. Willsher and Smith illustrate the potential of contact scanning methods utilising an eight element array coupled to an ANDSCAN [28] positional scanning system capable of resolving defects as small as 6mm in a carbon reinforced panel. It was found that the addition of eight element instead of the customary single probe lead to an improvement in scanning time of over 600% on real samples at a coarse resolution, although additional finer scanning would be required for defect characterisation.

Although the merits of through-air ultrasonic inspection have been evident for many years, it is only in the past decade or so that any substantial advances have been made in the field. Previously, air-coupled ultrasonics had been restricted to applications [29] such as range sensing, size control and level indicators at the lower range of the frequency scale, i.e. below 100kHz. The main technical obstacle in the non-destructive testing of the solids using air-coupled ultrasound is the acoustic impedance mismatch between the piezoceramic transducer (typically 33 MRayls) and the air media (434 Rayls), which leads to a massive insertion loss, approximately 100dB in the propagation of ultrasound from the transducer into the air. It was not until the late 1980's, that instrumentation such as high-power tone-burst generators, ultra low noise pre-amplifiers and new suitably sensitive piezoceramics were developed that facilitated the requirements for such a system. Fortunko et al. [29] describe a scanner using focussed piezoceramic transducers operating at frequencies between 500kHz and 1MHz to examine elastic wave propagation in samples of balsa wood and poplar in through-transmission. Rogovsky [30] demonstrated an air-coupled system employing 2.54mm focussed transducers operating at a frequency of 400kHz capable of single-sided and through-transmission, both at normal and oblique incidence (generation of Lamb and Rayleigh waves). Utilising this scanner, a variety of disbonds, delaminations and inclusions were detected in a number of composite materials. Rogovsky also outlined

possible enhancements for following systems such as the ability of the system to be portable and the need for single-sided inspection for in-situ testing.

In order to overcome the problem associated with the acoustic impedance mismatch between ceramics and air, matching layers can be introduced to the front face of the transducer to grade the impedance difference between the transducer and the load medium. Such matching layers increase the sensitivity of the transducer. The optimum matching layer is dependent on the number of layers, N, required and the acoustic impedances of the transducer Z_T and the surrounding media Z_C. The optimum impedance of the n^{th} layer [31] is given by the equation.

$$Z_n = \left(Z_C^{N+1-n} Z_T^n\right)^{\frac{1}{N+n}} \qquad \textbf{Eqn. 2.39}$$

Hence using Eqn. **2.39**, for a single matching layer attached to a solid piezoceramic radiating into an air load, an optimal acoustic impedance of approximately 0.1 MRayls is suggested. However, no viable material has been found with an acoustic impedance of this magnitude. Several attempts have been made to construct matching layers with this impedance, notably by Schiller et al. [32] and Stor-Pellinen et al. [33] who proposed the use of cork or balsa wood with acoustic impedances of 0.15 and 0.08 MRayls respectively. Although these materials met the design criteria, it was found that the attenuation suffered within the matching layers was excessive. Another area of interest was the application of aerogels [34] in matching layer manufacture, which are dried silica gels (SiO_2) with the water replaced by air. Although the acoustic impedance of such gels are in the region of 0.1 MRayls, the handling of such devices is difficult and reliable manufacture of required matching layer thickness was expensive in time and money [33]. Gerlach et al. [34] proposed a matching layer made of SiO_2 aerogel material for medical applications with an acoustic gradient across the thickness, i.e. high acoustic impedance at one face reducing to a lower acoustic impedance at the other face. One feasible material that has been employed for matching layer design is silicone rubber with an acoustic impedance of 1.0 MRayl. Fox et al. [35] showed that an improvement in insertion loss was possible using a quarter wavelength layer of silicon rubber to couple a range of piezoceramic transducer to air. Similarly, Tone et al. [36] and Yano et al. [37] demonstrated a dual matching layer concept for a 1MHz

piezoceramic transducer, that offered an improvement of 30-45 dB in insertion loss. The matching layer was constructed of one layer of silicone rubber (1.0 MRayls) bonded to a second layer of silicone rubber combined with low density microspheres, to give an acoustic impedance of 0.3 MRayls for the second layer. Two other interesting methods of matching transducers to lower acoustic mediums have been proposed by Fletcher and Thwaites [38] and Seyed-Bolorforosh [39]. Fletcher and Thwaites described the design and construction of a rigid matching layer consisting of multiple miniature horns to amplify the transmitted sound from a piezoceramic disc transducer. This design was demonstrated to give a 10dB pressure gain for the frequency range between 30 to 100kHz. Seyed-Bolorforosh illustrated an integrated matching layer design for use in the biomedical industry. Instead on bonding a single matching layer to the piezoceramic transducer, a series of orthogonal cuts were made into the ceramic and filled with a polymer mix to grade the acoustic impedance across the device.

Another well-documented field of investigation is the coupling to air via a secondary element or membrane. These transducers operate by coupling the vibration of the piezoceramic element, either radially or longitudinally, into a second membrane or vibrating film and are commonly referred to as flextensional transducers. The most commonly sited example of this is by Babic [40] who demonstrated the effectiveness of coupling the radial motions of solid ceramic to a vibrating aluminium membrane at 200kHz, to generate longitudinal vibrations in the membrane. This method being very similar to that employed by Newnham et al. [41, 42, 43] on flextensional or "Moonie" transducers using brass end caps to amplify the radial motion of the ceramic disk into larger axial displacements in the membrane caps. The problem associated with these transducers is the low frequency of operation, typically below 100kHz, which restricts use for through-air NDE. Similarly Okada et al. [44] fabricated a flextensional transducer incorporating an annular piezoelectric element bonded to different metal vibrating plates, with an additional exponential horn to amplify the generated sound. This design was calculated to produce an enhancement in output pressure of 10-20dB at ≈30kHz over conventional ultrasonic transducers, although with a reduced receive sensitivity.

To date, the only commercially available through-air inspection system [45] is made by QMI Inc., incorporating mechanically matched focussed piezoceramic transducers operating between 200kHZ and 1MHz in tone-burst operation. The AIRSCAN [45] has been successfully used to inspect various materials such as metals, carbon fibre laminates and honeycombs in through-transmission and Lamb wave inspection on a customised scanning jig.

2.4.3.2 Piezocomposites

By combination of active piezoceramic and passive polymer materials, a new range of ultrasonic transducer has been developed [46] which offer increased efficiency in acoustic coupling and sensitivity in comparison to solid ceramic, although predominantly narrowband in operation. There are a number of configurations possible for such transducers [47] by varying the geometries of the ceramic/polymer materials in the sensor, the most common of which are the 2-2 and 1-3 connectivity composites, as illustrated in Figure 2.14.

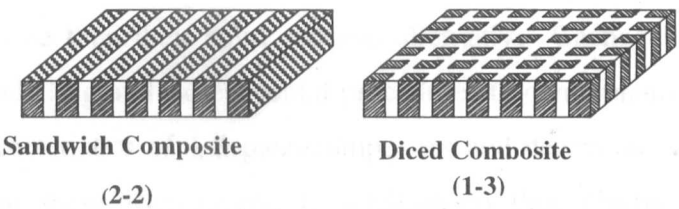

Figure 2.14 *Composite connectivity patterns*

2-2 composites, as described by Möckl et al. [46] are constructed by sandwiching together layers of ceramic and polymer to form a transducer with >30dB improvement in efficiency over conventional solid ceramic devices. 1-3 connectivity composites are constructed of active ceramic pillars embedded periodically within a passive polymer phase. These transducers are manufactured by the now standard method of 'dice-and-fill' introduced by Savakus [48]. This consists of a series of orthogonal cuts made into a solid ceramic block which are then filled with a passive polymer phase and the excess ceramic and polymer removed from either side. An alternative method was proposed by Bowen et al [49] using injection moulding to construct a series of free standing pillars by mixing the ceramic powder in a organic binder and injecting the flowable mixture into a mould, to be set by heat as a thermosetting reaction. Injection moulding, although initially expensive to set-up, offers a greater degree of design flexibility, allowing for

such novelties as differing pillar geometries. 1-3 connectivity composites offer a lesser degree of lateral clamping [50, 51] within the transducer structure, as compared to solid ceramic. This leads to a higher coupling coefficient, k_t, in addition to a reduced acoustic impedance (typically half that of ceramic, although lower impedances are possible). All these factors combine to illustrate that piezocomposite materials offer a more attractive approach for through-air ultrasonic inspection.

The majority of the work pertaining to the application of piezocomposite technology for through-air inspection appears to have been focussed at the Ultrasonics research laboratories of University of Strathclyde. The first investigation into the feasibility of such a system was completed in 1988 by Hayward and Gorfu [52], that demonstrated that although the insertion losses in such a system were in the region of 120dB, that it was possible using composite transducers to successfully propagate ultrasound in through-transmission for NDT purposes. Using composites at frequencies of 500kHz and 1.5MHz, it was possible to inspect samples of carbon fibre, glass and aluminium in through transmission and determine that these composite transducers were up to three times more sensitive than their solid ceramic alternative. Gachagan [51] implements finite element modelling and experimental procedures to comprehensively evaluate the performance characteristics of 1-3 piezocomposites and determine a set of guidelines for the design of these transducers. In addition to this, Gachagan utilised these improved composite transducers to illustrate through-air defect detection in carbon-fibre plates.

Advances in transducer technology and receive electronics have since led to the development of further inspection systems, such as the single sided scanning system design by Farlow and Hayward [3, 4]. This system utilised a pair of frequency matched piezocomposite transducers operating at 560kHz to generate and receive shear, Rayleigh and Lamb waves in a selection of thin plate materials, such as carbon fibre and aluminium. Defects down to the size of 2mm were detected in sheet aluminium and artificially generated defects and impact damage in carbon fibre plates were successfully detected. Kelly et al. [53] also demonstrated an improved through transmission system comprising of a single element transmitter coupled to an eight element receiver for increased scanning speed. The system operated at 600kHz with focussed transducers which employed a novel, modified room temperature vulcanised

(RTV) rubber matching layer that increased the transducer sensitivity by 23dB, capable of resolving 6mm defects in 3.7mm thick carbon fibre plates. The most recent development reported by Whiteley et al. [54] being the use of composite transducers for air-coupled thickness measurement of steel samples using longitudinal waves at just off normal incidence. Operating at a frequency of 500kHz, thickness gauging was performed on samples of 25.5mm steel with good accuracy at normal and elevated (150°C) temperatures.

2.4.3.3 Piezopolymers

Piezopolymer transducers have excellent dynamic properties due to their low vibrating mass and high mechanical damping [55]. Additionally, such transducers have a wide bandwidth of operation and low acoustic impedance properties, making them suitable to couple to media such as water or air. However, one of the most common piezopolymers, PVDF, exhibits a low electromechanical coupling coefficient ($k_t \approx 0.19$) in comparison to that of ceramic ($k_t \approx 0.49$) and also exhibits a considerably lower dielectric constant ($\varepsilon_r \approx 10$) again compared to ceramic ($\varepsilon_r \approx 1700$ for PZT-5A) [55, 56]. As such, piezopolymers have not found wide use in through-air ultrasonic applications with the exception of range finding for robotic navigation [58] and for calibration of other air-coupled transducers [56, 57].

2.4.4 Electrostatic transducers

In its simplest form, the electrostatic transducer consists of an electrically conductive backplate across which a thin dielectric membrane is stretched. This membrane has a conductive metallised film coated on the exterior surface, i.e. the surface opposite the backplate, hence sandwiching the dielectric and forming a capacitor. An external bias is then applied across the two electrodes, pulling the membrane down on the backplate, resulting is small air pockets being trapped between the film and the backplate. It is these small pockets of compressed air that produce oscillation in the membrane when an alternating signal is applied to the electrodes, or alternatively when an acoustic wave is incident on the front surface. Such devices offer good electromechanical coupling to air and a wide bandwidth of operation. Figure 2.15 illustrates the construction of a

typical electrostatic transducer, as manufactured at Strathclyde for the purposes of this Thesis.

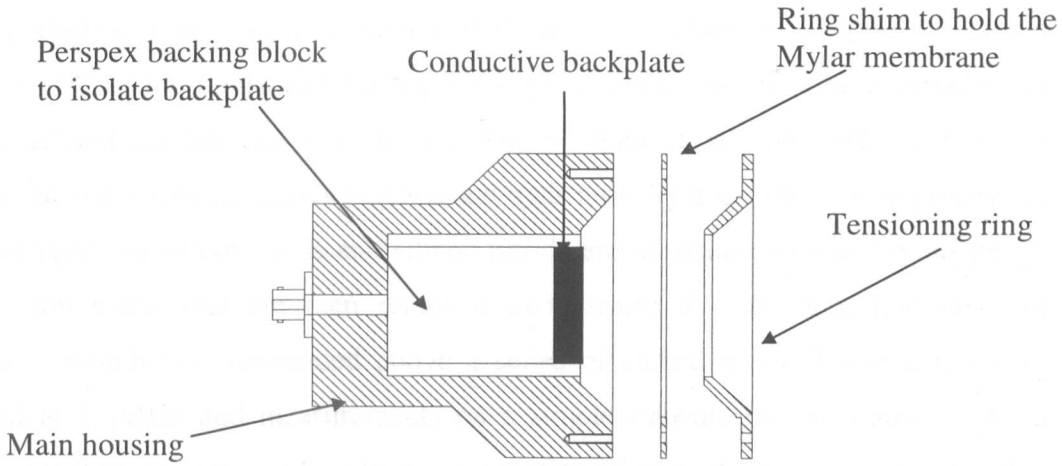

Figure 2.15 *Electrostatic transducer configuration*

A number of parameters influence the performance of this type of transducer. These include the roughness of the backplate, the thickness of the dielectric membrane, the bias voltage applied and the tensioning of the radiating membrane. Studies initially carried out by Carr and Wykes [59] and later by Munro and Wykes [60] illustrated that the surface finish of the backplate had considerable influence over the resonant frequency of the electrostatic transducer, noting that the uniform grooving of the backplate led to better control of the resonant frequency. In addition, it was noted that the tension of the membrane had little effect on the resonant frequency or bandwidth. Heitanen et al. [61] determined that the sensitivity and bandwidth for a grooved electrostatic increased as an inverse function of the depth and/or width of the grooves. It was also demonstrated that as the thickness of the membrane was decreased, the sensitivity was increased, with a fivefold improvement in received amplitude for a 2.5μm Mylar over that of 13μm Kapton. Further theoretical work on this subject was carried out by Hietanen et al. [62] and Mattila et al. [63], using computer models to predict the resonant frequency of v-grooved electrostatic transducers with good correlation between theory and experiment. An alternative to the conventional grooved backplate was described by Schindel et al. [64] consisting of micromachined pits on a silicon backplate that offered a much greater degree of reproducibility. The authors described a transducer with small machined pits of 80μm width and 18μm depth and a membrane of 2.5μm. This transducer had a –6dB bandwidth between 100kHz and

1.3MHz. It was also determined that an increase in bias voltage from 100V to 400V could effectively double the bandwidth of the transducer. Further work by Bashford et al. [65] illustrated the use of annular and Fresnel-zone plates to apodise the output pressure field of the transducer for focussed applications. On the similar principle of micromachined electrostatic transducers, Khuri-Yukab et al. [66, 67] describe the manufacture of a high frequency narrowband transducer by a silicon etching process. A series of layers of silicon oxide and silicon nitride are deposited on a highly doped, p-type silicon wafer that are then removed periodically to leave a nitride layer of miniature 'drumheads' suspended above a series of etched holes. These transducers operated at 1.8MHz and measurements on a simple transmit-receive pairing gave a system signal to noise ratio of 23dB at a separation of 1cm. It was also suggested that since the transducers are made from silicon wafer, that integrated receive electronics could possibly be designed on the rear of the transducers.

Ultrasonic testing using electrostatic transducers has been documented from the early 70's, with Luukkala and Meriläinen [68] demonstrating an inspection system utilising electrostatic transducers to generate and detect Lamb waves in 0.5mm thick aluminium plates through air. The transducer employed operated at 60kHz, but could only resolve defects of approximately 6mm diameter in the 0.5mm plates. Hutchins et al. [69] demonstrated the use of air-coupled electrostatic transducers excited by a unit impulse to measure material properties such as shear wave velocity in carbon fibre plates, as well as detection of defects ranging in size from 6.3mm to 25.4mm. Similarly, Schindel and Hutchins [70] used through transmission propagation to determine material velocities and thickness variations in differing materials by time-of-flight measurements of single pulse ultrasonic waves. Further to this, Wright et al. [71] used capacitive devices to detect defects in thin plates of different materials with Lamb waves and generate tomographic images of the plate under inspection. Laudabaum et al. [72] present similar systems utilising their micromachined ultrasonic transducers in tone-burst operation at a frequency of 2.3MHz for through-transmission of 1.9mm aluminium samples.

2.5 Limitations of previous air-coupled scanning systems

Over the last six years a variety of air coupled ultrasonic test systems have been developed within the Ultrasonics Research Group (URG) at the University of Strathclyde. These systems have been made possible by using specially developed piezocomposite transducers [4] and ultra low noise receiver electronics [3]. All of these new air coupled systems fall into one of two categories: single sided [3, 4] or through transmission [53]. Using a single sided inspection system it is possible to produce images of internal defects in thin plates which are made from almost any type of material. Particularly good results have been obtained with materials such as carbon fibre reinforced composite, which are difficult to test using alternative technologies [3, 53]. Unlike the through transmission systems, the single sided systems are ideal for in-service inspection, however, there are some restrictions. As discussed earlier in Section 2.2.2, all single sided systems make use of two ultrasonic transducers operating in pitch-catch mode [3]. The coincidence principle (Eqn. **2.38**) is used to adjust the angle of the transducers so that it is possible to efficiently generate and detect a desired Lamb wave mode in the test sample. For air-coupled operation it is essential that both transducers are set precisely to the correct angle. The tolerance on the angle depends on the diameter of the transducers and their beam profiles. Experiments with 30 mm diameter devices, operating in air, indicates that the angular tolerance is $\pm$ 0.5 degrees [3]. The tight angular tolerance required for the original fixed frequency Lamb wave test systems has led to two main operating restrictions [3, 4]:

- In order to test samples of different thicknesses it has been necessary to change the angle of the transducers. Reliability and ease of use would be greatly improved if it were possible to place the transducers in a head assembly which holds them in a fixed position for the lifetime of the equipment. This is particularly true if the equipment is to be used by an unskilled operator.

- More importantly, although it has been possible to produce an image of a defect which provides information on position and size, it has not been possible to accurately measure localised changes in thickness.

The main aim of this Thesis is to extend the capabilities of the single sided air coupled system by addressing these problems.

2.6 Proposed enhanced scanning system design

As with the fixed frequency systems, the design approach is centred around the use of the fundamental anti-symmetrical mode. Figure 2.16 illustrates the phase velocity dispersion curve for the a_o mode in aluminium determined by solving the frequency-thickness product equation (Eqn. **2.37**).

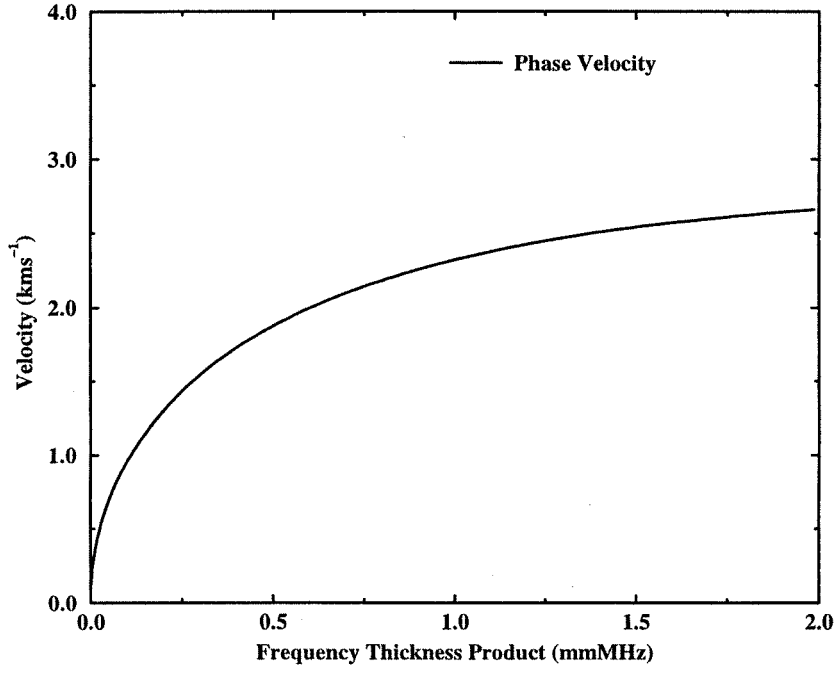

Figure 2.16 *Lamb wave dispersion velocities in aluminium for the a_0 mode*

This curve can then be used to establish the range of frequencies required to test samples with thicknesses in the range 0.5mm to 5mm. This is done by utilising the dispersion curve for the a_0 mode for a single fixed angle of incidence to determine the resultant phase velocity of the Lamb wave in the test specimen by using the coincidence principle, detailed in Section 2.3.

For example, by assuming a fixed angle of 8.6^0, and using the standard value for the velocity of sound in air of $330ms^{-1}$ it is possible to determine the phase velocity of the Lamb wave as being approximately $2200ms^{-1}$. By examining the dispersion curves shown in Figure 2.16, it is now possible to determine the fixed frequency-thickness

product figure that will be utilised within the scanning system. Consequently, for the stated angle of incidence of 8.6° and the corresponding phase velocity of 2200ms^{-1}, the system frequency-thickness product must remain constant at 0.76. Thus, the following equation (Eqn. **2.40**) can be utilised to determine thickness of a sample for the previously defined fixed angle of incidence.

$$thickness = \frac{0.76}{frequency} \qquad \textbf{Eqn. 2.40}$$

Hence, for a scanning system with a operational bandwidth of 800kHz centred around 600kHz it is possible to test and measure differing thicknesses without altering the angle of incidence, since the frequency-thickness product must remain constant for a fixed angle of incidence. Therefore for the system described, operating from 200kHz to 1MHz, the thickness of test specimen that can be characterised ranges from 0.76mm to 3.8mm.

2.7 System requirements

In order to construct this new system, it will be necessary to investigate alternative transducer technologies. Conventional piezoelectric methods of ultrasonic generation and detection in air suffer from inherently poor sensitivity and bandwidth. The poor sensitivity is attributed primarily to the substantial acoustic impedance mismatch between the transducer (e.g. 34 MRayl for a solid PZT 5A device) and air (434 Rayl). These problems have been addressed by a variety of methods, including the use of piezocomposite structures [51, 52], flextensional devices [40], matching layers [53], aerogels [34] and alternatively by such designs as the electrostatic or capacitive ultrasonic transducers [69] with varying degrees of success. Piezocomposite devices can be tailored by varying the polymer/ceramic volume fraction in order to alter the frequency and performance characteristics. They possess a higher electro-mechanical coupling coefficient than solid ceramic transducers which leads to more efficient energy transfer. Also, the generation of lateral modes is greatly reduced due to damping in the polymer. With a typical characteristic acoustic impedance of 15 MRayl, piezocomposite devices also offer an improved match with air. However, even with these devices the

total insertion loss is almost 140 dB. For the current application the most serious problem with all piezoelectric transducers is that they are essentially narrowband in nature.

This application requires transducers which can provide a much wider bandwidth of operation. A possible alternative is the electrostatic device which is advantageous for the type of work proposed due to its wideband nature, although the fragility of the thin front face membrane means that the transducer is not very robust and therefore questionable for use in many industrial applications.

The requirement for the transducers employed in this frequency agile Lamb wave system is that they should have a bandwidth which allows operation in the frequency range 200kHz and 1MHz and be robust enough for practical industrial implementation.

Another important consideration within the design of an air-coupled ultrasonic inspection system, relates to the performance of the receive electronics. Unsolicited electronic noise is a problem which plagues all electronic systems, however in an ultrasonic air-coupled scanner the intrusion of high levels of noise into the system can swamp the received signals which are typically of low magnitude, i.e. μvolts. One method of rejecting this electronic noise is through filtering the received signal and narrowbanding the amplifying electronics to the frequency of interest. However, paradoxically the proposed scanning system requires the transducers to have a wide bandwidth to facilitate the scanning of plates of differing thickness, while the receive electronics are optimised through narrowing the bandwidth of the receiver. Thus it is important to gain a full understanding of the noise mechanisms active within the piezoelectric scanner and develop the specialised receive electronics system required to fully implement this multi-frequency scanning system.

Incorporation of all of these features is required for multi-thickness testing of planar materials. It is intended that in the final design, the transducer head unit will be hand held and portable, similar to a computer mouse, for convenient scanning over the test specimen. The essential elements of the system, are as follows:

- Wide bandwidth ultrasonic devices which provide a good acoustic impedance match with air. Each device should have a -3dB bandwidth of approximately 800kHz centred around a frequency of 600kHz.

- An electronics system capable of modulating the received signal to the required frequency, filtering out the spurious and additional frequency components and interfacing with the computer acquisition hardware.

- Dedicated software package that controls all aspects of the system, including output voltage, frequency tuning and data analysis.

The basic elements of the new proposed frequency agile Lamb wave test system are illustrated in Figure 2.17.

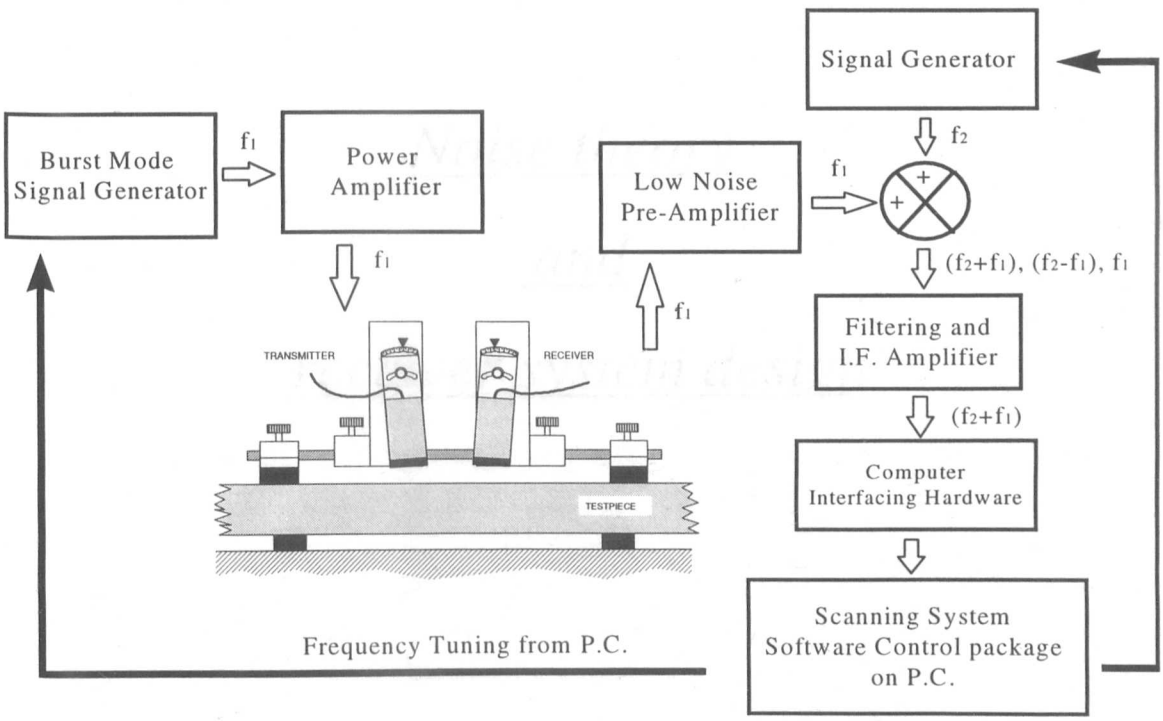

Figure 2.17 *Conceptual design for frequency agile NDE scanner*

Chapter 3

Noise theory and receiver system design

3.1 Introduction

When developing any air-coupled ultrasonic NDE scanning system it is essential that careful consideration of the associated transmission and reception electronics are made with a view to the overall scanner performance. The design of good low-noise reception hardware is of fundamental importance, where the desired characteristics of high gain and high sensitivity are integral to the system's ability to detect the low amplitude signals inherent in air-coupled operation. However, the additional problem associated with the design proposed in the previous Chapter is that it is inherently difficult to provide high gain and good selectivity to a system over such a wide bandwidth.

This Chapter reviews the major noise sources within a typical ultrasonic receiver and illustrates their influence on the overall system signal to noise ratio (SNR). Further to this, it discusses the need for tuneable amplification in order to minimise the noise bandwidth of the reception electronics, introducing modulation and heterodyne theory. The design of the receive system electronics is then described, detailing the different constituent sections within the design and their relevant importance with respect to the aforementioned noise theory.

3.2 Evaluation of noise sources

Electronic noise is defined in Horowitz and Hill [73] as "unwanted signals that obscure the desired signal". Minimisation of noise is of critical importance in the case of ultrasonic receiver systems where the received signals are of low magnitude. It is therefore essential that when designing low-noise electronic systems for use in ultrasonic NDT, to determine the overall noise in order to evaluate the performance of the design and maximise the signal to noise ratio (SNR). However, in the case of a piezoelectric receiver system, the problem is more complex due to the nature of the receiving sensor and the frequency dependence of the noise generated within the receiver system [2].

It is impractical to measure noise at its source, since most noise voltages are typically in the nanovolt region. Additionally, noise is not necessarily generated at source but rather generated diffusely across the whole 'front end' package. Therefore noise detected at

the output of an amplifier or receiver constitutes a number of different noise mechanisms. Of these noise mechanisms, there are three components that will contribute the bulk of the noise to the overall receive system. These are *Transducer Noise, Amplifier Noise* and *Environmental Noise* and are now explained briefly.

3.2.1 Transducer noise

Transducer Noise is the intrinsic noise introduced into the system, by the actuating device itself. In the case of the piezoelectric thickness-mode transducer, the dominant noise mechanism is the noise generated by the (real) resistive part of the transducer operational impedance. This noise is known as Johnson noise [74], or more commonly as *Thermal Noise*. This is the noise associated with random carrier movements in a conductor due to thermal agitation. The resultant sum of electron movement within a conductor is not necessarily zero at any time instant, although the integrated sum does average to zero over a period of time. At any time instant the current resulting from this random movement of charge can develop a voltage across the resistance of the conductor. This form of noise is only present in real (or bulk) resistive elements and the mean square voltage is given by the Nyquist relationship [75].

$$E_S = \sqrt{4KTRB} \qquad \textbf{Eqn 3.01}$$

where,

K = Boltzmann's Constant (1.38×10^{-23} W-s/K)

R = Resistance of Conductor (Ω)

T = Temperature of the Conductor (K)

B = Noise Bandwidth (Hz)

where E_S is the r.m.s. thermal noise voltage of a given resistance R, and is normally expressed in $V/\sqrt{Hz}$ for unity noise bandwidth. The bandwidth of the electronic system is important, since the noise spectrum is flat, with the noise extending uniformly over all frequencies, i.e. a system with a wide operational bandwidth will contain a greater amount of noise within that system.

Therefore, the front end of the receive system (i.e. the transducer itself) can be represented in the form of the noise equivalent circuit, as shown in Figure 3.01.

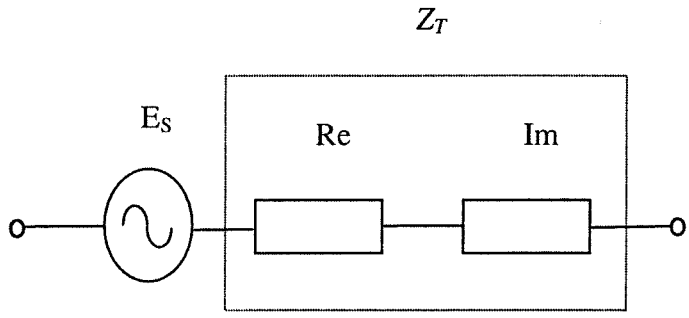

Figure 3.01 *Thermal Noise Equivalent Circuit*

Hence the transducer is represented equivocally by a noise voltage generator in series with the transducer impedance separated into both real and imaginary elements.

By considering a piezoceramic composite transducer, it is possible to simulate the relevant noise mechanisms active within the structure. In this instance, the following transducer was simulated in order to characterise the intrinsic noise parameters.

> Piezoceramic composite of 50% volume fraction of ceramic to epoxy of 1-3 connectivity combining PZT-5H ceramic and CY1301/HY1300 Hard-Set Epoxy, Coupling coefficient, k_t of 0.606, 2.61mm thickness and designed for operation as a receiver at 700kHz. Air loaded and backed.

Now, by examining the operational impedance spectrum shown in Figure 3.02, it is apparent that the impedance of the device is frequency dependent. The theoretical results presented were calculated using a system noise model [2] based on the linear systems model developed by Hayward [76].

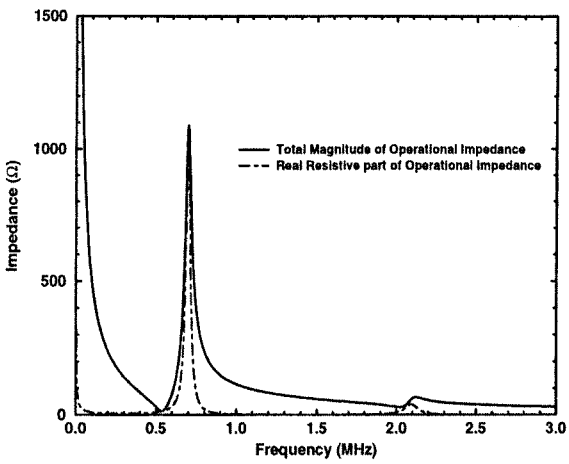

Figure 3.02 *Simulated Impedance Response of Generated PZT-5H Transducer*

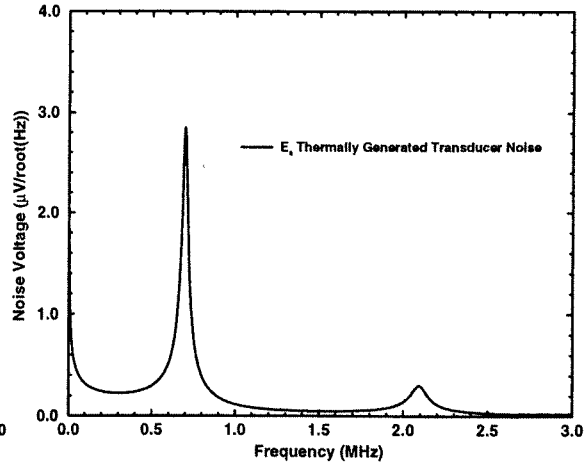

Figure 3.03 *Theoretical Transducer Noise*

As illustrated in Figure 3.02, the impedance response of the piezocomposite transducer exhibits a frequency response with defined peak in the impedance at approximately 700 kHz and a minimum at 550 kHz, these two frequency points are referred to as the frequency of mechanical (f_m) and electrical (f_e) resonance respectively. The electrical resonant frequency defines the optimum frequency of operation for a piezoelectric transducer operating in the transmit mode and the mechanical resonant frequency pertains to the normally preferred frequency for voltage reception (when operating into an infinite electrical load impedance).

In accordance with the theory presented, the thermally generated transducer noise should therefore also exhibit similar frequency dependence. It can therefore be determined theoretically, using Eqn. **3.01**, that the effective noise signature produced by the real resistive element of the transducer operational impedance is as illustrated in Figure. 3.03. It is thus apparent that the noise voltage contributed to the system by the transducer will not be constant with frequency, but will instead be a frequency dependent term, which will follow the spectrum of the operational impedance, developing maximum noise voltage at the fundamental frequency of mechanical resonance. The relatively large d.c. value of the associated transducer noise is due to the real (resistive) part of the impedance magnitude is infinite at d.c. This contribution is reduced when the transducer noise is evaluated with a pre-amplifier arrangement, due to the practical low frequency cut-off of the amplifier.

By examining *Thermal Noise,* Eqn **3.01**, it is apparent that not only will the transducer noise be influenced by the frequency of operation, but also by the environmental conditions under which the device will be operating, namely the temperature. As the temperature of the device is increased, through either work-environment conditions or high-power driving of the transducer, the thermal noise will also increase. Figure 3.04 illustrates the influence of temperature over the thermal noise generated in the transducer example given previously. It illustrates that even a substantial temperature increase in operating conditions will only lead to a small increase in thermal noise generated. Note that this figure does not account for any changes incurred in the material properties of the piezocomposite as the temperature is increased.

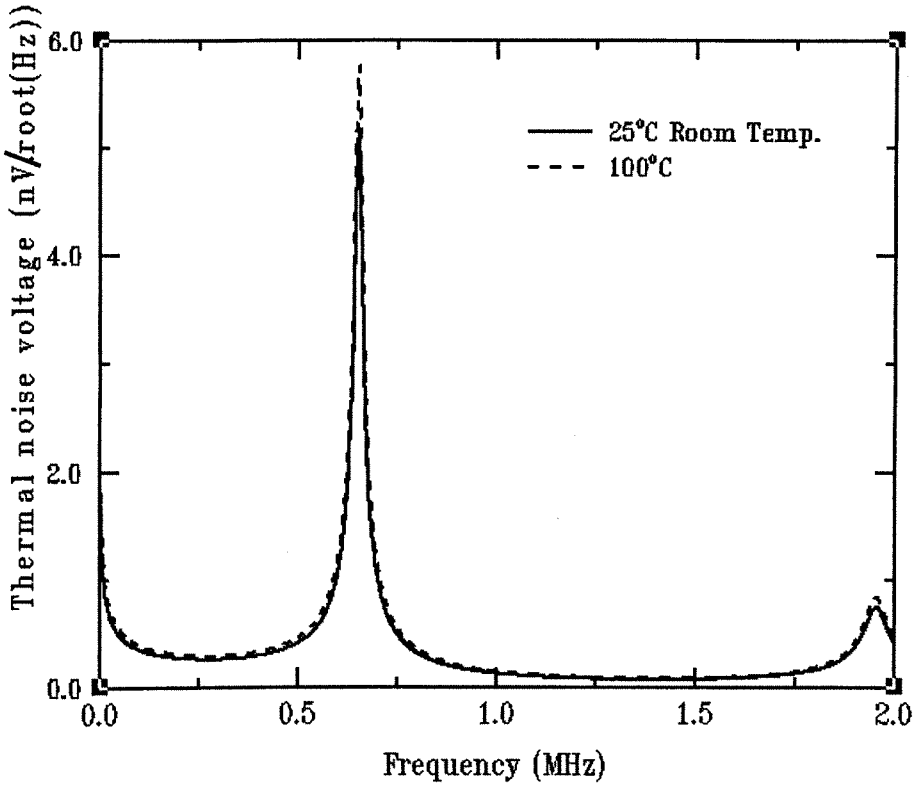

Figure 3.04 *The influence of temperature on the thermal noise spectrum*

3.2.2 Amplifier noise

In order to simplify the calculation of noise sources active within an amplifier, it has been determined [73, 77] that the noise within any amplifier can be referred to its input, allowing convenient manipulation for analysis purposes. In the case of a pre-amplifier arrangement, this consists of two main noise mechanisms. These are the Equivalent Noise Input Voltage (E_n) and the Equivalent Noise Input Current (I_n) of the amplifier.

Therefore, using standard noise notations [78], the amplifier can be illustrated, as in Figure 3.05.

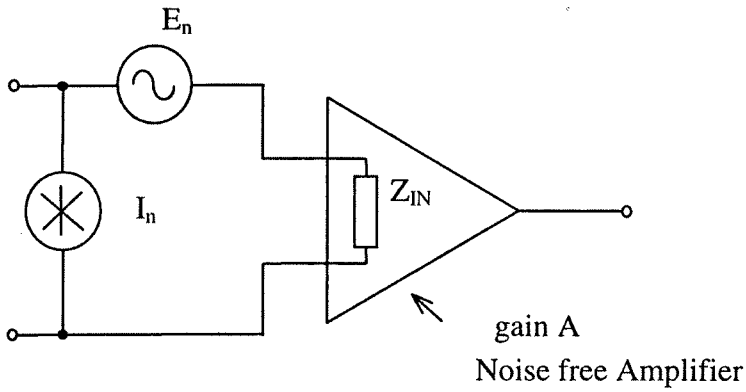

Figure 3.05 *Equivalent Noisy Amplifier*

These two noise mechanisms E_n and I_n, normally represent the contributions exhibited by the amplifier through a combination of *Thermal Noise* and *Shot Noise*. The thermal noise voltage is contributed to the system by the various resistive parts incorporated within the receive electronics. The equivalent input noise current is mainly generated by what is known as *Shot Noise*. This phenomenon arises due to the random fluctuations in current flow about a mean or d.c. level. For example, assume that each current carrier corresponds to one unit of electronic charge, shot noise current is then defined by,

$$I_S^2 = 2\,q\,I_{DC}\,B \qquad \textbf{Eqn. 3.02}$$

where,

I_{DC} = D.C. current value

q = charge of an electron

Shot Noise is usually associated with current flow across a potential barrier, e.g. a p-n junction. Current flowing through transistors, diodes, etc. is not smooth and continuous, but analogous with a pulsing effect. As a result, the pulsing flow of the electrons across the potential barrier has a granular effect and the variations from this effect is referred to as shot noise.

Another form of electrical noise inherent within amplifiers (particularly those utilising semi-conductors) is low-frequency noise, often referred to as $1/f$ noise. This noise, as

the name suggests, is mainly prevalent at frequencies below a few hundred Hertz. In bipolar transistors, $1/f$ noise arises from surface recombination and current leakage across the reverse-biased collector junction. In modern transistors, the later effect dominates and $1/f$ noise is found to be strongly dependent on collector current. Therefore $1/f$ noise is given by,

$$E_{\frac{1}{f}}^2 = K_1' \ln\left(\frac{B}{f_1}\right) \qquad \textbf{Eqn. 3.03}$$

where,

K_1' = A Device Constant

B = The amplifier bandwidth

f_l = The amplifier low frequency cut-off

This would appear to indicate that $1/f$ noise tends to infinity at very low frequencies. However, the amplifier lower cut-off prevents this from happening. This type of noise is not of great significance in the present investigation, since we are interested primarily in the noise performance of composite transducers, where the main frequencies of operation are in the 100kHz – 1MHz range. However it was felt that this form of noise should be covered in passing, since many ultrasonic applications operate at much lower frequencies than those being investigated. Examples include below resonance hydrophones and other detectors.

Therefore, the main sources of noise that shall be considered as being prevalent within the receive electronics of the transducer system are the thermal noise of the various resistive elements, and the *Shot Noise* developed by the associated transistor junctions. By considering the equivalent noise circuit derived for the receive system, shown in Figure 3.05, and the equivalent noise input equation Eqn. **3.05** (See Section 3.3), it is apparent that the equivalent input noise voltage, E_n, of the amplifier is independent of the transducer and therefore is also frequency independent. In other words, the noise voltage of the amplifier should be a constant figure only dependent on the amplifier transfer function, when measured at the amplifier output terminals.

However, in the case of the equivalent input noise current, I_n, there are differing circumstances, in that the total equivalent noise voltage related to this noise current is the product of I_nZ_T, where Z_T is operational impedance of the transducer. Since there is this connection between these two factors, it is apparent that the noise current contribution will be frequency dependent due to the behavioural response of the transducer. Not only this, but the temperature of the receiving device will have a direct effect on the overall noise voltage produced by the amalgamation of both these terms. Hence, the current/impedance linked term will produce a noise vs. frequency response at room temperature (298K) as in Figure 3.06. In this example, the value assigned to I_n is $1\ pA/\sqrt{Hz}$, a typical value for input noise current for a low noise pre-amplifier.

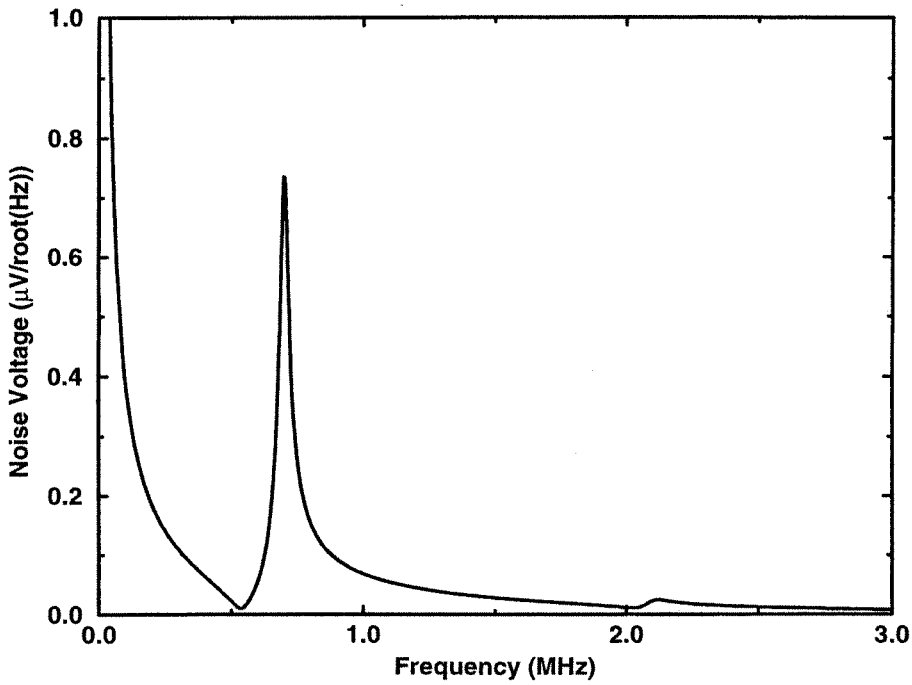

Figure 3.06 *Noise Voltage generated by Amplifier Noise Current*

3.2.3 Environmental noise

Environmental Noise, or r.m.s. background noise as it is also known, is a collective term for all the forms of noise that are extraneous to this kind of electronic system. For example, ambient noise in airborne transducer systems, sea-state noise in sonar applications and even electro-magnetic noise developed by motors used for rotating sonar arrays, all these factors come under the specification of environmental noise. For the purpose of simulating this noise within the receive system noise model, it is

represented by a random Gaussian distribution with a mean of zero, and the r.m.s. value specified by the user. Mathematically, the distribution can be described as

$$f(x) = \frac{1}{\sigma\sqrt{2\pi}} \exp - \left[\frac{(x-\mu)^2}{2\sigma^2} \right] \qquad \textbf{Eqn. 3.04}$$

where,

μ = The mean or average value.

σ = The standard deviation or r.m.s. value of the variable, x.

The function f(x), is referred to as the probability density function. In the case of the noise being dependant on a certain frequency range, i.e. *Sea-State Noise*, the distribution can then be weighted to reflect this frequency dependence by increasing the magnitude of noise at lower frequencies, for example.

3.3 Equivalent noise model for a piezoelectric receiver

In order to evaluate the noise sources active within a piezoelectric receiver, the electrical equivalent circuit for the device must be obtained. Thus, consider a thickness mode piezoelectric transducer of specific acoustic impedance Z_C, with an arbitrary, planar wave of force (F_F) incident on the transducer front face and an arbitrary lumped impedance (Z_E) connected across directly across the transducer electrodes. Consequently, the incident wave of force, generates an output voltage between the electrodes (V_O) and can be illustrated thus,

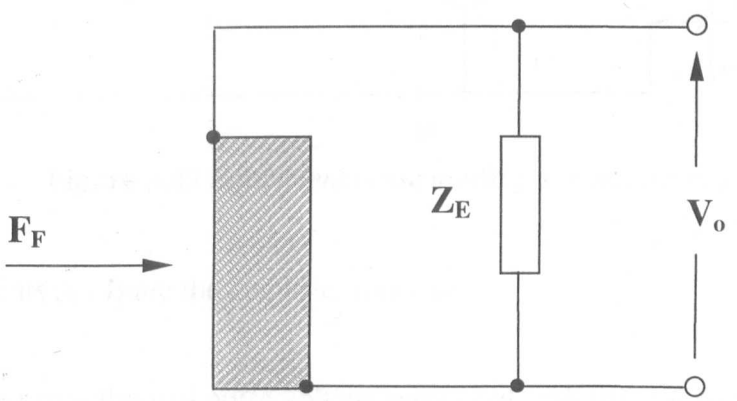

Figure 3.07 *Piezoelectric receiver schematic*

It has been previously determined [2, 76], that this can be expressed in terms of a Thevenin equivalent circuit of the transducer. As illustrated in Figure 3.08, where the voltage ($v_{O\text{-}C}$) under open-circuit conditions i.e. ($Z_E \rightarrow \infty$) and the transducer operational impedance (Z_T) can be resolved by a linear systems modelling approach [76, 79].

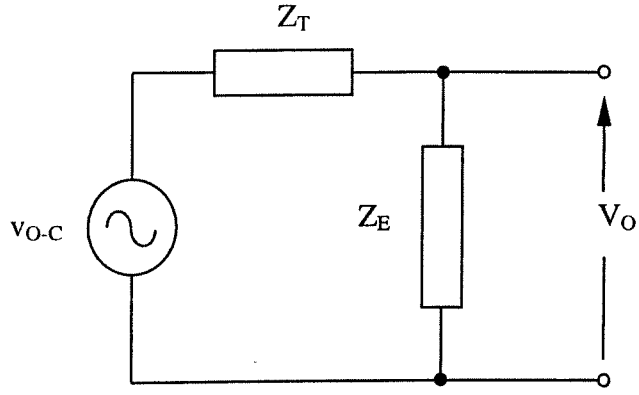

Figure 3.08 *Thevenin equivalent receiver circuit*

Thus, a complete system noise model for a piezoelectric receiver can be found by utilising the Thevenin equivalent of the receiving transducer, in addition to the conventional definitions of noise generated by an electronic system. This is illustrated in Figure 3.09, where the receive electronics replace the arbitrary lumped impedance, Z_E.

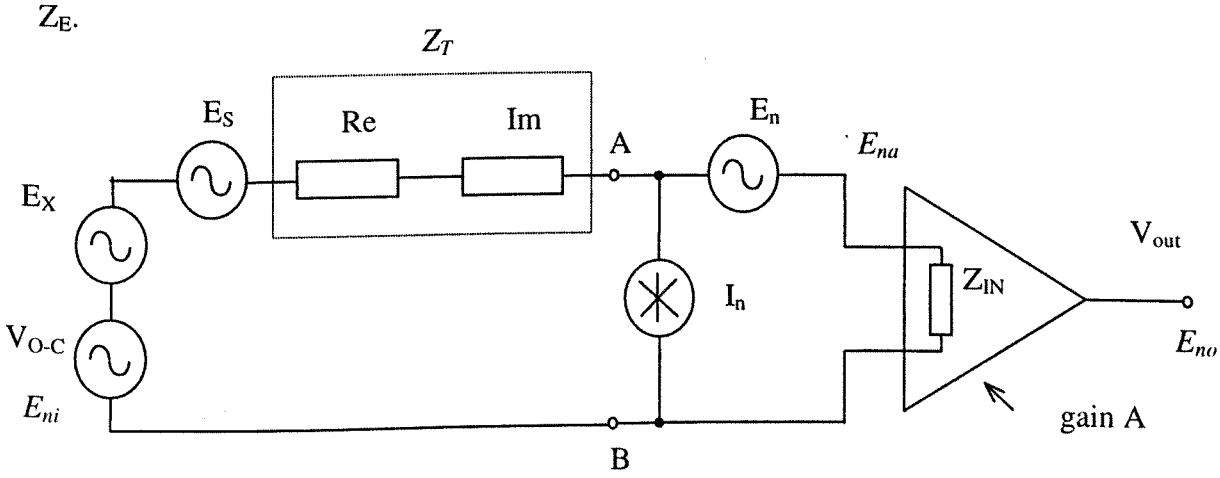

Figure 3.09 *Equivalent noise model for a receive system*

Note that points A - B are the amplifier terminals.

where,

E_S is the r.m.s. thermal noise voltage associated with the real part of the transducer impedance.

E_X is the r.m.s background or environmental noise voltage, e.g. sea-state noise.

E_n, I_n are noise voltage and current generators respectively, representing amplifier noise. They represent lumped contributions from thermal and shot noise sources within the actual amplifier. Consequently, the amplifier can be considered noise-free, since all sources are contained within E_n and I_n.

$V_{o\text{-}c}$ is the open circuit signal voltage generated by the transducer in reception.

Z_T is the operational impedance of the receiving transducer, constituting of real (Re) and imaginary (Im) parts.

Z_{IN} is the input impedance of the amplifier

From Figure 3.09, it can be determined that the mean square sum of the noise generated at the input of the amplifier is:

$$E_{na}^2 = \underbrace{E_S^2\left(\frac{Z_{IN}}{Z_T+Z_{IN}}\right)^2}_{\textit{Transducer Noise}} + \underbrace{I_n^2\left(\frac{Z_{IN}\cdot Z_T}{Z_{IN}+Z_T}\right)^2 + E_n^2\left(\frac{Z_{IN}}{Z_T+Z_{IN}}\right)^2}_{\textit{Amplifier Noise}} + \underbrace{E_X^2\left(\frac{Z_{IN}}{Z_T+Z_{IN}}\right)^2}_{\textit{Environmental Noise}} \quad \textbf{Eqn. 3.05}$$

Hence the signal to noise ratio SNR at the output of the receiver can be determined as follows,

$$SNR_{o/p} = \frac{\left[V_{O\text{-}C}^2\left(\frac{Z_{IN}}{Z_T+Z_{IN}}\right)^2\right](\omega).(H(\omega))^2}{\left[E_S^2\left(\frac{Z_{IN}}{Z_T+Z_{IN}}\right)^2 + I_n^2\left(\frac{Z_{IN}\cdot Z_T}{Z_T+Z_{IN}}\right)^2 + E_n^2\left(\frac{Z_{IN}}{Z_T+Z_{IN}}\right)^2 + E_X^2\left(\frac{Z_{IN}}{Z_T+Z_{IN}}\right)^2\right](\omega).(H(\omega))^2} \quad \textbf{Eqn. 3.06}$$

Where $H(\omega)$ is the amplifier transfer function and generally exhibits bandpass characteristics, that may be approximated by the following equation.

$$H(\omega) = \frac{1}{\left(1+j\omega/\omega_1\right)\left(1+j\omega_2/\omega\right)} \quad \textbf{Eqn. 3.07}$$

Where ω_1 and ω_2 are the lower and upper cut-off frequencies respectively of the amplifier and j is the complex operator.

Hence, implementation of these equations within the linear systems noise model [2, 76] allows the designer to graphically represent the spectral signal to noise ratio characteristics of a receiver system. As an example, consider the through-transmission of ultrasound in a 1mm aluminium plate using a pair of 50% volume fraction, 1-3 connectivity piezocomposite transducers operating in air, as illustrated in Figure 3.10.

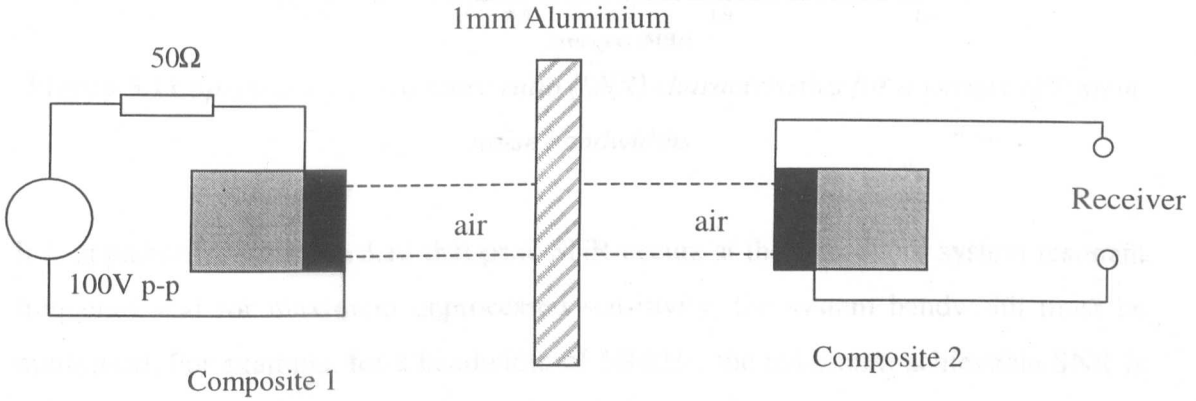

Figure 3.10 *Modelled through-air inspection system*

Three cases are presented, corresponding to a system noise bandwidth of 1Hz, 20kHz, and 500kHz. For the purposes of simulation, the composites are assumed to operate at a resonant frequency of 500kHz in both transmission and reception, are matched mechanically to the air environment and the pre-amplifier has input voltage and current noise parameters of $800\,pV\sqrt{Hz}$ and $1\,pA\sqrt{Hz}$ respectively. An excitation voltage of 100V p-p is also assumed. The resultant theoretical spectral signal to noise ratios are illustrated in Figure 3.11 calculated at the output of the receive network.

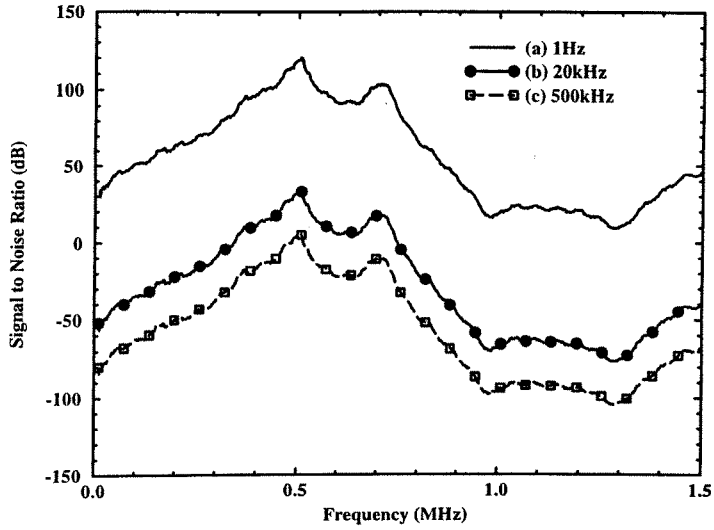

Figure 3.11 *Spectral signal to noise ratio (SNR) characteristics for a variety of system noise bandwidths*

It is apparent from Figure 3.11 that peak SNR occurs at the transducer system resonant frequency and for maximum unprocessed sensitivity, the system bandwidth must be minimised. For example, for a bandwidth of 500kHz, the maximum achievable SNR is in the region of 2.5dB, increasing to 35dB at 20kHz and the impractical figure of 112dB for a 1Hz noise bandwidth. This illustrates that by implementing narrowband techniques to an air-coupled NDE scanning system will lead to an enhanced performance over a typical wideband amplification methodology.

3.4 Influence of amplifier input impedance on SNR performance

The input impedance of the amplifier holds a direct relation to the amount of noise generated within the system. By examination of Figure 3.09 and referring to Eqn. **3.05** it is apparent that the impedance of the transducer and input impedance of the amplifier act as a voltage divider when the noise sources are referred to the input. There are two cases that may arise for differing amplifier configurations that should be considered. The first case corresponds to the input impedance of the amplifier, Z_{IN}, being much greater than that of the transducer, i.e. in the case of a voltage amplifier. The second case corresponds to where the transducer impedance dominates, i.e. a low input impedance current amplifier. Typically, Z_{IN} is in the region of >10kΩ for a voltage amplifier and <20Ω for a current amplifier.

(i.) For the case $Z_{IN} >> Z_T$ (Voltage Amplifier) the noise produced at the output of the amplifier becomes,

$$E_{no}^2 = A^2\left(E_S^2 + I_n^2.Z_T^2 + E_n^2 + E_X^2\right).H^2(\omega)$$

(ii.) When Z_{IN} is small and finite (Current or Transimpedance Amplifier) the associated noise voltages produced within the amplifier system are determined as follows, with the noise observed at the amplifier input given in Eqn. **3.05**.

$$E_S^2\left(\frac{Z_{IN}}{Z_T + Z_{IN}}\right)^2.H^2(\omega) \quad - \quad \text{Transducer noise at output}$$

$$I_n^2\left(\frac{Z_{IN}.Z_T}{Z_T + Z_{IN}}\right)^2.H^2(\omega) \quad - \quad \text{Amplifier current noise at output}$$

$$E_n^2\left(\frac{Z_{IN}}{Z_T + Z_{IN}}\right)^2.H^2(\omega) \quad - \quad \text{Amplifier voltage noise at output}$$

By computing $\left(\frac{Z_{IN}}{Z_T + Z_{IN}}\right)^2$ for either of these two cases, then all other noise sources can be evaluated. Note, with the introduction of the current amplifier and the lower input impedance Z_{IN} that this system offers, the noise produced by each comparative element of the system will be reduced due to the voltage divider network produced by Z_{IN} and Z_T. Therefore, utilising the theoretical noise model it is possible to illustrate the influence that the input impedance exerts over the SNR performance of the amplifier.

3.5 Noise in multiple stage amplifier systems

The problem with designing analogue receivers is that inevitably, it is not practical for a specialised amplifier to be designed in a single stage. This means that multiple amplifiers must be cascaded together in order to deliver the desired gain, bandwidth, etc. Moreover the noise from each of these stages must then be determined in order to characterise the overall noise figure of the analogue system.

This can be illustrated by considering the following example. Figure 3.12 describes two amplifiers in cascade, the first stage is terminated in a resistor R_L and is driven by a voltage source of resistance, R_S. The power gain of each stage of the amplifier is G_1, G_2 with the noise factors of F_1 and F_2 respectively. Where noise factor is defined as "*the ratio of the available output noise power per unit bandwidth to the portion of that noise caused by that actual source connected to the input terminals of the device, measured at the standard temperature of 290K*" [78]. Hence, noise factor can be represented by the following equation.

$$F = \frac{\text{Total available output noise power}}{\text{Portion of output noise power caused by } E_t \text{ of source resistance}}$$

Hence for a two stage cascaded network.

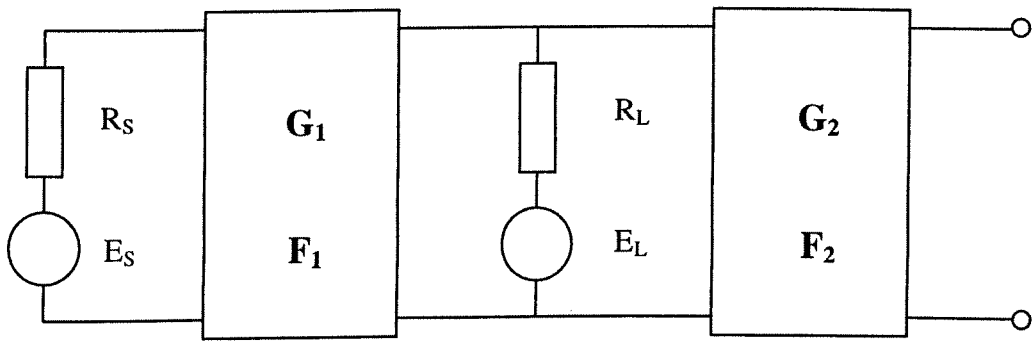

Figure 3.12 *Cascaded analogue amplifier*

Using the alternative definition of thermal noise power as defined in [78], stage 1 can be determined as,

$$N_{i1} = \frac{E_s^2}{R_s} = 4kTB = x \text{ (i.e. available noise power due to source resistance)}$$

Therefore, an alternative expression for F is given by

$$F_1 = \frac{N_o}{G_1 x}$$

Hence,

$$N_O = F_1 G_1 x$$

Where, N_O is the noise at the output of the first stage due to the first amplifier alone. In order to determine the total noise power at the output of the first stage, the contribution to the load resistance R_L is added.

$$N_L = \frac{E_L^2}{R_L} = 4kTB = x$$

Therefore, the total noise power at the output of the first stage N_O is equal to,

$$N_{O1} = F_1 G_1 x + x$$

$$= x(1+F_1 G_1) \qquad \textbf{Eqn. 3.08}$$

Hence, the corresponding noise power contribution at the input of the second stage will be identical to that of N_{O1} given in Eqn. **3.08** and the output noise power for the second stage acting alone would be,

$$N_{O2} = F_2 G_2 x \qquad \textbf{Eqn. 3.09}$$

However, this contains a portion of G_2x due to the thermal noise component of R_L. In order to not duplicate this, it must be subtracted from the total noise power appearing at the output of the second stage. Thus, total noise power at the output is defined as,

$$N_{OT} = G_2\, x(1+F_1 G_1) + F_2 G_2 x - G_2 x$$

$$N_{OT} = G_2 x(F_2 + F_1 G_1) \qquad \textbf{Eqn. 3.10}$$

Hence, defining the overall noise figure of the two-stage system to be,

$$F_{1,2} = \frac{N_{OT}}{G_1 G_2 x}$$

$$F_{1,2} = \frac{G_2 x + G_2 x F_1 G_1 + F_2 G_2 x - G_2 x}{G_1 G_2 x}$$

$$F_{1,2} = F_1 + \frac{F_2 - 1}{G_1} \qquad \textbf{Eqn. 3.11}$$

Importantly, providing the gain of the first stage is sufficiently high, i.e. greater than 10, only the first stage of a cascaded analogue system is critical in noise performance terms.

3.6 Hardware requirements

The main electronic requirements for the proposed ultrasonic reception system are high gain and low noise characteristics with minimal signal distortion [78]. For example, in the case of an air-coupled ultrasonic inspection system, the typical magnitude of signal received at the transducer is in the order of 50μV. Whereas, the desirable detection voltage for further signal processing would be approximately 1V, requiring a voltage gain of around 20000 or 86dB improvement. In the system detailed, the transducers within the scanning arrangement will be at a fixed angle of incidence and the frequency of transmission will be varied in order to tune to the thickness of the test specimen. Therefore, the input stage of the receive system must be able to accommodate the full bandwidth range of the transducers. The problem that this presents is that as the bandwidth of an analogue system in increased, the noise bandwidth of that system also increases leading to a contamination of the received signal and with the magnitudes involved in air-coupled ultrasonic systems, this represents a considerable problem. The proposed scanning arrangement has an operational bandwidth of 800kHz and it would therefore be impractical to build a tuneable filter for this range of frequencies, thus the solution must be achieved in a different way.

As mentioned previously, one of the inherent problems within the ultrasonic receiver is the frequency range over which the receiving pre-amplifier must operate. One way of minimising the noise contributed to the system by these extraneous frequency components is by careful selection of the amplifier used and incorporating a method of frequency rejection [77], for example, the use of bandpass filtering prior to amplification to extract the received signal from the persistent background noise. The resultant effect is to minimise the available operational bandwidth to only that required, i.e. designing the amplifier response to the transducer characteristics. The problem with this method is that this leads to specialised pre-amplifier arrangements, which can only be utilised for the transducers with which the amplifier has been designed and are not as versatile as general purpose amplifiers. Improvement is required in the area of filtering and detection along the lines of frequency agile approach, in other words, a good tuneable filter capable of tracking the frequency of operation to a higher resolution.

By examination of the problem it is apparent that a conflict of interests arises within the interaction of the filtering and the operational bandwidth of the amplifier. The problem is that in order to achieve a good output gain from the amplifier; it is recommended to operate around the mid-band gain of the amplifier. This in turn limits the choice of amplifier for air-coupled ultrasonic applications to those with their -3dB bandwidth within the frequency range of 20kHz and 2MHz. This range being the typical frequency span used for ultrasonic non-destructive inspection. Therefore, traditionally, amplifiers have been chosen as a compromise between good noise characteristics and acceptable bandwidth with the shortfall in the bandwidth performance augmented by additional filtering techniques.

However in the proposed system, the receiver must be capable of operating anywhere in the range of frequencies from 200kHz to 2MHz and still maintain a high degree of frequency selectivity and noise rejection. It is therefore expensive, both in time and financially, to design a tuneable filter that locks into the received frequency and shifts the centre frequency of the filter accordingly. An alternative elegant way of circumventing these frequency problems would be by modulating the incoming signal with the use of a *Superheterodyne receiver* [73, 77] and, in addition, use a fixed frequency high order filter to reduce extraneous noise. Schindel et al. [80] have reported the use of a commercial heterodyning amplifier (Hallicrafters Co., Model SX-62A) to successfully improve the available SNR within an air-coupled system.

3.6.1 The Superheterodyne receiver

The aforementioned problem is that in a test system operating over wide bandwidth of frequencies, there is a discrepancy between the frequency of operation and the frequency of optimal performance for the receiver itself. Therefore, by utilising a similar method to the supersonic heterodyne or "superhet" principle used in radio transmission [77], an alternative reception technique can be found. The heterodyne receiver disposes of the multi frequency problem by translating all the incoming signals so that the carrier frequency is, in effect, changed to a new value, which is constant for all input frequencies. Most of the pre-detector amplification is then carried out at this frequency, which is referred to as the intermediate frequency (I.F.). The basic features of a heterodyne receiver are shown in Figure 3.13.

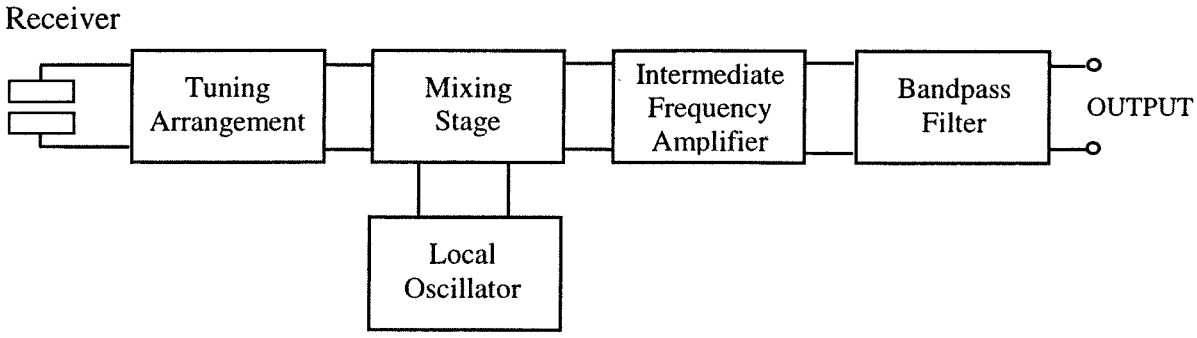

Figure 3.13 *Schematic of a superheterodyne receiver*

The use of frequency modulation [77] to change the frequency of the received signal to a single desirable frequency, allows the designer to filter more effectively and selectively. The additional advantage with this system is that the carrier frequency used to modulate the received signal is referenced from the transmission electronics and therefore requires no manual intervention. This method is commonly used in commercial radio to reference multiple frequencies to a single intermediate frequency.

With traditional amplifiers, providing high gain and good sensitivity over a wide range of frequencies is not easily achieved, requiring careful design so that instability in the system is prevented. However, getting a good selectivity and gain at one particular frequency is relatively straight forward. Therefore, if all the incoming signals are converted to one frequency, then all of the receiver's gain and selectivity can be supplied at this one frequency. This results in a highly stable, frequency selective and sensitive receiver, and is the principle upon which heterodyning operates.

This fixed or relative frequency, the so-called intermediate frequency (I.F.) can be higher or lower than the transmitted signal and is generated by mixing the incoming signal with a signal from a local oscillator. This local oscillator is simply a tuneable R.F. oscillator that is ganged (connected) with the input frequency, such that the frequency is always offset by a constant degree. Therefore, as the input frequency increases, the local oscillator will adjust accordingly so that the frequency difference between the two is constant.

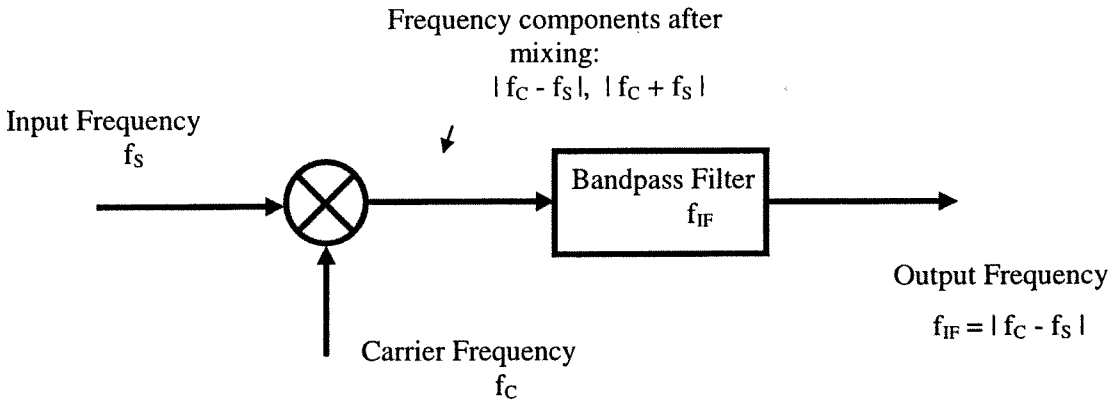

Figure 3.14 *Block diagram representation of frequency modulation*

This mixing process produces two signals as shown in Figure 3.14, by the use of a multiplier. The principle of operation can be explained as follows.

Input signal: $x(t) = m(t)\cos(2\pi f_S t)$

Carrier signal: $x_C(t) = A\cos(2\pi f_C t)$

Therefore,

$$y(t) = x(t) \cdot x_C(t)$$

$$= m(t)\cos(2\pi f_S t)\, A\cos(2\pi f_C t)$$

$$= \frac{Am(t)}{2}\cos\left[2\pi(f_C + f_S)t\right] + \frac{Am(t)}{2}\cos\left[2\pi(f_C - f_S)t\right]$$

$$= \frac{Am(t)}{2}\cos\left[2\pi(f_C + f_S)t\right] + \frac{Am(t)}{2}\cos\left[2\pi f_{IF} t\right] \qquad \textbf{Eqn. 3.12}$$

The preceding analysis illustrates that two signals, the sum and the difference signals, are produced. It is the difference between the two signals that is used as the I.F. and is amplified by a narrow bandwidth tuned amplifier called the I.F. strip of the receiver. In conjunction with the radio receiver principle, the I.F. of the system has been chosen to be similar to an AM receiver I.F. (typically 455kHz) at the system midband of 500kHz. This was chosen for the intermediate frequency due to the abundance of inductive and capacitive components available for this frequency of operation and since it was around

the midband gain point of the selected amplifier, but any other frequency can equally be selected. The resultant I.F. signal is then filtered further to eliminate the "sum" signal and provide better noise rejection.

The only problem associated with this form of receiver is the problem of imaging, (i.e. the receiver will pick up and modulate an undesirable frequency, sometimes referred to as 'birdies', these are tuneable carrier waves generated by the receiver itself, often coming from the carrier frequency or local oscillator. To combat this problem, careful screening must be made of the carrier input and other associated electronics pertaining to the signals that are to be mixed. The result is a wideband receiver system with all the advantages of narrowband noise rejection techniques, and with the addition of envelope detection and buffering stages, can be used to produce an electronics package suitable for interfacing with available computer data acquisition hardware.

3.7 Receive system design

The main discourse of this Chapter so far, has pertained to the noise inherent within an analogue receive system and the methods of reducing this noise. Typically, amplifiers are designed with constraints such as gain, bandwidth and input impedance as the foremost important criteria. However, in the instance of an analogue receiver for air-coupled ultrasonic applications, the noise performance of the system is of tantamount importance due to the low magnitudes of signal encountered, typically 10-100μvolts in the 100kHz to 1MHz range. The noise reduction methodology has already been discussed, now the system design is explained. Figure 3.15 illustrates the salient design features of the frequency agile receiver system.

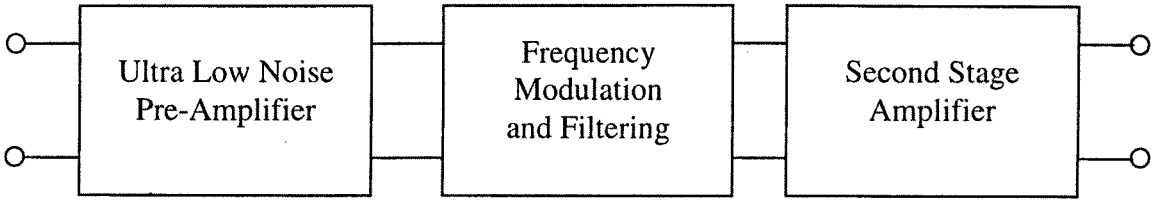

Figure 3.15 *Frequency agile receiver schematic*

As discussed previously, the transducer impedance and the first stage of the amplifier determines the ultimate limit of equivalent input noise (Section 3.4 & 3.5). Therefore, in order to optimise the overall noise performance of the receiver system careful selection of the initial amplifier section must be made. As a high noise figure for the input pre-amplifier would cause degradation in signal to noise performance throughout the whole system. By careful examination of the earlier theoretical work, it is apparent from **Eqn. 3.05** that a lowering of the input impedance of the amplifier, results in a lower overall noise voltage contributed to the system. This condition is realisable by the implementation of a current amplifier and its merits have previously been documented [81-83]. The current feedback amplifier offers a wide bandwidth input to the amplifier consistent with the needs of this system, allowing for a low input impedance amplifier which will provide a better impedance match to the transducers. Additionally, the reduction in input impedance means that there is less noise gathered from the surrounding environment through the cabling acting as an antenna. The advantage that this offers is that the pre-amplifier electronics do not have to be located close to the transducer, unlike voltage amplifiers with higher input impedances. In these instances, it is advisable for the voltage amplifier to be connected to the transducer with the shortest possible leads to reduce the influences of cable capacitance and noise pick-up

The current-feedback amplifier used as the initial stage in the pre-amplifier was an AD811 ultra-low noise amplifier from Analogue Devices. As described in the data sheet, included in Appendix A.

"The AD811 is a wideband current-feedback operational amplifier, optimised for broadcast quality video systems. The –3dB bandwidth of 120MHz at a gain of +2 make the AD811 an excellent choice for all video systems. The AD811 is also excellent for pulsed applications where the transient response is critical. Because the AD811 is a current feedback amplifier, this bandwidth can be maintained over a wide range of gains. The AD811 also offers low voltage and current noise of $1.9\,nV/\sqrt{Hz}$ *and* $20\,pA/\sqrt{Hz}$ *respectively, and excellent dc accuracy for wide dynamic range applications."*

In accordance with the theory presented in Section 3.5 for cascading amplifiers, rather than incorporating all the gain into a single stage, it can be split across two amplifiers. Using two amplifiers, the noise within the amplifier network from the second amplifier can be nearly nullified, as long as the initial gain stage has a voltage gain of at least 10. Hence, the gain in the two stages is split such that the input amplifier has been configured in accordance with the manufacturers recommendations, providing a gain of 10 or 20dB, whereas the second stage is more powerful, with a voltage gain of 100 or 40dB. The circuit illustrated in Figure 3.16 was implemented.

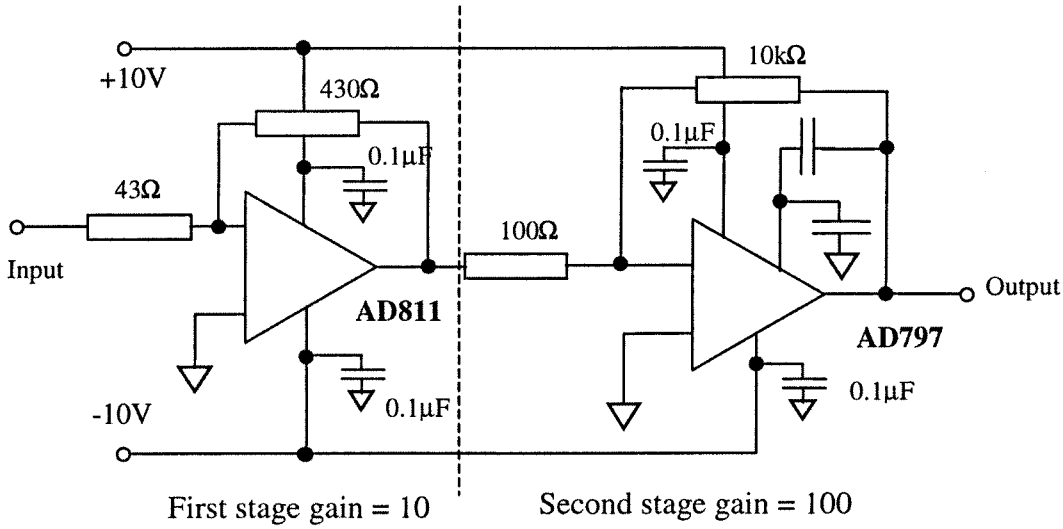

Figure 3.16 *Ultra-low noise cascaded current/voltage pre-amplifier*

The amplifier used in the second stage of the cascaded network also exhibits exceptional low noise characteristics, with an input noise voltage of $0.9\,\mathrm{nV}/\sqrt{\mathrm{Hz}}$ and an input noise current of $2\,\mathrm{pA}/\sqrt{\mathrm{Hz}}$. Although this amplifier has superior noise characteristics to that used for the first stage, the input impedance of this amplifier is substantially higher, approximately $2\mathrm{M}\Omega$. Hence, if this amplifier was used for the initial stage of the cascade amplifier, more atmospheric noise would be introduced to the system at the input, due to the cable attaching the amplifier to the transducer acting as an antenna. Moreover, a high input impedance coupled to long cable lengths also increases the possibility of oscillation in the amplifier, due to ringing in the cabling.

The frequency response of the pre-amplifier was determined by utilising a HP33120A function generator to produce a 1 volt peak-to-peak signal, which was then passed

through a 1:1000 attenuator to reduce the magnitude of the signal in order not to saturate the amplifier, as illustrated in Figure 3.17.

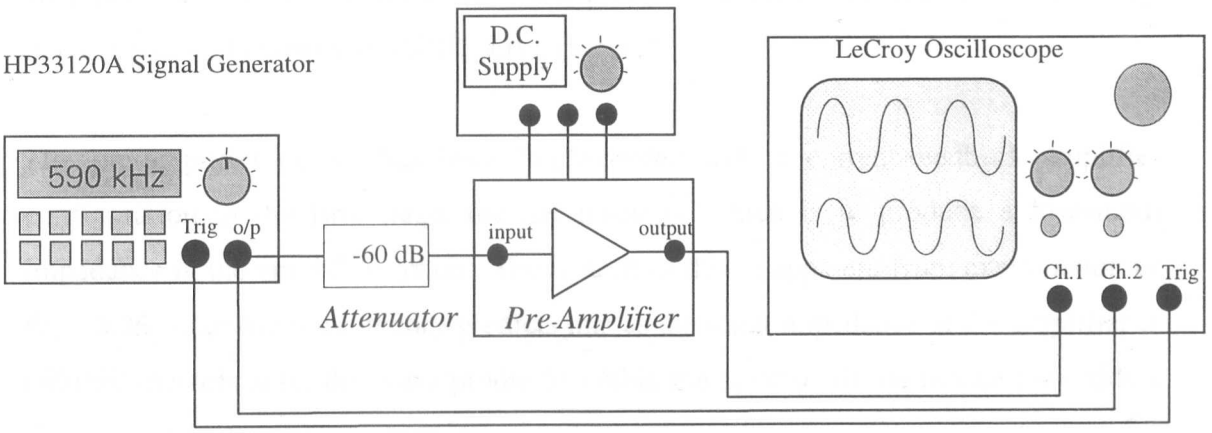

Figure 3.17 *Experimental apparatus for amplifier bandwidth measurement*

The input signal was then varied with respect to frequency and the output signal magnitude was measured driving the 1MΩ load on a LeCroy digitising oscilloscope, as illustrated in Figure 3.18.

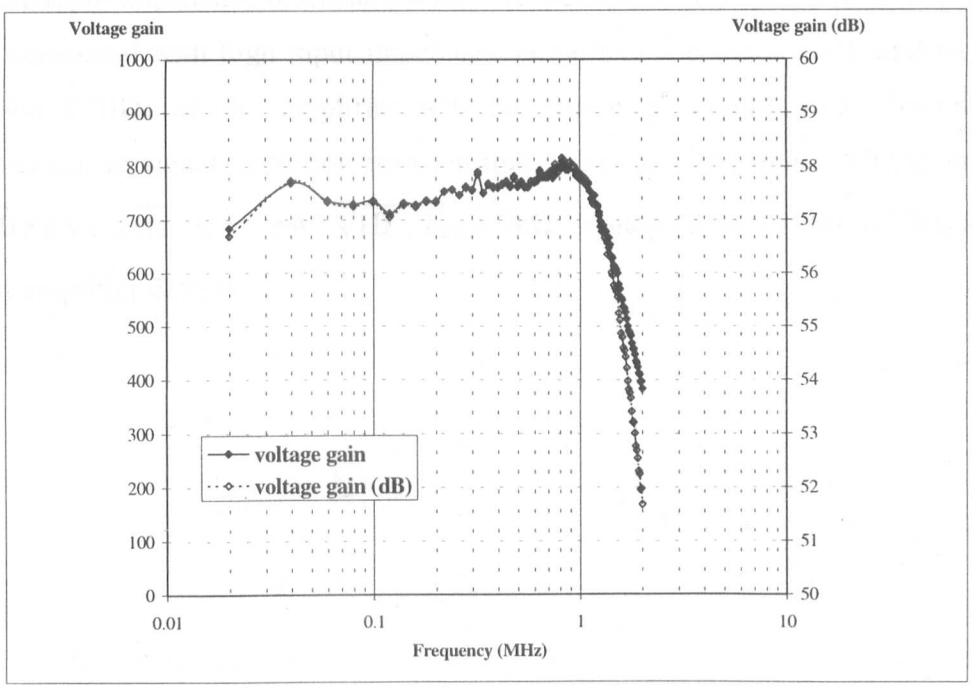

Figure 3.18 *Frequency response of pre-amplifier arrangement*

Since this is the input stage of the receiver system, a receiver that is essentially being designed to receive a wide range of input frequencies and deliver a narrowband output, the frequency response of the initial pre-amplifier will define the operational bandwidth

of the receiver. Therefore, although it has been stated that wideband amplifiers generate a wider noise bandwidth, it is essential that this stage have a large enough bandwidth to encompass all the desired frequencies of operation, since modulation and filtering in the latter stages will enhance the SNR performance.

The pre-amplifier circuit has been implemented with a current-feedback amplifier configuration in the first stage, the net result of which is to produce a low input impedance in the amplifier system. The benefit of this is apparent from examination of Eqn. **3.05**, since the noise theory predicts that as the input impedance of the amplifier is reduced towards zero, the noise produced within the system will be reduced towards a factor of $1/Z_T$. Although, by examining Eqn. **3.06,** it is apparent that this reduction in noise will not result in a higher SNR, because the reduction factor is applied simultaneously to the input signal. However, the most important aspect of this noise reduction is that the inherent system noise is actively being minimised, which is a pre-requisite for low-noise analogue system design. Additionally, as mentioned previously since the input impedance of the amplifier is reduced, so too is "pick-up" or the antenna effect associated with high input impedance amplifiers and the overall total harmonic distortion (THD) of the amplifier will be improved. Figure 3.19 illustrates the improvement in signal distortion between that of an ultra-low noise voltage amplifier (E_n = 0.8 nV / $\sqrt{Hz}$, I_n = 1 pA / $\sqrt{Hz}$, Z_{IN} = 7kΩ , Voltage gain = 1000 (60dB)) and the current amplifier detailed.

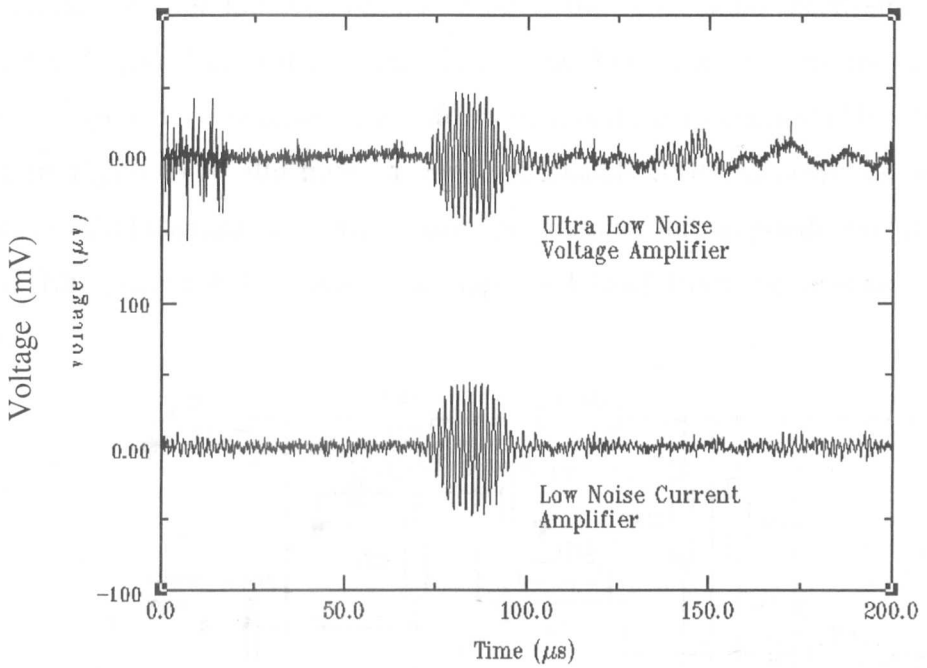

Figure 3.19 *Comparison of signal-to-noise improvement using current amplifiers over conventional voltage amplifiers.*

Using a similar arrangement to that described for the calculation of the pre-amplifier frequency response (See Figure 3.17), a 1volt, 10 cycle tone burst was applied at the input of the two amplifiers via the 1:1000 attenuator, and the resultant amplified signal captured on a LeCroy digitising storage oscilloscope. What is apparent from Figure 3.19, is that although the overall noise floor of the signal shows only slight improvement, the distortion factor of the signal from the current amplifier is improved markedly over that of the voltage amplifier. In other words, the trace either side of the received signal demonstrates less distortion for the current amplifier with respect to the voltage amplifier. By examining Figure 3.19, it is apparent that extraneous noise has been developed between 0-25μs due to 'pick-up' from the firing circuitry driving the transmitter and further distortion is evident after 100μs possibly due to ringing in the amplifier after reception of the signal.

Consequently, by measuring the received signal strength with respect to the average noise level, the calculated SNR for the current amplifier was 45dB@500kHz in comparison to 31dB@500kHz from the previously utilised low noise voltage amplifier.

The second stage of the receiver hardware is the modulation electronics, which as detailed in Figure 3.15 and described in Section 3.6.1, converts the frequency of the incoming signal to a second standardised intermediate frequency (I.F.). The circuit layout in Figure 3.20 illustrates a single sideband (SSB) receiver, essentially this comprises of a balanced mixer with carrier suppression for amplitude modulation and a passive filter network to remove the upper sideband from the resultant modulated signal.

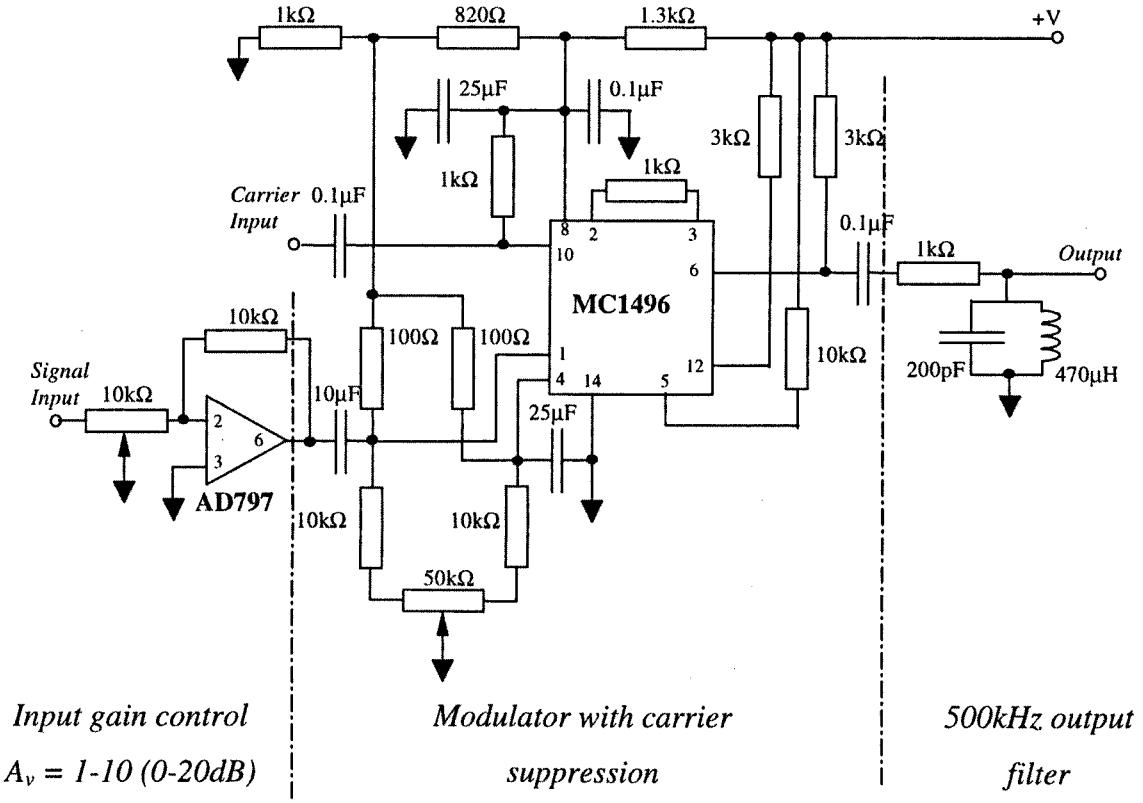

Figure 3.20 *Amplitude modulator with carrier suppression and upper sideband filter.*

The filtering of the upper sideband is implemented by the use of a simple RLC bandpass filter, which can be designed for the given centre frequency by the following equation.

$$f_o = \frac{1}{2\pi\sqrt{LC}} \qquad \textbf{Eqn. 3.13}$$

In this instance, where the frequency of operation is 500kHz, the values for the inductance (L) and the capacitance (C) are given as 470µH and 200pF respectively. The addition of the resistor in the network allows control of the Q, or quality factor of the

filter and is defined as the measure of the sharpness of the peak. This can be determined as the centre frequency of the filter divided by the width at the –3dB points, or as:

$$Q = \omega_0 RC \qquad \textbf{Eqn 3.14}$$

where, $$\omega_0 = \frac{1}{\sqrt{LC}}$$

Figure 3.21 below, illustrates the frequency response of the filter network and defines the 3dB bandwidth to be approximately 20kHz and hence a Q of 25 for a centre frequency of 500kHz. Also illustrated in Figure 3.21, is the influence of the variable resistor on the Q of the filter network. It is apparent that as the resistor value is decreased, the Q of the filter also decreases, as shown in Equation **3.14.**

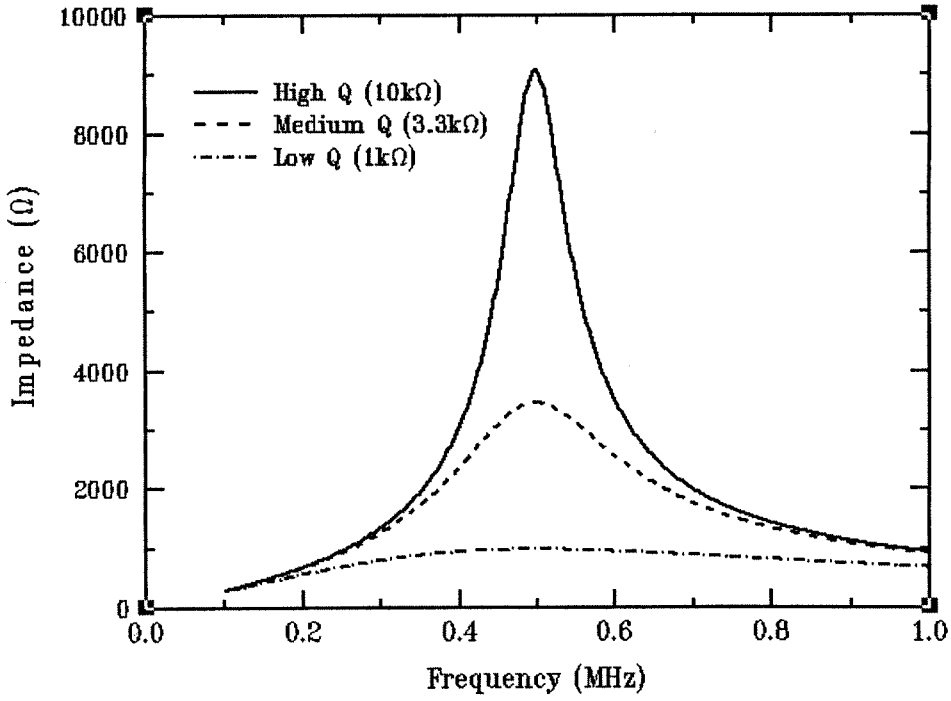

Figure 3.21 *Frequency response of the RLC filter.*

The last section of the receiver arrangement is the I.F. amplifier stage, where further gain can be provided to the system (if required) via a simple low noise voltage feedback amplifier. The gain stage is followed by a second passive filter, which reduces the noise bandwidth of the system further and therefore allows the introduction of this further

gain without degradation of the system noise performance. This I.F. gain stage provides a further improvement in signal strength of between 20 to 40dB, with a narrowband filter with manually controlled Q-factor and output buffering capable of driving computer interface boards is illustrated in Figure 3.22. Generally, computer acquisition cards for data capture have input impedances of 50Ω, hence the output of the receiver electronics incorporates a OPA633 video driver to facilitate transfer of signals to PC for subsequent analysis.

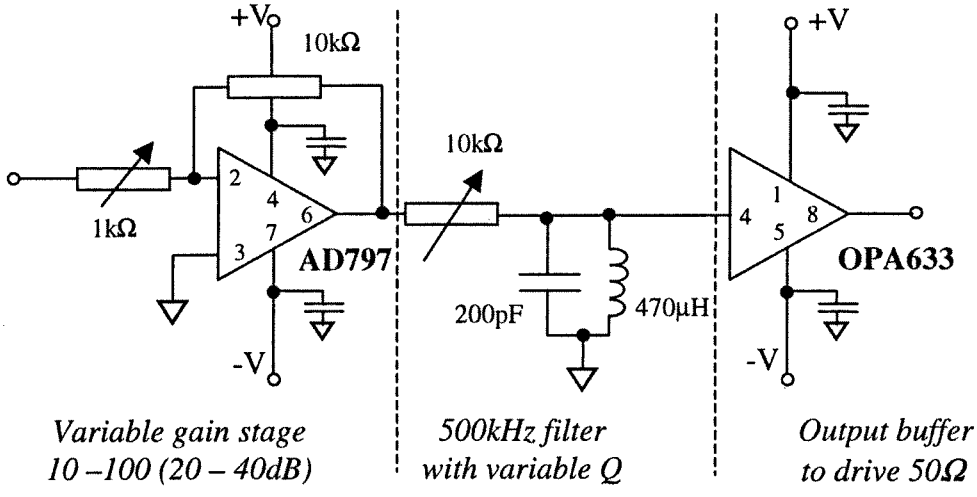

Figure 3.22 *Intermediate frequency amplifier with bandpass filter and buffer stage*

Therefore, utilising the heterodyne receiver concept it is possible to produce a system that offers the aspects of high gain and good selectivity across a high operational bandwidth. Consequently, it is possible to simulate the reception of a signal of similar magnitude to that detected in through-air ultrasonic Lamb wave operation using the experimental configuration shown in Figure 3.17. A 600kHz tone-burst of 10 cycle duration and 50mV amplitude was applied to the input of the attenuator and the resultant signal generated is illustrated in Figure 3.23. Here, Trace 1 depicts the signal generated across the terminals of the oscilloscope from the output of the attenuator and Trace 2 represents the same signal after heavy averaging and applying a vertical zoom with a factor of 10. The initial received signal being in the order of 50μvolts, which compares favourably by that measured from a practical system. Figure 3.24 illustrates the resultant signal after amplification by the pre-amplifier and heterodyne system, illustrating the effectiveness of the overall receiving system, where the output peak-to-

peak amplitude from the system is approximately 8 volts and has a SNR figure of 41dB with no averaging applied.

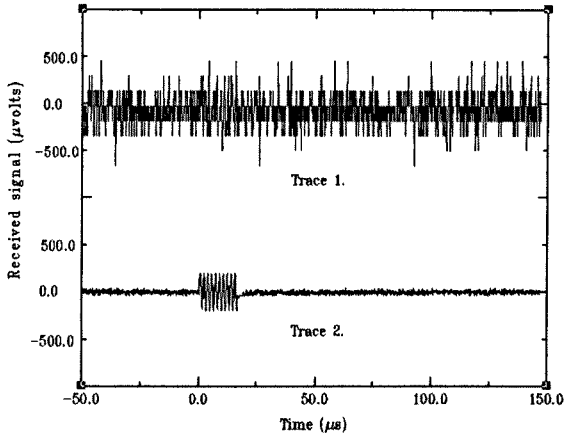

Figure 3.23 *Signal at input of receiver system*

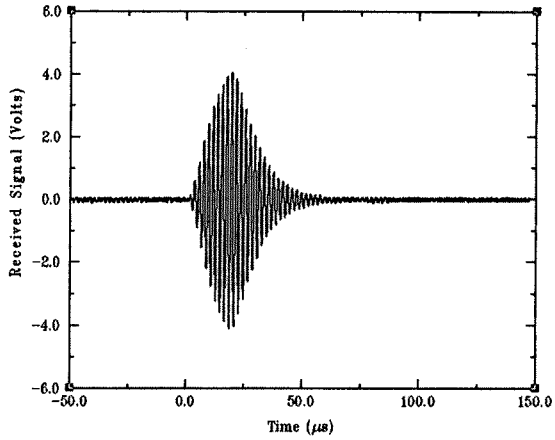

Figure 3.24 *Resultant signal after modulation and amplification*

The new heterodyne receiver offers an input frequency range of 10kHz to 2MHz, providing a SNR performance of 41dB, system gain of approximately 103dB and an output restricted bandwidth of 20kHz centred around an intermediate frequency of 500kHz.

This is illustrated in Figure 3.25, where the frequency domain plot shows the received signal before and after modulation. The peak on the right, illustrates the frequency at which the transmitter is operating (≈600kHz) and the peak on the left indicates the frequency at the output of the heterodyne amplifier (≈500kHz). Therefore, in this example, there has been a 100kHz frequency shift applied to the incoming signal in order to refer it to the I.F.

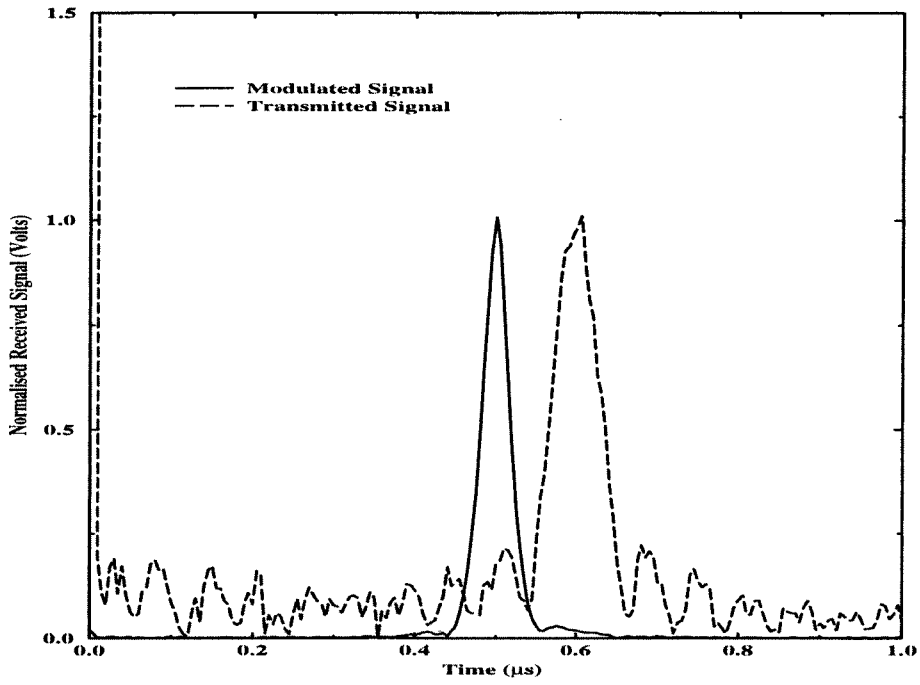

Figure 3.25 *Illustration of frequency shifting within heterodyning receiver*

3.8 Conclusions

This Chapter has shown that careful consideration of many factors including intrinsic transducer noise, electronic noise and bandwidth of operation is essential for the design of an ultrasonic receiver system. It is also apparent that one of the major noise contributions within the system is that of Thermal or Nyquist noise generated within the transducer itself and while this is unavoidable, it should be taken into consideration when specifying the design criteria for any proposed receiver electronics.

The design methodology of a frequency agile receiver system has been documented and the resultant system offers ultra-low noise receive electronics with high gain characteristics, approximately 103dB across the system and narrowband procedures to reduce the overall system noise bandwidth to approximately 20kHz.

Now that the electronic requirements of the new Lamb wave scanning system have been addressed, i.e. a receiver system capable of low-noise amplification over a wide range of input frequencies, the next stage in the scanner development is to develop a range of transducers capable of robust operation over this frequency range.

Chapter 4

Theoretical techniques for assessment of piezocomposite transducer system performance

4.1 Introduction

The theoretical modelling of ultrasonic systems has become an integral development tool within the ultrasonic industry for the design and optimisation of transducer technology. Such modelling is essential in order to reduce overall development costs and gain a more intimate knowledge of transducer operation. The increased availability of computing power now allows the designer to model accurately the transducer behaviour and its interaction with the surrounding media. For the proposed scanning system, there is a requirement for transducers with greater bandwidth than currently associated with piezocomposites. Utilising finite element modelling techniques it is possible to experiment with a number of design iterations to determine the feasibility of these transducers, while not incurring the costs of continual practical prototyping.

This Chapter details the design process and background required to construct a finite element model of a piezoelectric transducer. An introduction will be made to the limitations and design criteria that must be observed in order to accurately model such devices. This Chapter is intended as a brief introduction to theoretical modelling techniques employed in finite element modelling to aid the reader's understanding of the transducer development described in the following Chapter. The modelling package utilised was the commercial version of the ANSYS® package [84], version 5.4 which has an unlimited number of nodes and elements allowing for extremely complex models.

Additionally, theory is presented relating to a software package [85] designed internally within the University of Strathclyde for the calculation of acoustic beam profiles, directly from surface displacement data produced by the finite element code. The theoretical modelling of this acoustic beam profile allows the designer to determine the practicality of any modelled transducer and tailor subsequent iterations of the design for narrower beam width or alteration of focal distances.

4.2 Review of Finite Element Modelling

Finite element modelling (FEM) [86] is a mathematical technique, whereby a large complex structure can be divided into a collection of smaller volumes (finite elements) for analysis. In the instance of a piezoelectric structure, each of these finite elements has a set of equations, which governs the behaviour of each constituent element. This ensures that the displacement, pressure and charge are continuous across the element boundaries and that all the boundary conditions are satisfied.

As the number of elements within the model is increased, the overall accuracy of the modelled representation increases, this is especially prevalent in models with complex geometries such as cylinders and annuli. Figure 4.01 illustrates the improvement in accuracy afforded by increasing the number of elements used to construct a cylindrical model. However, as the number of elements incorporated into the model increases, so does the computation time required to solve the model. The division of the volume into the subsequent elements is referred to as *meshing*.

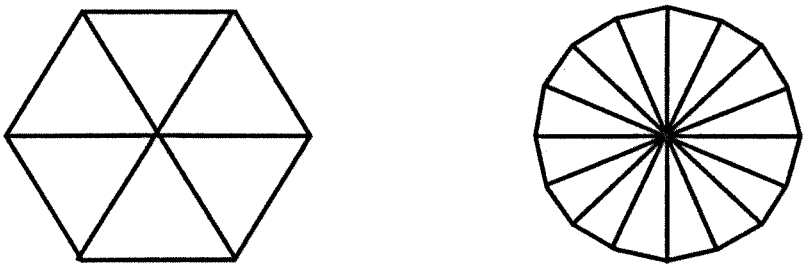

Figure 4.01 *Improvement in modelled representation with additional elements*

When operating with finite element analysis (FEA), it is important to define a set of initial design assumptions, in order to limit the overall complexity of the modelled domain, as illustrated in Figure 4.02. In the case of piezoelectric modelling, these primary assumptions should include aspects such as transducer boundary conditions, e.g. is the transducer radiating into air or water? If the transducer is operating in air, then it is not normally necessary to model a surrounding medium of air, when the initial (void) boundary conditions may suffice. However, if the transducer is immersed in water, then is becomes necessary to include the fluid medium into the model parameters. Therefore, by limiting the overall number of modelled factors within this

domain, it is possible to focus on the primary requirements of the model. In addition, any reduction in domain limits will lead to reduced computational time.

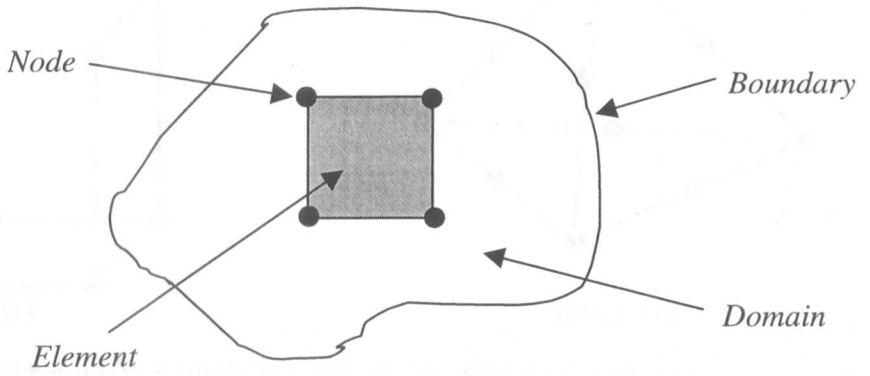

Figure 4.02 *Fundamentals of FEM*

The basic modelled *domain* is constructed from a series of discrete points, referred to as *nodes,* which form a lattice framework that defines the overall modelled entity. These nodes are in turn connected together to form a number of small finite *elements*. Each of the nodes within this framework has a number of *degrees-of-freedom* (DOF) associated with that node. Ultimately, it is the user's choice of element which limits the number of DOF that are to be modelled. Typically elements have DOF which include temperature, voltage, pressure and displacement, in all axes. It is possible to reduce the number of DOF modelled when selecting the element type by flagging which of the options is not relevant to the user's application within the software. Each element has to have nodes associated with each of the element vertices, in order to transfer information relating to the specified DOF between adjacent elements. Typically, in a three dimensional solid brick shaped element there are 8 nodes, connected to the vertices of the element, however more complex elements are available whereby the element possess additional mid-point nodes which are located on the centre of each edge. The additional nodes increase the accuracy of the modelled entity, but increase the overall complexity of the model. Efforts have been made throughout the modelling phase of this Thesis to utilise elements with a lower order of nodes in order to minimise computation time without compromising accuracy. Figure 4.03 shows the two primary elements that have been utilised, the standard 8 node brick shaped element (SOLID5) and the 10 node tetrahedral block (SOLID98) for more complex structures.

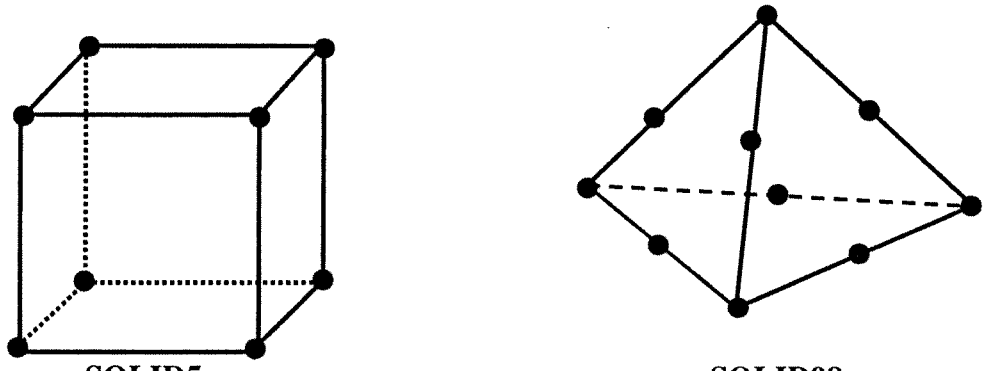

Figure 4.03 *Standard piezoelectric element modelling blocks*

The final consideration when defining the domain of the model is the *boundary* conditions pertaining to the overall system. Is the transducer radiating into water? Does the composite have backing? Are the edges of the composite constrained within a holder? All these factors must be considered and the appropriate boundary conditions defined by the user.

4.3 Methods of Finite Element Analysis

Within all forms of FEA, the general structure of the analysis is broken down into three sequential procedures. These are;

Pre-processing – this is where the user defines the operational parameters of the modelled structure (model geometry, DOF & boundary conditions).

Solution – where the matrices are created within the model using the appropriate solving equations.

Post-processing - where the subsequent results generated by the solver can be analysed and additional information calculated.

4.3.1 Finite Element Analysis techniques

Within the FEM package, there are four different types of analysis that can be performed upon the test structure, these are *static, modal, harmonic* and *transient.* All forms of analysis are governed by one general equation, given by

$$[\mathbf{M}]\ddot{\mathbf{u}} + [\mathbf{C}]\dot{\mathbf{u}} + [\mathbf{K}]\mathbf{u} = \mathbf{F} \qquad \textbf{Eqn. 4.01}$$

where,

[M] is the mass matrix
[C] is the damping matrix
[K] is the stiffness matrix
u is the displacement vector
F is the forcer vector

Each point above the vector indicates differentiation with respect to time. Each of the different forms of analysis, use differing initial conditions within the general equation relating to the force vector. These are not discussed in detail here, as a knowledge of the finite element mechanics is not required, but the mathematical manipulation is explained by Zienkiewicz and Taylor [86] and the relevance of the mechanics to piezoelectric structures is covered by Bennett [87] and Reynolds [88].

Static - Static analysis is used to calculate steady state behaviour, such a incident pressure between two bodies at rest and is not of relevance to this study.

Modal - Modal analysis is the determination of the natural resonant frequency modes and shapes (i.e. structural displacement) within the elastic structure. This analysis technique is useful for determination of both thickness and lateral modes of vibration within the piezoelectric structure.

Harmonic - Harmonic analysis describes the process whereby the structure is excited by a sinusoidal load of a given amplitude and frequency. Thus,

components such as displacement, force and charge can be solved for the given structure in ANSYS®. By use of an iterative solving method, this can be run consecutively across a range of frequencies to determine the operational characteristics of the piezoelectric device.

Transient - Transient analysis operates in a similar manner to harmonic, however, in this instance the device under inspection is subjected to a time dependent load. Using this form of analysis it is possible to examine wave propagation through differing media and examine resultant transmitted pulse shapes of piezoelectric transducers.

4.4 Modelling conditions

4.4.1 Model meshing

Due to the hierarchical nature of designing a finite element model, the meshing procedure has traditionally been implemented by the placing of nodes along modelled lines and keypoints by user definition. For example, if the modelled structure is uniform and has a periodic nature, such as a composite device, the user selects a given group of lines and applies the required scale of meshing, as shown in Figure 4.04.

Before meshing, outer lines selected and split

After meshing, with user defined line sizing.

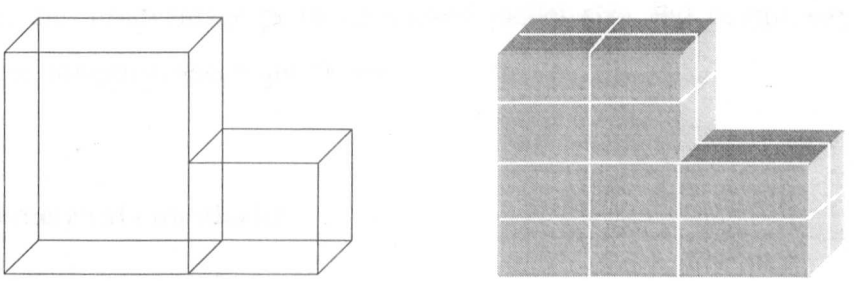

Figure 4.04 *User defined meshing*

This technique is limited in its scope of operation since in more complex geometries it becomes harder to define accurately the desired meshing characteristics. Additionally in the piezoelectric analysis to be considered in this Thesis, commonly utilised electrically

coupled elements such as SOLID5 and SOLID45 (an electrically uncoupled 8-node brick used for polymers) are impractical, as the structure of these elements are restricted to brick or prism shapes. Clearly in models utilising curves and other non-regular volumes there will be problems in defining suitable meshing conditions. However, within the ANSYS® package there are alternative coupled elements such as SOLID98 and SOLID72 (tetrahedral elements) and a *smartsize* procedure, which automatically fits elements to given geometries. This procedure allows the user to mesh much more complex structures with a degree of designability, controlling such aspects as mesh size, element shape priority and *free* or *mapped* meshing. Mapped meshing is as close an approximation to user defined meshing as possible, whereas free meshing fits the elements in what appears to be a random manner determined by the computer solving routines as illustrated in Figure 4.05.

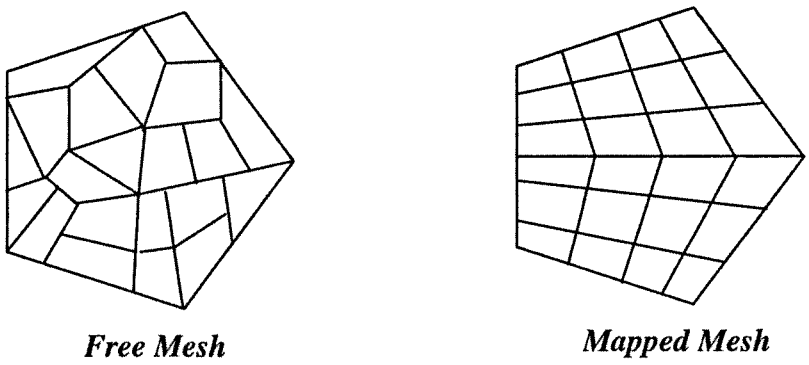

Figure 4.05 *Examples of computer generated meshing*

Although this free meshing system offers a more robust method of meshing complex structures, the disadvantage is the increased model size and complexity, leading to much larger computational requirements.

4.4.2 Symmetrical boundaries

As discussed previously, it is necessary for the FE model to have a sufficiently fine mesh in order for the information in each node to be accurately transferred. However, if the model is meshed too finely, then the computational requirements and solving time will be excessive. A method by which the complexity of the model can be reduced, is the application of symmetrical boundaries to the finite element model whenever

possible. With a uniform structure such a 1-3 connectivity piezocomposite device, where there are periodic ceramic pillars embedded within a polymer matrix, it is possible to reduce the overall size of the model considerably. Figure 4.06 illustrates the structure of a composite device, where the dark region signifies the ceramic and the lighter volume is the polymer, highlighting the minimum volume required for modelling purposes. In this instance, symmetrical boundaries are applied to faces in the x, y and z direction resulting in a model with *eighth symmetry*. The resultant section of polymer and ceramic is referred to as a *unit cell,* with the complete model comprising multiples of this cell.

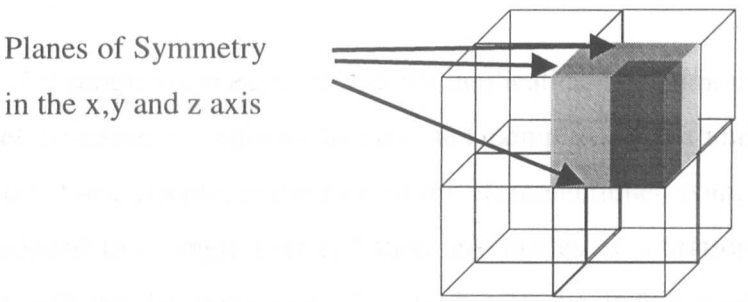

Figure 4.06 *Symmetrical boundaries*

For annular or circular devices, symmetry has to be applied within a polar co-ordinate system in order to accurately represent the practical device. The degree of symmetry possible in such a system is dependent upon the periodicity of the device and complexity of structure. For example, a solid ceramic disc can be significantly reduced in size, down to a small arc section of the transducer, whereas an annular composite will be restricted by the internal structure of the pillars. The maximum degree of symmetry that can be applied will dissect the pillars diagonally at 45°, so that cylindrical symmetry can be applied, as illustrated in Figure 4.07.

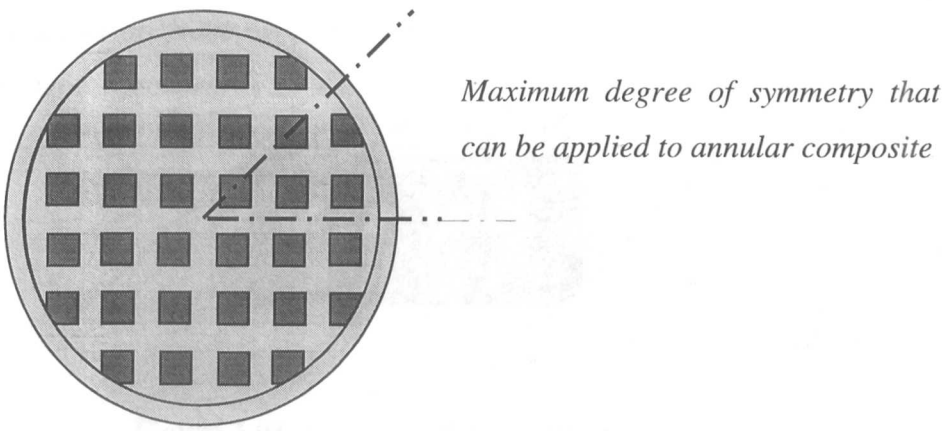

Figure 4.07 *Symmetrical restrictions for annular models*

One of the inherent problems associated with the application of symmetrical boundaries is as the model structure is reduced in size and complexity, certain aspects of its behaviour are lost. For example, in the case of the aforementioned composite device, if the model is reduced to a single unit cell then any modes of vibration arising in the width direction will not be supported. This is due to the inability of the model to determine the width of the transducer from the given single element cell. Therefore, any periodic waves formed in the composite device due to the width dimensions of the plate will not be modelled accurately. Thus, it is apparent that the degree by which the designer reduces the model is critical to the accuracy of the final analysis.

4.5 2½ Dimensional modelling technique

As discussed, the size of the model governs the resultant computation time required to solve the model. Additionally, over simplification of the model can lead to an inaccurate solution. Since the main area of transducer research within this Thesis is the modelling of 1-3 connectivity composites, the only accurate method of representing these devices is via three dimensional modelling. However, another possible method of modelling was suggested by Reynolds [88], whereby a thin section of the complete device was modelled with symmetrical boundaries on two sides of the model as illustrated in Figure 4.08. With the application of symmetry in such a manner results in a device which is effectively infinite in one direction while having accurate dimensions in the second axis. In this form of model, any width mode vibrations active within the device will be supported in one axis and computation time will be significantly reduced.

Symmetrical boundaries on front and rear face produce effectively infinite bar composite

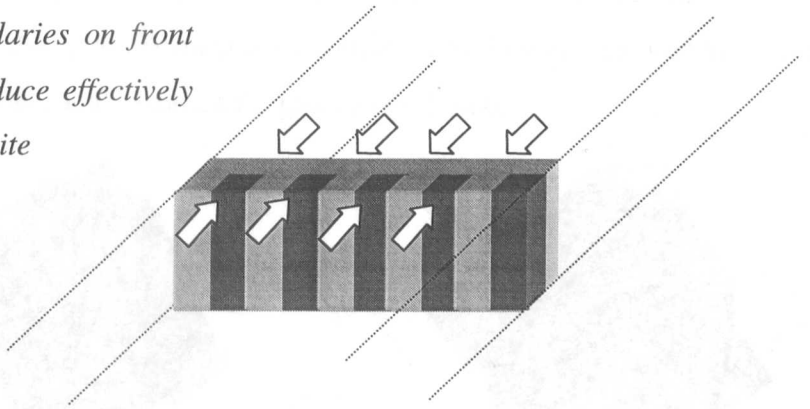

Figure 4.08 *2.5D modelling approach*

4.6 Output information

The resultant information available after model solving falls into two main categories of interest, transducer displacement (vibration within the device structure in the three fundamental directions) and the operational impedance and phase of the composite device. It is this interaction with the model that allows the designer to observe visually the motion within the transducer substructure. By using post-processing techniques, it is possible to extract this displacement information to calculate the magnitude and phase of the surface vibration and therefore determine the predicted acoustic emission field through a second theoretical modelling package. For example, consider the transducer shown in Figure 4.09. This transducer comprises of a 40% volume fraction 1-3 connectivity piezocomposite composed of PZT-5H ceramic and CY1301/HY1300 hard-set epoxy. The transducer is mounted in a 30mm diameter plastic holder and is matched for operation in water with a quarter wavelength matching layer manufactured from hard-set epoxy.

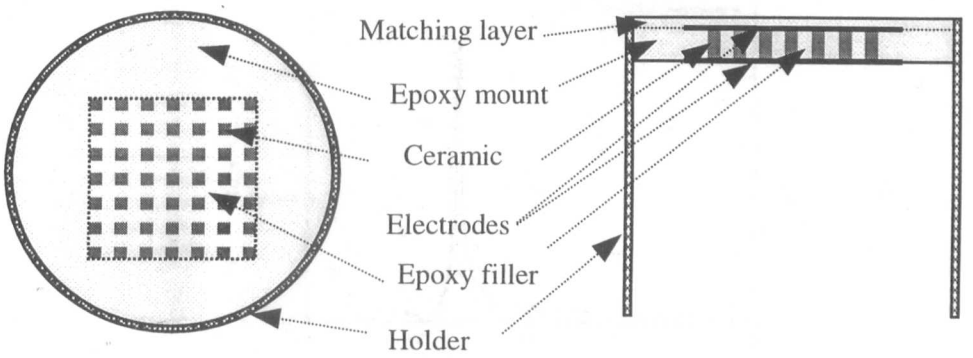

Figure 4.09 *Construction of modelled 1-3 piezocomposite transducer*

Figures 4.10 (a & b) represent (a.) the amplitude of the surface displacement profile and (b.) the phase of the given surface displacement profile when excited with a 10 cycle tone burst at the electrical resonant frequency of 425kHz.

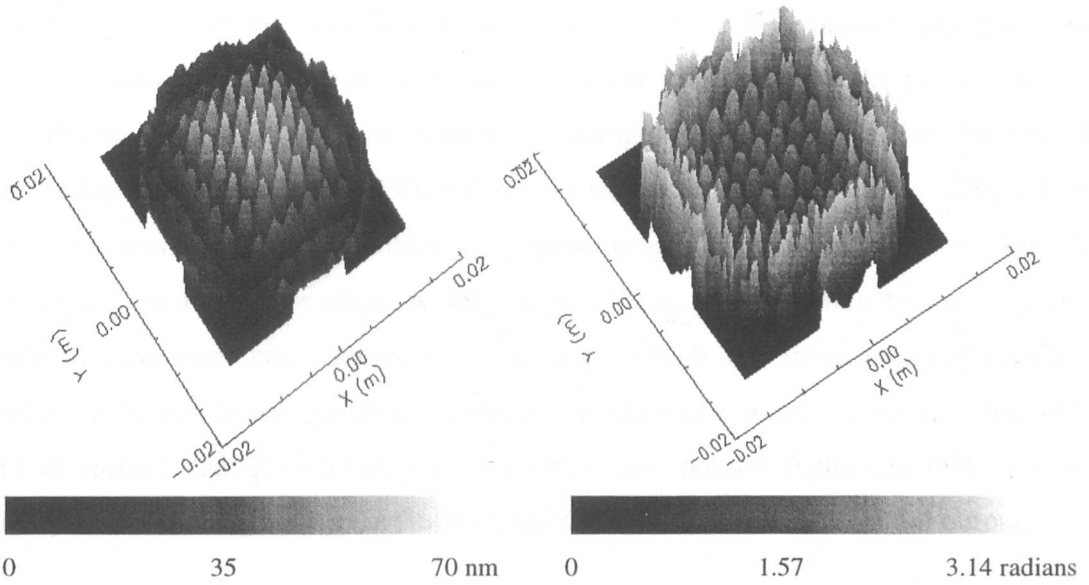

Figure 4.10(a & b) *Amplitude and phase surface displacement profiles generated using ANSYS® FEM code.*

Moreover, by capturing the voltage generated across each of the nodes on one of the transducer faces and processing the data within ANSYS®, it is possible to determine the transducer operational impedance characteristics of the piezocomposite transducer. Consider a 50% volume fraction 1-3 piezocomposite constructed of PZT-5A ceramic and CY1301/HY1300 hard-set epoxy with a thickness of 2.88mm. Using ANSYS® it is possible to compare operational impedances of simulated and experimental results as shown in Figure 4.11

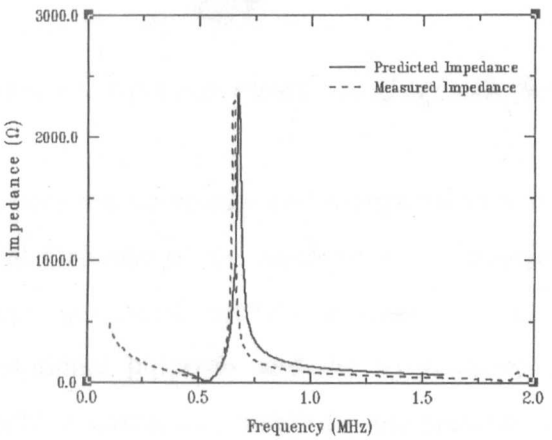

Figure 4.11 *Comparison of simulated and experimental impedance characteristics*

4.7 Theoretical beam profiling

A software package has been designed within the University of Strathclyde, which allows the generation of acoustic radiation patterns for both theoretical and practical ultrasonic devices radiating in both air and water. This simulation programme is implemented through the Visual-Numerics package Pv-Wave [89]. The theoretical method adopted by Benny et al. [90] utilises the traditional Rayleigh integral [91]. This method has been incorporated within a computer program in a discrete form which is compatible with the Finite element data output. Thus, it is possible to integrate the surface displacement characteristics determined through the finite element package ANSYS® into the beam profiling software by imposing a grid topology onto the resultant surface displacement profile (magnitude and phase). Although, this requires further post-processing within the finite element model to re-order the nodal output.

The approach is based upon the evaluation of the Rayleigh integral, examining the acoustic pressure field generated by a planar surface S_r surrounded by a rigid baffle, as illustrated in Figure 4.12.

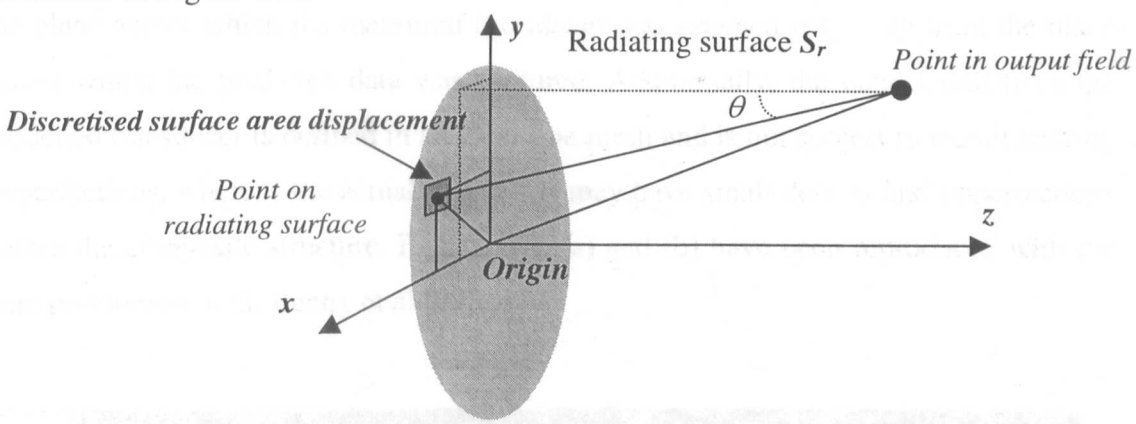

Figure 4.12 *Geometrical representation of acoustic field calculation*

To allow comparison between computed and experimentally measured pressure beam profiles, the directional response of the hydrophone is incorporated within the code. Therefore, if equations governing the displacement of the radiating surface are discretised for computational purposes and the hydrophone directional response is incorporated, a complete, discrete, expression for the pressure at any point in the field can be obtained and implemented for numerical beam profile prediction.

Additionally incorporated within the modelled capabilities are considerations such as attenuation with respect to frequency, temperature, pressure and relative humidity (for operation in a gaseous medium) resulting in a powerful design tool for ultrasonic transducer systems.

To demonstrate the power of this theoretical modelling tool, an example with a simple piezoelectric transducer is detailed. In the example illustrated, the transducer used was a simple piezocomposite, which was measured using the laser vibrometer arrangement described in Appendix B, to determine the surface displacement characteristics. The resultant surface displacement was processed using the discretised theoretical method described, to produce a predicted acoustic emission profile. Additionally, the actual beam profile of the transducer was calibrated using the beam profiling scanner available within the Laboratories in the University of Strathclyde, again, as described in Appendix B. The resultant beam profiles shown in Figures 4.13 (a) and (b) illustrate the correlation between experimentally derived data and that predicted theoretically. The discrepancies between the two are due to the limitations in measurement equipment i.e. the plane across which the measured transducer was scanned may vary from the plane across which the predicted data was captured. Additionally, the data output from the modelled transducer is defined in an ideal fine mesh and is not subject to manufacturing imperfections, whereas the actual transducer may have small defects and imperfections within the composite structure. Figures 4.13(a) and (b) have been reproduced with the kind permission of G. Benny et al [90].

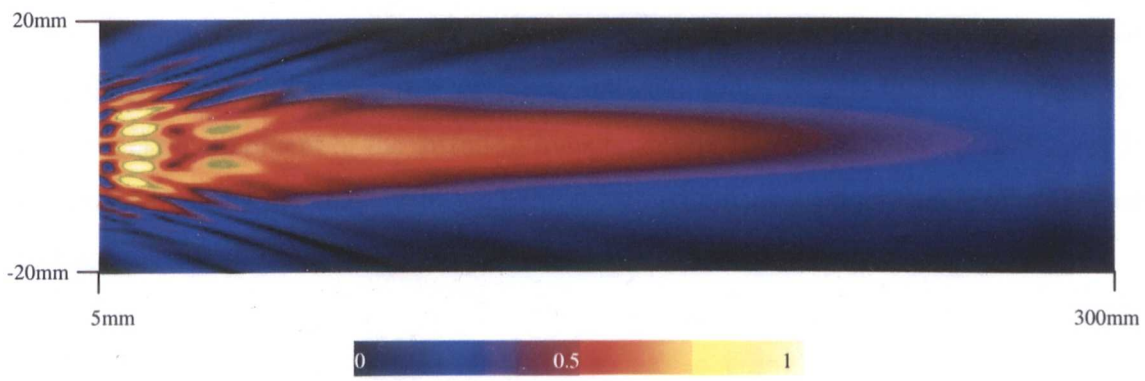

Figure 4.13(a) *Measured beam profile of simple piezocomposite transducer*

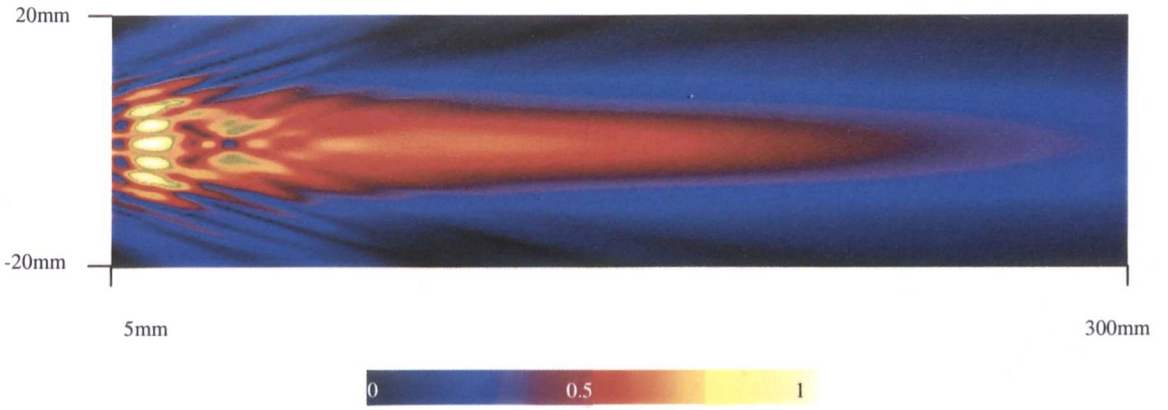

Figure 4.13(b) *Simulated beam profile from experimentally determined surface profile*

4.8 Conclusions

This Chapter illustrates the principles involved in finite element modelling, highlighting the importance of careful consideration of the initial conditions and boundary assumptions. Although finite element modelling is a powerful tool, if the modelled domain is too complex or incorporates too many elements then the computational requirements will exceed the available resources.

A brief description has also been given into the theory of operation behind the beam profiling software package. Illustrating that given a surface profile of a radiating source, either experimentally measured or simulated, accurate acoustic emission fields can be calculated.

This Chapter has provided the reader with a basic understanding of some of the techniques used in the practice of finite element modelling, which allows for the theoretical development of the differing transducer configurations. This is a precursor to the following Chapter that deals with the development of a novel range of wideband piezocomposite transducers.

Chapter 5

Development of a new range of wideband piezocomposites

5.1 Review of piezocomposite technology

A composite device by definition, is a "design made up of two or more individual parts". Piezocomposite transducers are constructed of two constituent phases, incorporating an active piezoceramic and a passive polymer material. This transducer technology enables the designer to tailor the properties for specific applications. One important design criterion is the ceramic to polymer volume fraction, which governs the specific acoustic impedance of the composite transducer. By varying the ratio of ceramic material within the structure of the device with respect to the volume of polymer filler, the volume fraction of the transducer can be altered.

$$Volume\ fraction\ (\%) = \left(\frac{Ceramic\ \ pillar\ width}{Pitch} \right)^2 * 100\% \quad \textbf{Eqn. 5.01}$$

It is the addition of the polymer material, which offers an increase in transducer sensitivity and improved impedance matching to media of lower specific acoustic impedance, such as air and water, compared to piezoceramic sensors.

Figure 5.01 illustrates a 1-3 connectivity piezocomposite consisting of active ceramic pillars embedded within a passive polymer matrix. The annotations 1 and 3 relate to the *connectivity* of the ceramic and polymer within the device respectively. Namely, the number of directions in which it is possible to connect the material to the outer boundaries without intersection of the second material.

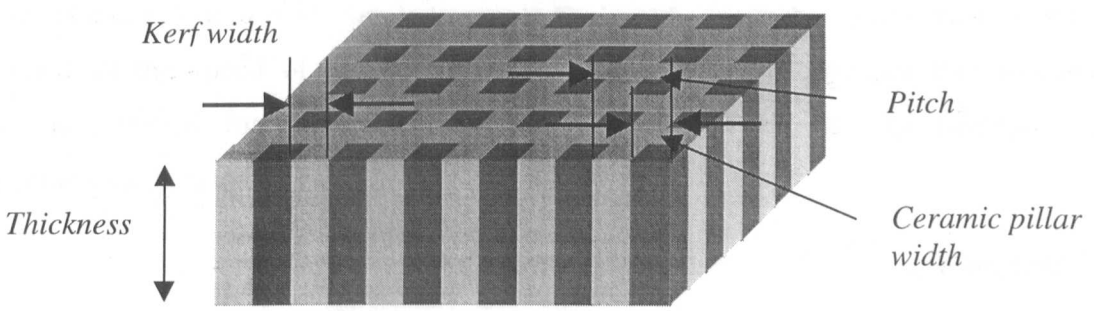

Figure 5.01 *1-3 Connectivity Piezocomposite*

The standard method of manufacture for the 1-3 composite is the "dice & fill" technique developed by Savakus [48], whereby two sets of slots are cut orthogonally into a ceramic block. An epoxy resin is then poured into the slots to provide a passive polymer matrix. The composite is then lapped to remove the excess ceramic and epoxy and reduce the transducer to the desired thickness. An alternative method, developed by Bowen [49], involves *injection moulding,* whereby the powdered ceramic material is injected into a periodic mould with a chemical binder, the mixture is then subjected to high temperature until the ceramic sinters and reforms within the mould. The resultant structure of free standing pillars is then bound within a polymer matrix and poled. Injection moulding enables fine scale transducer structures to be manufactured that are unrealisable with standard dice and fill techniques, although at an increased initial cost.

The resonant behaviour of a 1-3 connectivity piezocomposite device is exceptionally complex due the periodicity of the piezoceramic pillars embedded within the polymer matrix structure. It is as a result of this regular structure that a number of vibrational resonance modes are generated, both in the thickness and lateral directions each with their own frequency of operation and mode shape.

5.1.1 Thickness mode resonance

The fundamental thickness mode resonance of a piezocomposite transducer is typically the most dominant mode active within the transducer structure. This mode is governed by the overall thickness of the device and is caused by the longitudinal vibration within the piezoceramic pillars, in the height or thickness dimension. The wavelength for this mode is equivalent to twice the thickness of the transducer thickness and the velocity is defined as the speed of the sound travelling longitudinally through the thickness direction. Hence, for a composite with defined thickness of d_t, the frequency of thickness mode resonance can be calculated by

$$f_t = \frac{nv_t}{2d_t} \qquad \textbf{Eqn. 5.02}$$

where,

f_t is the resonant frequency in the thickness direction

v_t is the sound velocity in the thickness direction

n is the wave number

In this case, n is limited to only odd harmonics (1,3,5...) due to the assumption that the transducer will always have significantly higher acoustic impedance than that of its surrounding media. These harmonics are due to additional reverberation within the composite structure, although the magnitudes are reduced through damping with increased frequency.

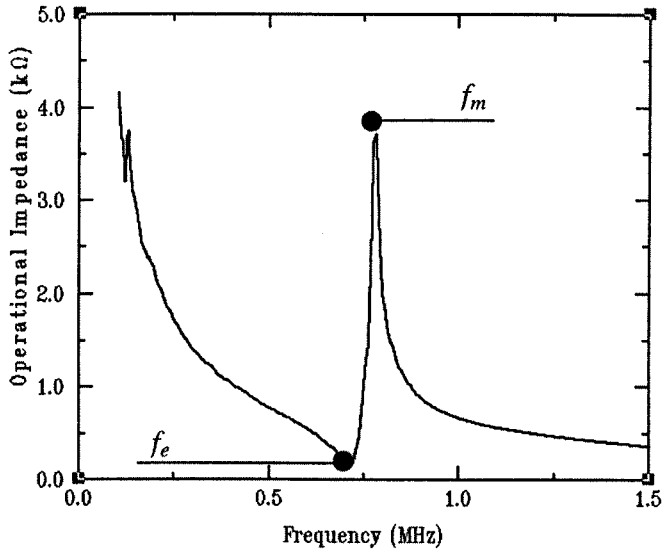

Figure 5.02 *Operational impedance of a piezocomposite transducer*

All resonance modes exhibit a distinct impedance characteristic with respect to frequency. Figure 5.02 illustrates a typical transducer impedance response, highlighting the two primary frequencies of interest, these being f_e and f_m, the electrical and mechanical resonances respectively. The electrical resonant frequency is shown as the impedance minimum and is defined as the optimal frequency of operation for transmission [92]. This defines the frequency at which the transducer will displace most when excited by a driving voltage. Conversely, the peak on the impedance response illustrates the optimal frequency for reception [92] under open circuit conditions. The small mode present on the left hand side of the figure at approximately 120kHz is the width dilation mode due to lateral dimensions of the transducer.

5.1.2 Lateral resonance modes

Lateral modes differ from thickness or longitudinal modes in that instead of travelling in the thickness or 3 direction, these modes travel along the width of the transducer, in the 1 and 2 directions. To explain, the characteristics exhibited from piezoelectric materials depend upon the orientation of the poling axis. This orientation governs the direction of vibration displayed by the piezoelectric material. 1 and 2 correspond to the x and y axes respectively, while 3 relates to the z-axis and 4 through 6 refer to rotations around the previous axes. In piezoceramics, the conventional axis of polarisation is in the z-axis or 3 direction, hence the notation of axes can be shown as in Figure 5.03.

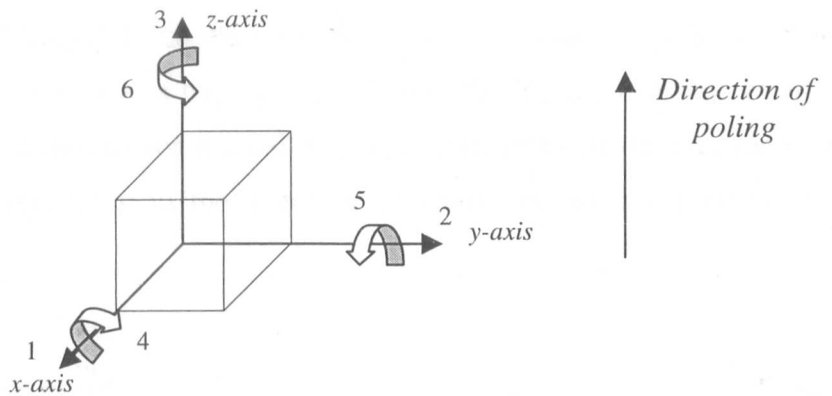

Figure 5.03 *Diagram of axes notation*

Lateral waves are travelling perpendicular to the thickness mode and are governed by the velocity of sound in the width direction. There are a number of different lateral modes active within a 1-3 connectivity composite transducer, these are *width-dilatational, inter-pillar* and *intra-pillar* modes. The influence these lateral modes exert over the transducer performance is governed by the *aspect ratio* of the transducer. Which is defined as the ratio of the ceramic pillar width to its height. It is not the intention of this Thesis to investigate these modes in detail, (this occurrence has been covered in greater depth by authors such as Gururaja et al [93, 94], Reynolds [88] and Gachagan [51]) only to comment upon there existence and influences. These modes are now discussed briefly.

Width-dilatational resonances are due to the overall width of the transducer structure and can propagate waves in either radial and transverse form, dependent upon the

transducer geometry. Typically, these modes have little influence upon the transducer performance being in the low kHz range and therefore do not interfere with the thickness mode operation.

Inter-pillar resonances are modes that arise due to standing wave patterns being generated within the periodicity of the composite structure. Namely, as the piezoceramic elements within the structure vibrate in the thickness direction 3, a certain proportion of this displacement is coupled into the lateral directions 1 and 2, dependent upon the polymer material parameters. This lateral motion generates shear waves within the composite structure which, depending on the ceramic and polymer periodic spacing, can lead to standing waves within the device. These phenomena can cause significant problems in the design of transducers with low volume fractions. Substantial work has been carried out in this area by Auld and Wang [95, 96] and Gururaja et al [93, 94]. Commonly, the frequency for vertical/horizontal inter-pillar mode resonance (i.e. inter-pillar modes propagating in the 1 and 2 direction) are governed by the following equation.

$$f_{hv} = \frac{nv_S}{2d_p} \qquad \textbf{Eqn. 5.03}$$

where,

f_{hv} is the inter-pillar resonant frequency in horizontal/vertical direction

v_S is the shear velocity of the sound within the polymer

d_p is the centre-to-centre separation between pillars

The diagonal case, i.e. standing waves supported in the diagonal direction are determined by Equation **5.04**.

$$f_d = \frac{nv_S}{d_p} \qquad \textbf{Eqn. 5.04}$$

where,

f_d is the inter-pillar resonant frequency in the diagonal direction

v_S is the shear velocity of the sound within the polymer

d_p is the centre-to-centre separation between pillars

More recently, Reynolds [88] has suggested modifying this equation to account for the generation of Lamb waves within the composite platelet structure. Through practical and analytical investigation it was determined that the conventional Brillouin scattering theory used to determine the behaviour of these modes, while producing adequate numerical results, failed to accurately describe the mechanism for generation of the lateral modes. In depth investigation revealed that there were in fact Lamb waves being generated in the composite structure, due to the periodically spaced pillars acting as pressure 'sources'. These sources generate Lamb waves of wavelength equal to the pillar spacing, and velocity dependant upon the material composition of the device. Therefore, it was concluded that a more accurate means of calculating the frequency of inter-pillar resonance would be:

$$f_{hv2} = \frac{v_{phase}}{2d_p} \qquad f_{d2} = \frac{\sqrt{2}v_{phase}}{d_p} \qquad \textbf{Eqn. 5.05}$$

where,

f_{hv2} is the modified inter-pillar resonant frequency in the horizontal/vertical case

f_{d2} is the modified inter-pillar resonant frequency in the diagonal case

d_p is the centre-to-centre separation between pillars

v_{phase} is the phase velocity of the Lamb wave within the polymer where:

$$v_{phase} = v_{rpoly} + (volume\ fraction)^2(v_{rcer} - v_{rpoly})$$

v_{rpoly} is the Rayleigh velocity of the polymer

v_{rcer} is the Rayleigh velocity of the ceramic

Intra-pillar resonances are again influenced by the microstructure of the composite, however on this occasion, they are only critical in piezocomposites with high aspect ratios i.e. aspect ratios greater than 0.5, as the lateral resonances impinge upon the thickness mode resonance. These modes tend to be prevalent in thin film composites which have a much higher frequency of operation, outwith the scope of this investigation.

5.2 Bandwidth improvement in piezocomposite transducers

The analysis of the various resonant modes present within the piezocomposite structure illustrates that although the fundamental mode of operation is traditionally in the thickness direction, multiple frequencies are possible from the device. Indeed, it is the reverberation within the composite structure which governs the transducer bandwidth, the longer the vibration lasts, the narrower the bandwidth. Hence, it is apparent that if these reverberations are diminished, or damped, then the bandwidth associated with the device will be increased. This has been typically implemented by the addition of mechanical damping or matching [97, 98] to the composite and forms the traditional methodology for the enhancement of transducer bandwidth. Mechanical damping is achieved by the addition of a backing block to the rear face of the transducer, of higher acoustic impedance than said transducer, to reduce the amount of internal reverberation caused by wave reflection at the rear face of the composite. The main disadvantage associated with this technique is that the addition of the backing block leads to reduction in the sensitivity of the transducer. This behaviour has been well investigated by Kossoff [97] and Desilets [98], further to this, finite element analysis (FEA) by Bennett [87] suggested that a compromise value for the acoustic impedance of the backing block to be half that of the active material selected. This value was suggested as a concession between loss of sensitivity and increase in available bandwidth.

Hossack [92] proposed an alternative method for improved bandwidth of 1-3 connectivity composites by utilising non-standard ceramic pillar geometries within the composite structure. This consisted of three different ceramic pillar geometries with non-uniform lateral dimensions and uniform thickness. Using FEA, the resonant frequencies of each pillar geometry were isolated and identified from the respective pillar aspect ratio. It was found that the non-uniform pillar geometry offered an improvement in bandwidth, approximately 50kHz, but the practicality of the design was restricted by introduction of unwanted resonances due the altered aspect ratios. Another method analysed utilising FEA by Hossack [92], was the use of non-uniform thickness within the transducer structure to extend the thickness mode resonance of the device. Originally investigated experimentally by Bowen et al. [102], the theory predicts that if one section of the composite is vibrating in the thickness mode, the adjacent non-resonating area will also displace due to the lack of stiff clamping between the

bordering regions. Although an approximate improvement of 150kHz in system bandwidth was found, it was determined that tapered composite design lead to a non-uniform surface displacement, which would prove prohibitive in transducer design and therefore had limited use.

Another approach to bandwidth enhancement was investigated by Gachagan [51] whereby the methodology involved was to use a backing medium to couple the lateral and thickness modes within the transducer. By construction of a low volume fraction (20%) piezocomposite transducer with a large aspect ratio, greater than 0.1, lateral mode resonances were introduced into the device microstructure. Through application of a Perspex backing block it was possible to couple effectively between the fundamental thickness and first lateral mode resonances, thereby increasing the bandwidth of the composite. However, as with other associated backing techniques, it was found that the introduction of the damping media led to a degradation in transducer sensitivity, by a factor of three over conventional narrowband composites.

5.3 A novel approach to bandwidth enhancement

From the illustrated examples in the previous Section, it apparent that although it is possible to increase the bandwidth characteristics of a composite device by the addition of a damping medium at the rear face of the transducer, this leads to a significant reduction in the transducer sensitivity. Of all the illustrated approaches only one does not require this methodology, namely the construction of non-uniform thickness transducers [92]. However, the author was of the opinion that this technique was of limited value due to the non-uniform displacement of the device. This, coupled to the limitation of the manufacture to a tapered design, using a wire saw to cut a standard piezocomposite device at an offset angle, led to the dismissal of this idea.

The problem associated with piezoceramic transducers of variable thickness is the inherent difficulty in machining the ceramic material. The use of standard techniques such as grinding or drilling with steel carbide tools is extremely difficult due to the brittle structure of the ceramic material. Any attempt to machine inevitably leads to the destruction of either the ceramic, the machining tool or more commonly both. In

addition to this, the high temperature generated in the machining process due to high friction may also lead to the depoling and destruction of the ceramic material.

However, one area of investigation appears to offer more scope for improvement than was first thought. Although the ceramic itself cannot be machined as a solid block, it is feasible that when the ceramic is embedded with the passive polymer phase as a piezocomposite device, it may be possible to alter the transducer structure. As discussed, the inherent difficulty in ceramic machining is the cutting of the rigid ceramic due to the brittleness of the ceramic and the build up of heat within the structure. However, if the ceramic is embedded within the polymer phase, then the overall volume of ceramic is decreased significantly, meaning less ceramic to be machined. In addition, since the area of ceramic to be machined is smaller and held within the polymer matrix rather than clamped in bulk piezoceramic, the pillars are allowed some degree of motion that limits the amount of strain and thus breakage. Consequently, the manufacturing process of these piezocomposites is relatively straightforward.

5.4 Modified thickness piezocomposite device

5.4.1 Simple dual thickness composite

As stated previously if properly designed, the thickness mode resonance of a given transducer is typically the most dominant mode active within the structure. Therefore, utilising the proposed manufacturing technique it should be possible to remove a section of the piezocomposite device in order to generate a second thickness mode resonance within the composite.

Consider a specimen 1-3 connectivity composite with a 50% volume fraction constructed of PZT-5A piezoceramic and CY1300/1301 Ciba-Geigy hard-set polymer. The transducer has an initial thickness of 2.52mm and is both backed and loaded by air. Using the simple equation for calculating the mechanical resonance (Eqn. **5.02**) the thickness requirement for a frequency spacing of 110kHz was determined. Therefore, utilising a milling machine, a 0.4mm deep section of composite material was removed from one half of the transducer, leaving a step thickness of 2.12mm Further details of the transducer material parameters can be found in Appendix C.

Figure 5.04 shows a graphical illustration of the resultant piezocomposite, with a clear difference in size between the two thicknesses.

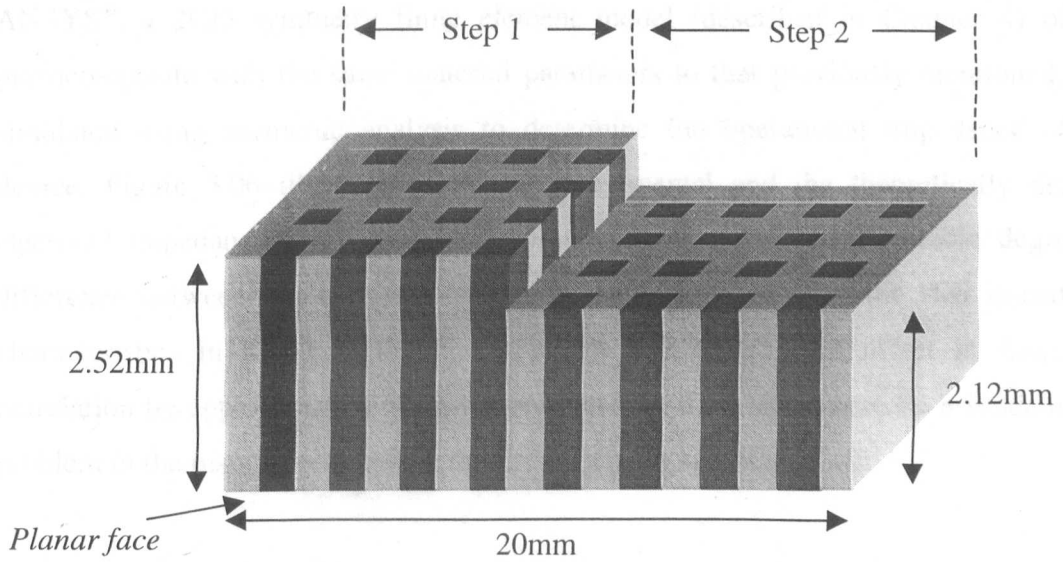

Figure 5.04 *Representation of dual thickness piezocomposite device*

From examination of Figure 5.05 it is evident that there are two clear impedance minima within the transducer operational impedance response, at approximately 590kHz and 710kHz. It can therefore be concluded that the introduction of the second thickness to the composite structure has led to the generation of an additional thickness mode resonance in the device.

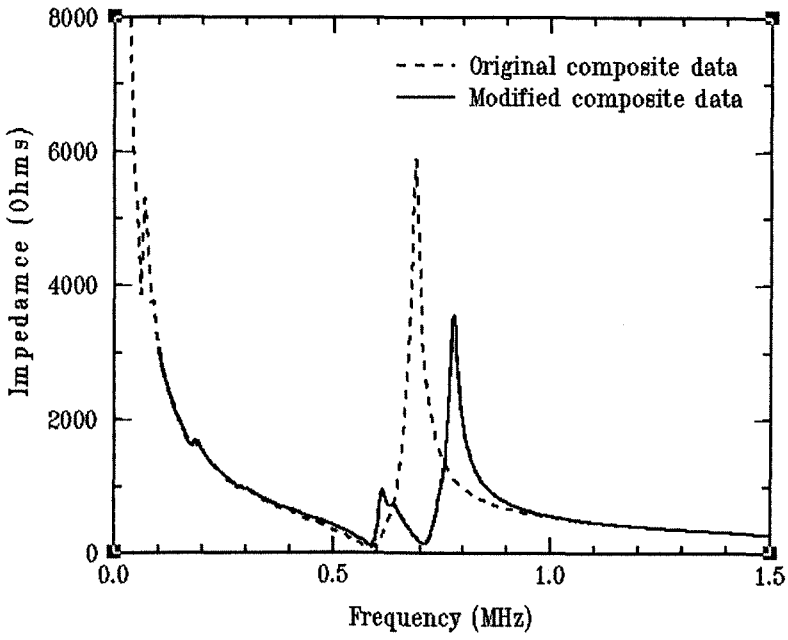

Figure 5.05 *Operational impedance of original composite and modified composite*

In addition to the manufacture of one of these devices, a finite element model was constructed to simulate the theoretical behaviour of the proposed transducer. Using ANSYS®, a 2½D symmetry finite element model (described in Chapter 4) of the piezocomposite with the same material parameters to that previously mentioned, was simulated using harmonic analysis to determine the operational impedance of the device. Figure 5.06 illustrates both the experimental and the theoretically derived electrical impedance characteristics. Interestingly, there is a considerable degree of difference between the two sets of results. By examination of the two impedance characteristics in Figure 5.06, it is apparent that there is an offset in frequency correlation by approximately 60kHz. Consequently, there appears to be a fundamental problem in the results predicted by the finite element analysis (FEA).

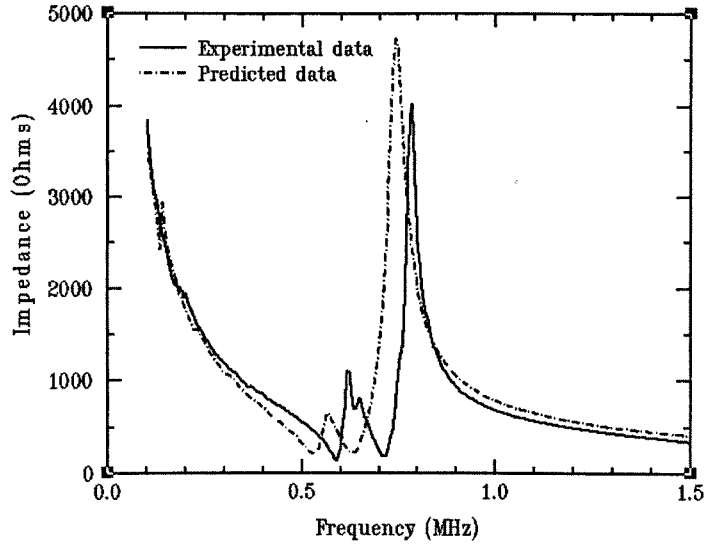

Figure 5.06 *Comparison of experimental and predicted impedance characteristics*

In order to determine the cause of this discrepancy, between the theoretical and experimental results, further analysis was performed to isolate the individual thickness sections on the dual thickness model, by examining the impedance of each section. Moreover, by experimentally isolating these individual sections of differing thickness and electroding each area separately, the impedance characteristics for each section can be determined experimentally and compared with those predicted by theory, as illustrated in Figure 5.07. Thus, it is apparent from the theoretically predicted results that there is a problem associated within the modelling of the electrical resonances of each composite section.

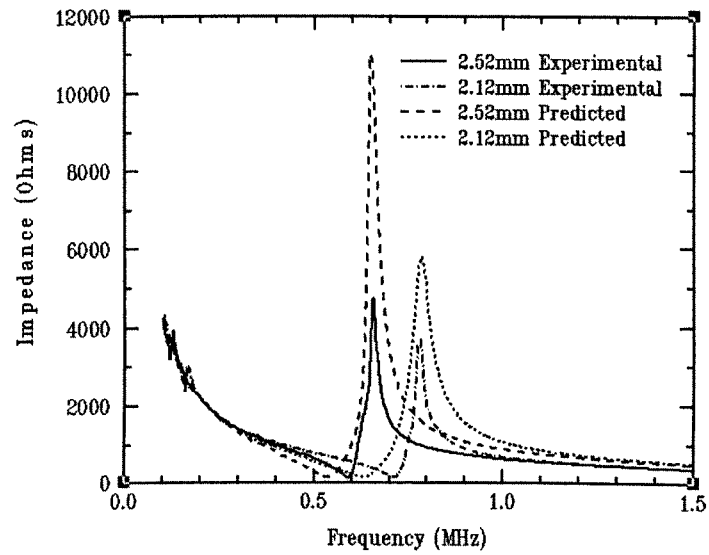

Figure 5.07 *Comparison of isolated thickness sections from both experimental and theoretically predicted data*

By examination of Figure 5.07 it is apparent that there is good correlation between the frequency of mechanical resonance in the theoretical and experimental data. This is to be expected as the overall thickness of the device governs the mechanical resonance of the transducer through the previously defined equation, Eqn. **5.02**. However, it is the apparent difference in the electrical resonance of each thickness section of the device that is interesting. Using the equation detailed below (Eqn. **5.06**), it is possible to calculate the electromechanical coupling coefficient, k_t, of the composite transducer in the thickness direction.

$$k_t = \sqrt{\frac{\frac{\pi f_e}{2 f_m}}{\tan\left[\frac{\pi f_e}{2 f_m}\right]}} \qquad \textbf{Eqn. 5.06}$$

This coupling coefficient is utilised as a simple gauge of the transducer efficiency at the thickness mode resonance, determining the amount of electrical energy converted to mechanical displacement and vice versa. The ideal, non-realisable, value for this coupling coefficient is 1, more typically a well designed/manufactured transducer has a k_t of approximately 0.65. The Using Eqn. **5.06** to calculate the coupling coefficient of the 2.52mm thick section of the composite results in a k_t of 0.467 and 0.602 from the experimental and theoretical results respectively. Similarly, the k_t of the thinner, 2.12mm thick section is 0.438 (Experimental) and 0.638 (Simulated). Thus it can be seen that there is a considerable difference between the predicted coupling coefficients of both sections to that measured experimentally. This is consistent with a poorly constructed piezocomposite structure, or depoling of the ceramic within the composite. As postulated previously, the machining of solid ceramic was found to be impractical due to the brittleness of the ceramic and the resultant temperature rise induced depolarisation the solid ceramic. It is therefore possible that machining of the piezocomposite structure could generate such a depoling effect through overheating during the machining phase. The difference in the measured k_t of each two thickness sections (0.467 in Step1 and 0.438 in Step2) is 0.029 or 6% decrease over the thickest section, which when compared to the original coupling coefficient for the non-machined composite (k_t = 0.586) illustrates that the machining process effects both sections of the composite rather than the actual machined section.

Firstly, in order to verify that the FEA was accurately modelling a single thickness piezocomposite, a second 1-3 connectivity composite was constructed from PZT-5H ceramic and CY1301/HY1300 hard-set epoxy with a volume fraction of 55%. As before, a model was constructed in ANSYS® to simulate the impedance characteristics predicted by theory and the results are illustrated in Figure 5.08

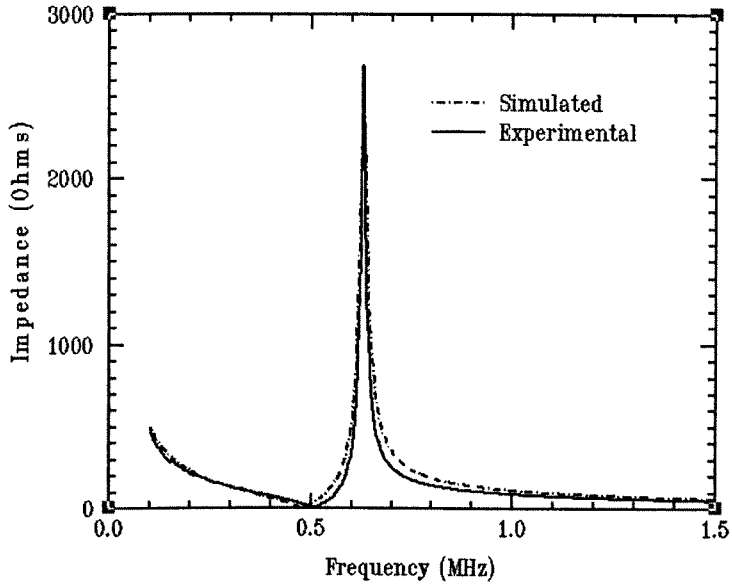

Figure 5.08 *Comparison of experimental and simulated results for single thickness piezocomposite*

By examination of Figure 5.08, it can be concluded that the coupling coefficient of the experimental device (k_t = 0.625) is slightly lower than that predicted by theory (k_t = 0.696). As demonstrated previously, in each instance the frequency of mechanical resonance is predicted accurately, but the measured electrical resonance is higher than that predicted by the finite element analysis. This illustrates that there is a degree of depoling in the construction of the piezocomposite transducers. Figure 5.09 illustrates more clearly the differences between the predicted electrical resonance and that actually determined experimentally.

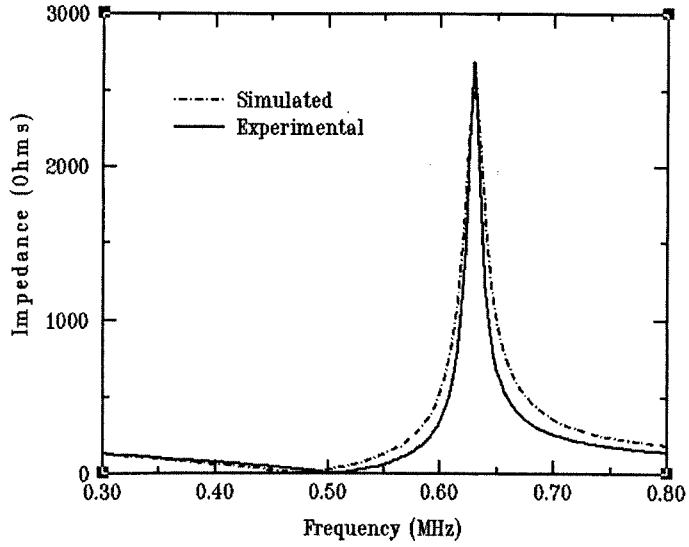

Figure 5.09 *More detailed examination of impedance responses*

However, this form of depoling is most likely not the major problem in the dual thickness composite example, as the change in k_t between the modelled step thickness and that measured, is considerably higher (0.467 for experimental and 0.602 for theory). Therefore, it appears that the milling process does have an adverse effect on the k_t of the composite, the large mismatch between the experimental and predicted impedance responses was due in part to the original construction of the composite and substantially by depoling from the milling process.

In order to determine whether this is the case, another 1-3 connectivity composite was manufactured, with a volume fraction of 56%. This composite was then reduced in thickness using the similar milling process used for the construction of the dual thickness composite transducer. Figure 5.10 illustrates the comparison between experimental and predicted impedance results before the milling process and Figure 5.11, the impedance results after milling.

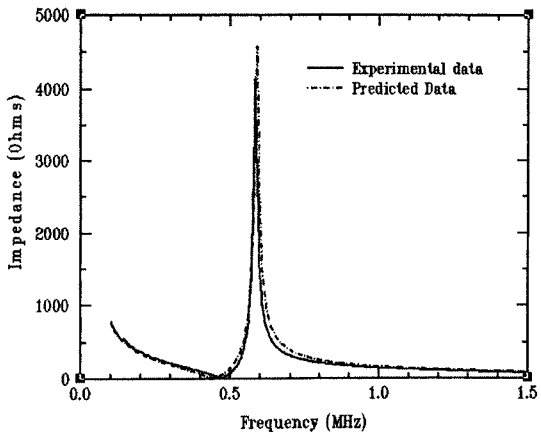

Figure 5.10 *Impedance characteristics before milling process*

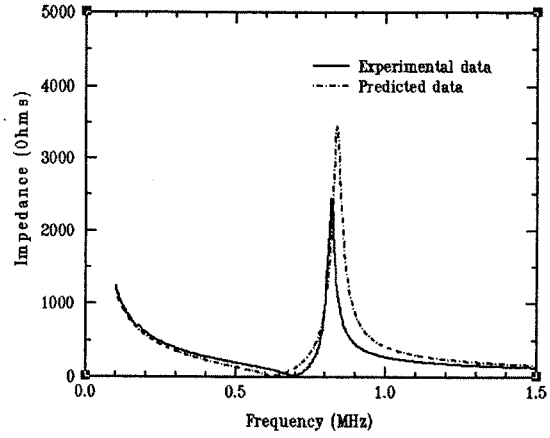

Figure 5.11 *Impedance characteristics after milling process*

It is apparent from Figure 5.10 that the k_t of the experimental device is lower than that predicted by theory (0.696 for theory and 0.640 for experiment), again this discrepancy is due to either poorly poled ceramic or depoling in the manufacturing process, although the difference in k_t at this stage is not that considerable. However, after the composite has been treated to the milling process there is a much greater degree of depoling evident, as illustrated in Figure 5.11. In this instance, the k_t for the simulated composite transducer is 0.699 and the 0.562 for the coupling coefficient measured from the experimental impedance response. From this, it can be concluded that the milling process has reduced the k_t of the composite transducer. However, the drop in k_t (0.696 $\rightarrow$ 0.562) is not considered to be overly detrimental, as coupling coefficients between 0.55 and 0.6 are considered acceptable for good composite transducers.

It was originally proposed that machining of the composite structure would not have an adverse influence on the transducer, however it is apparent that the milling process may have resulted in the depoling of the ceramic due to excess heating within the pillar structure. One possible manner in which to rectify this problem would be to re-pole the composite structure after machining had taken place. This is commonly achieved with solid ceramic by heating the transducer to its Curie temperature (365°C for PZT-5A and 195°C for PZT-5H) in a bath of oil and applying an electric field across the terminals while cooling to realign the dipoles in the ceramic. However, further work is required to determine what effect this heating would have on the polymer filler of a piezocomposite and therefore this approach was not attempted.

Modelling a uniform thickness piezocomposite, proved that this problem was inherent in the modelling of all composite transducers, only to a lesser degree. Possible reasons for this apparent discrepancy could be due to inaccuracies in the material parameters supplied by the manufacturer, or the manner in which structural damping is applied within the modelling process. ANSYS® utilises a simplified damping matrix solution, which restricts comprehensive tailoring of the material damping properties. As a result, the damping ratio has to be a compromise between the damping characteristics for the material at electrical resonance and mechanical resonance. Ideally, it should be possible to include a dynamic damping ratio method, which included damping characteristics of the material across the entire frequency range. Since this cannot be easily implemented, future work in transducer design and optimisation should place greater emphasis on material characterisation, both before and after construction of the transducer.

Additionally, the modelling parameters do not allow for the simulated depoling of the active ceramic structure. As such, the material properties used to define the material matrix macro within ANSYS® are installed from the material parameters supplied by the ceramic manufacturer, in this instance Ferroperm [99]. Equation **5.07** represents an alternative form to the thickness mode electromechanical coupling coefficient.

$$k_t = h_{33}\sqrt{\frac{\varepsilon_{33}^S}{c_{33}^D}} \qquad \textbf{Eqn. 5.07}$$

where,

h_{33} is the piezoelectric charge constant in the thickness direction

c_{33}^D is the stiffness coefficient of the ceramic under constant electric charge density

ε_{33}^S is the permittivity constant under constant strain in the thickness direction

Each of these variables in the coupling coefficient, are governed by the permittivity, stiffness and elastic coefficients of the given ceramic material. The manner in which altering these material parameters influences the coupling coefficient and thereby simulate the depoling process in the ceramic is a complex relationship. Presently, no accurate method is available within the ANSYS® modelling structure for the prediction of depoled ceramic structures. It is proposed that future work should be focussed on implementing an accurate method of applying a depoling function within the FEA.

5.4.2 Surface displacement analysis of dual thickness composite

Analysis has shown that altering the thickness of one section of a piezocomposite transducer introduces a second thickness mode resonance into the composite structure. However what is still undetermined, is the mode of operation of the transducer, i.e. how the composite will vibrate when excited by an electrical signal. This can be explored by both experimental and theoretical analysis, to determine the vibrational displacement of the transducer front face, thereby illustrating the output characteristics.

Using a laser interferometer (detailed in Appendix B.), the surface displacement from the planar face (i.e. the non-machined face) of the dual thickness piezocomposite transducer was measured across a range of frequencies, incorporating the two dominant electrical resonances when the transducer was excited by a 1volt, 10cycle tone burst signal. The results of these scans are illustrated in Figures 5.12(a-j), which shows a plan view or surface profile of the entire composite front face. Note, maximum displacement is signified by the darker regions in all graphic profiles.

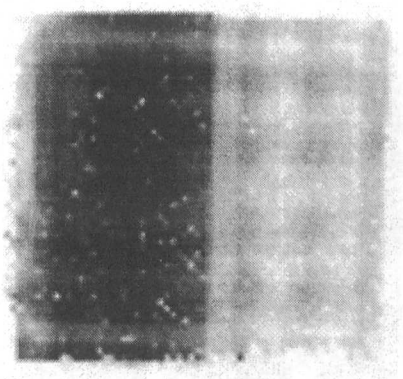

(a.) 560kHz

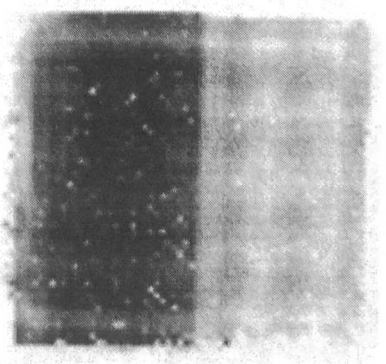

(b.) 580kHz

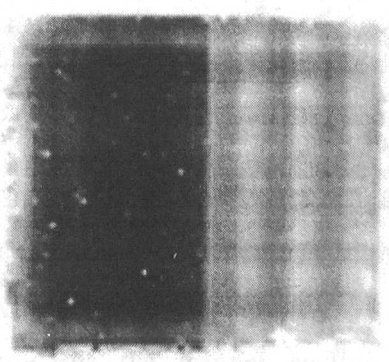

(c.) 600kHz

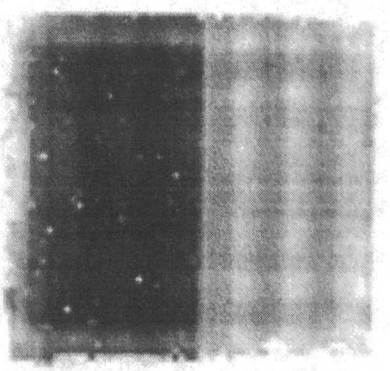

(d.) 620kHz

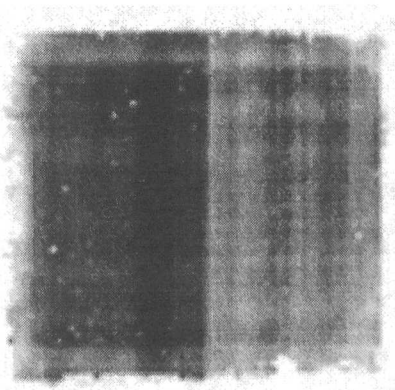

(e.) 640kHz

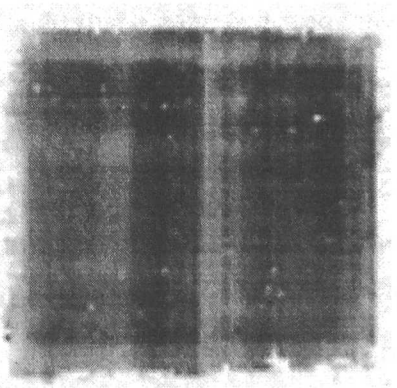

(f.) 660kHz

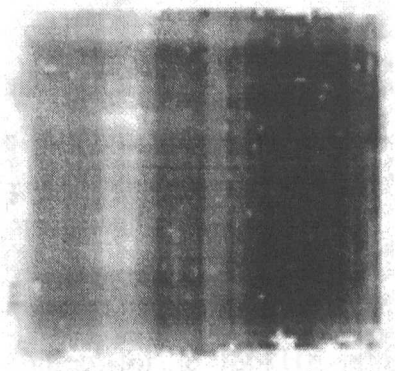

(g.) 680kHz

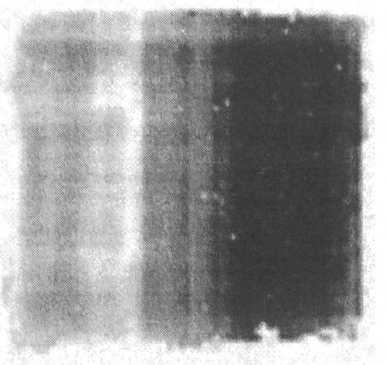

(h.) 700kHz

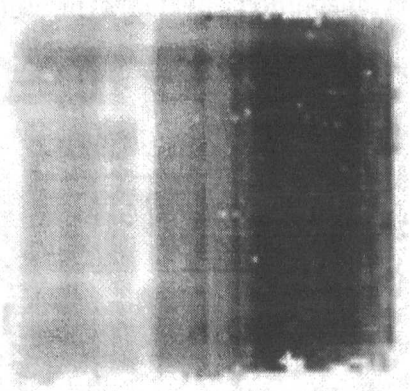

(i.) 720kHz

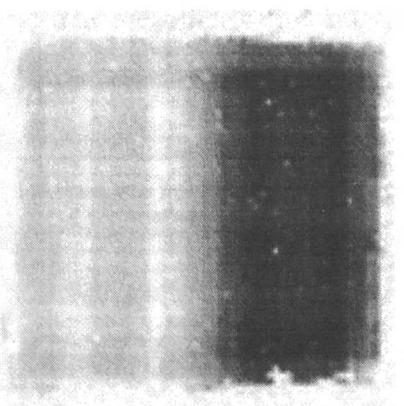

(j.) 740kHz

Figures 5.12 (a-j.) *Surface displacement profiles for dual thickness composite*

From examination of the surface profiles, it is evident that the thickness mode vibration dominates at the first electrical resonance at 580kHz within the thicker section on the left-hand side of the composite transducer. As the frequency is increased, the vibrational profile of the device changes such that the dominant area of vibration moves towards the thinner section on the right-hand side, at a frequency of 710kHz, corresponding to the electrical resonance of the second section.

As discussed previously, there is a considerable discrepancy in frequency correlation between the theoretically predicted impedance responses and those derived experimentally, although both clearly illustrate the additional thickness mode resonance in the impedance response. This has been shown to be a result of manufacture of the composite structure and further depoling due to the milling process, which cannot be accurately modelled at the present time within the FEA code. However, since it is only possible to experimentally determine the motion of the front face in transmission rather than reception, it is the electrical resonance frequency that is paramount in this investigation. Therefore in order to draw comparisons between the theoretical and experimental displacement of the device, the surface displacements produced by FEA have been shifted in frequency by approximately 60kHz. This allows the corresponding displacements for the electrical resonances predicted by theory and those produced in practice to be overlaid on the same graph.

Figures 5.13 (a-j) illustrate the surface displacement of the planar face from a cross section for a 180kHz frequency range at 20kHz intervals. A small graphical representation of the transducer has been attached to each of the plots to distinguish the area in which the composite is vibrating. Note that the pillar representation is not to scale.

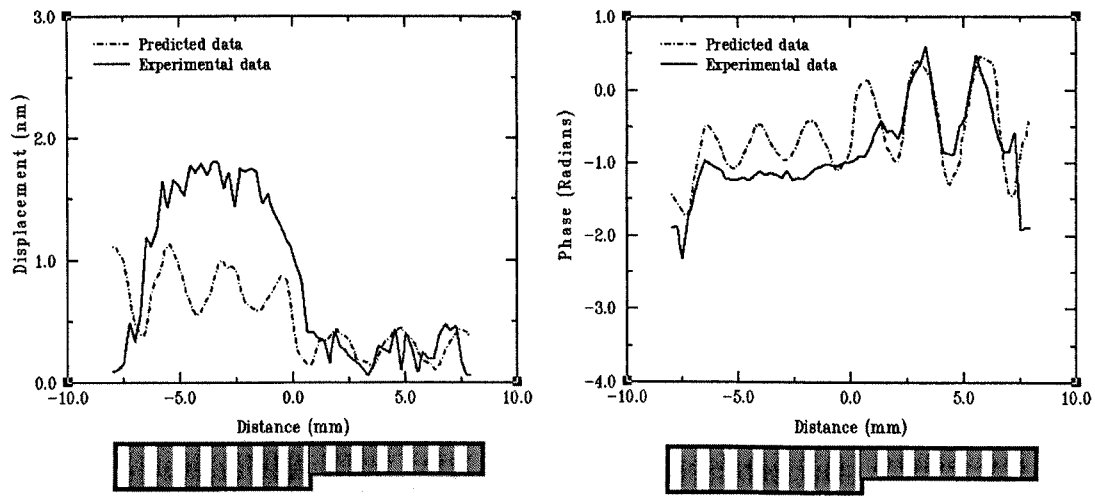

Figure 5.13(a.) *Cross sectional data (Experimental at 560kHz, Predicted at 500kHz)*

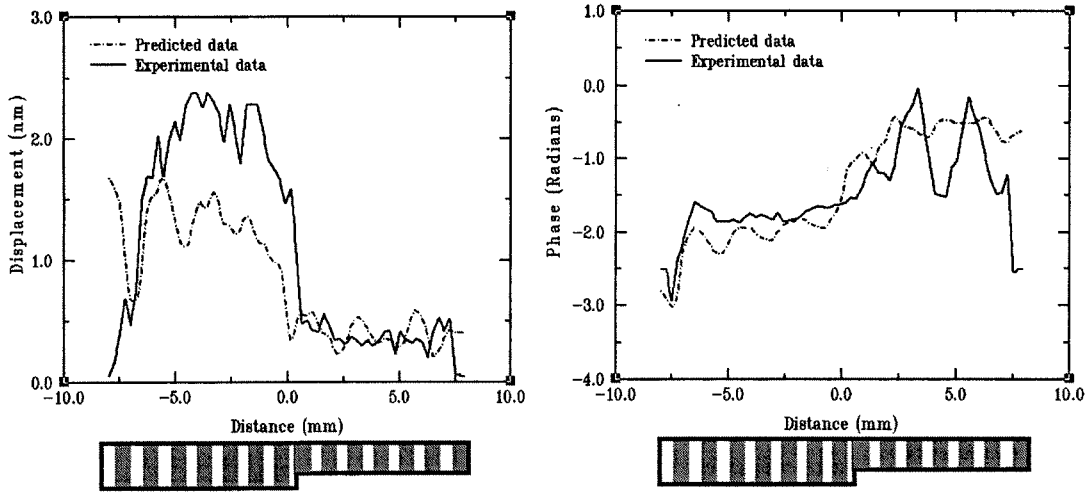

Figure 5.13(b.) *Cross sectional data (Experimental at 580kHz, Predicted at 520kHz)*

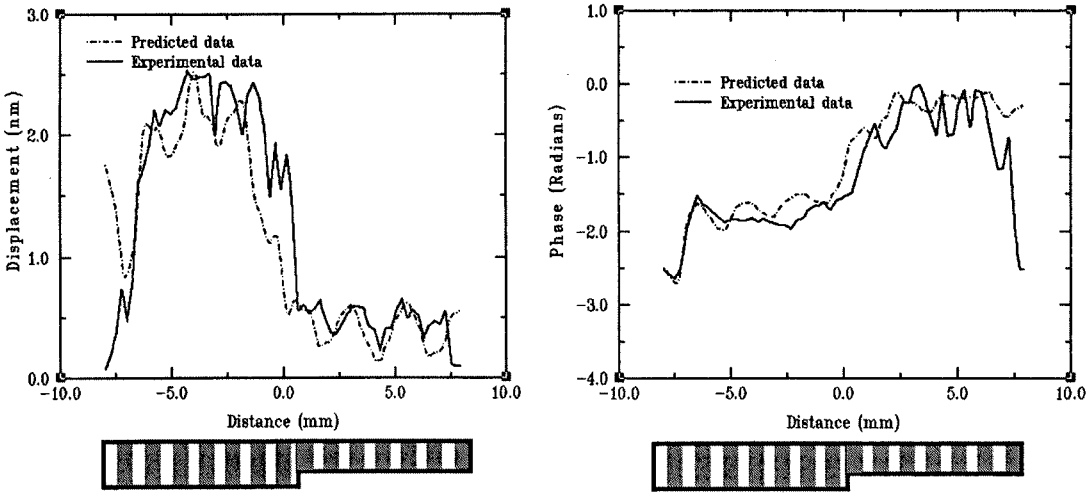

Figure 5.13(c.) *Cross sectional data (Experimental at 600kHz, Predicted at 540kHz)*

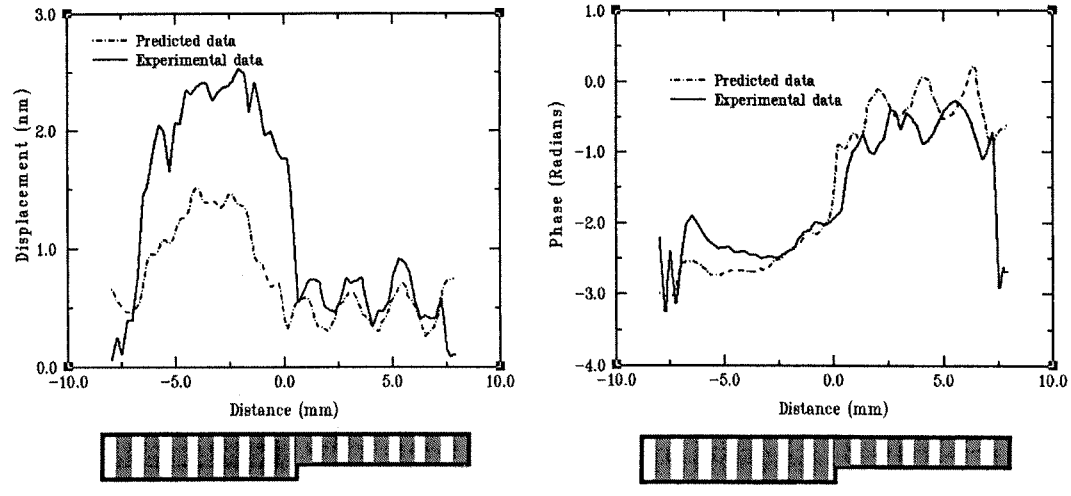

Figure 5.13(d.) *Cross sectional data (Experimental at 620kHz, Predicted at 560kHz)*

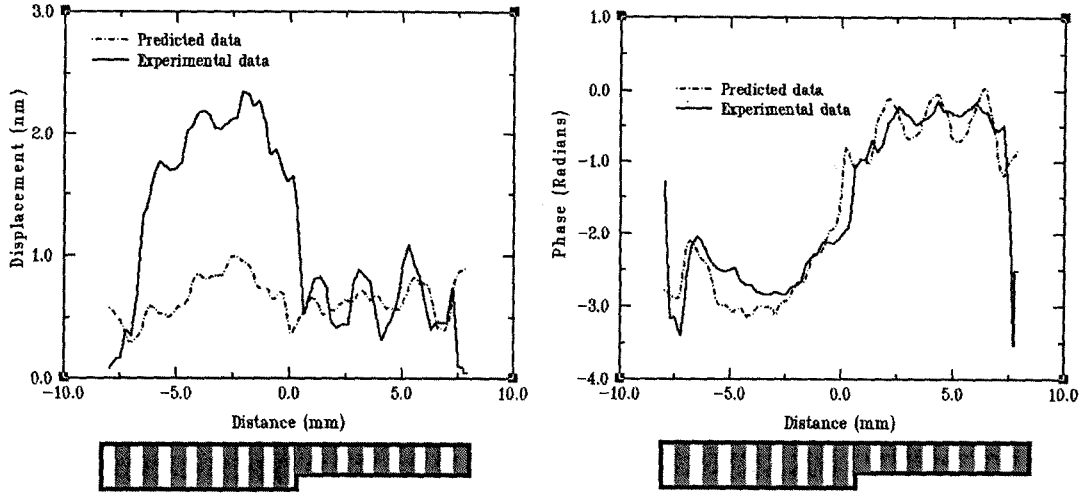

Figure 5.13(e.) *Cross sectional data (Experimental at 640kHz, Simulated at 580kHz)*

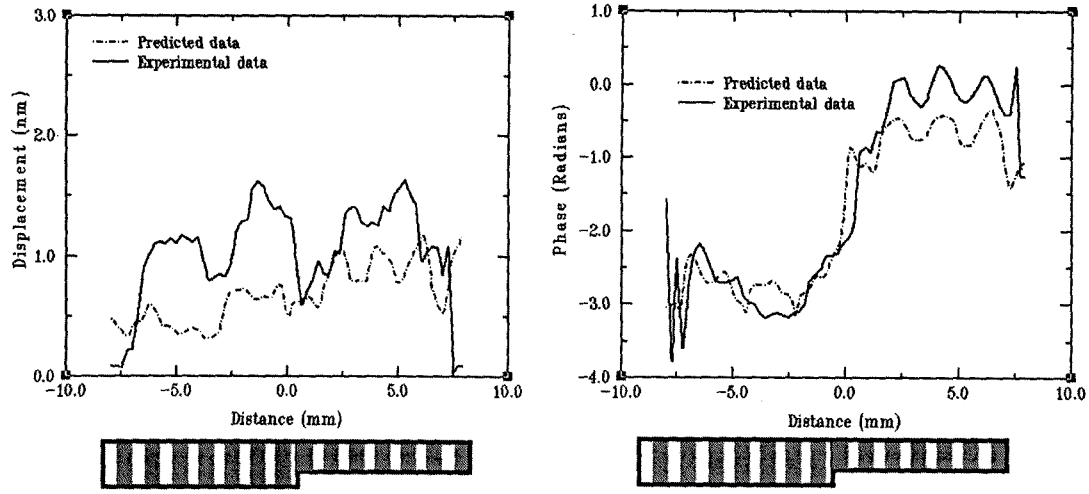

Figure 5.13(f.) *Cross sectional data (Experimental at 660kHz, Predicted at 600kHz)*

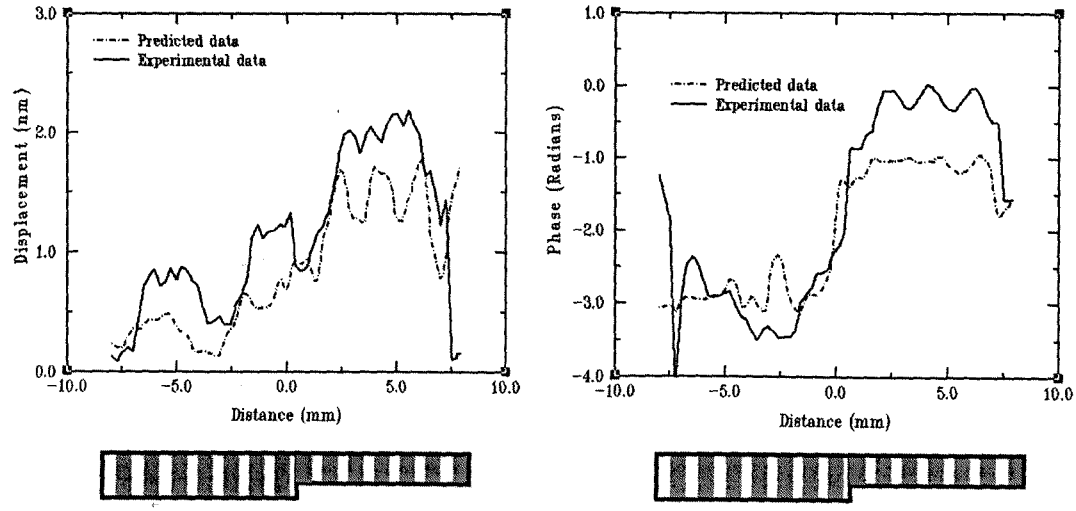

Figure 5.13(g.) *Cross sectional data (Experimental at 680kHz, Predicted at 620kHz)*

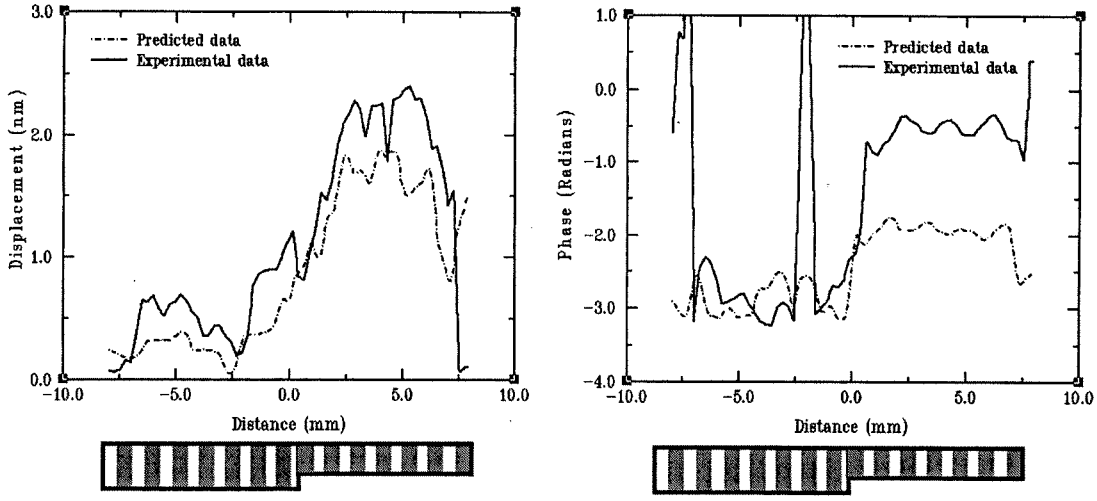

Figure 5.13(h.) *Cross sectional data (Experimental at 700kHz, Predicted at 640kHz)*

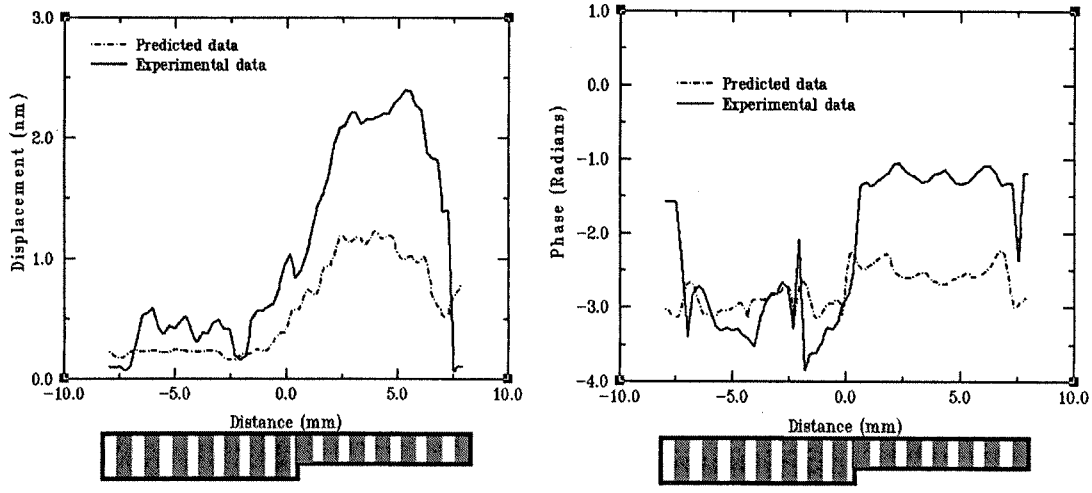

Figure 5.13(i.) *Cross sectional data (Experimental at 720kHz, Predicted at 680kHz)*

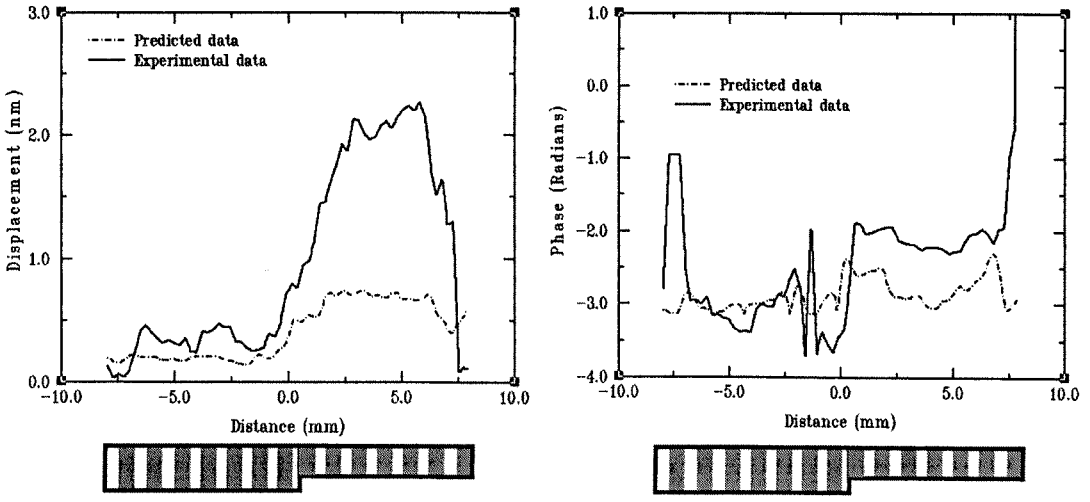

Figure 5.13(j.) *Cross sectional data (Experimental at 740kHz, Predicted at 680kHz)*

By referring to the cross sectional information for the dual thickness piezocomposite, it is apparent that although both theory and experiment indicate a similar trend in vibration displacement with respect to increasing frequency, the frequencies at which the maximum displacements occur are quite different. This is due to the previously highlighted problem associated with the depoling of the ceramic in the piezocomposite, meaning that the electrical resonances of the two thickness steps in the experimental device are higher than those predicted by theory. However the magnitude of displacement for these two thickness mode vibrations are very similar (approximately 3nm peak). Therefore, although the frequencies of maximum displacement associated with each thickness step do not match exactly, this does illustrate that the model is predicting the displacement behaviour of the transducer across the given frequency range. Moreover, comparison of the phase characteristics for the dual thickness composite across the frequency range show a close correlation between experiment and those results predicted by FEA. Note that the artefact in the phase in Figure 5.13(h) is due to phase wrapping, i.e. where a phase change of over 180° from the phase reference takes place in the laser interferometer. This is normal in most laser interferometers and can be rectified with signal processing.

Another important aspect of this transducer design, is the mode of vibration between the two electrical resonances. As illustrated in the cascade of surface profiles in Figures 5.12(e-g), when the frequency is varied in the region between the two thickness modes, both thicknesses of the composite exhibit vibration in the longitudinal direction although at a reduced magnitude of displacement. Reference to the cross sectional data in Figures 5.13(e-g) illustrates that the magnitude of vibration in these sections at the intermediary frequencies are reduced by a factor of two. Interestingly, at the intermediate frequencies of 640kHz to 680kHz (Experimental, Figures 5.13(e-g)), the phase characteristics show a phase change of π radians, or 180°, between the two step thicknesses. This indicates that both the steps are displacing, but are however, in anti-phase to one another. Figure 5.14 displays this thickness mode displacement for the dual thickness composite at 660kHz, where the anti-phase displacement between adjacent sections is clearly evident.

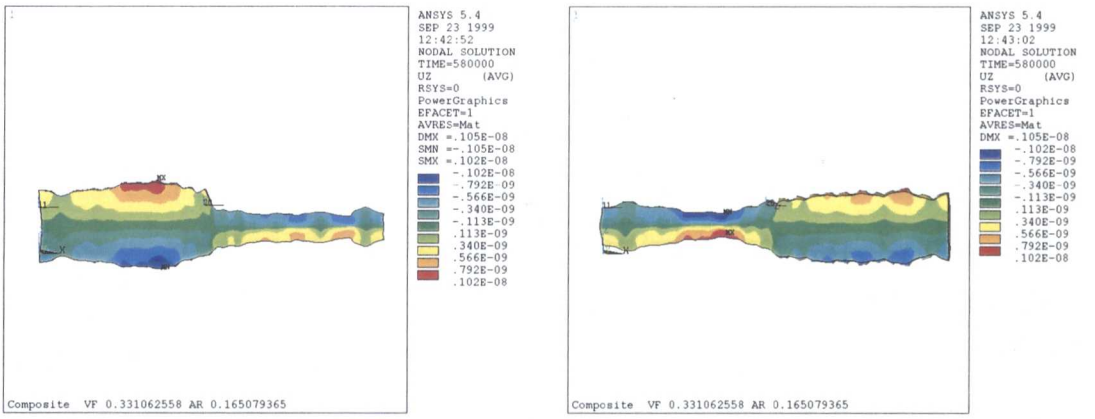

Figure 5.14 *Mode of displacement of dual thickness composite at 660kHz*

Further investigation of this phenomenon, utilising FEM and linear systems modelling [76], indicated an interesting mechanism associated with the fundamental thickness vibration mode exhibited in the piezocomposite structure. Using the linear systems model, the force magnitude and phase of the front face vibration was calculated for a piezocomposite transducer, constructed of PZT-5A ceramic and CY1301/1300 epoxy to a 50% volume fraction, as shown in Figure 5.15.

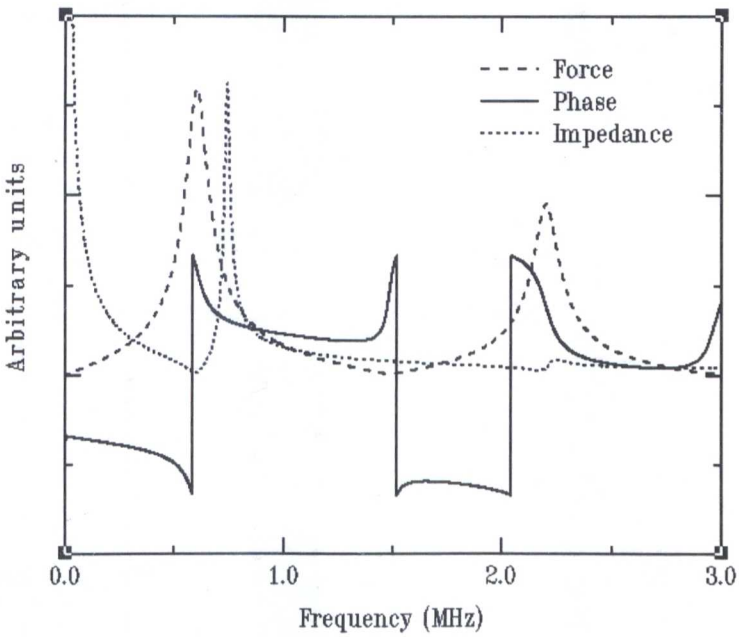

Figure 5.15 *Transducer output characteristics*

From Figure 5.15, it is apparent that as the frequency tends towards the electrical resonance (580kHz), the output force from the front face increases (due the secondary piezoelectric action [76] producing positive current feedback in the composite structure)

until the electrical resonance is achieved. Thereafter, the front face force decreases as the feedback into the system changes from positive to negative. This is illustrated in Figure 5.15 by the changing phase characteristics whereby, at the electrical resonance, the phase exhibits a change of π radians or 180°. This is further validated by examining the mode of vibration of a single ceramic pillar, before and after electrical resonance, utilising FEM. Figure 5.16 depicts this change in phase for a frequency of operation 10kHz below and above the electrical resonance of the composite. With the phase referenced to the centre of the device, it is apparent that the mode of displacement reverses from a contraction towards the centre, to an expansion outwards after the electrical resonance (denoted by the magnitudes on the scales). Note that for speed of calculation, a unit cell model (as described in Chapter 4) has been implemented.

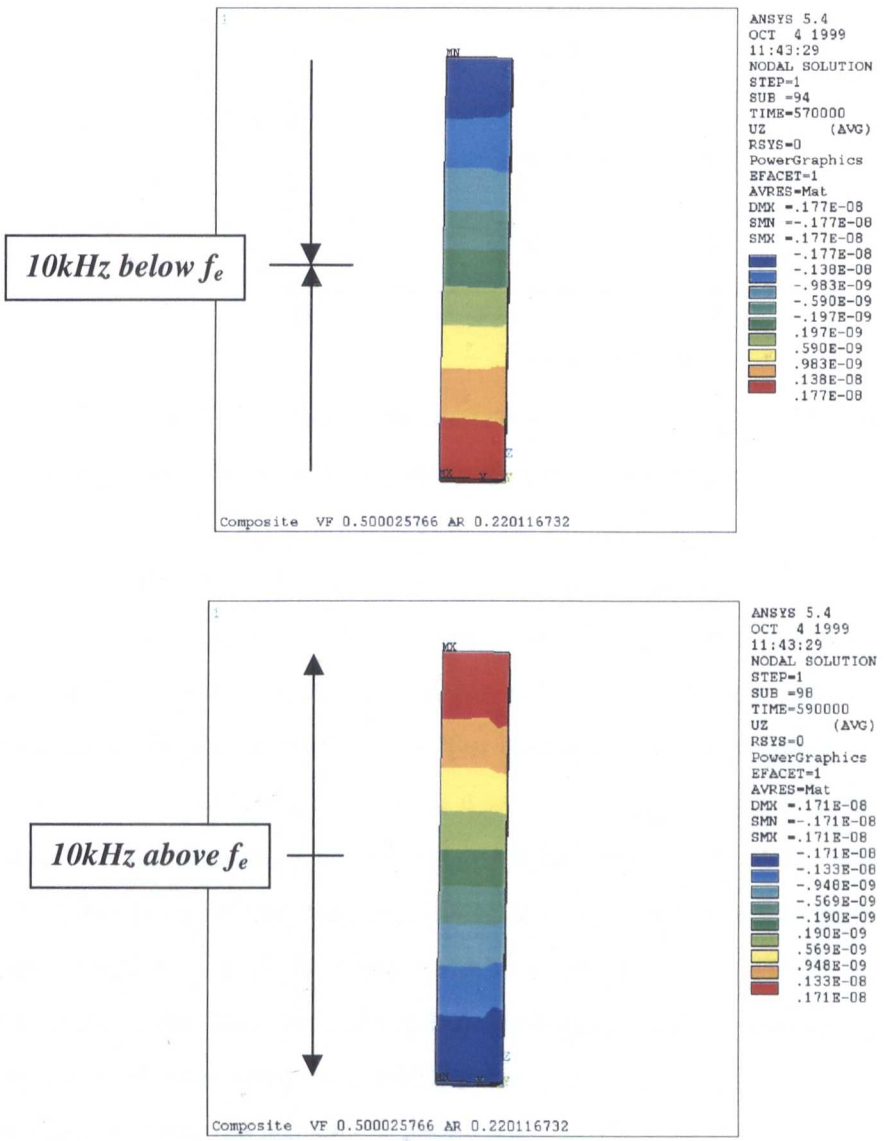

Figure 5.16 *Illustration of phase reversal at electrical resonance*

Consequently, by examining the impedance characteristics of the two thickness sections of the dual thickness composite in Figure 5.17, it is apparent that at 660kHz (indicated by the dotted line), the 2.12mm section will be experiencing positive current feedback due to secondary piezoelectric action, while the 2.52mm section will be undergoing negative current feedback. Thus, as illustrated experimentally and theoretically (Figure 5.13(f.)), there will be a phase difference of π radians between adjacent sections.

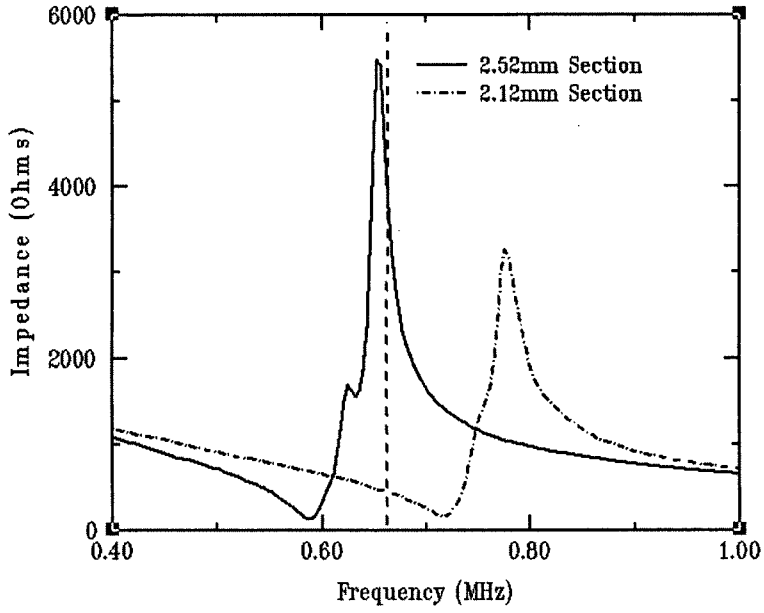

Figure 5.17 *Impedance characteristics of individual sections in dual thickness composite, illustrating frequency of operation that displays anti-phase vibration.*

Although the FE model of the dual thickness composite clearly illustrates the inclusion of a second thickness mode resonance and shows good correlation with the manner in which the vibration pattern changes across a frequency range, a number of other interesting disparities are evident. For example, at the frequency of the first impedance minimum (520kHz experimental), it is apparent that there is a dominant width mode active in the simulated transducer. Although this is not clear in the results measured using the laser interferometer. This may be due to the nature in which the transducer was modelled, i.e. 2½D, where infinite symmetrical boundaries are applied in the in-plane direction. Therefore, the thin modelled slice will be seem as an infinite bar, this is turn may have resulted in a width mode being generated which, in practice cannot be sustained due to the transducer geometry.

Additionally, the magnitudes of the longitudinal displacements for the measured results are greater and more sustained over frequency for the second thickness mode resonance than those predicted by theoretical analysis. Theory predicts that the majority of the longitudinal displacement in the thinner section will have dissipated by approximately 40kHz past the second electrical resonance. However, the experimental results show a more prolonged displacement for a further frequency period in the actual composite. It was found experimentally, that the displacement in the second thickness section continued until after 800kHz with a peak displacement of 1nm. One possible solution could be due to fact that the second step of the manufactured transducer was found to be of non-uniform thickness, due to imprecise machining and therefore would be slightly more wideband.

5.5.1 Impedance analysis of the multi-mode piezocomposite device

It has been shown that the introduction of a second thickness mode resonance can be facilitated by the addition of a second thickness to a composite device. Additionally, although the comparison between the theoretical and measured impedance does not provide complete confidence in the accuracy of the modelling of the impedance characteristics, the depoling problem associated with the modelled results shows little influence in the vibration of the composite structure. As such, the two step transducer design can be seen as the proof of concept for the tailoring of differing thicknesses to introduce further thickness modes at the expense of a small amount of depoling.

However, from the examination of the results determined in the previous Section it is apparent that with the electrical resonances set 100kHz apart, that the two modes of vibration act reasonably independently. While this has implications for other areas of operation, such as torpedo guidance or mine hunting (where separate frequencies are required for detection and interrogation), this device will not have sufficient bandwidth required for the proposed NDE application. Thus, by reducing the frequency step separation between thickness modes a more uniformly displacing transducer should be achievable.

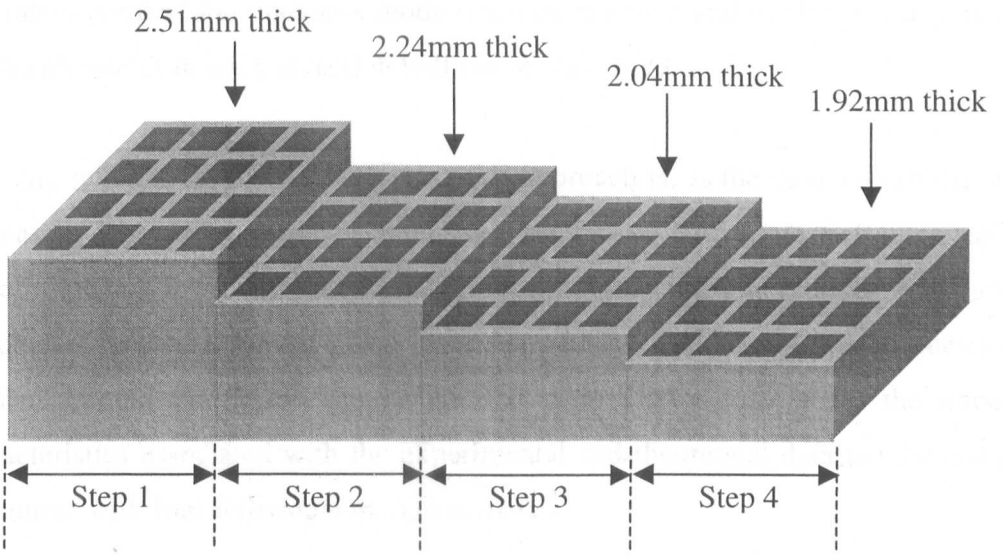

Figure 5.19 *Picture of a 4 step composite device*

Now, consider a piezocomposite device, measuring 30mm by 30mm, constructed of PZT-5A ceramic and CY1300/1301 Ciba-Geigy hard-set polymer to a 50% volume fraction, as shown in Figure 5.19. Using the technique described previously, three sections of the composite structure are removed to produce a device with four unique thicknesses. The various parameters associated with this transducer are listed in table 5.01.

	Thickness (mm)	Kerf (mm)	Pitch (mm)	Aspect Ratio
Section 1	**2.51**	**0.252**	**0.844**	**0.236**
Section 2	**2.24**	**0.252**	**0.844**	**0.264**
Section 3	**2.09**	**0.252**	**0.844**	**0.283**
Section 4	**1.92**	**0.252**	**0.844**	**0.308**

Table 5.01 *Step parameters for multi-step piezocomposite transducer*

As with the previous two step transducer, the impedance of the multi thickness composite was measured experimentally and compared with that predicted within the FEA package. In this instance again, the dimensions of the composite inhibit full or even half symmetry modelling, therefore the 2½D modelling technique was used. This method allows a considerably faster analysis of the device in question, reducing the overall complexity of the model and the computational requirements. While the method accurately predicts the thickness mode resonances and lateral modes in the x-direction, any width modes in the y-direction will not be supported.

The only inherent problem perceived in this approach is, as the thickness of the steps is decreased, the aspect ratio for the given section of composite will increase. This sometimes leads to the introduction of aforementioned inter-pillar modes in the width of the device, however, for the given pillar periodicity of the composite in question this problem should not arise. The results shown in Figure 5.15 detail the impedance characteristics associated with the experimental and theoretical data for the composite transducer with four individual thickness modes.

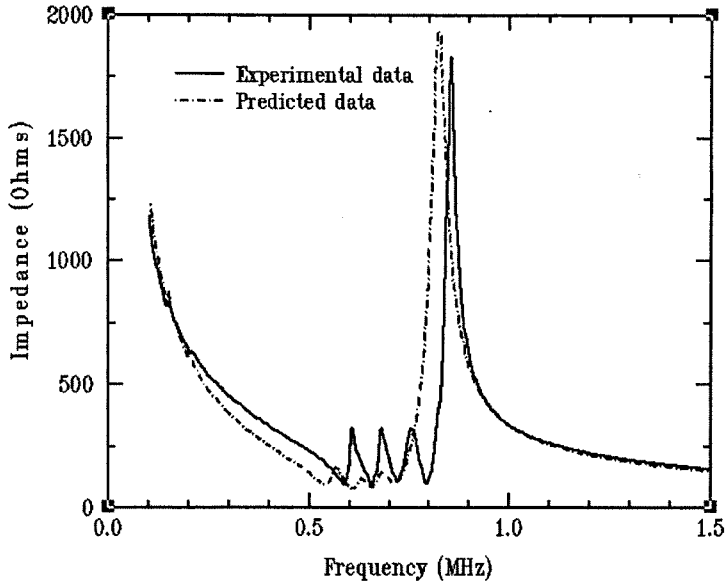

Figure 5.20 *Operational impedance of multi-thickness composite (exp & sim)*

As with the previous model, it is apparent that there has been a degree of depoling in the construction of the composite transducer. In order to determine if this was as a result of the machining process, or was inherent in the composite before the milling took place, the original impedance characteristics of non-machined composite was compared with that predicted by theory, as illustrated in Figure 5.21.

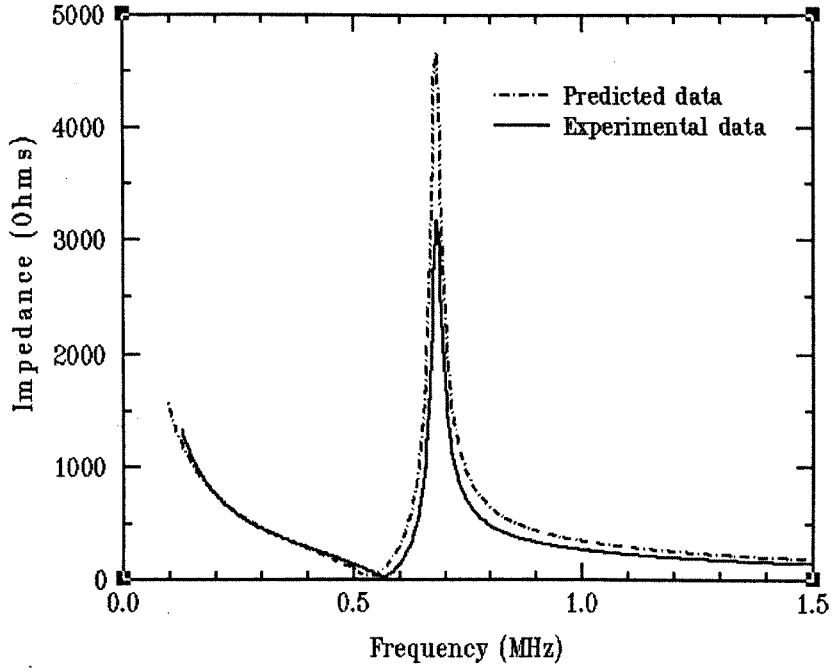

Figure 5.21 *Comparison of experimental and theoretical data before the machining process*

It is apparent from Figure 5.21 that there was already depoling present in the composite transducer before any additional machining was carried out on the device. Using Equation **5.06**, the coupling coefficient for the original composite is 0.6, whereas the theory predicts a k_t of 0.64, which in terms of mismatch is very slight. Subsequently, predicted data was computed for the isolated step thicknesses and compared with that measured on the impedance analyser, see Figures 5.22(a-d).

Figure 5.22 *Comparison between theory and experiment of isolated thickness sections*

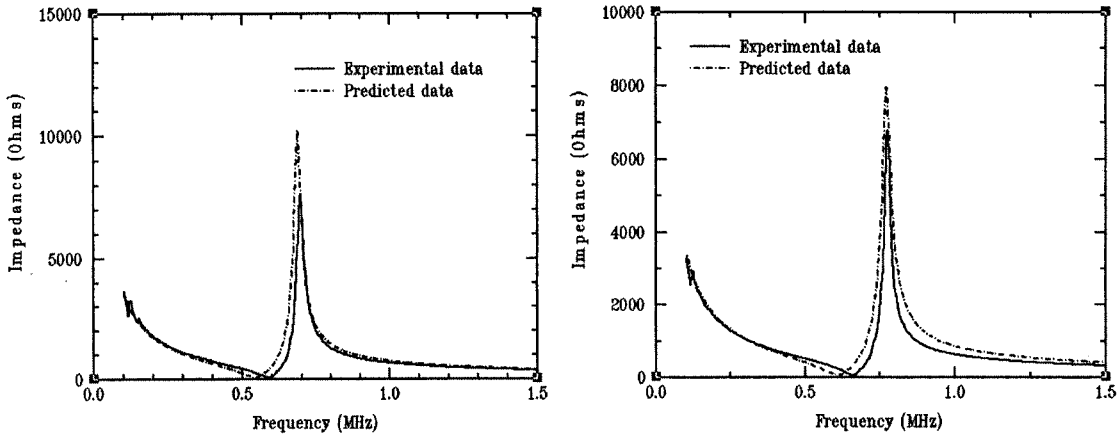

(a.) 2.51mm thickness section

(b.) 2.24mm thickness section

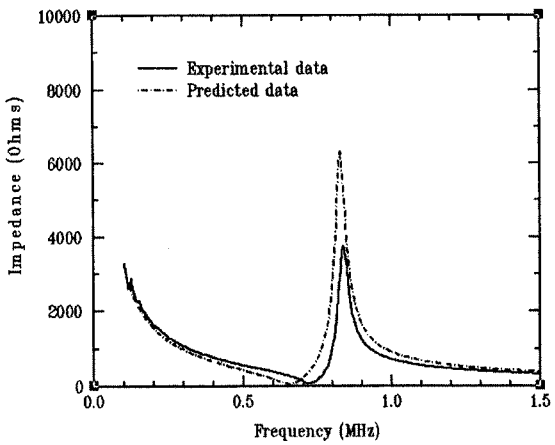

(c.) 2.04mm thickness section

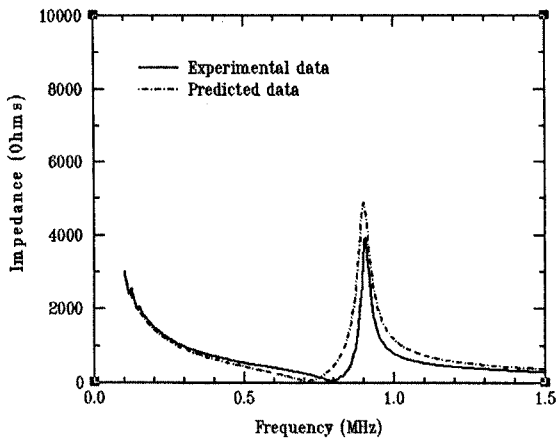

(d.) 1.92mm thickness section

By referring to Figures 5.22(a-d) it is apparent that there is a significant degradation in the coupling coefficient of each thickness section due to depoling of the composite in the milling process. By calculation, the coupling coefficient for each of the milled sections is consistently around 0.57 compared to 0.65 as predicted from the FEA. By comparing this coupling coefficient with that of the original composite (k_t = 0.6), it is apparent that once again the milling process has added to the depoling factor. Again,

this degree of depoling is not substantial and in comparison to that exhibited by the original dual thickness composite, is very favourable.

5.5.2 Output characteristics of the multiple thickness piezocomposite

Utilising the laser interferometer scanning apparatus described in Appendix B, it was possible to measure the magnitude of surface displacement across the front face of the multi-frequency composite. The front face of the transducer is again defined as the planar surface of the transducer, rather than the irregular stepped surface. This planar surface provides a simple geometry for scanning and a reference plane for subsequent beam profiling.

Figures 5.23(a)-(h) represent the surface displacements profiles from the front face of the device when excited by a 1volt tone burst of 10 cycles with a period of 1kHz using a HP33120 function generator, performed across a range of frequencies from 540kHz to 840kHz in steps of 20kHz. Figures 5.23 c, g, j and n illustrate the displacement on the surface at the electrical thickness mode resonances for each individual step, while the remaining plots illustrate the changing surface displacement profiles between the four distinct thickness modes illustrated in the impedance characteristics. Again, the darker regions indicate the areas of greater displacement.

Figure 5.23 *Surface displacement profiles for four step composite across frequency of operation*

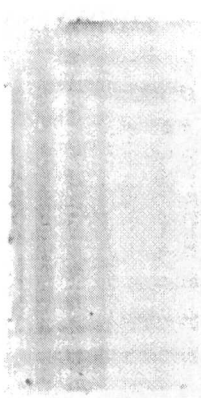

(a.) 540kHz

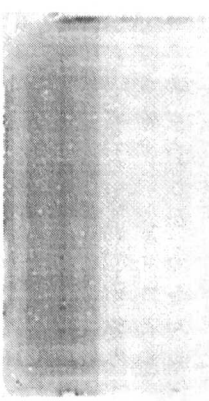

(b.) 560kHz

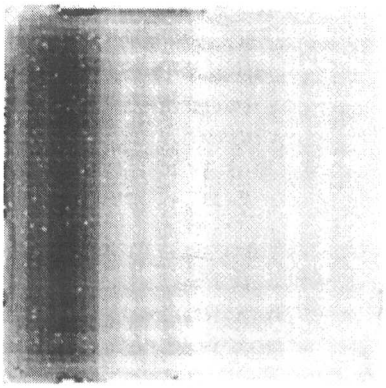

(c.) 580kHz

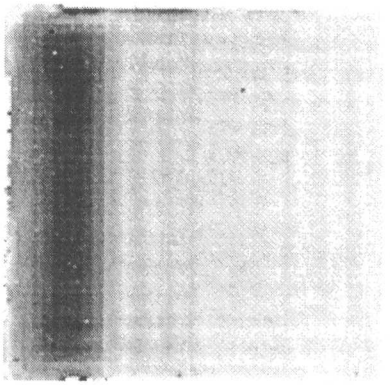

(d.) 600kHz

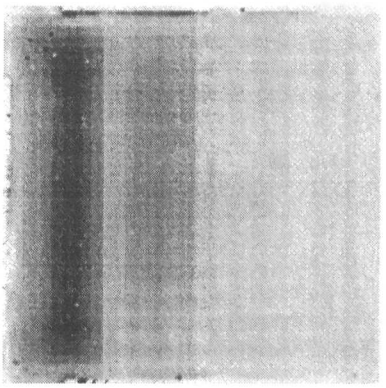

(e.) 620kHz

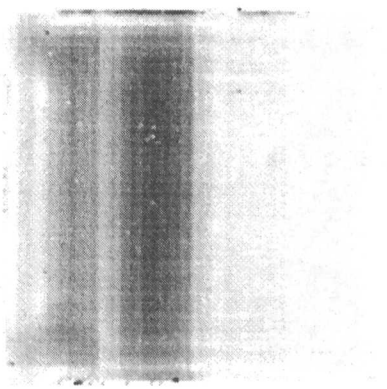

(f.) 640kHz

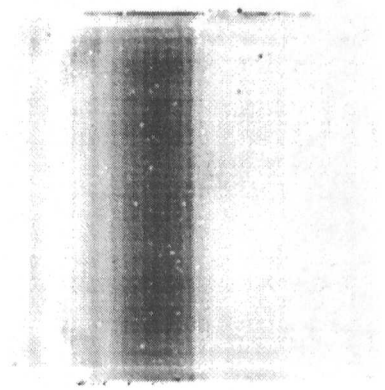

(g.) 660kHz

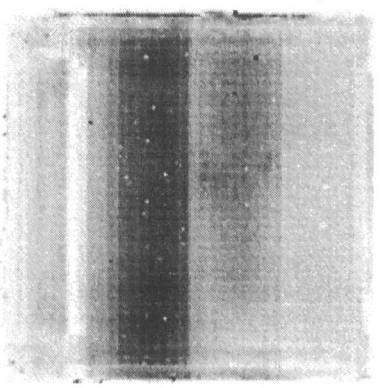

(h.) 680kHz

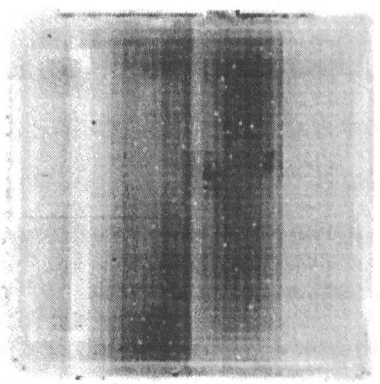

(i.) 700kHz

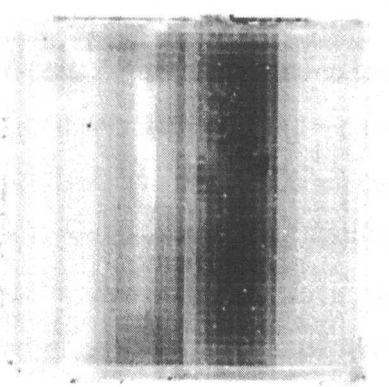

(j.) 720kHz

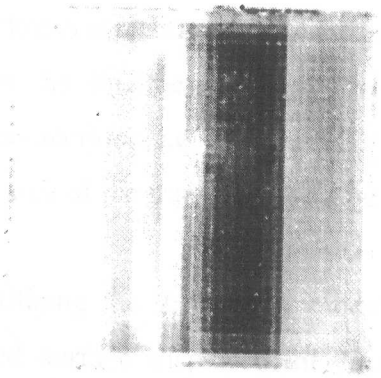

(k.) 740kHz

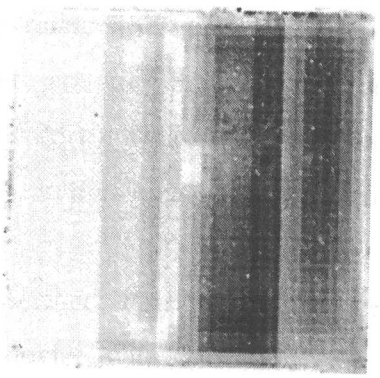

(l.) 760kHz

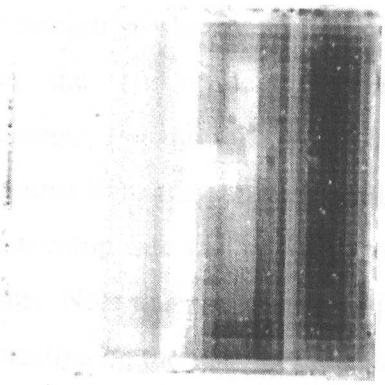

(m.) 780kHz

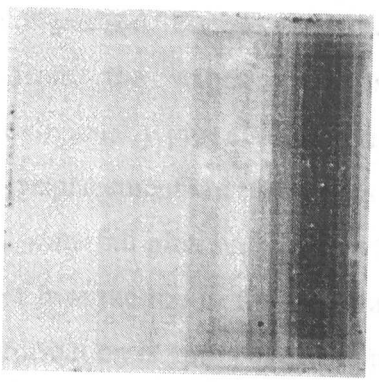

(n.) 800kHz

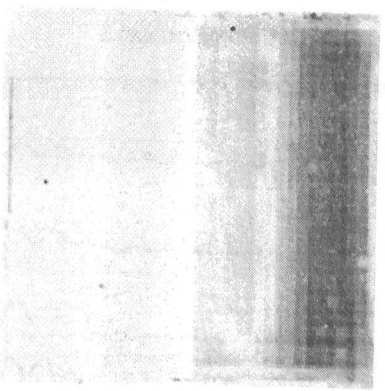

(o.) 820kHz

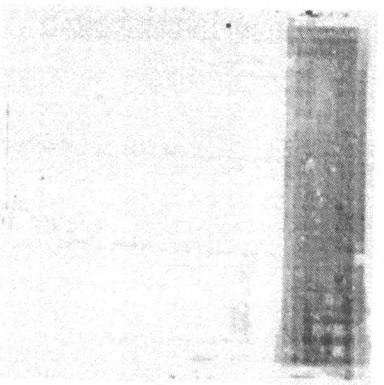

(p.) 840kHz

Note that the disparity in shading of the surface displacement profiles is due to the non-uniform scaling factor incorporated to illustrate the displacement trend across the transducer. Figures 5.23 (a-p) illustrate the changing displacement profile of the four step composite transducer, with electrical resonances at 580kHz, 660kHz, 720kHz and 800kHz for steps 1 to 4 respectively. It is apparent that at these four discrete frequencies, that the predominant displacement is that of only the associated thickness region in the thickness direction. However, as the frequency of operation is shifted between the electrical resonances, neighbouring thickness sections begin to vibrate in

the thickness direction. It also apparent that with the reduced frequency step separation between the thickness modes, that there is greater coupling between the adjacent thickness sections, i.e. Figures 5.23(f.), 5.23(i.) and 5.23(l.). This in turn implies that a greater area of the transducer will be active when used in transmission or reception.

Now utilising the 2.5D FEA model previously described, it is possible to generate predicted surface displacements for a composite device with four thickness steps. Figures 5.24(a-d) represents the displacement of the transducer when examined through a cross section of the multi-step composite. For comparison, Figures 5.24(a-d) also illustrate the cross sectional data extracted from the experimental surface displacements. For the sake of brevity, rather than individually plot each experimental result against its corresponding predicted result, the displacement characteristics of the multi-step composite will be represented as a vertical waterfall plot, with data in 20kHz increments. Note that the lowest frequency of interest is at the top of the waterfall plot and the scaling on the y-axis of the cross sectional information is 1nm per division.

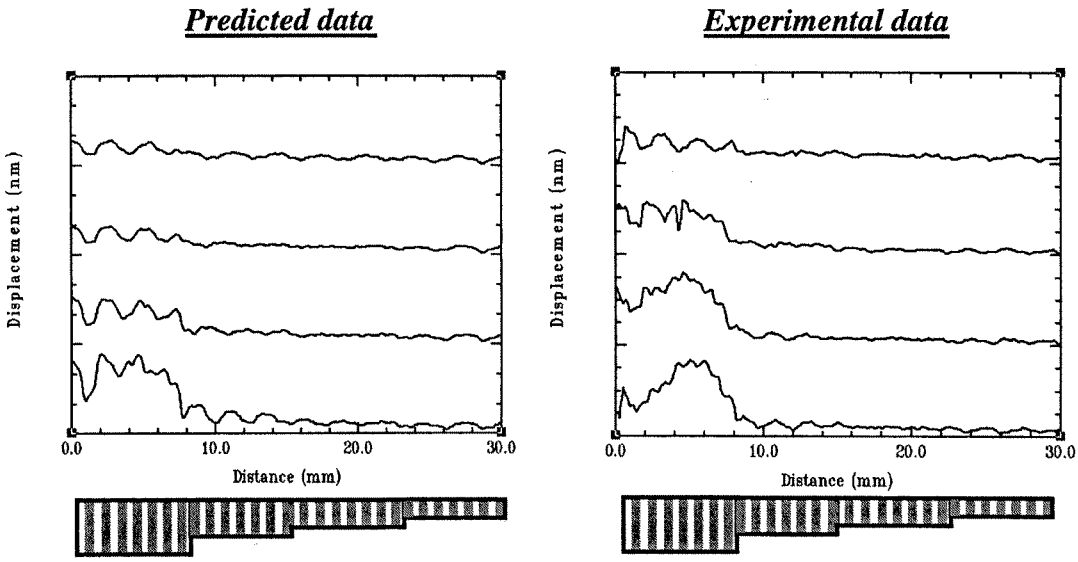

Figure 5.24(a) *Cross sectional displacement (Predicted 480kHz-540kHz, Experimental 540kHz-600kHz)*

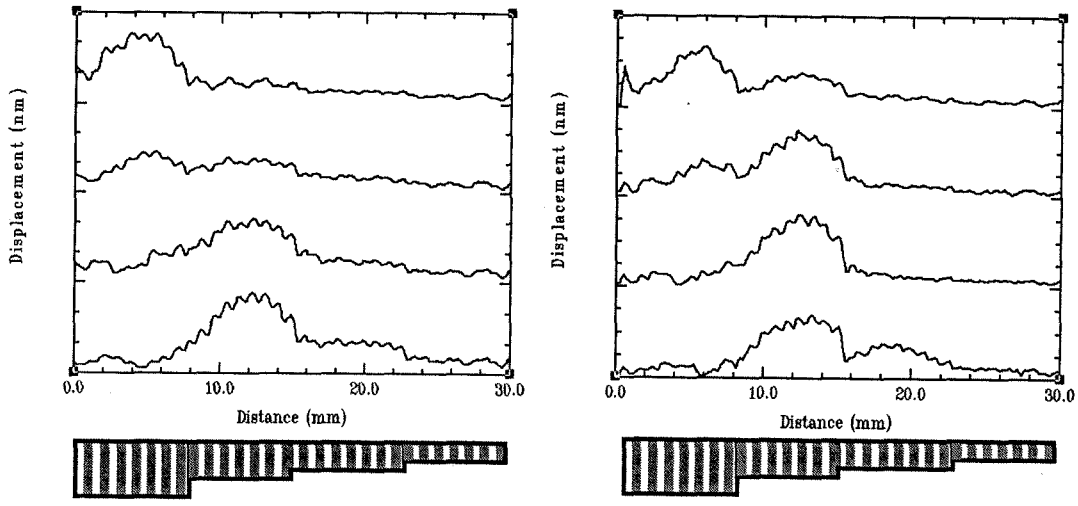

Figure 5.24(b) *Cross sectional displacement (Predicted 560kHz-620kHz, Experimental 620kHz-680kHz)*

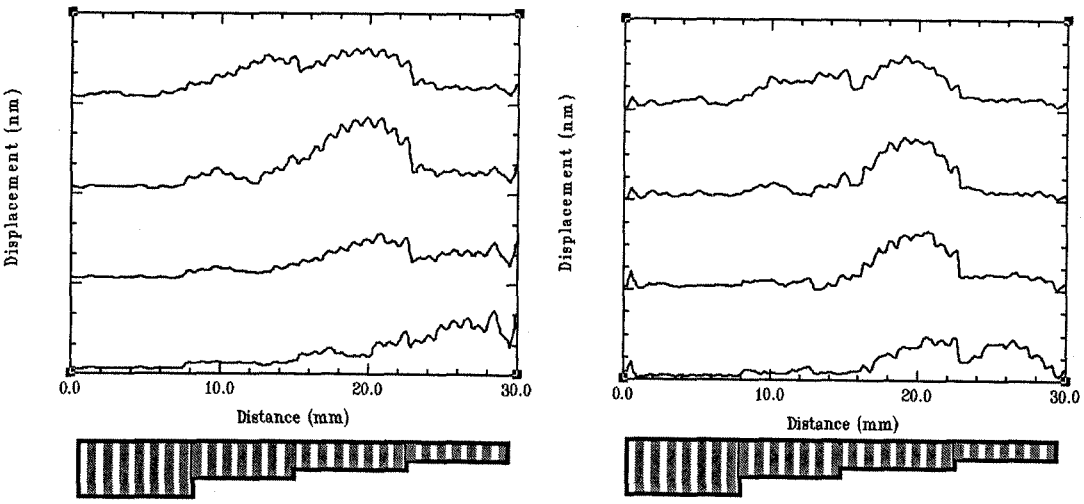

Figure 5.24(c) *Cross sectional displacement (Predicted 640kHz-700kHz, Experimental 700kHz-760kHz)*

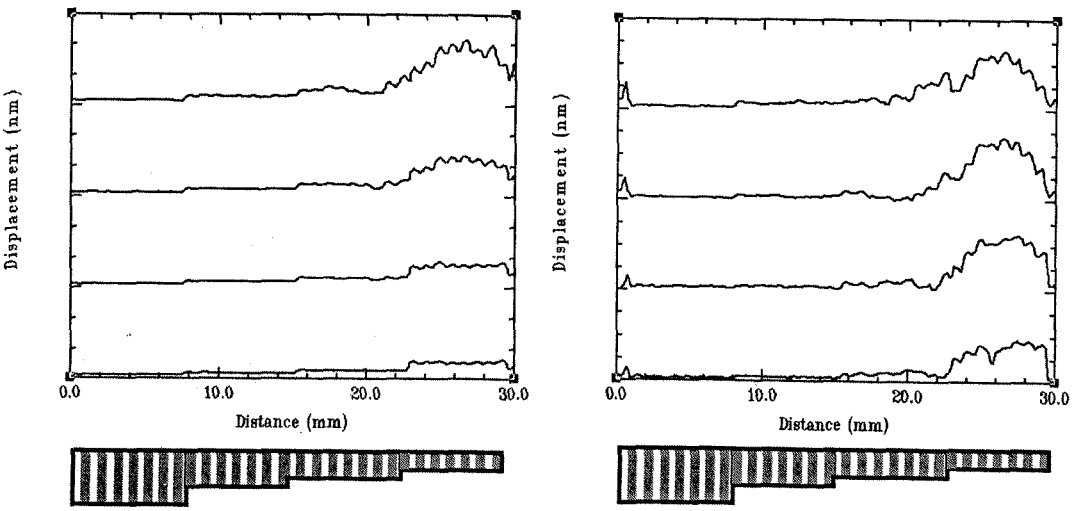

Figure 5.24(d) *Cross sectional displacement (Predicted 720kHz-780kHz, Experimental 780kHz-840kHz)*

By comparison, it can be seen that the nature of the surface displacements predicted by the ANSYS® model shows good correlation to that determined experimentally. The only area of disagreement being with the exact frequency of operation, which as previously covered is due to the depoling of the composite structure altering the frequency at which the electrical resonance occurs. As with the previous dual thickness example, the magnitude of displacement exhibited by the measured device is greater (4nm at peak displacement) and more sustained, after the electrical resonances than that predicted by FEA (3nm at peak displacement). Moreover, the FEA once again predicts a width mode in the region of the first electrical resonance of the composite. As mentioned previously, this may be due to the symmetrical method of analysis utilised or may perhaps due to the unsupported nature of the thickest step.

5.5.3 Acoustic field profile of stepped composite transducer

When designing a composite transducer for operation within a non-destructive evaluation (NDE) scanning system, it is essential that the acoustic field, or beam profile of the transducer is characterised fully. The beam profile of the transducer effectively describes the direction and intensity of the sound propagating from the transducer towards the test sample. In order to determine the beam profile of these new composite devices, the four-step thickness transducer was measured within the beam measurement hardware, described in Appendix B. and examined across a range of frequencies. The effective bandwidth of the composite transducer is approximately 220kHz, with four separate thickness mode resonances at 580kHz, 660kHz, 720kHz and 800kHz, therefore profiling was done at these four dominant frequencies and a range other of intermediary points.

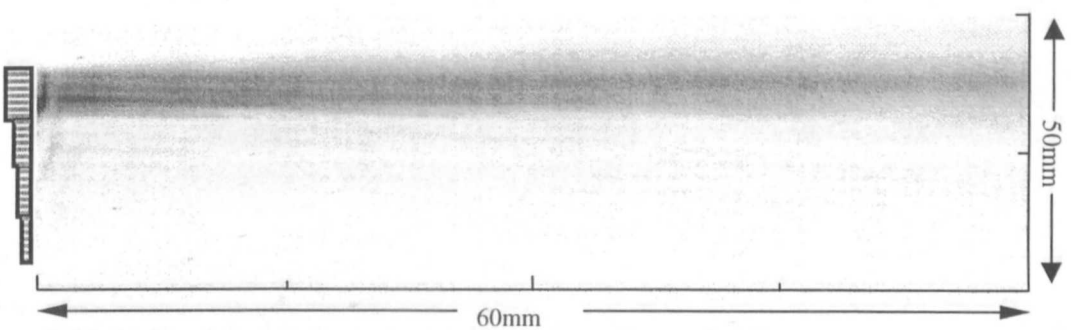

Figure 5.25(a.) *Experimentally measured beam profile at 580kHz*

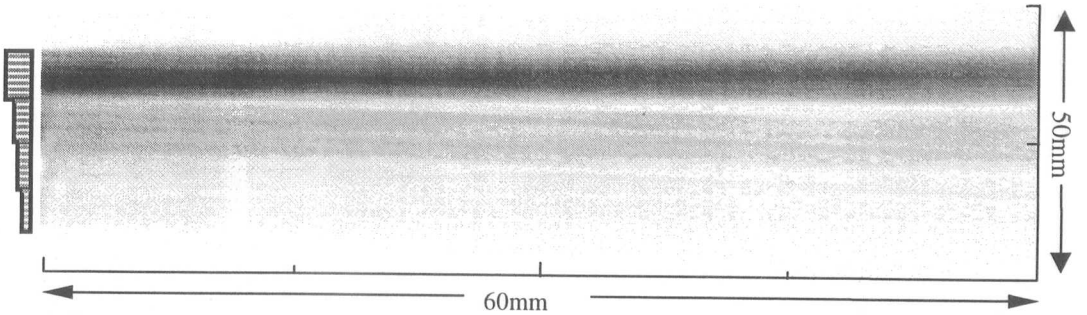

Figure 5.25(b.) *Experimentally measured beam profile at 600kHz*

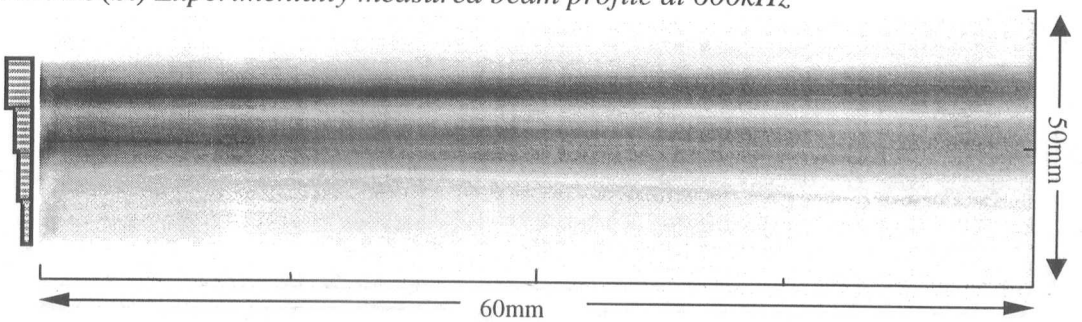

Figure 5.25(c.) *Experimentally measured beam profile at 620kHz*

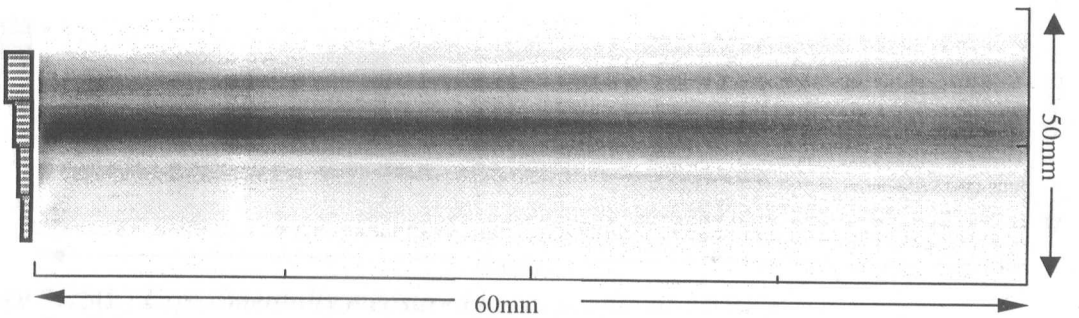

Figure 5.25(d.) *Experimentally measured beam profile at 640kHz*

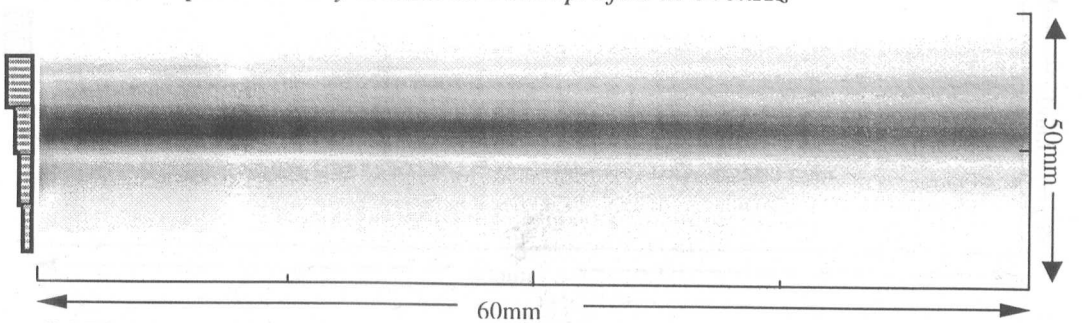

Figure 5.25(e.) *Experimentally measured beam profile at 660kHz*

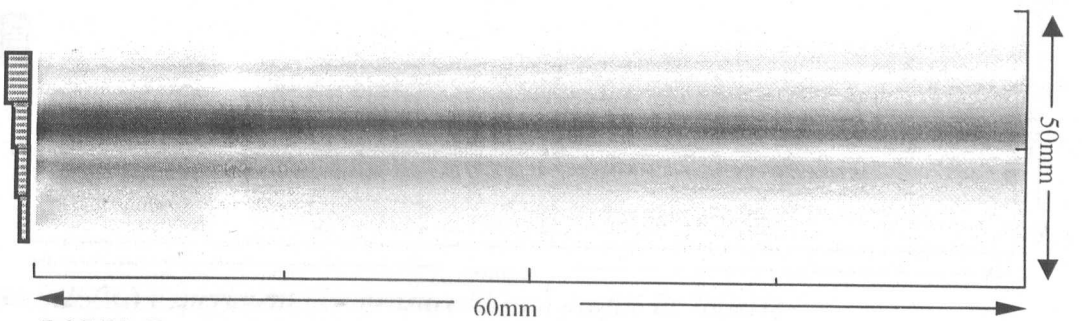

Figure 5.25(f.) *Experimentally measured beam profile at 680kHz*

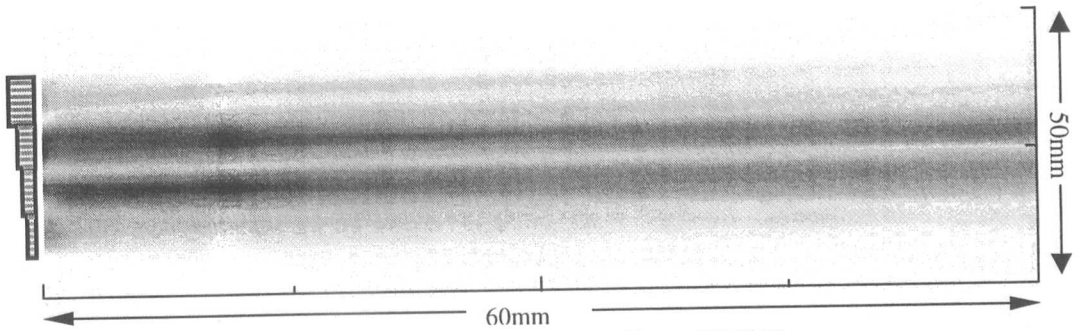

Figure 5.25(g.) *Experimentally measured beam profile at 700kHz*

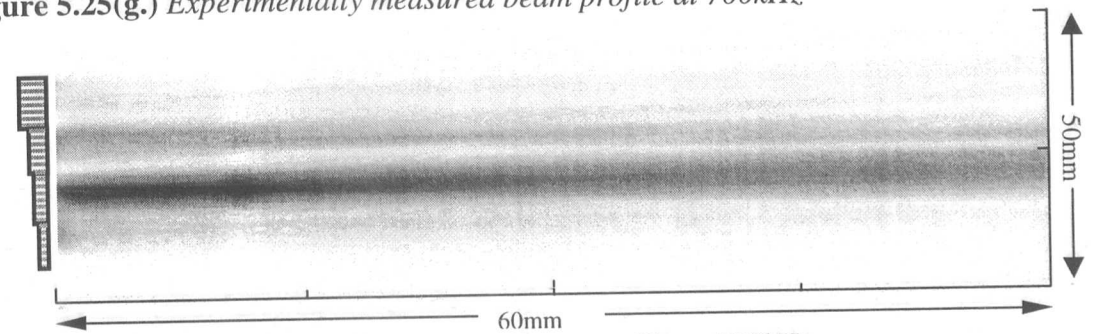

Figure 5.25(h.) *Experimentally measured beam profile at 720kHz*

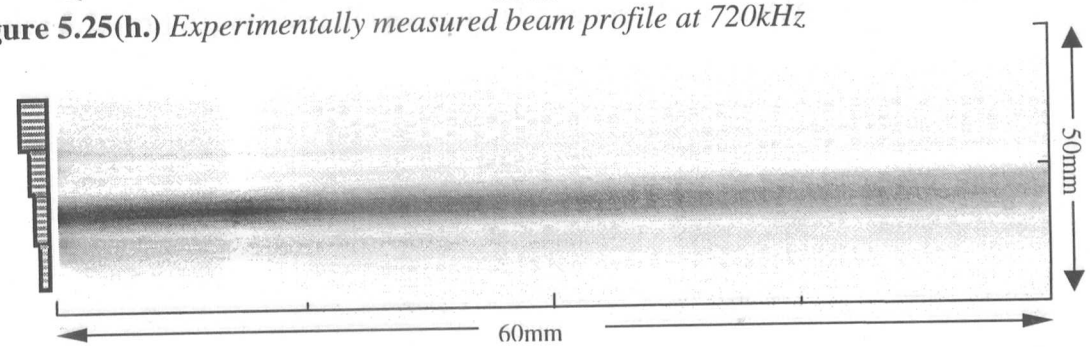

Figure 5.25(i.) *Experimentally measured beam profile at 740kHz*

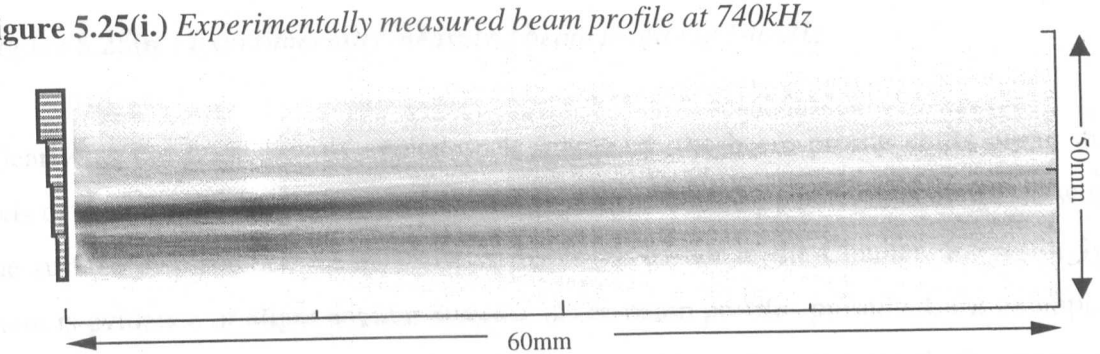

Figure 5.25(j.) *Experimentally measured beam profile at 760kHz*

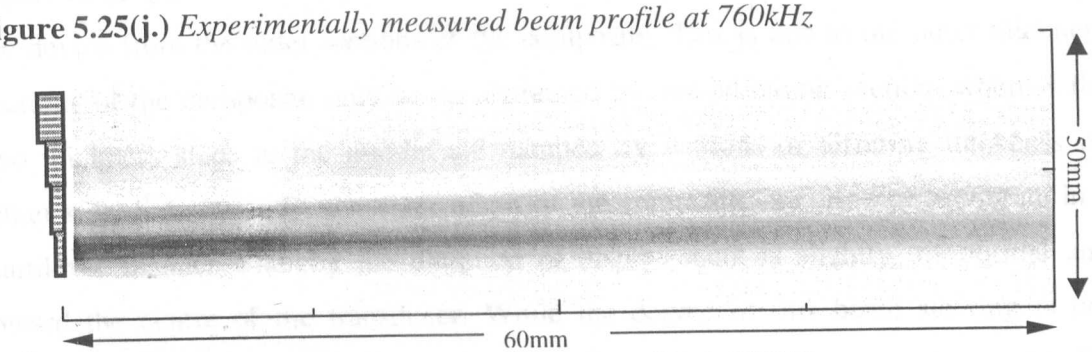

Figure 5.25(k.) *Experimentally measured beam profile at 780kHz*

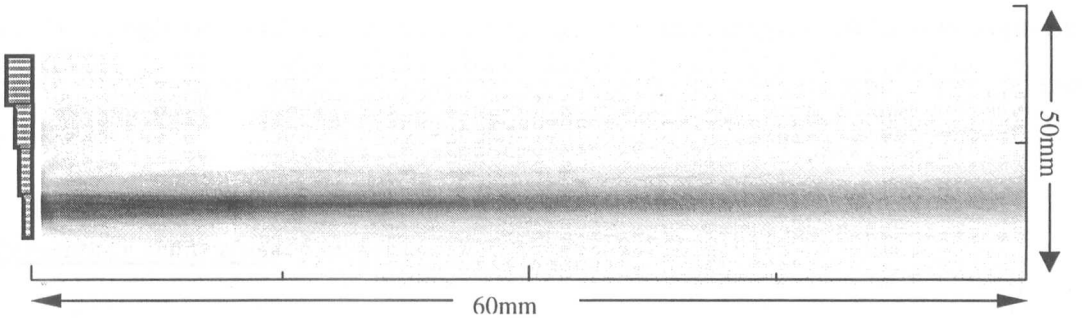

Figure 5.25(l.) *Experimentally measured beam profile at 800kHz*

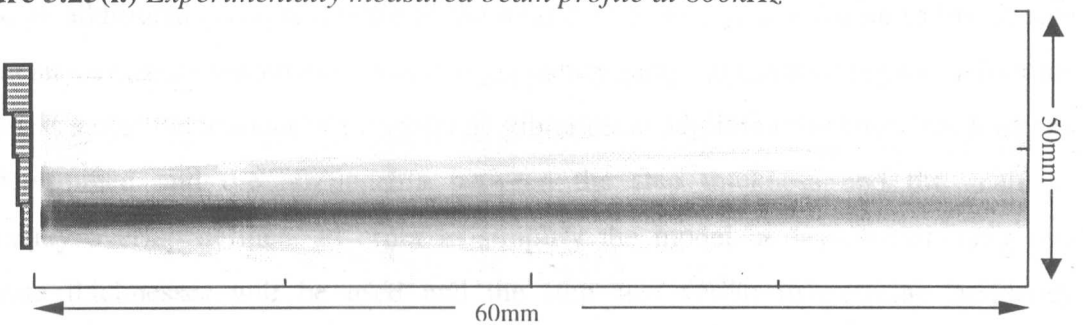

Figure 5.25(m.) *Experimentally measured beam profile at 820kHz*

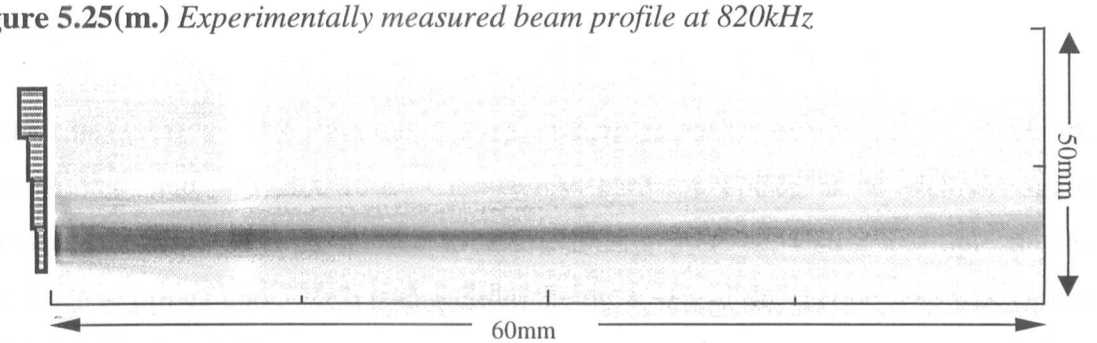

Figure 5.25(n.) *Experimentally measured beam profile at 840kHz*

Clearly, as the frequency of excitation is increased, the beam profile shifts along the axis of the transducer towards the thinner sections of the composite, in accordance with the surface displacement characteristics displayed earlier in the Chapter. Interestingly, there is evidence of slight angular steering in the beam profiles presented, for example, Figures 5.25 (a, b, m and n.) show a small degree of beam steering towards the centre of the device from the outer sections of the composite. This is due to the outer thickness sections of the composite only being restrained by one adjoining section, whereas the two thickness steps in the middle are damped by sections of differing thickness on either side. Subsequently, the outer edges of the composite are allowed to vibrate in a cantilever manner whereby the direction of displacement is slightly off normal and toward the centre of the transducer. While the degree of this beam steering is not significantly degrading the performance of the transducer, this trait is not favourable for the application for which these transducer are being designed. This is because any

alteration in angle of incidence of the acoustic wave to the structure under investigation is likely to result in an inability to efficiently generate the given Lamb wave for the plate thickness.

5.6 Frequency separation

Through additional post-processing of the modelled results, it is possible to investigate the mean surface displacement across the frequency range. By examining the individual thickness steps, the amount of sympathetic vibration in adjoining thickness sections can be determined and the relationship between the step thickness and the scale of frequency overlap defined. In order to simplify the model, a device with only two separate thicknesses will be used and the step size varied to examine frequency separation.

In this instance, a 33% volume fraction piezocomposite comprising of PZT-5A piezoceramic and HY1300/1301 Ciba-Geigy hard-set epoxy is modelled, again complete transducer parameters are available in Appendix C. Using a simple model with 4 active pillars under each step section, the thickness of the second step was varied as detailed in table 5.02.

	Thickness (mm)	Aspect Ratio	f_e (kHz)	f_m (kHz)
Base composite	**2.767**	**0.15**	**500**	**607**
+10kHz	**2.713**	**0.153**	**510**	**619**
+20kHz	**2.660**	**0.156**	**520**	**631**
+40kHz	**2.562**	**0.162**	**540**	**655**
+60kHz	**2.470**	**0.168**	**560**	**680**
+80kHz	**2.385**	**0.174**	**580**	**704**
+100kHz	**2.306**	**0.18**	**600**	**728**
+120kHz	**2.231**	**0.186**	**620**	**753**
+140kHz	**2.161**	**0.192**	**640**	**777**
+160kHz	**2.096**	**0.198**	**660**	**825**

Table 5.02 *Step parameters for differing frequency separations*

By post-processing of the modelled step surface, an average surface displacement with respect to frequency can be determined and illustrated in Figure 5.26. This was calculated by summing the total nodal displacement in the thickness direction and dividing the by the number of nodes in the model at each frequency.

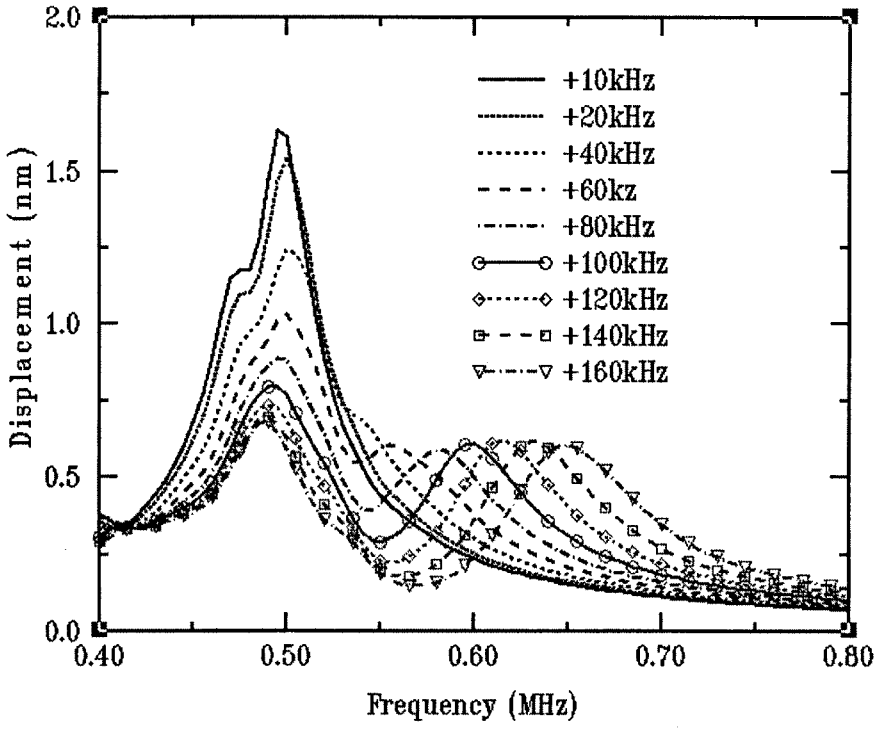

Figure 5.26 *Average displacement of the planar face of stepped composite for differing step thicknesses with respect to frequency*

From these modelled results, it is apparent that as the step size is reduced between the between the two adjacent thickness sections, the amount of vibration in the adjoining area is naturally increased. However, once the frequency separation between the two sections is increased beyond 100kHz, then the amount of sympathetic vibration transferred to the adjacent thickness step will be negligible. Therefore, the logical progression indicates that an alternative transducer arrangement would be a series of small steps cut into the composite to form a ramped transducer. Although this should increase the overall area of vibration, the thickness mode vibration in one area will still only propagate to surrounding thicknesses within 60-80kHz of the original resonance. This geometry of transducer would be similar to the ramped design investigated by Hossack [92] and therefore exhibit the same limitations on non-planar displacement over the range of frequencies required. This would have the effect of shifting the area

under inspection in the mode of operation proposed for this transducer, as shown in Figure 5.27. While this form of transducer has been demonstrated in a solid piezoceramic form by Germain and Cheeke [103, 104] for acoustic microscopy, it has never found application in the piezocomposite form suggested by the author.

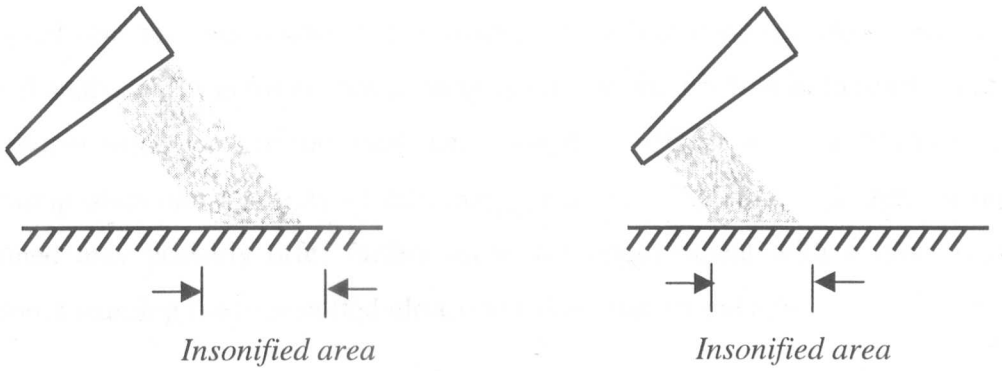

Figure 5.27 *Problems associated with non-planar vibration*

One possible solution may be to consider machining two ramps onto the back of the composite rather than just one. The problem with this approach is that the size of the composite in the lateral direction would be quite large and therefore reduce the overall sensitivity of the device to detection of only the larger flaws. However, by turning the composite on a lathe, a conical composite structure could be formed which would offer a compact transducer with uniform thickness in a radial direction which should produce a much more uniform beam pattern for inspection in the near field.

5.7 The conical composite design

5.7.1 Impedance analysis

Previously, the manufacture of a radially machined transducer composite was not considered due the aforementioned problems of tooling ceramic. However, through practical analysis it was found that as long as the volume fraction between the ceramic and polymer filler was not too great, i.e. lower than 70%, it was feasible to machine these composites into a variety of different geometries. The conical design previously mentioned may possibly offer further scope for improvement with a more uniform vibration, focussing the transmitted ultrasound along the central axis.

A 50% volume fraction 1-3 connectivity composite comprising PZT-5A ceramic and hard-set CY1300/1301 polymer was used to investigate the feasibility of this form of design. Using a standard metal working lathe, a conical transducer to the dimensions described in Figure 5.28 was constructed.

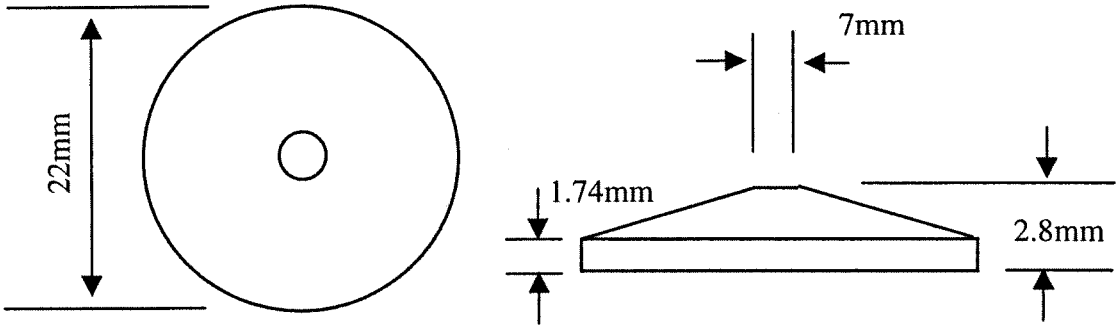

Figure 5.28 *Conical composite geometry*

These parameters are such that the transducer has an initial electrical resonance of approximately 580kHz ranging up to a maximum electrical resonance of 900kHz. By confining the device bandwidth to this range, the machined angle on the rear face of the transducer was limited to below 10^0. As the angle machined onto the rear face increases, conversely the number of pillars likely to be activated in the media surrounding the ceramic at thickness mode resonance decreases. By selecting this low angle for the rear face, the frequency separation should be such that a minimum of 4 pillars per radial thickness, should be displaced simultaneously through sympathetic

vibration in the adjoining radial thickness sections. The composite was then electroded with silver on both upper and lower surfaces and the impedance measured with the HP4194 impedance/gain-phase analyser. Figure 5.29 illustrates the impedance characteristics of the machined conical device. The extended impedance minimum is evident on the impedance response of the conical transducer.

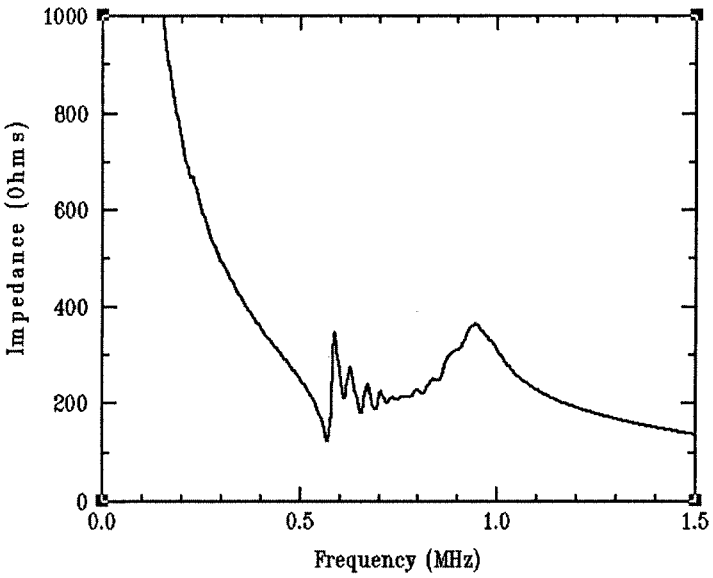

Figure 5.29 *Measured impedance of prototype conical composite transducer*

Now, in order to determine fully the mode of operation of this transducer, a finite element model was constructed to predict the substructure displacements active within the transducer. In this instance, it was not possible to use the 2.5D modelling approach, as the circular nature of the model does not support this symmetry option. The lowest possible reduction factor that this form of model can use is 1/8 symmetry, which will dissect the pillars in the x-y axis by 45°, hence when the symmetry is applied in the cylindrical co-ordinate system the cone will be represented accurately. Although it would be advantageous to model the conical device as a whole, the computing facilities available meant that the processing requirements would be too time intensive. Figure 5.30 illustrates the volumetric representation of the implemented model,

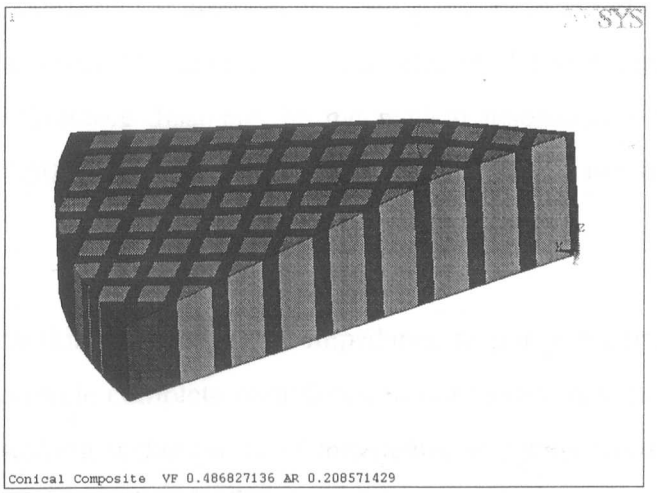

Figure 5.30 *Model geometry for conical device*

Utilising harmonic analysis, it was possible to determine the predicted impedance characteristics of the modified composite device and this response is shown in Figure 5.31 with the experimentally derived data for comparison. By examining Figure 5.31 it is apparent that the model predicts a similar impedance behaviour to that of the transducer with evidence of the depoling problem previously discussed. Both modelled and measured responses exhibit the elongated impedance minima and have similar ramped phase characteristics.

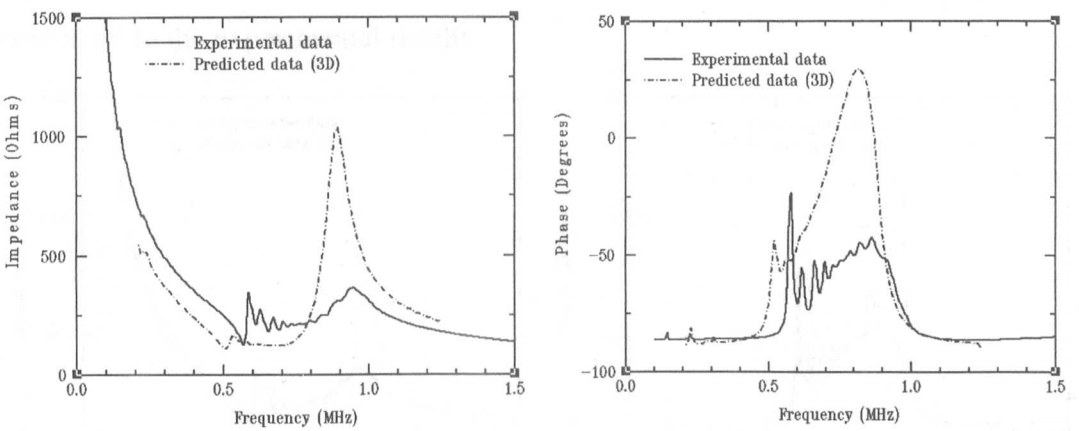

Figure 5.31 *Comparison between theoretical and measured impedance responses*

The differences between the measured data and that predicted by the model may be attributed to a number of differing factors, slightly angular misalignment on the rear face, striations on the ceramic from the cutting tool and modelling inaccuracies. The main apparent difference is the dominance of the highest mechanical mode (950kHz) due to the outer diameter thickness, which is not duplicated, in the measured results.

This is due to the fabricated transducer not being perfectly circular in shape. This in turn means that the outer diameter of the manufactured transducer has non-uniform thickness and will therefore dissipate the mechanical resonance across the frequency range 800kHz to 950kHz, instead of a defined mechanical resonance predicted by theory at 950kHz.

However, even with this knowledge, the impedance response predicted using the FEA package does not provide complete confidence in the model. Another possibility could be the complex meshing technique with tetrahedral elements (SOLID98), instead of standard block elements (SOLID5). The use of these tetrahedral elements was necessary to model such a structure (due to the non-uniform device geometry), but drastically increases the model size and complexity. Since these elements are arranged in a random nature, rather than the typical periodic manner, the node alignment for passing degrees of freedom (DOF) information will be more complex. Additionally, due to the complexity of the model shape and the requirement of the model to process in a reasonable time, the number of elements used to mesh the model has to be restricted. Therefore, in order to determine if the FEA was correctly modelling the conical transducer, a 2D model has coded with higher meshing quality to analyse the FEA code. Figure 5.32 illustrates the resultant simulated impedance and phase characteristics compared to the experimental results.

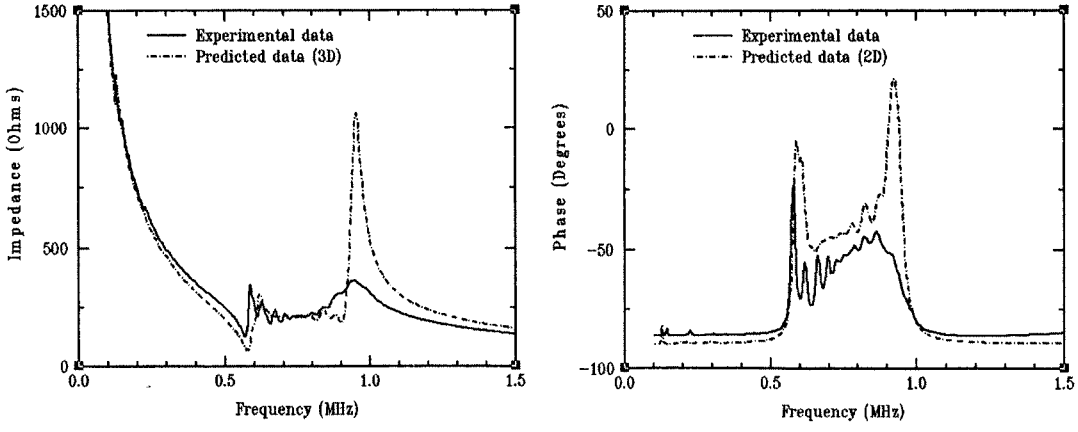

Figure 5.32 *Comparison of experimental and 2D simulated transducer characteristics*

By referring to Figure 5.32 it is apparent that the 2D model gives a much more accurate representation of the conical composite design. It should be noted that the greater degree of correlation between the simulated and experimental electrical resonances are

due to the 2D modelling approach representing the transducer as a 2-2 connectivity composite rather than a 1-3 connectivity composite. This in turn alters the f_e and f_m of the transducer, albeit fortuitously in this instance, due to the change in calculated volume fraction between the 2D and 3D model. The dominance of the outer diameter thickness at 950kHz is again due to the symmetrical properties of the model, was not seen in practice.

Due to computational limitations, it was not possible to model the conical composite in 3D in a greater frequency resolution than exhibited here, as the time required to extend this analysis would have been restrictive. With more powerful processing tools available, this frequency range can be further expanded and the number of elements used within the 3D modelling approach can be extended to more accurately model the conical composite design.

5.7.2 Experimental surface displacement characteristics

In order to characterise the resonant behaviour of these conical devices, the laser interferometer was used to determine the magnitude and mode of surface displacement exhibited by this form of composite. As with the previous stepped composites, these devices were evaluated across a range of frequencies, in order to determine their nature of operation.

The conical composite was excited by a 1volt tone burst of 10cycle duration and 1kHz burst repetition from a HP33120A function generator, the resultant displacement information was acquired using the Polytec laser scanner. The dotted lines on the surface displacements signify the outer diameter of the conical composite.

Figure 5.33 *Surface displacement configuration of conical composite across operational bandwidth*

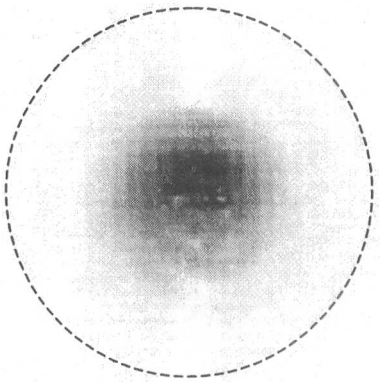

(a.) 560kHz

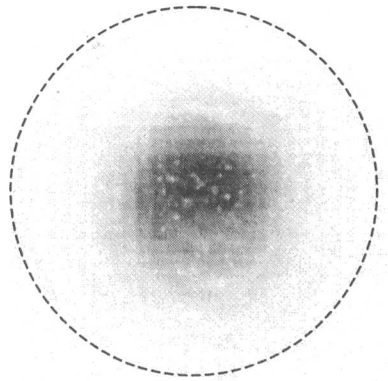

(b.) 580kHz

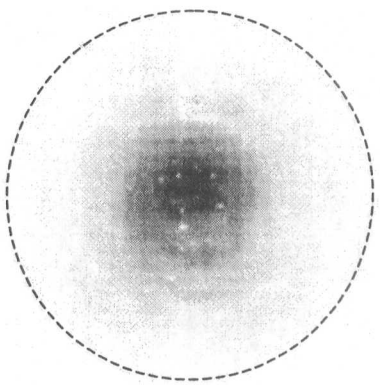

(c.) 600kHz

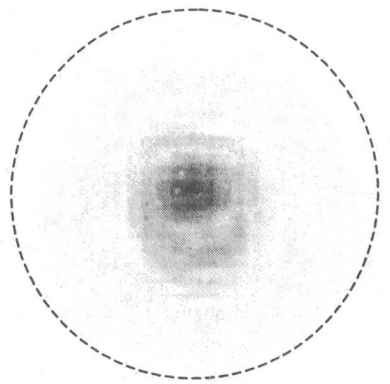

(d.) 620kHz

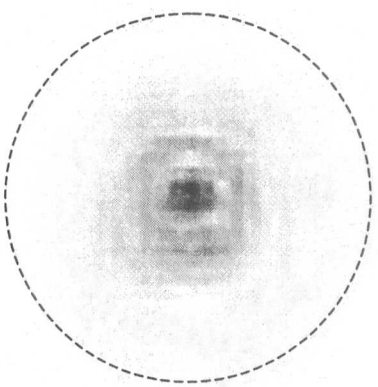

(e.) 640kHz

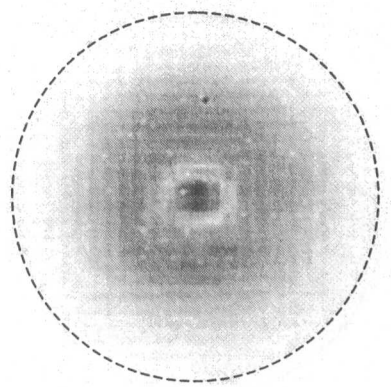

(f.) 660kHz

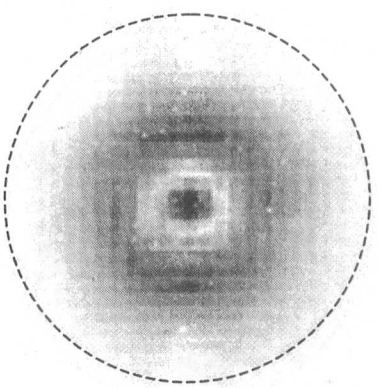

(g.) 680kHz

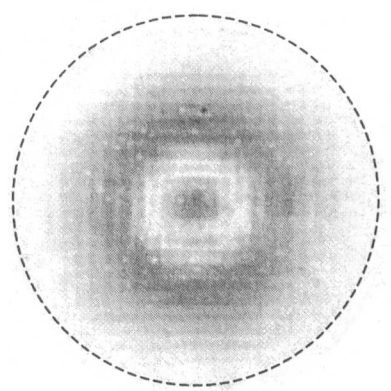

(h.) 700kHz

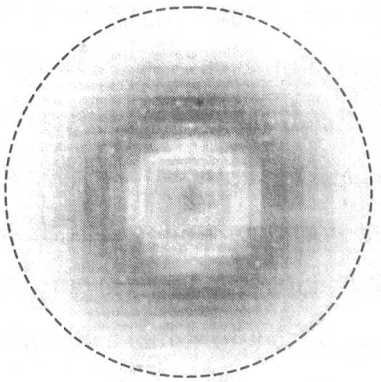

(i.) 720kHz

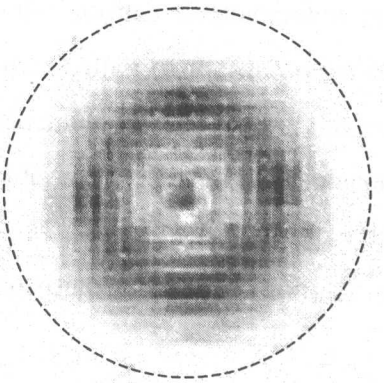

(j.) 740kHz

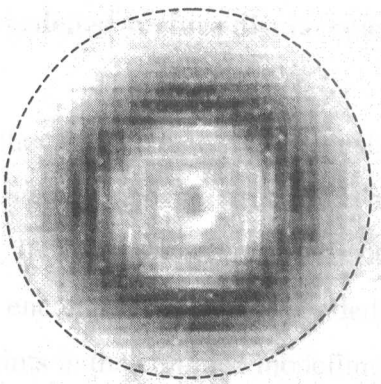

(k.) 760kHz

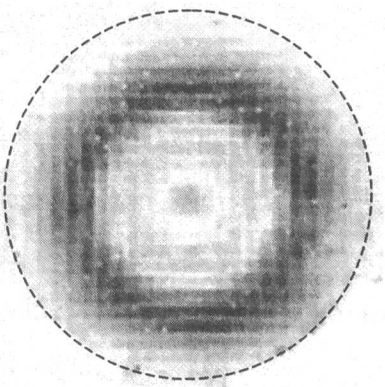

(l.) 780kHz

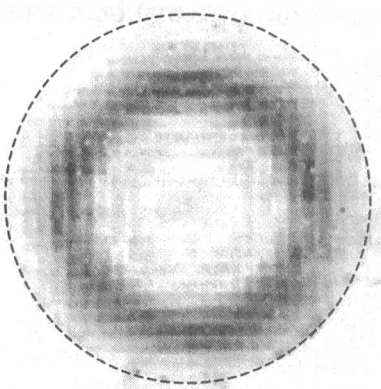

(m.) 800kHz

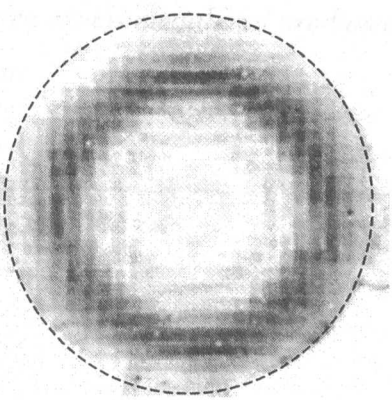

(n.) 820kHz

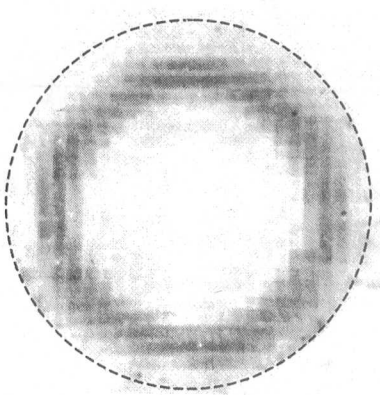

(o.) 840kHz

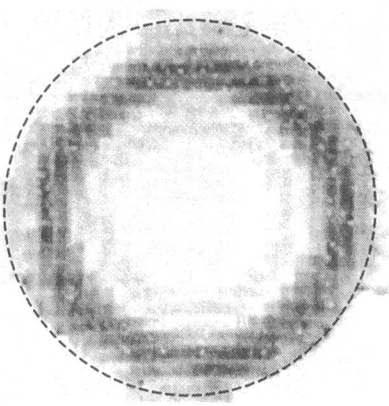

(p.) 860kHz

As with previous examples, the darker regions on the surface displacement profiles signify the areas of greatest displacement, although the scaling of the diagrams is non-uniform. Figures 5.33(a-p) detail the surface displacement exhibited by the conical device across the specified frequency range. By considering the different displacements in terms of increasing frequency, it is apparent that as the frequency of operation is increased, the area of vibration within the transducer disperses in an annular nature toward the outer radius of the composite structure.

5.7.3 Modelled surface displacement characteristics

Using the model structure previously defined (Figure 5.30), the surface displacement of the conical composite structure was analysed for comparison with the experimental results. In this instance, the transducer was only modelled across a small frequency range, encompassing the extended electrical resonance of the device due to time constraints in the complex modelling of this composite device.

Figure 5.34 *Cross sectional comparisons between experimental and predicted composite behaviour*

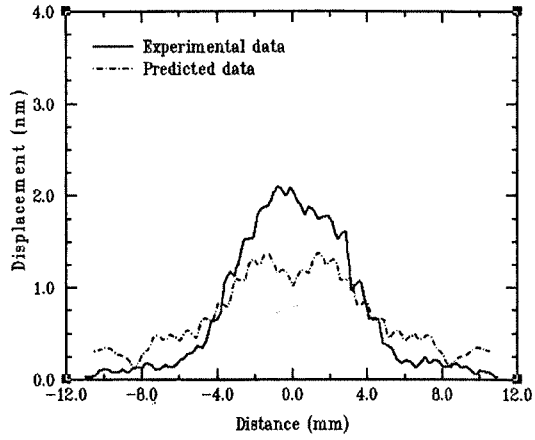

(a.) 560kHz

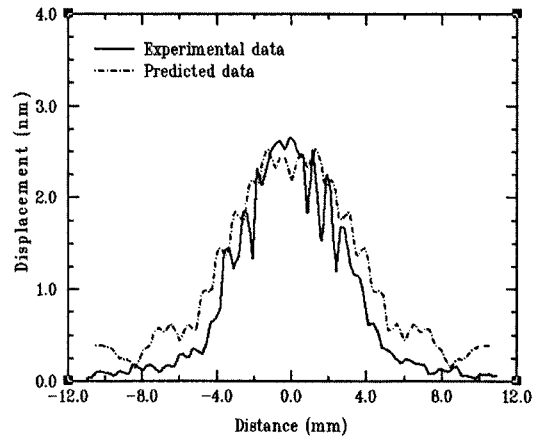

(b.) 580kHz

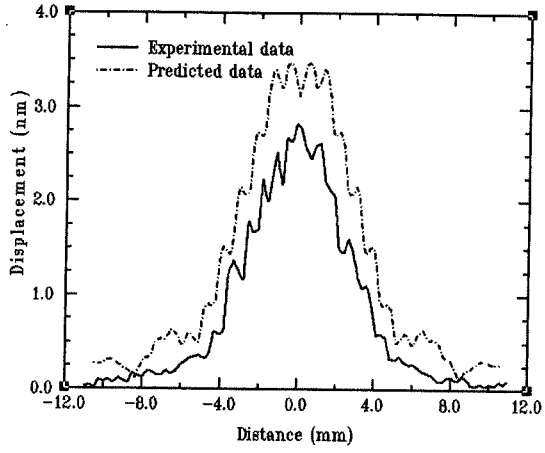

(c.) 600kHz

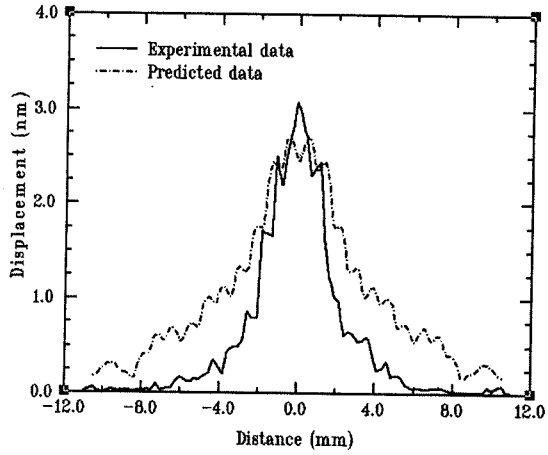

(d.) 620kHz

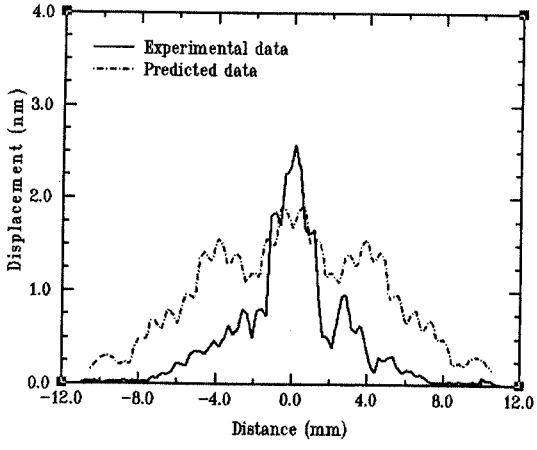

(e.) 640kHz

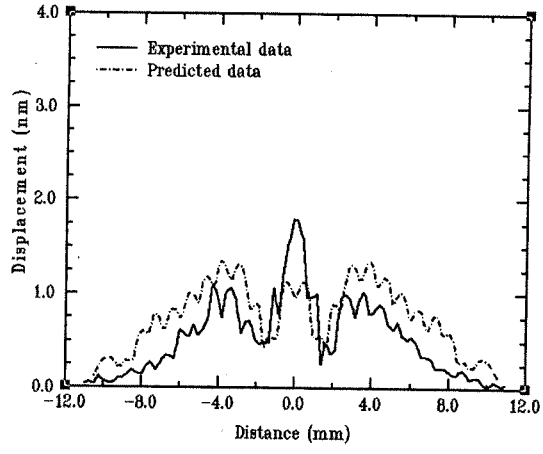

(f.) 660kHz

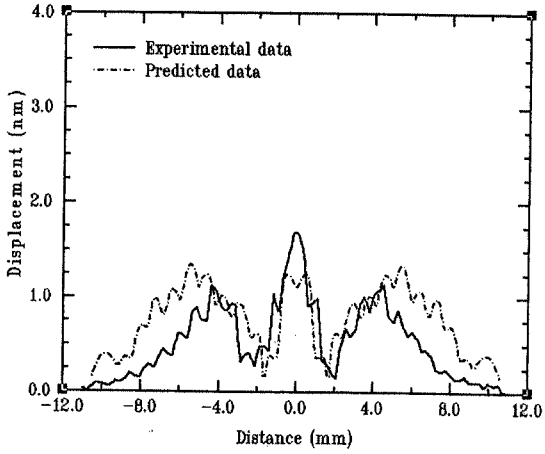

(g.) 680kHz

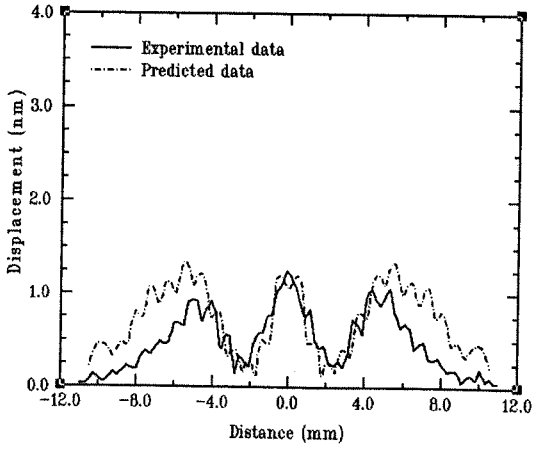

(h.) 700kHz

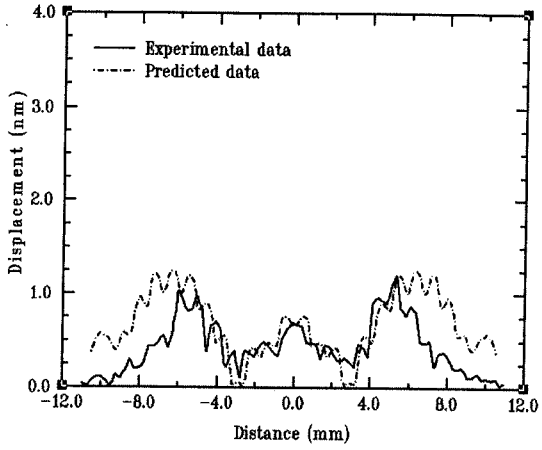

(i.) 720kHz

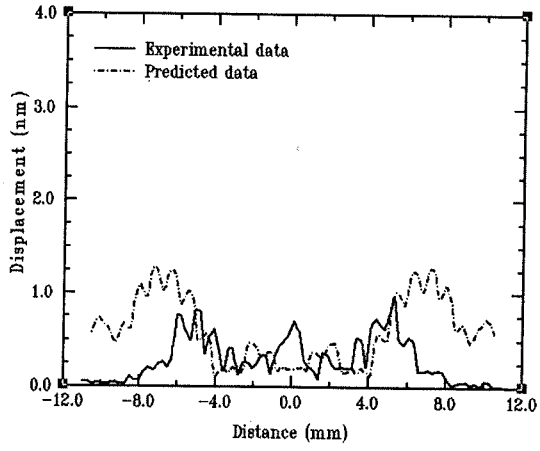

(j.) 740kHz

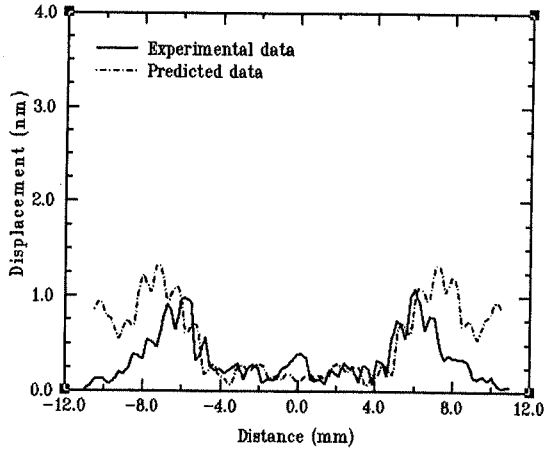

(k.) 760kHz

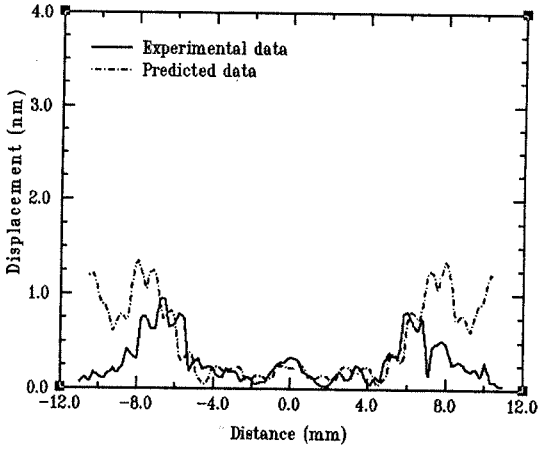

(l.) 780kHz

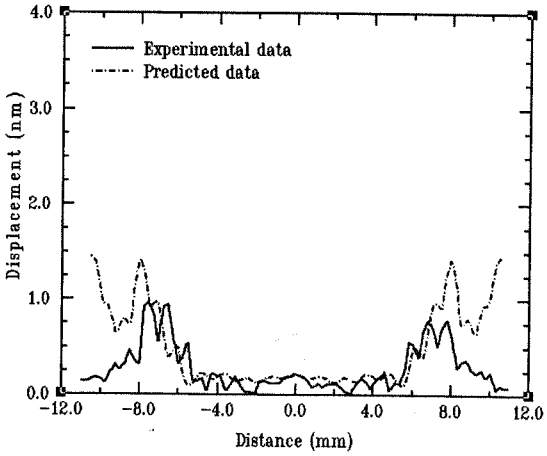

(m.) 800kHz

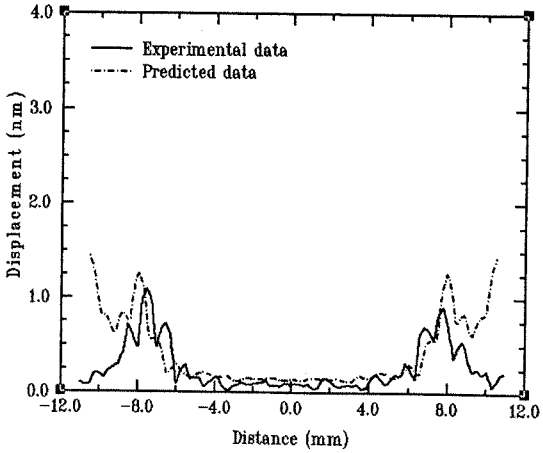

(n.) 820kHz

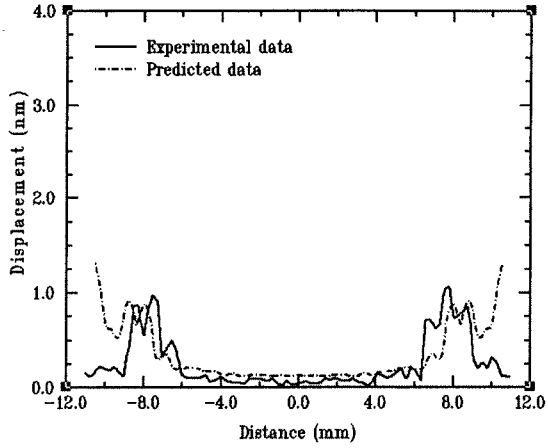

(o.) 840kHz

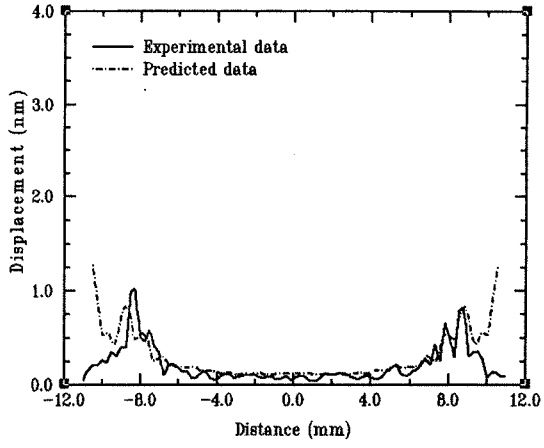

(p.) 860kHz

Figures 5.34(a.) to 5.34(p.) illustrate the good correlation in the cross sectional surface displacement of the conical composite planar surface. The modelled transducer exhibits similar characteristics to that determined experimentally, with the initial displacement at the centre from the lowest frequency spreading outwards to the outer radius as the frequency is increased. Note that cross sectional results were taken through the central axis of the conical transducer. From Figures 5.34(j-p) it can be seen that the model predicts a greater degree of the vibration at the outer diameter of the composite. This is due to the fact that the edges of the modelled composite are free to vibrate, whereas in the practice, the transducer was fitted in a casing in order to be scanned on the interferometer. Therefore, this casing will have acted to slightly damp the vibration in the outer circumference of the transducer.

By examining the experimental and predicted results at one of the midband frequencies, i.e. a frequency whereby the pillars under the ramped area are active, it is possible to evaluate the amount of frequency spreading into adjacent pillars. Consider the conical composite transducer at an intermediate frequency of 700kHz. Figure 5.35 illustrates the surface displacement determined by the laser interferometer and Figure 5.36 represents that generated by the finite element model.

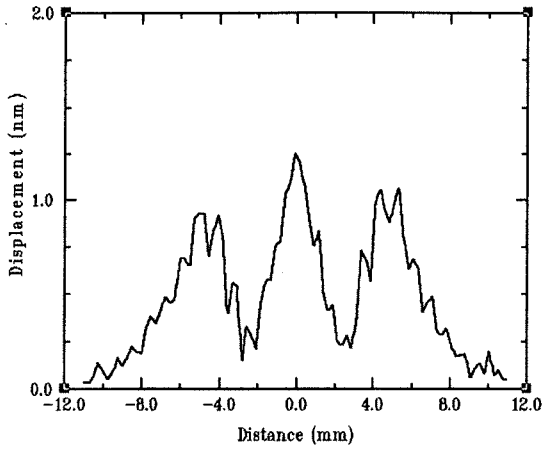

Figure 5.35 *Experimental displacement of conical composite at 700kHz*

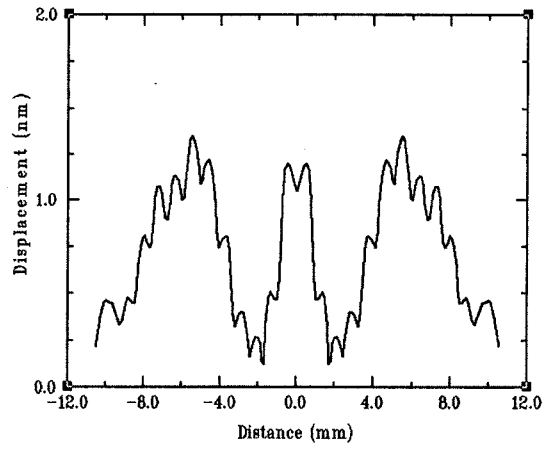

Figure 5.36 *Modelled displacement of conical composite at 620kHz*

By comparison of these two sets of results, it can be seen that the correlation between both measurement and prediction is good. Both exhibit the characteristic annular vibration, with a transferred sympathetic vibration in the adjacent pillar sections. By further examination of the cross sectional data, it can be seen that this propagated vibration to the surrounding media is almost Gaussian in its distribution, centring around the region of composite which is operating at thickness mode resonance. Interestingly, the cross sectional data shows a large magnitude of displacement in the centre of the transducer. This appears to be a width mode formed by the focussing of the annular vibration pattern, which when analysed through FEA animation appears to be a symmetrical wave front propagating in the radial direction. All of this information indicates clearly the accuracy possible through modelling of the composite and gives the designer a good degree of confidence in the FEA approach.

It is apparent throughout the surface displacement profiles that the conical devices do not exhibit any inter pillar mode resonances. For example, Figure 5.37 shows the device operating at a midband frequency, with an overall annular displacement. However, by examination of the plot it is apparent that each active ceramic pillar displacing by a greater degree than the surrounding polymer, with the adjacent pillars displacing with a lesser magnitude, but still more dominantly than the polymer matrix.

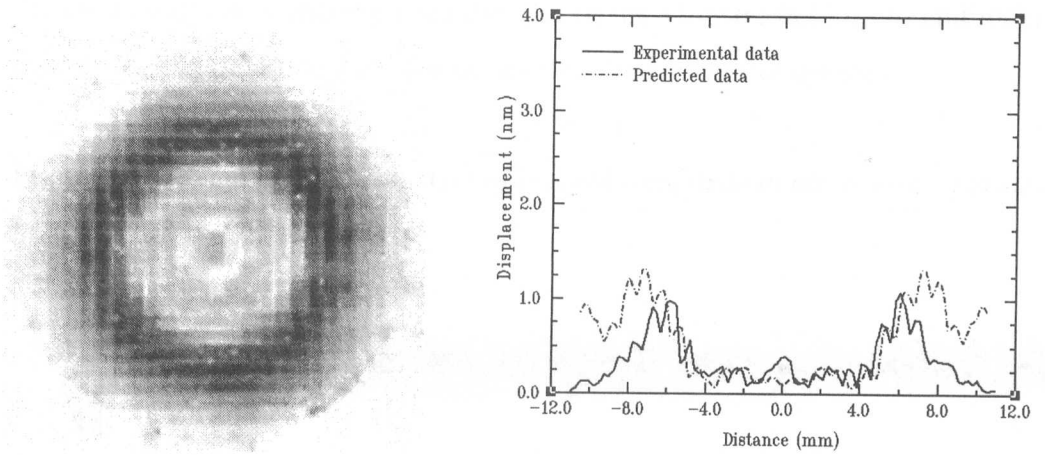

Figure 5.37 *Surface displacement profile and x-sectional profile at 760kHz*

This indicates that the each of the pillars within the device is operating more dominantly in a thickness mode direction. Considering the changing aspect ratio of the composite device, this is quite surprising as generally when the aspect ratio of composite is increased beyond 0.1 lateral modes are introduced into the structure. The reason for this lack of inter-pillar mode resonance, is that the non-uniform rear face of the composite transducer eliminates the periodicity of the pillar structure at a specific thickness. That is, the only abounding ceramic pillars within the transducer of the same thickness are in a radial direction, therefore standing waves cannot be formed between surrounding pillars. This means that the transducer will operate pre-dominantly in the thickness mode direction.

5.7.4 Acoustic beam profile analysis

Again, employing the extensive calibration facilities available within the research group in the University of Strathclyde, the pressure displacement beam profiles of the conical composite devices were evaluated in air. Using the 3-axis scanning facility coupled to a calibrated hydrophone, the conical composite was scanned across a range of frequencies through the central axis of the transducer, concentrating upon the radiated pressure response within the near field. All the scans presented illustrate the beam profile of the conical transducer from a range of 1mm to 60mm from the front face. This is the area is of most interest for the perceived mode of operation, namely the generation of asymmetrical Lamb waves within a test plate in close proximity to the scanning head.

This scanning range encompasses the area of the acoustic field up to and including the near-field / far-field boundary for most of the frequencies of operation.

Figure 5.38 *Beam profile responses of conical composite in air, across operation range*

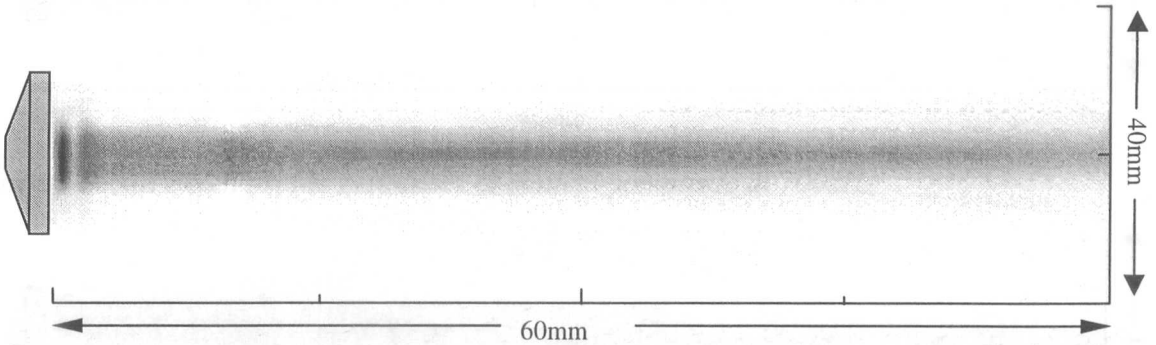

Figure 5.38(a.) *Beam profile responses of conical composite at 550kHz*

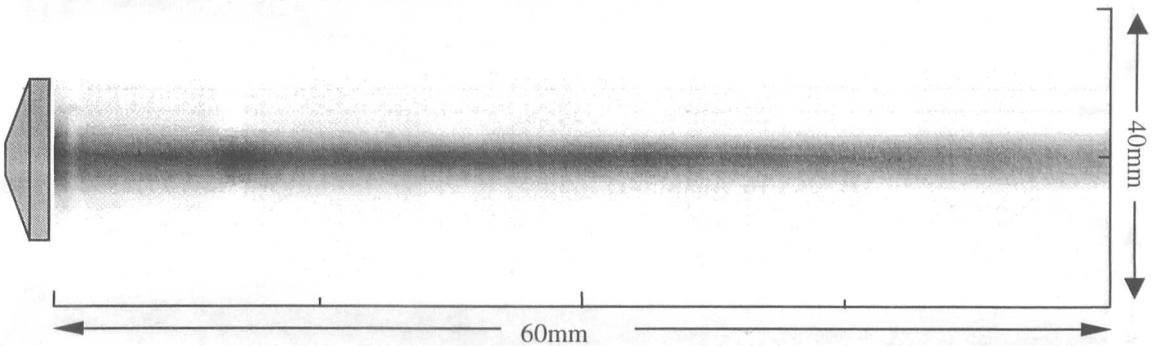

Figure 5.38(b.) *Beam profile responses of conical composite at 600kHz*

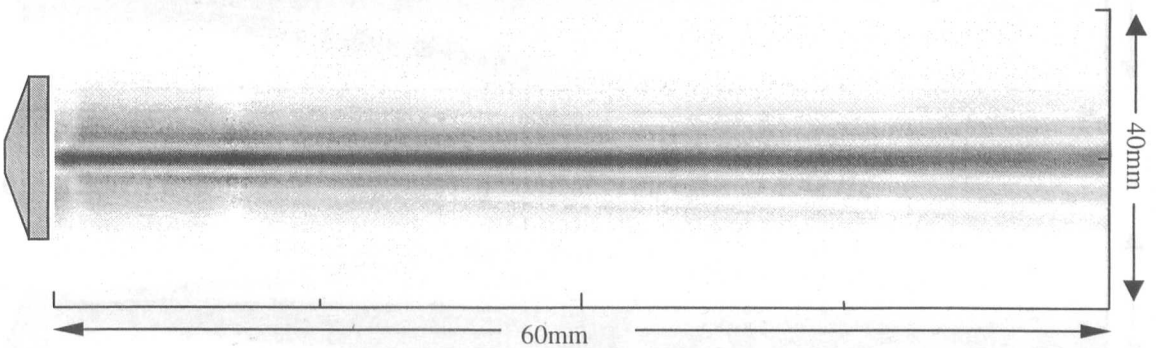

Figure 5.38(c.) *Beam profile responses of conical composite at 650kHz*

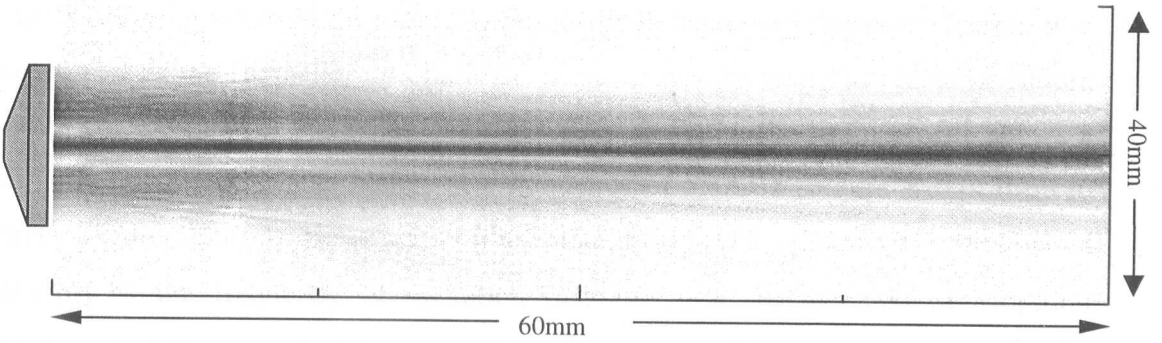

Figure 5.38(d.) *Beam profile responses of conical composite at 700kHz*

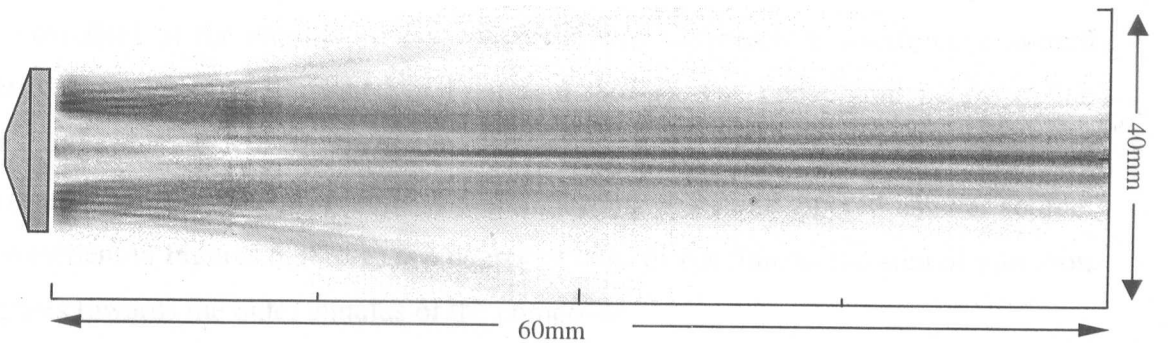

Figure 5.38(e.) *Beam profile responses of conical composite at 750kHz*

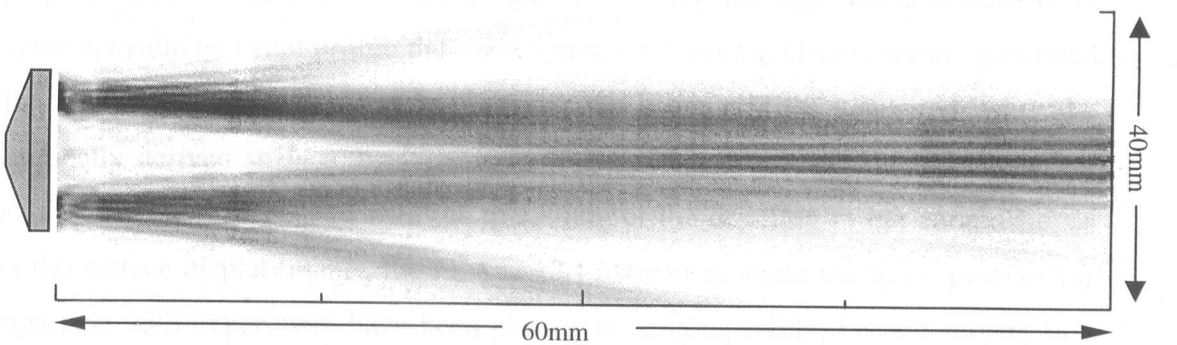

Figure 5.38(f.) *Beam profile responses of conical composite at 800kHz*

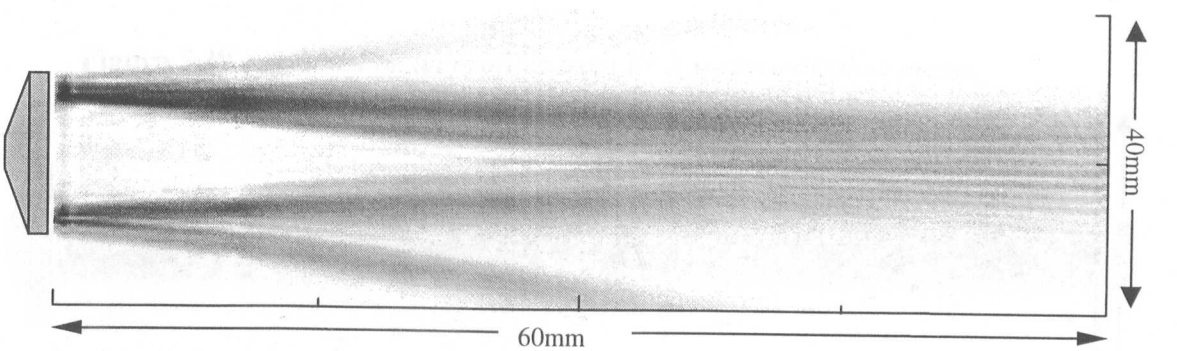

Figure 5.38(g.) *Beam profile responses of conical composite at 850kHz*

By examining the measured acoustic responses of the conical composite design, it is apparent that as the frequency of operation is increased, the acoustic radiation pattern becomes consistent with that of an annular source. Initially, the beam profile shows a good, almost coherent planar source at a frequency of 550kHz (Figure 5.38(a.)) up to 650kHz (Figure 5.38(c.)). However, as illustrated in the surface displacements (Figures 5.38(a–p)) as the frequency of operation increases, the surface area of vibration disperses annularly towards the outer radius of the composite device. This in turn will have a direct influence upon the radiated beam pattern, leading to a focussing effect in the near field as the annular source converges with constructive interference around approximately 35mm, illustrated in Figures 6.38(d-g). The convergent nature of the near-field radiation will be due to the distribution of the sympathetic vibration around the dominant pillar thickness mode vibration, leading to a more tapered annular source. Also evident in Figures 5.38(e-g) is a degree of edge diffraction, as the area of vibration migrates towards the outer annulus of the composite.

Implementing the theoretical beam profile prediction package [89], described in Chapter 4, synthetic beam profile data was generated from the displacements generated in the finite element model. Firstly, consider the beam profiles generated using the theoretically derived surface displacements, illustrated in Figures 5.39(a-g). Note that due to the problem associated with the modelling of the depoling in the composite, as with the surface displacements, the FEA results used to generate the beam profiles for comparison with experiment have been chosen to be comparable, i.e. are subject to a frequency decrement of 80kHz.

Figure 5.39 *Predicted beam profiles from FEA surface displacements*

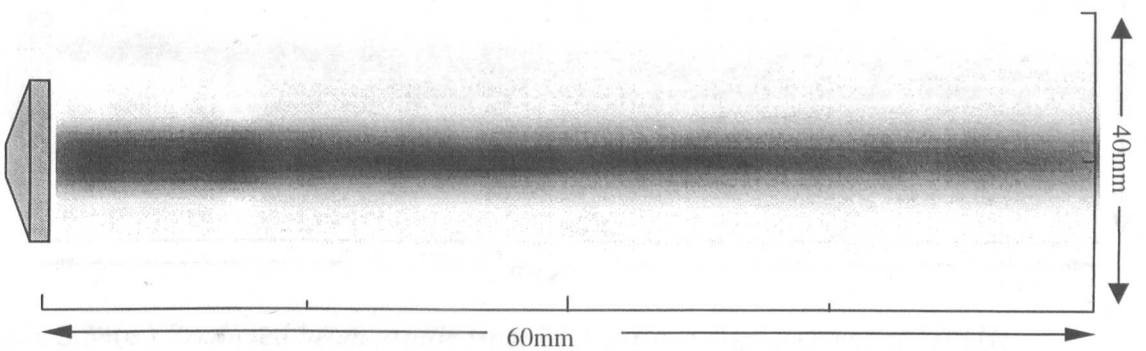

Figure 5.39(a.) *Predicted beam profile from FEA surface displacement at 470kHz*

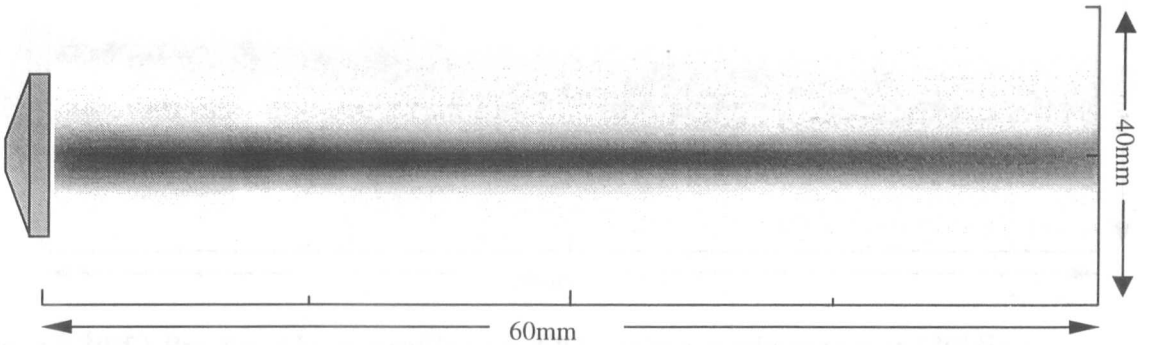

Figure 5.39(b.) *Predicted beam profile from FEA surface displacement at 520kHz*

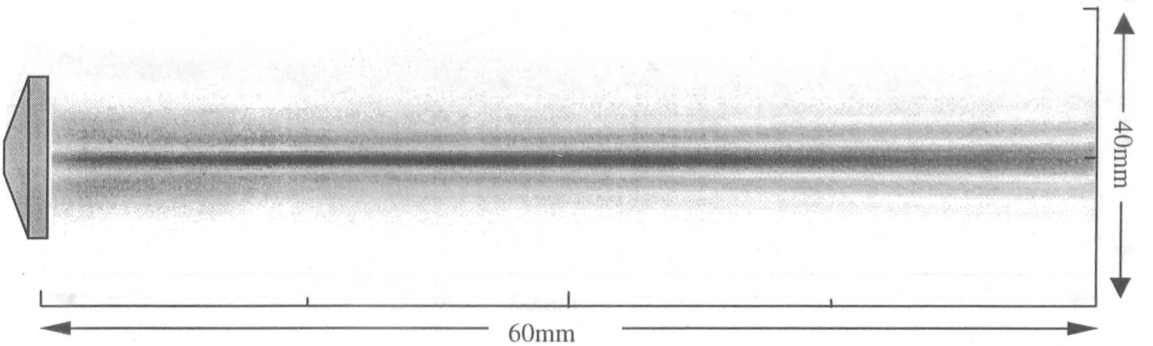

Figure 5.39(c.) *Predicted beam profile from FEA surface displacement at 570kHz*

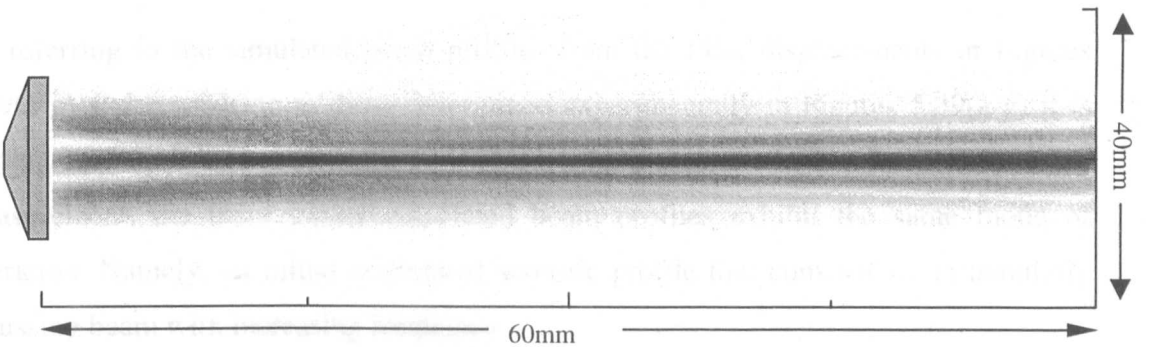

Figure 5.39(d.) *Predicted beam profile from FEA surface displacement at 620kHz*

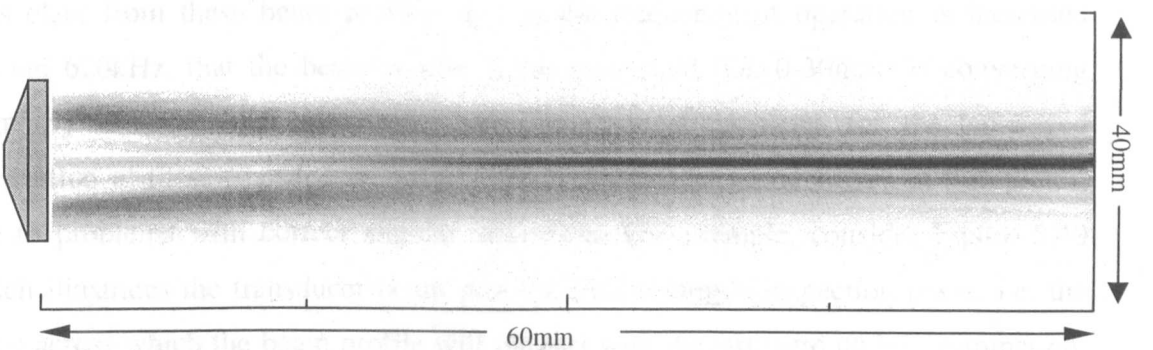

Figure 5.39(e.) *Predicted beam profile from FEA surface displacement at 670kHz*

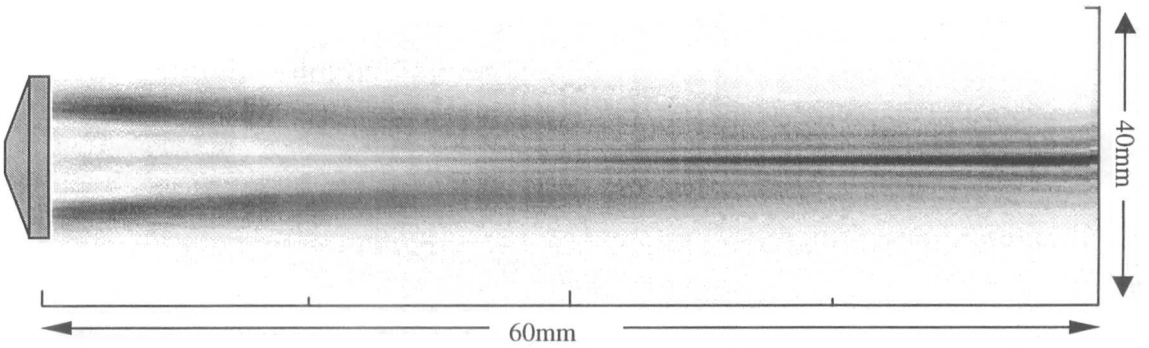

Figure 5.39(f.) *Predicted beam profile from FEA surface displacement at 720kHz*

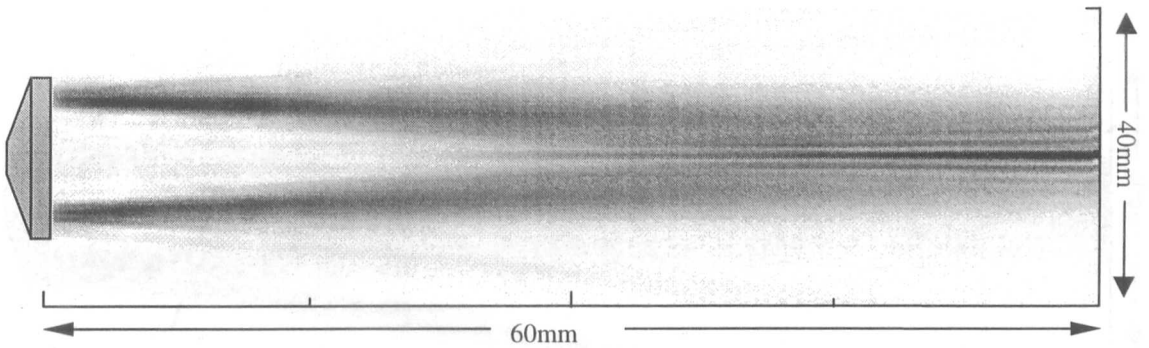

Figure 5.39(g.) *Predicted beam profile from FEA surface displacement at 770kHz*

By referring to the simulated beam profiles from the FEA displacements in Figures 5.39(a-g) and comparing to those determined experimentally in Figures 5.39(a-g) it is evident that there is good correlation between both sets of results. As illustrated by measurement, the theoretically calculated beam profiles exhibit the same mode of operation. Namely, an initial collimated acoustic profile that converts to an annularly focussing beam with increasing frequency.

It is clear from these beam profiles that as the frequency of operation is increased beyond 620kHz, that the beam profile in the near field (i.e. 0-30mm) is converging angularly towards the central axis. This may present problems for the envisaged application of these transducers, namely the generation of Lamb waves in thin plates, due to problems with correct angular alignment. For example, consider Figure 5.40 which illustrates the transducer beam profiles with a sample inspection plane, i.e. the plane across which the beam profile will interact with the structure under examination, for both the (a.) collimated and (b.) converging sources.

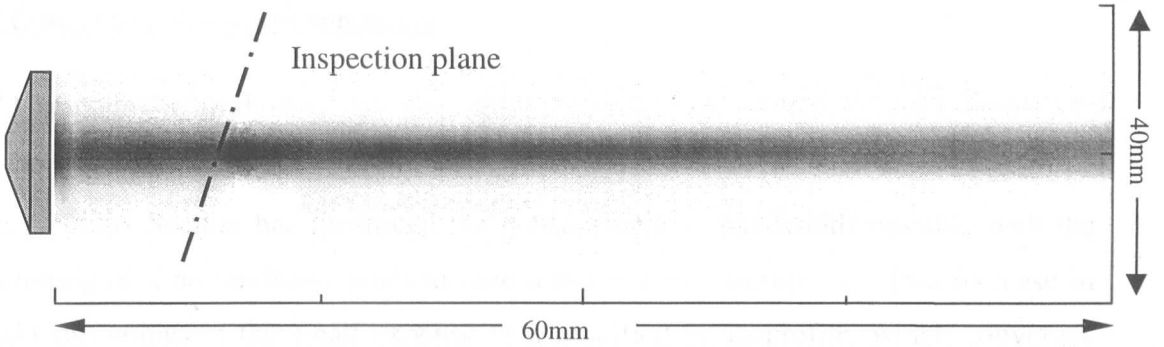

Figure 5.40(a.) *Intersection of inspection plane with transducer beam profile at 600kHz*

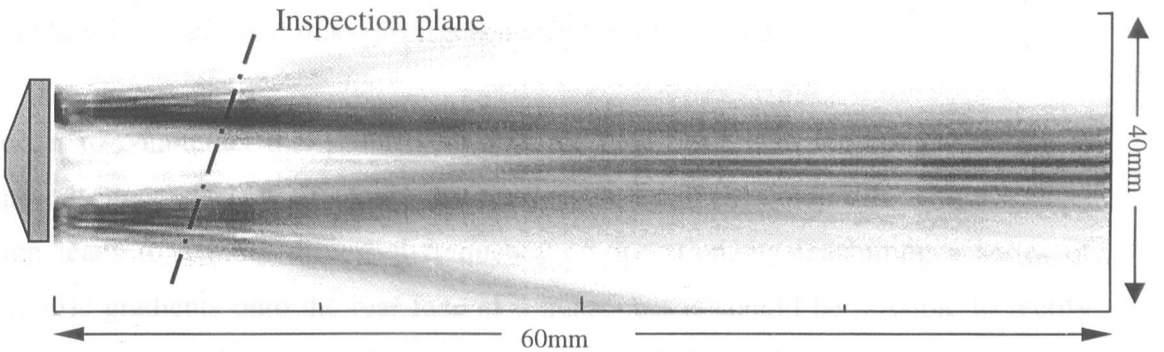

Figure 5.40(a.) *Intersection of inspection plane with transducer beam profile at 850kHz*

It is thus apparent that for a converging source, the area of inspection on the plate surface will be altered from that of the collimated beam, with the acoustic energy incident in an annular pattern around the initial area inspected by the focussed beam. Additionally, the slight angular offset of the incident beam on the scanning plane will lead to a slight reduction in the efficiency of generating the desired Lamb wave. While it is perceived that this should have a small influence on the efficient generation of the Lamb wave modes in the platelet structure, future work in this field should focus on the development of matching layers with acoustic gradients or convex geometry to counteract this problem.

Note however, if the inspection plane is moved further into the far field, for example 45mm, then the angular offset mentioned will not present such a problem as the acoustic field in this region is more collimated and focussed. However, for the current application of these transducers it is impractical to operate in this area of the field structure, as this would increase the separation of the transducers from the sample and hence the overall size of the scanning head.

5.8 Concentric Saw-tooth composite

5.8.1 Impedance analysis

The previous Section has illustrated the enhancement in bandwidth possible with the machining of a non-uniform gradient onto a circular piezocomposite. This increase in bandwidth comes at the small expense of a modified beam profile, which converges slightly towards the central axis of acoustic emission. While it is perceived that this beam convergence will not be overly detrimental in the proposed NDT application, it would be advantageous if this convergence could be eliminated.

In order to counteract this problem, a possible modification to the conical design is proposed. Since it has been shown that the machining of the composite with a conical design leads to a more dispersed frequency of operation, by machining a series of concentric gradients onto the rear face of a transducer is should be possible to rectify the annular nature of the conical composite to a more uniform displacement. It is hoped that by introducing a series of rings that the acoustic profile of the transducer will become more uniform in nature. Additionally, the transducer will exhibit similar enhanced bandwidth characteristics to that of the previously described conical composite.

A 60% volume fraction 1-3 connectivity composite comprising of PZT-5A ceramic and hard-set CY1300/1301 polymer was used to investigate the practicality of this form of design. As before, using a standard metal working lathe, a conical transducer to the dimensions described in Figure 5.41 was constructed.

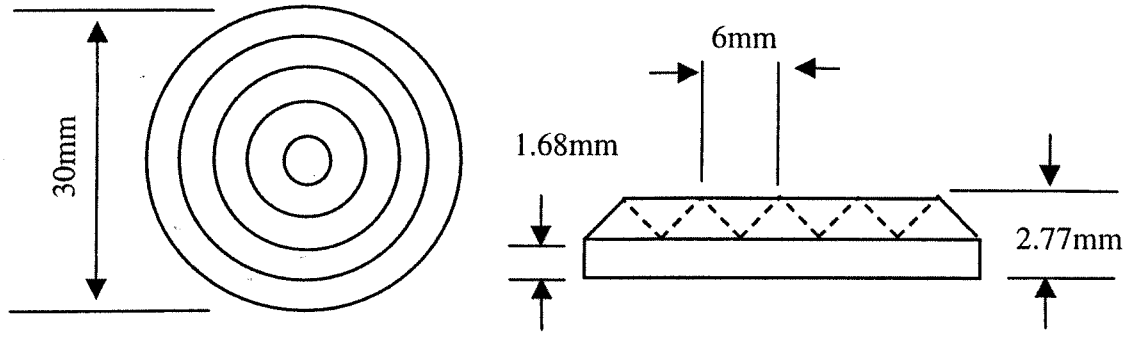

Figure 5.41 *Saw-tooth composite geometry*

The composite was then electroded with silver on both upper and lower surfaces and the impedance measured with the HP4194 impedance/gain-phase analyser. Figure 5.42 illustrates the impedance characteristics of the saw-tooth composite device.

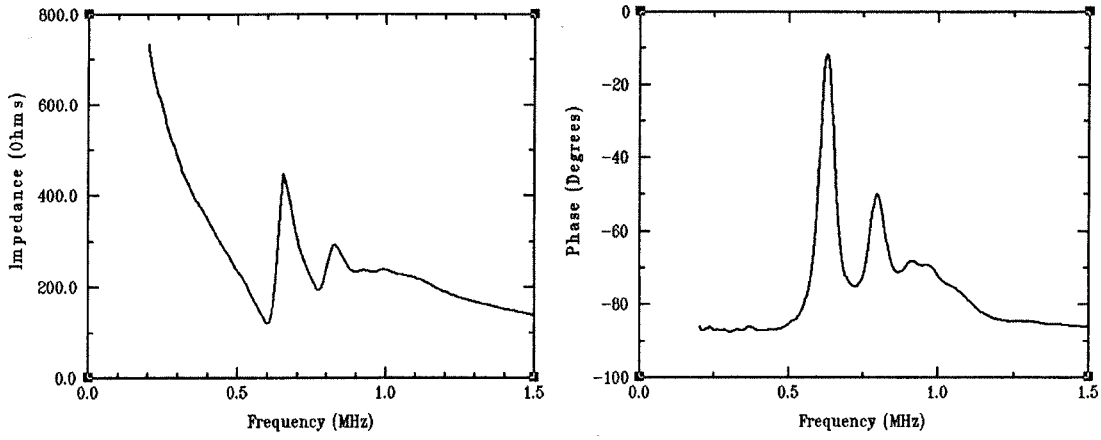

Figure 5.42 *Measured impedance of prototype saw-tooth composite transducer*

In this instance, the impedance characteristics of the new device are hard to distinguish. The two main modes in the composite will be due to the thinnest and thickest radial sections, which have the greatest overall surface area and hence will be dominant in the impedance response. However, due to the inability to model f_e accurately when there is depoling in the composite device, it can not be definitively concluded that the minima at 600kHz and 800kHz are related to these two thickness sections. Also, due to the structural geometry of the transducer it is not possible to electrically isolate these sections and determine the impedance characteristics of these thicknesses. Therefore, by inference it is assumed that the minimum at 600kHz is related to the radial thickness of 2.77mm and the 900kHz minimum to that of the 1.68mm section. The interference with the final frequency of mechanical resonance is associated with the imperfection of the circular nature of the transducer leading to a non-uniform outer diameter thickness, as previously with the conical transducer.

As before, a 3D FE model of the aforementioned composite structure was developed and is illustrated in Figure 5.43. This model was constructed as an $1/8^{th}$ symmetry model to reduce the computational solving time required to generate the transducer characteristics.

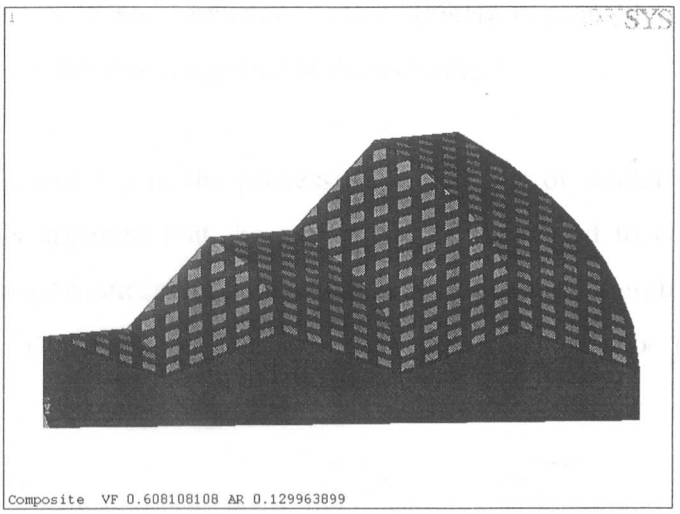

Figure 5.43 *Volumetric representation of saw-tooth FE model geometry*

It was found that the complex geometry of this modelled transducer increased the processing time required to generate the impedance characteristics of this composite, even the most modest frequency resolution possible required many weeks. Therefore 2D modelling was utilised to examine the theoretically predicted results, as with the conical composite this will only result in an approximation, due to the inability to model circular geometries in 2D. Figure 5.44 illustrates the comparison between the experimental and simulated impedance responses.

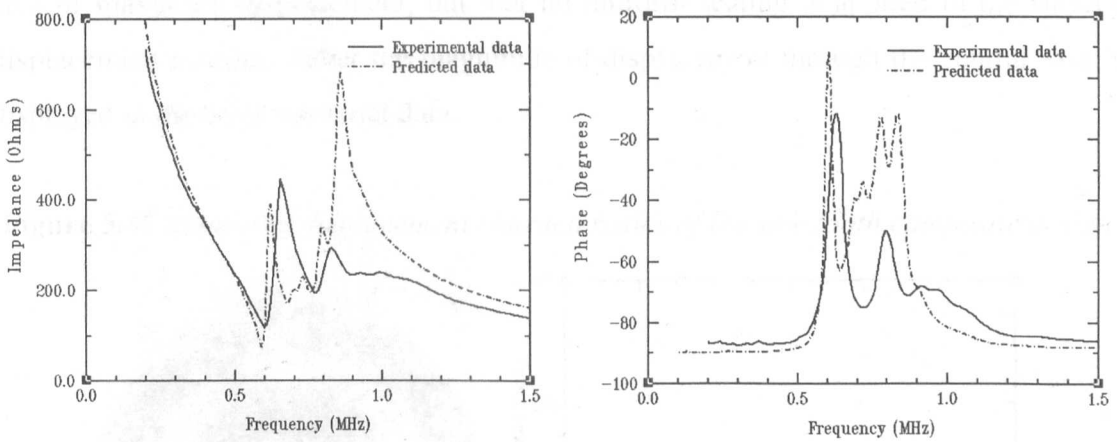

Figure 5.44 *Comparison in experimental and FEA data for saw-tooth composite*

From this analysis, it is apparent that there are considerable discrepancies between the experimental and predicted data, although both have minima at the two previously distinguished electrical resonance frequencies. As postulated also, it appears that the

lack of a dominant mechanical resonance after 800kHz is probably due to the lack of uniform thickness on the outer diameter of the transducer.

From these results and due to the processing restrictions of modelling the saw-tooth design in 3D, it is apparent that the use of the FEA method to compare modes of displacement in the transducer is not practical in this example. Therefore, the remaining analysis of this design of composite will be restricted to purely measured characterisation.

5.8.2 Surface displacement characteristics of saw-tooth composite design

Once again, the laser interferometer was employed to determine the surface displacement profile of the saw-tooth composite design across a frequency range. All operating parameters are identical to those previously described for the interrogation of the preceding composite transducers. For the sake of brevity, the frequency range has been restricted between the two dominant frequencies of electrical resonance and both the surface displacement profiles and the cross sectional magnitude information are presented concurrently in Figures 5.45(a-m). Note that the darker region signifies the area of maximum displacement, but that no uniform scaling is applied to the surface displacement profiles, rather the magnitude of displacement through the central axis is displayed in the cross sectional data.

Figure 5.45 *Measured displacement characteristics of the saw-tooth composite design*

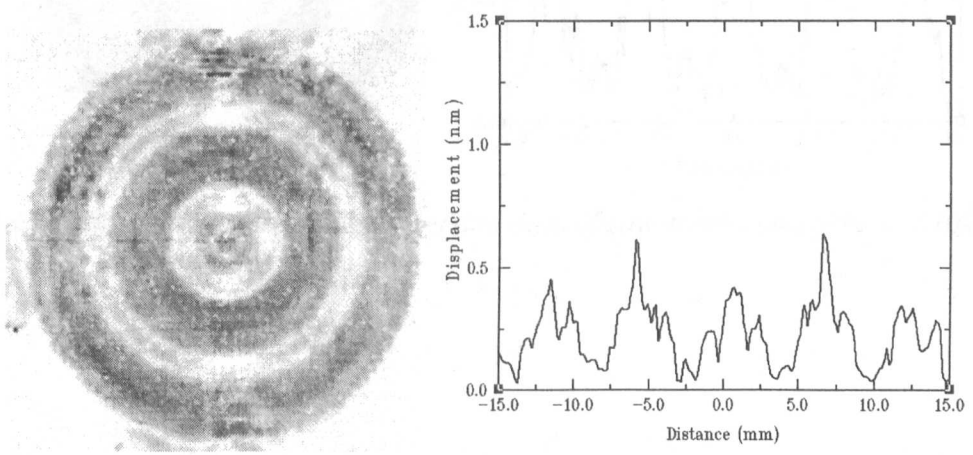

(a.) Surface displacement and x-section data of saw-tooth composite at 560kHz

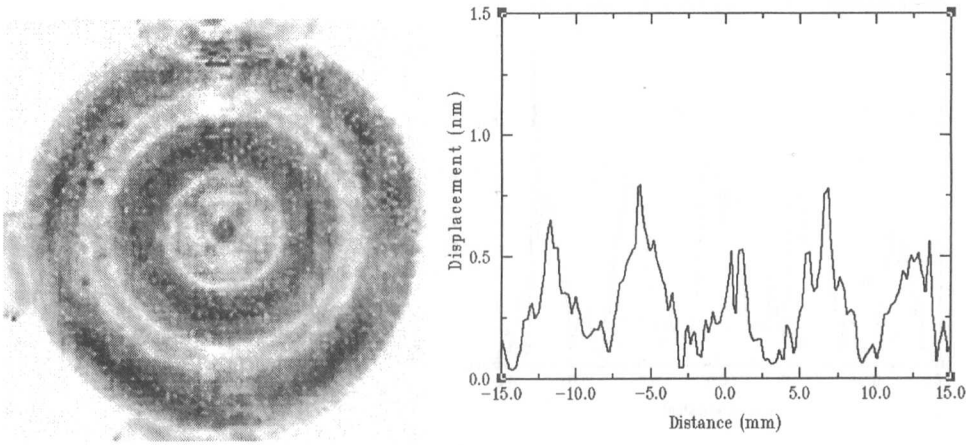

(b.) Surface displacement and x-section data of saw-tooth composite at 580kHz

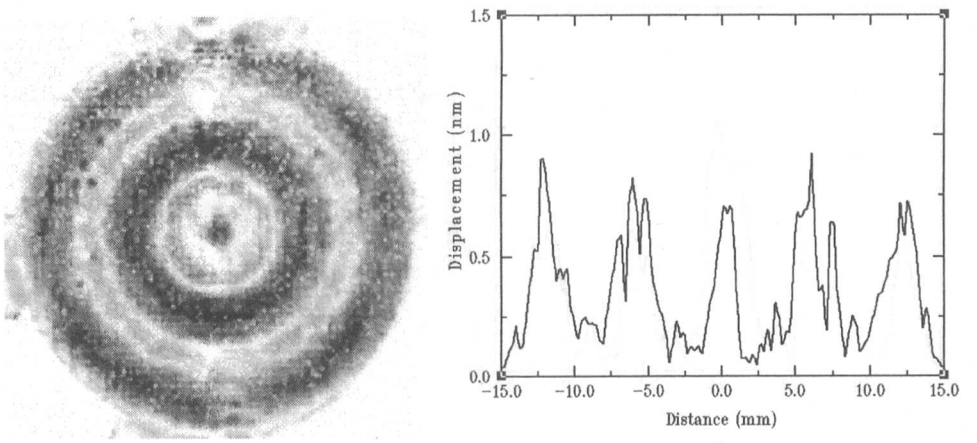

(c.) Surface displacement and x-section data of saw-tooth composite at 600kHz

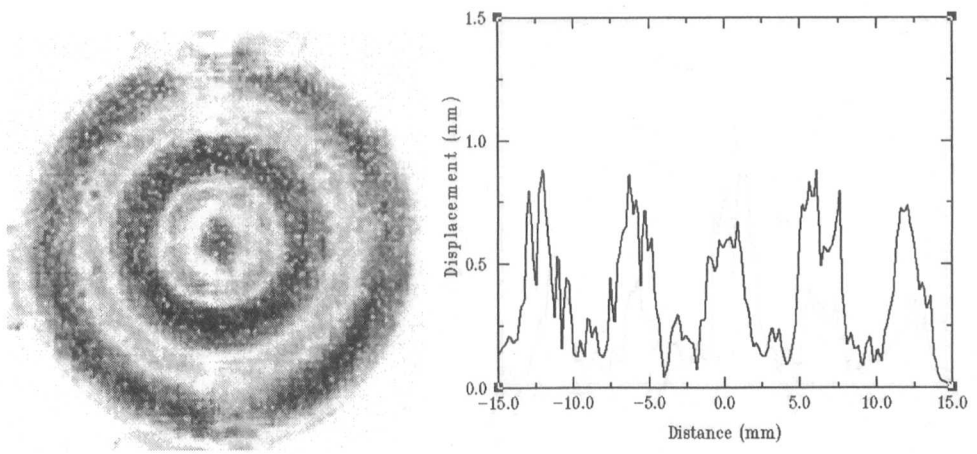

(d.) Surface displacement and x-section data of saw-tooth composite at 620kHz

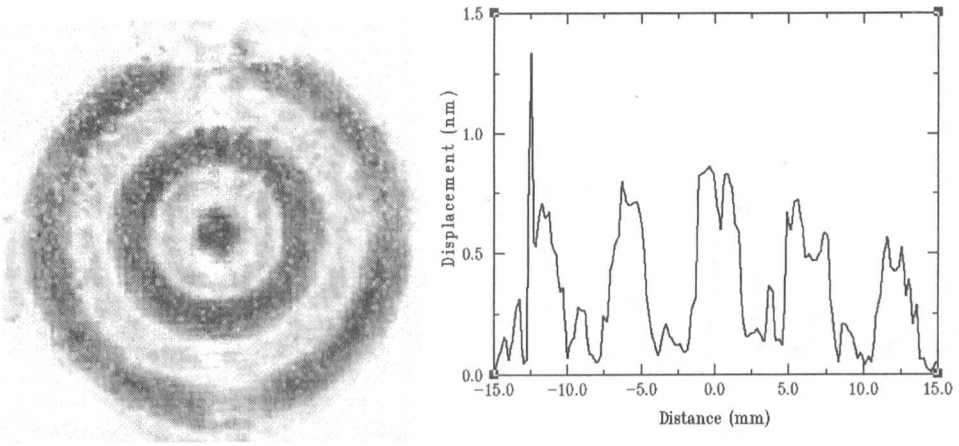

(e.) Surface displacement and x-section data of saw-tooth composite at 640kHz

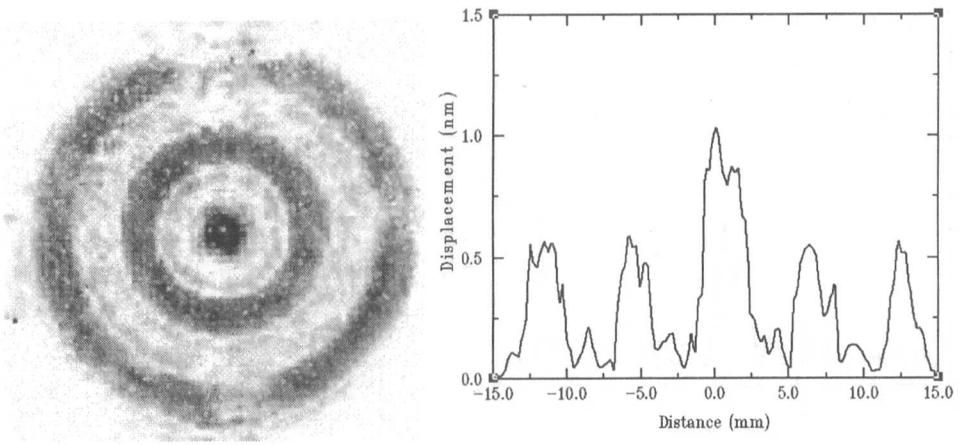

(f.) Surface displacement and x-section data of saw-tooth composite at 660kHz

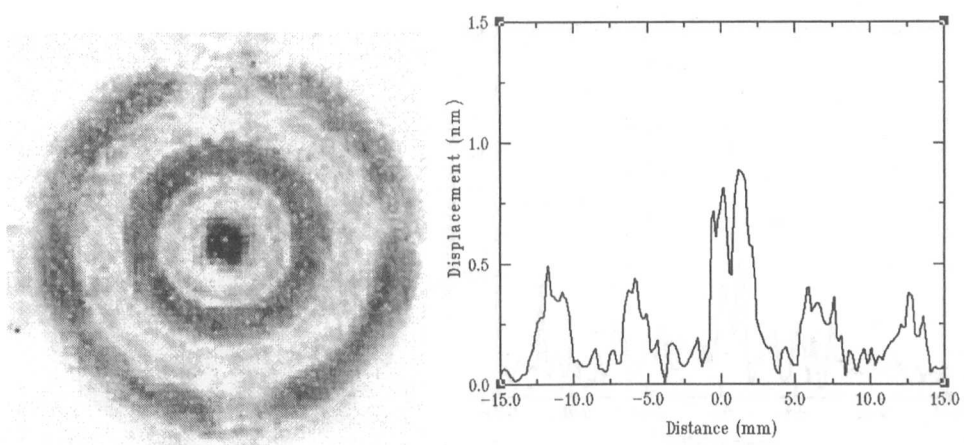

(g.) Surface displacement and x-section data of saw-tooth composite at 680kHz

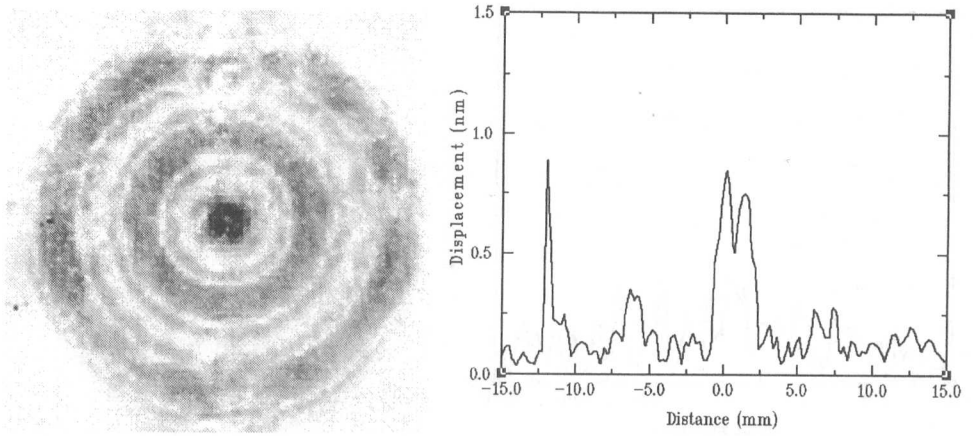

(h.) Surface displacement and x-section data of saw-tooth composite at 700kHz

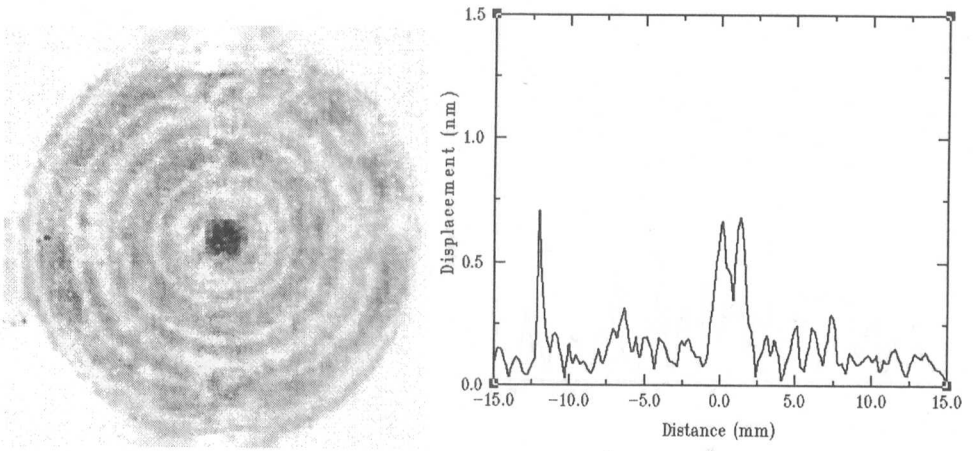

(i.) Surface displacement and x-section data of saw-tooth composite at 720kHz

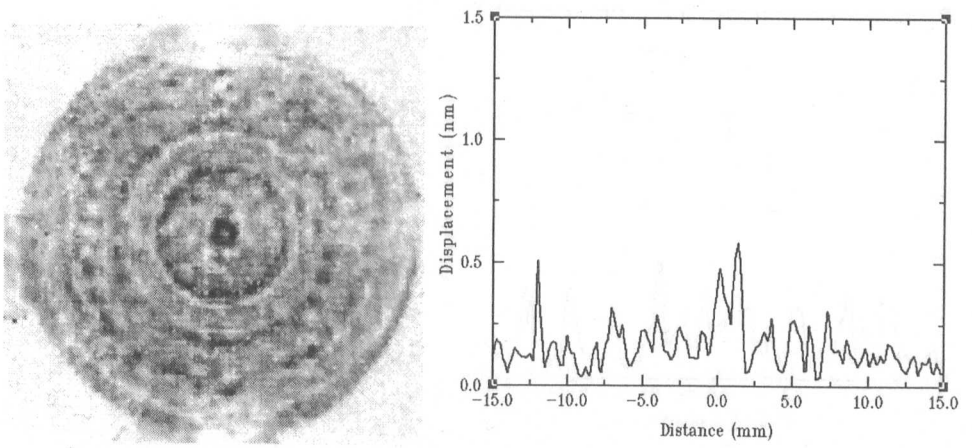

(j.) Surface displacement and x-section data of saw-tooth composite at 740kHz

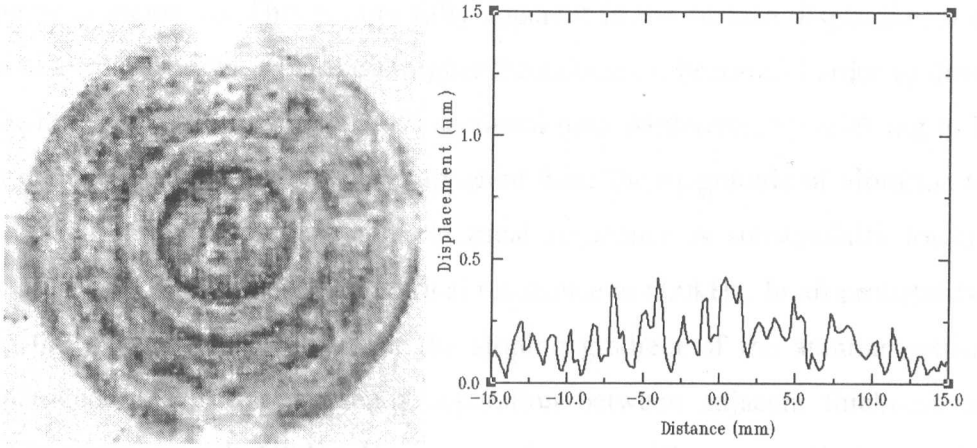

(k.) Surface displacement and x-section data of saw-tooth composite at 760kHz

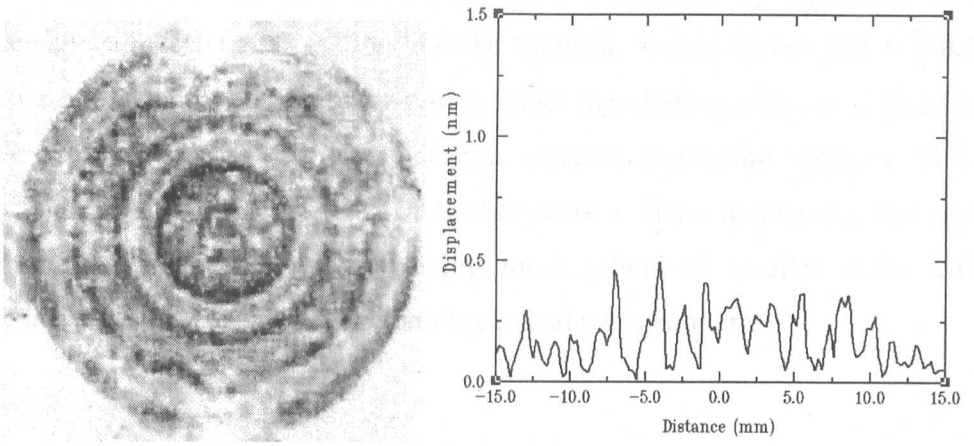

(l.) Surface displacement and x-section data of saw-tooth composite at 780kHz

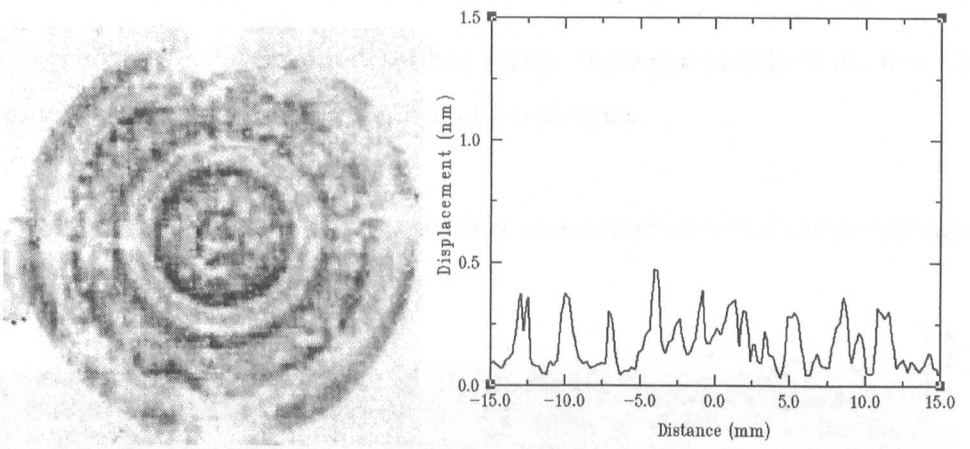

(m.) Surface displacement and x-section data of saw-tooth composite at 800kHz

Consequently by examination of the results presented in Figure 5.45, it can be that the introduction of additional annular sections of sloping composite leads to further annular displacement in the transducer. The displacement characteristics are such that the vibration spreads annularly from the thicker sections to the thinner radial sections as the

frequency is increased. This is only fully apparent in the surface displacement profiles of the saw-tooth design, as at these higher frequencies it becomes harder to distinguish the displacing sections from the cross sectional data. Moreover, by referring to Figures 5.45(a-c) and Figures 5.45(k-m) it is apparent there the magnitude of vibration towards the second dominant frequency of electrical resonance is substantially lower (by a factor of 2) than that of the first electrical resonance at 600kHz. In all probability this is due to the number of pillars under the sloping gradient of the annular sections. As demonstrated earlier, the frequency separation between adjacent thickness sections should be approximately 60kHz. However in the case of the saw-tooth design, the angle of machining on the rear face means that there is a frequency separation of 200kHz between the thickest radial section and the thinnest, spread across just 6 pillars. It is therefore likely that the number of pillars under the sloping sections is insufficient to support strong coupling vibration between adjacent displacing sections. In order to rectify this problem, it proposed that further work is done to increase the number of pillars under the gradient by producing more pillars of smaller scale within the composite, for machining of more complex transducer geometries.

5.8.3 Acoustic beam profile analysis of saw-tooth composite design

Using the calibration equipment described earlier, the beam profile of the new design of composite was investigated over a range of frequencies.

Figure 5.46 *Beam profiles of new composite transducer across a range of frequencies*

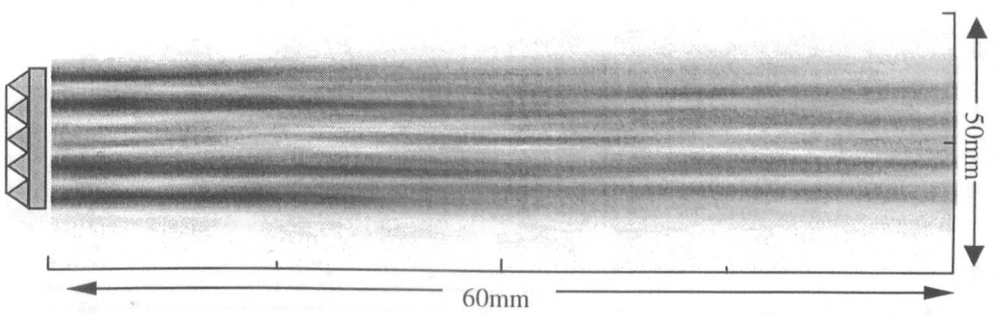

(a.) Beam profile of saw-tooth composite at 580kHz

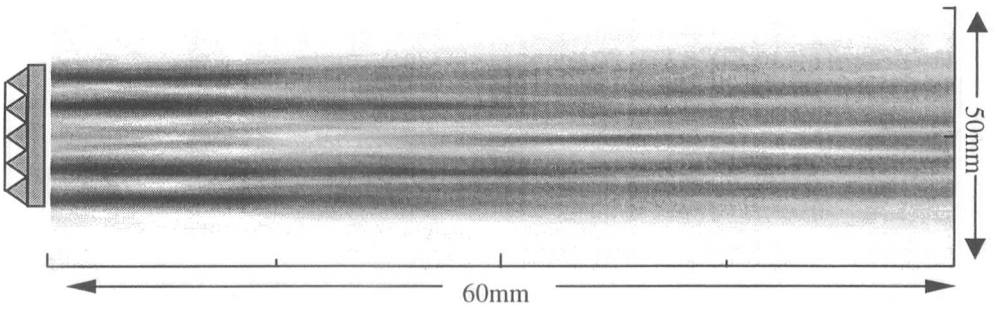

(b.) Beam profile of saw-tooth composite at 600kHz

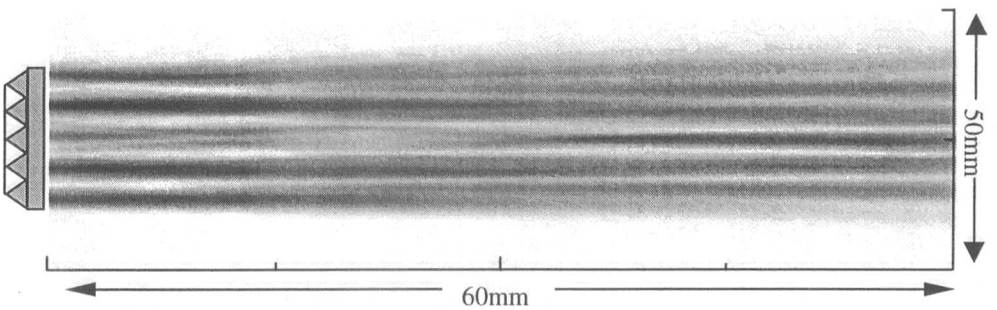

(c.) Beam profile of saw-tooth composite at 620kHz

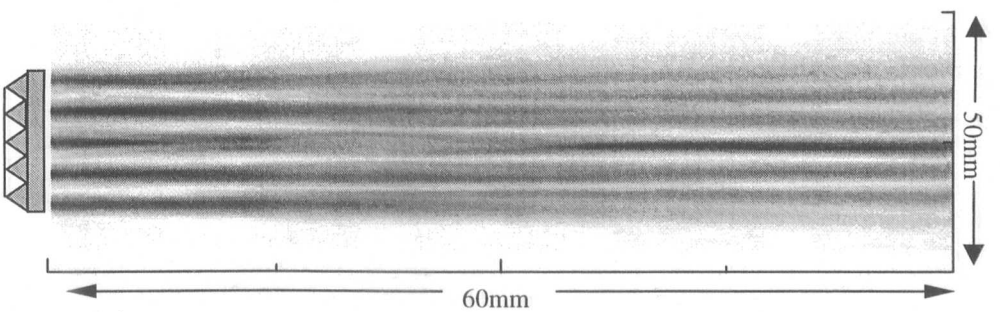

(d.) Beam profile of saw-tooth composite at 640kHz

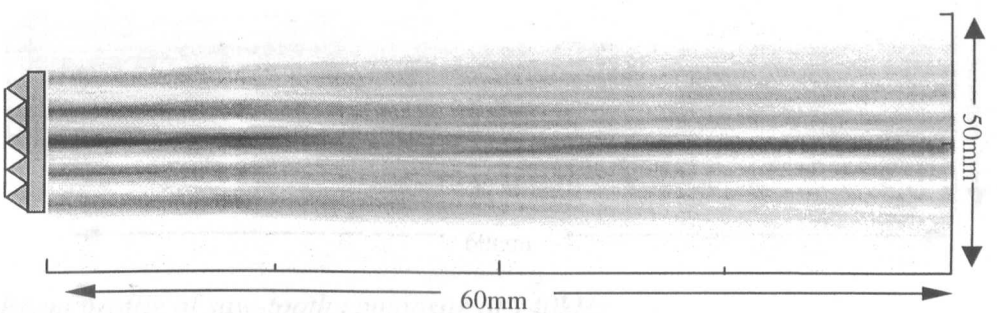

(e.) Beam profile of saw-tooth composite at 660kHz

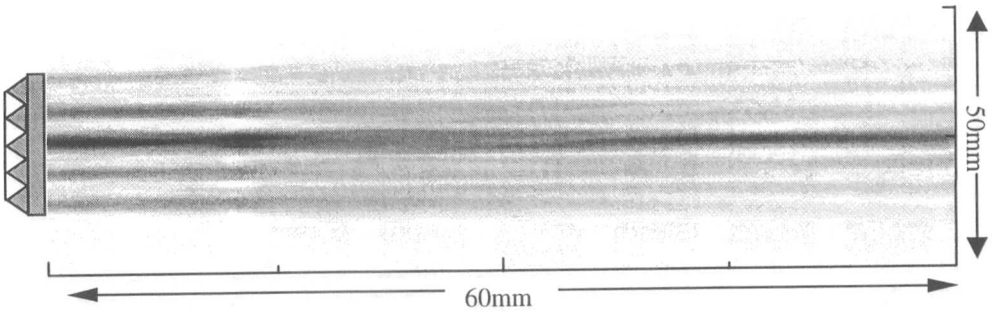

(f.) Beam profile of saw-tooth composite at 680kHz

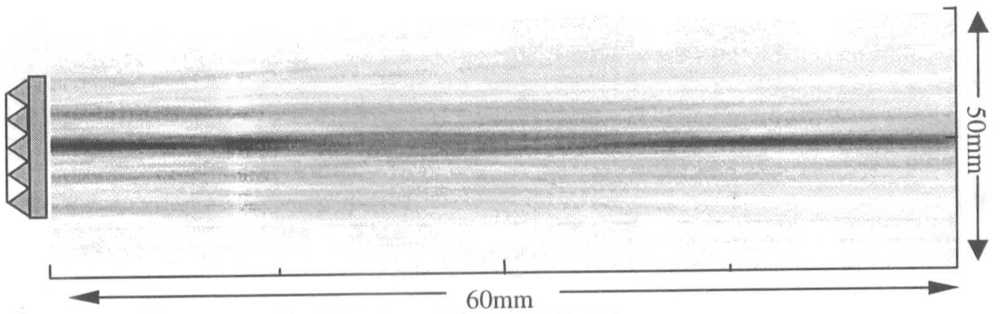

(g.) Beam profile of saw-tooth composite at 700kHz

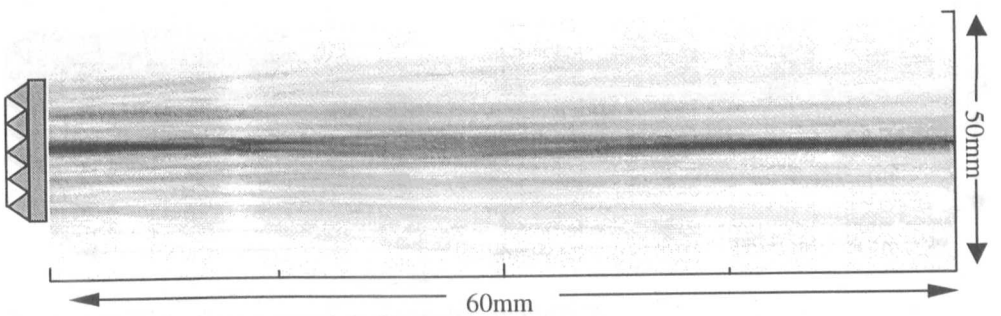

(h.) Beam profile of saw-tooth composite at 720kHz

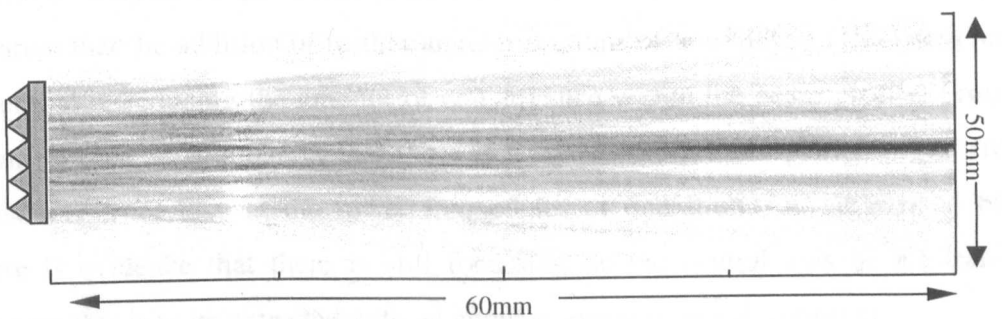

(i.) Beam profile of saw-tooth composite at 740kHz

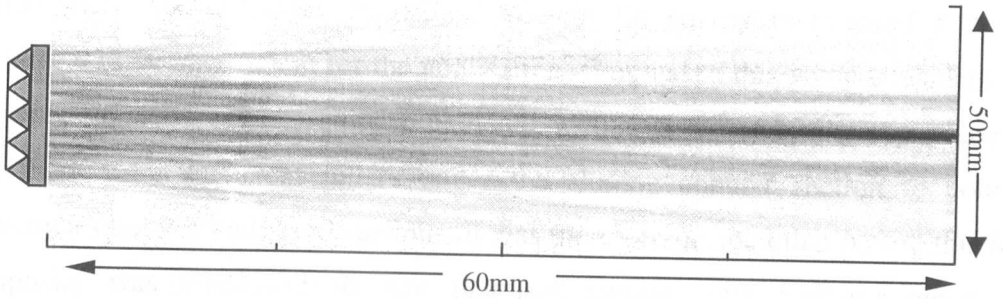

(j.) Beam profile of saw-tooth composite at 760kHz

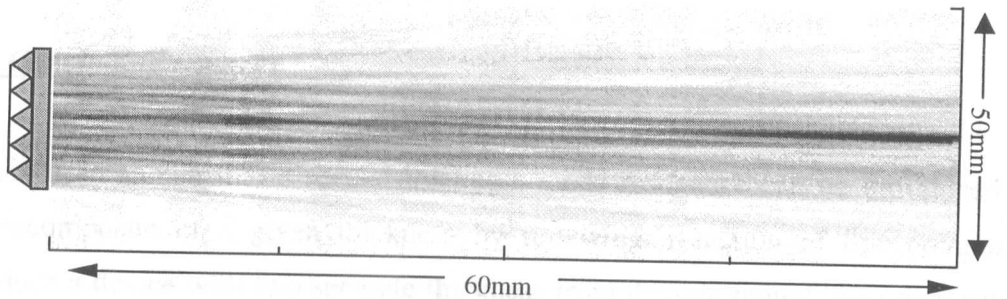

(k.) Beam profile of saw-tooth composite at 780kHz

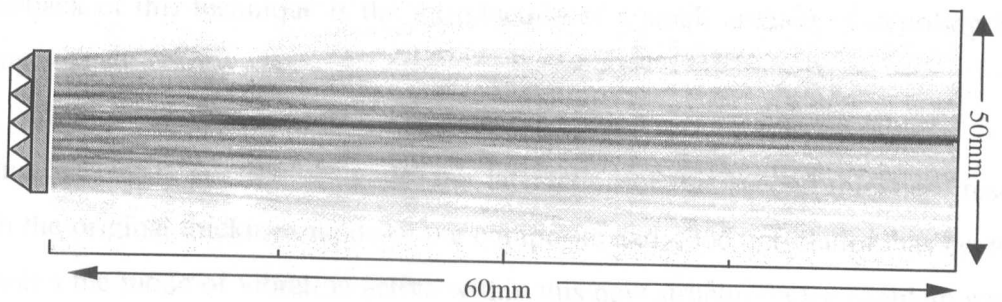

(l.) Beam profile of saw-tooth composite at 800kHz

Through analysis of the beam profile characteristics of this composite design, it is apparent that the addition of further annular sections of non-uniform thickness has been beneficial in reducing the amount of convergence within the beam profile. From these beam profiles, it is apparent that there is a considerably more planar output from the transducer front face at the lower frequencies of operation, i.e. 580kHz to 660kHz. There is evidence that there is still focussing on the central axis of the transducer, however this is to be expected with an annular source of any description.

While the beam profile characteristics exhibited by this composite appear to be ideal for the proposed application in Lamb wave generation, the overall magnitude of

displacement and therefore the extent of acoustic energy propagated into the air medium will be insufficient for the application. Coupled to this is the considerable size that the composite would require to be made, with present machining capabilities, such that there were sufficient pillars under the sloping annular section to couple the frequencies between adjacent sections. It was therefore decided that before this form of composite was employed in any practical system, that further comprehensive investigation would be required.

5.9 Concluding remarks

It has been shown that a second thickness mode resonance can be introduced into a piezocomposite of a given thickness by removing a section of this composite, to produce a device with two separate thickness from the one monolithic composite. This can be facilitated though simple machining techniques such as milling or grinding, whereas previously it was thought that it was impractical to machine piezoceramic. One drawback of this technique is the introduction of a small amount of depoling into the composite structure.

Using FEA, it is possible to model the interaction of this second thickness resonance with the original thickness mode of the composite and good correlation has been found between the mode of vibration active within this new structure. One problem still to be addressed within the analytical method, is the implementation of a mathematical depoling factor to simulate the loss in electromechanical coupling coefficient in any composite. The inability of the FE model to predict this depoling effect leads to confusion in the results presented, however, the multi-frequency concept and the mode of vibration is supported by the presented theory.

Further to this, subsequent results have been presented illustrating the influence of additional thickness steps to the composite design and initial recommendations made as to frequency separation between thickness steps to ensure generation, or not, of sympathetic vibration in adjacent thickness sections. The suggested frequency separation for sympathetic vibration transfer between sections being 60kHz and over 140kHz for reasonable isolation between steps.

From this analysis, the possibility of further more complex was discovered and subsequently investigated. While the saw-tooth design, described in the preceding section, does appear to offer a more uniform beam profile, it was decided to utilise the conical transducer design for incorporation into the proposed scanning system. This transducer configuration has shown good correlation with the computed FEA data and has a wider bandwidth than that currently associated with unbacked piezocomposites, 300kHz in comparison to 30kHz of standard single thickness composites.

The beauty of this form of transducer design, is the almost infinite number of structural iterations possible to the designer. The geometrical machining of the transducer structure allows the designer to tailor the properties of the piezocomposites to their needs. For example, dual thickness transducers for generation and detection of ultrasound a two discrete frequencies, thereby reducing the need for two separate composites, one for each frequency. Alternatively, shaped composites can reduce the need for matching layers to focus the acoustic beam, as illustrated in the conical composite example. The only obstacle with this form of transducer design is the current composite manufacturing capabilities using the standard 'dice and fill' technique. As mentioned previously, it is advantageous to have as many pillars as possible under the angular gradient of the composite in order to transfer vibration between adjacent thicknesses. This requires numerous small tightly spaced ceramic pillars to be cut from the original ceramic block and this requires a thin saw blade. However, the smaller the saw blade width, the smaller the blade depth (in order to prevent oscillation in the blade). Currently, the smallest available blade is 25-30μm wide, which is capable of cutting to a depth of 0.5mm. This effectively restricts the manufacture of composites to transducers operating around 3-4MHz, which is considerably out-with the scope this investigation and the perceived Lamb wave scanner application.

Chapter 6

Performance of the new Lamb wave scanner

6.1 Introduction

The earlier Chapters of the Thesis have presented the theoretical possibility of using a swept frequency approach to inspect planar samples of differing thickness without the need to alter the transducer angular alignment. Subsequent research has detailed the design of specialised transducers and electronics to facilitate this mode of inspection. This Chapter firstly demonstrates the proof of concept, for frequency agility, utilising wideband electrostatic devices to generate and receive Lamb waves in plates of differing thickness and detection of defects in said plates. Secondly, in order to improve the robustness of the scanner design, results are presented employing the novel wideband piezocomposite transducers incorporated within the scanning assembly.

6.2 Proof of concept

Although theoretically feasible, altering the frequency to tune air-coupled Lamb waves into differing thicknesses of plates without angle manipulation has never been implemented. In order to verify the concept, it was decided to utilise the wide bandwidth available through electrostatic transducer technology. As previously stated, such transducers may be problematic for application within an industrial environment, but they are more than sufficient for operation under controlled laboratory conditions.

6.2.1 Electrostatic transducers

One form of electrostatic transducer consists of an electrically conductive backplate across which a thin dielectric membrane is stretched. This membrane has a conductive metallised film coated on the exterior surface, i.e. the surface opposite the backplate, hence sandwiching the dielectric and forming a capacitor. An external bias is then applied across the two electrodes, pulling the membrane down on the backplate, via electrostatic forces resulting in small air pockets being trapped between the film and the backplate. It is these small pockets of compressed air that produce oscillation in the membrane when an alternating signal is applied to the electrodes, or alternatively when an acoustic wave is incident on the front surface. These small pockets of air also provide the wide bandwidth characteristics of the electrostatic, since the surface finish

on the backplate governs the size and distribution of the air bubbles captured between the backplate and the membrane film, which in turn defines the resonant frequency of the transducer [64].

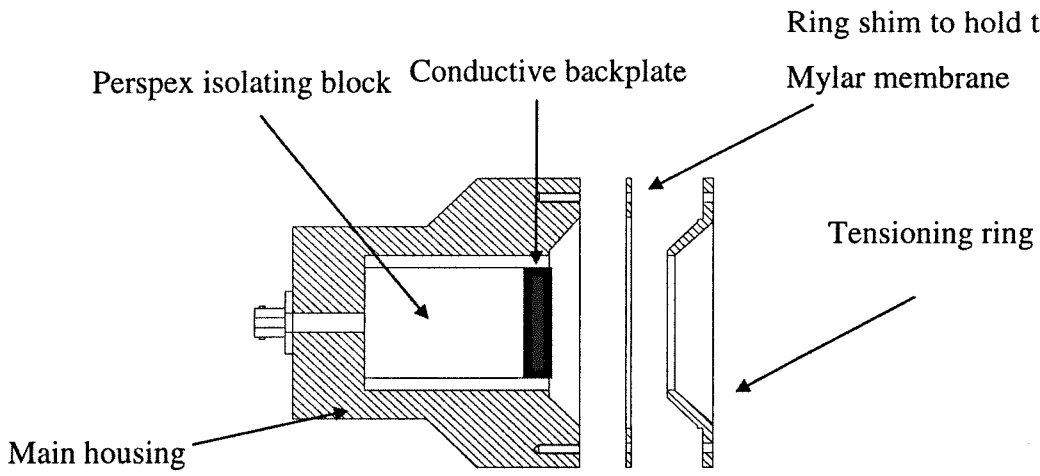

Figure 6.01 *Electrostatic transducer configuration*

Figure 6.01 illustrates the design of the electrostatic device used within this testing phase. Since the main requirement within this section is wide bandwidth operation, which is governed by the surface finish of the backplate and the thickness of the Mylar membrane [59, 60], a polished brass 30mm∅ diameter backplate was chosen in combination with a 3.5μm Mylar membrane. Note: ∅ represents a technical notation for circular diameter. The conductive backplate was mounted within a Perspex block to isolate the high tension bias from the external aluminium grounded housing and the electrode on the front membrane. The front ring provides a small degree of tensioning to the membrane to smooth the Mylar film and reduce the likelihood of point charge build up. That is, when an impurity is trapped behind the film layer or a wrinkle is evident in the membrane, charge builds up around that point until the dielectric within the Mylar film breaks down and the backplate short-circuits to the front face ground electrode. When this happens, the transducer is destroyed and the membrane must be replaced.

The frequency response of the transducer was determined by measuring the pulse-echo response from the transducer excited with a 110V impulse from a PR5052 Panametrics transmit/receive pulser unit, as detailed in Figure 6.02.

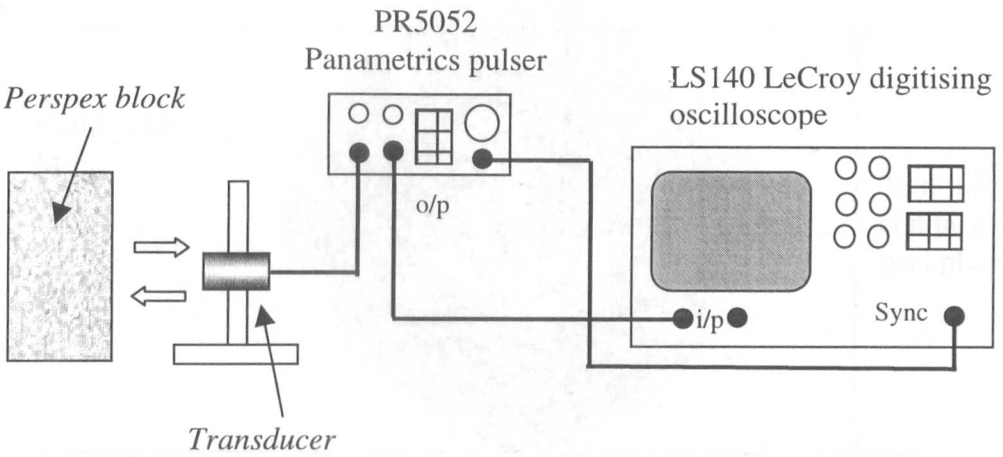

Figure 6.02 *Experimental arrangement for determining transducer bandwidth*

The received signal was captured on a LS140 LeCroy storage oscilloscope and converted from the time domain to the frequency domain using a Fourier transform implemented in subsequent software analysis. The resultant frequency response for this configuration of transducer is illustrated in Figure 6.03 and shows a –6dB bandwidth of 1MHz centred round a frequency of 600kHz.

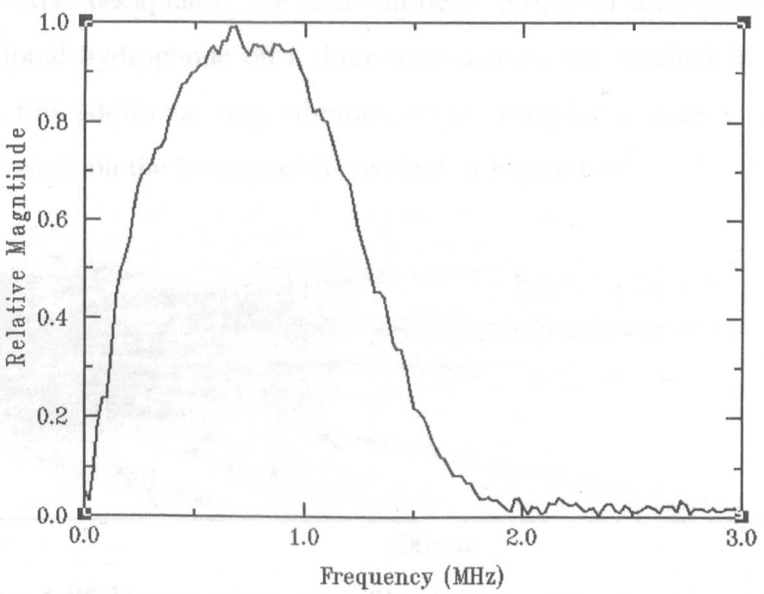

Figure 6.03 *Frequency response of electrostatic transducer*

Utilising the Polytec laser interferometer system, detailed in Appendix A, the surface displacement of the electrostatic transducer was examined at the 600kHz centre frequency of the transducer and is illustrated in Figure 6.04.

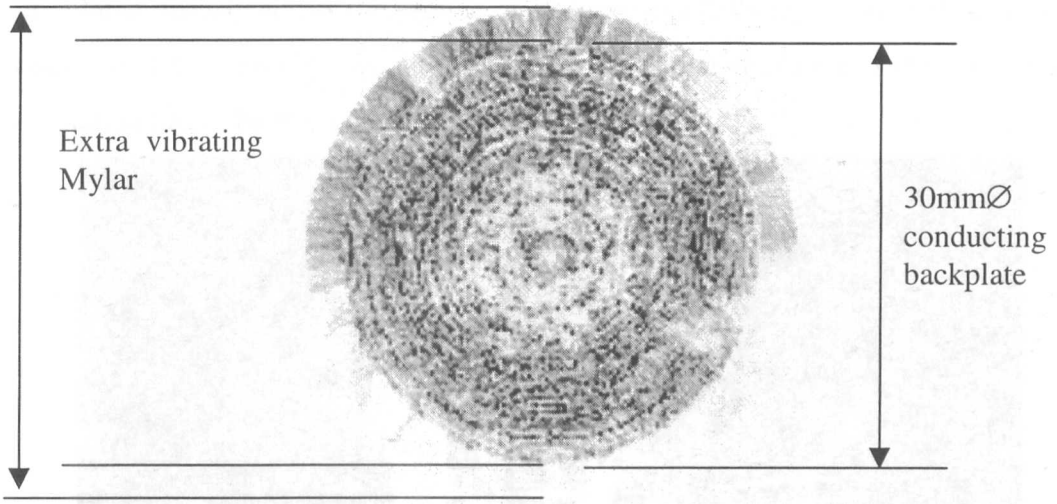

Figure 6.04 *Surface displacement of electrostatic transducer at 600kHz*

It is apparent by examination of Figure 6.04 that the distribution of vibration on the front face of the transducer is random in nature, with vibrating pockets of air dispersed evenly across the backplate of the transducer. The smoother outer ring signifies the vibration in the superfluous Mylar membrane (i.e. Mylar that is not directly positioned over the conductive backplate). The resultant beam profile of the transducer, measured using a directional hydrophone on a three axis scanner (as detailed in Appendix B.), illustrates that this additional ring vibration on the transducer leads to increased edge wave characteristics on the beam profile, evident in Figure 6.05.

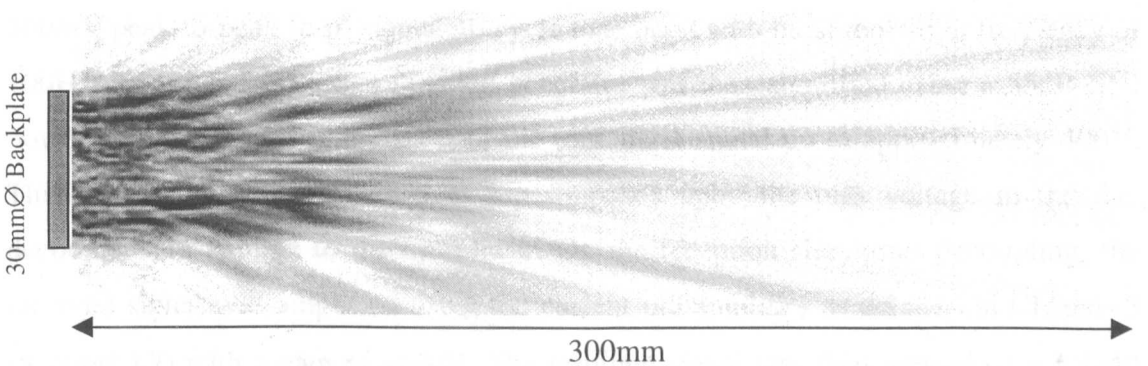

Figure 6.05 *Measured beam profile of electrostatic transducer in air*

6.2.2 Initial testing

The electrostatic transducers described were attached to the angular manipulator illustrated in Figure 6.06, which allowed angular alignment of the transducer off normal incidence to the surface of the test specimen. This permits the transducers to be

manipulated linearly across the sample plate and to vary the separation between the two transducers. Consequently, the angular holder will be stationary and the sample under examination has to be moved manually for inspection.

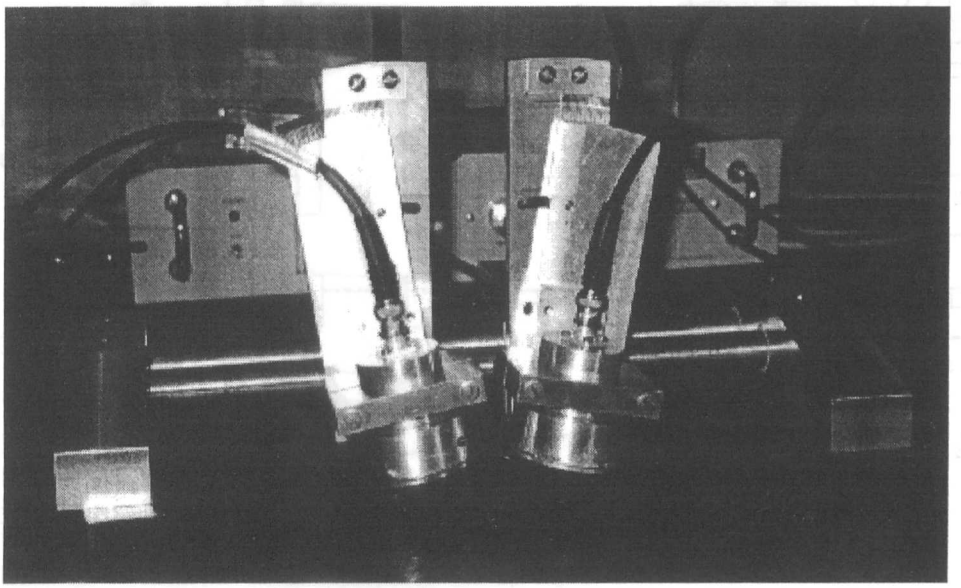

Figure 6.06 *Angular alignment jig for prototype system*

Both transducers were biased with 250 volts d.c. from a 475R Brandenburg high voltage supply through a simple d.c. capacitive filter to decouple the bias voltage from receiver and transmitter and prevent the applied d.c. voltage damaging these components. For transmission, a HP33120A function generator was used to produce a 300mV peak-to-peak (p-p) signal, 10 cycle tone burst with burst repetition frequency of 100Hz. The signal from this function generator was then amplified using a 55dB ENI power amplifier to bring the level of the tone burst signal up to approximately 400V. This transmitter voltage was then superimposed upon the bias voltage in the d.c. decoupler and applied to the transducer. On the reception side, after decoupling, the received signal was amplified using the current pre-amplifier as detailed in Chapter 3 (Section 3.7) with a gain of ≈60dB. The resultant signal was then viewed on a LS140 LeCroy digitising storage oscilloscope and the data captured on floppy disk. Note: the heterodyne amplifier was not initially employed in the arrangement. The experimental apparatus described is illustrated in Figure 6.07.

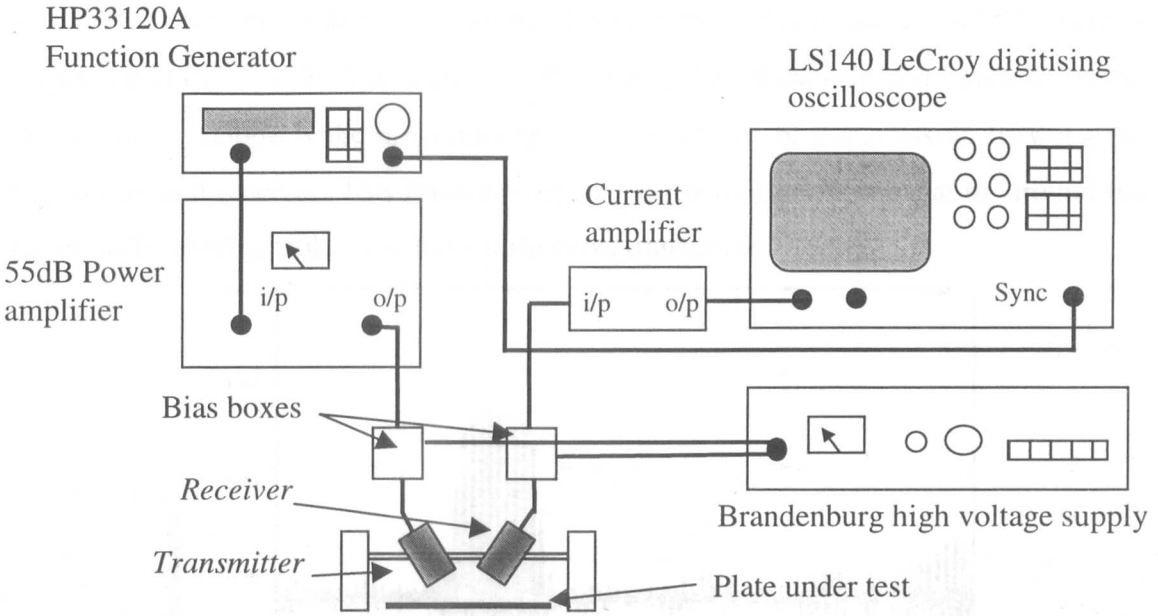

Figure 6.07 *Experimental arrangement for Lamb wave testing*

Initially, the transducers were excited at a frequency of 540kHz. The angle of each transducer was adjusted in order to generate and detect the fundamental anti-symmetrical mode (a_0) within a 1.41mm sample of aluminium plate. The angle of the transducer for efficient generation and detection of this mode was calculated to be 8.6^0 using the coincidence principle. As illustrated in Figure 6.08 this corresponds to a phase velocity of $2200ms^{-1}$ and a frequency thickness product of 0.76mm-MHz.

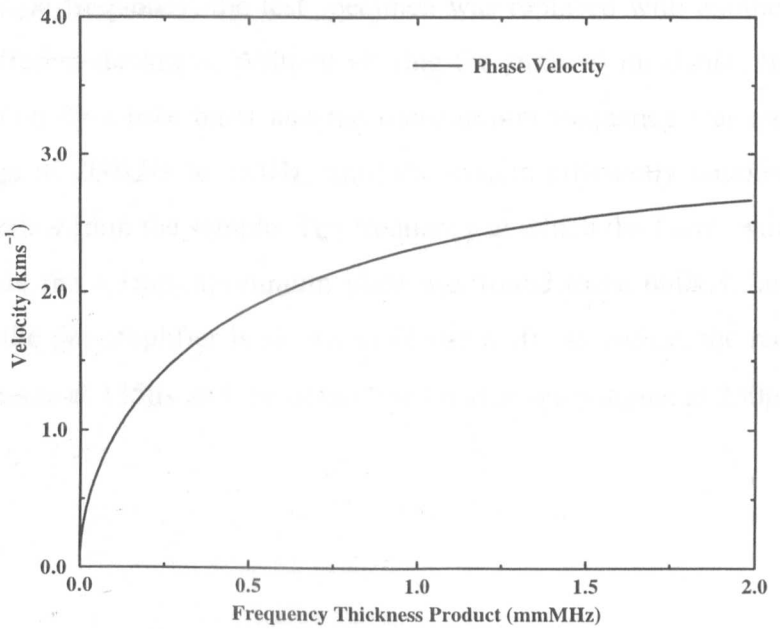

Figure 6.08 *Dispersion curve for a_0 Lamb wave in aluminium*

The signal received with the transmitter being driven at a frequency of 540 kHz is illustrated in Figure 6.09. The signal at 135μs being that of the received Lamb wave and the signal at ~230μs is the breakthrough from direct line of transmission between the transmitter and receiver. This breakthrough is caused by sound propagating around the paper baffle used to isolate the transmit/receive transducer.

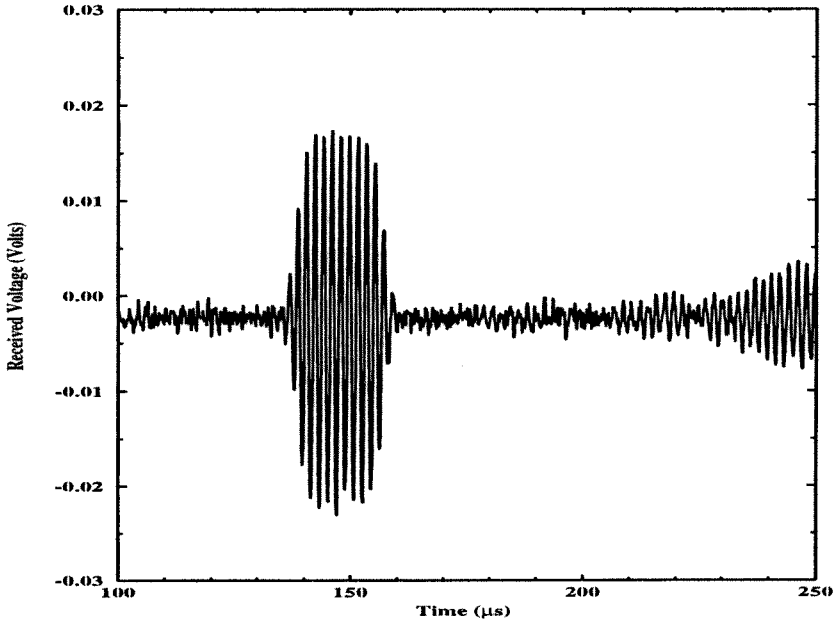

Figure 6.09 *Fundamental anti-symmetrical mode generated in 1.41mm aluminium*

After the alignment of the transducer pair had been established to generate a_0 Lamb waves for a single frequency, the test specimen was replaced with another aluminium sample of a different thickness. Without altering the angle of incidence, the transducer was again excited by a tone burst and the transmission frequency was swept across a frequency range of 200kHz to 1MHz, until the system efficiently coupled into the a_0 Lamb wave mode within the sample. The frequency at which the Lamb wave mode was generated within the 1.1mm aluminium plate was found to be 680kHz and the signal received from the pre-amplifier is shown in Figure 6.10. As before, the received Lamb wave signal arrives at 135μs and the direct line breakthrough signal at 230μs.

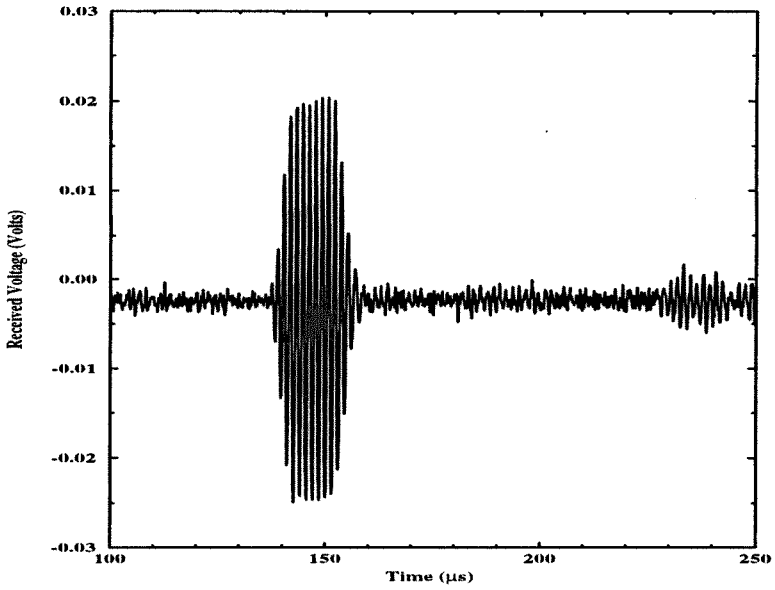

Figure 6.10 *Fundamental anti-symmetrical mode generated in 1.1mm aluminium*

By referring this operational frequency and the thickness of the plate back to the frequency-thickness (fd) product, it is apparent that the fd product is the same as before, hence the phase velocity will also be identical. This simple experiment illustrates the feasibility of utilising a single pair of ultrasonic transducers at a fixed angle of incidence, to generate Lamb waves within differing thicknesses of test specimen. However, it is apparent from Figures 6.09 and 6.10 that the received signal magnitude is quite low (<50mV), even when employing a specially developed low noise pre-amplifier in the receiver system.

Following the previously described initial experiments, the new heterodyne receiver system was used to demonstrate thickness monitoring. The test sample consisted of a 1.14mm aluminium plate containing a machined defect. The 'defect' was a 20x100mm area on the reverse side of the plate where the thickness of the material was reduced by 20%.

Figures 6.11 and 6.12 show the received signals corresponding to the required Lamb wave mode being generated and detected in both the normal thickness region and the defective region of the plate respectively, both the received signals and heterodyned signals are shown to illustrate the additional gain and noise rejection that can be achieved using this technique.

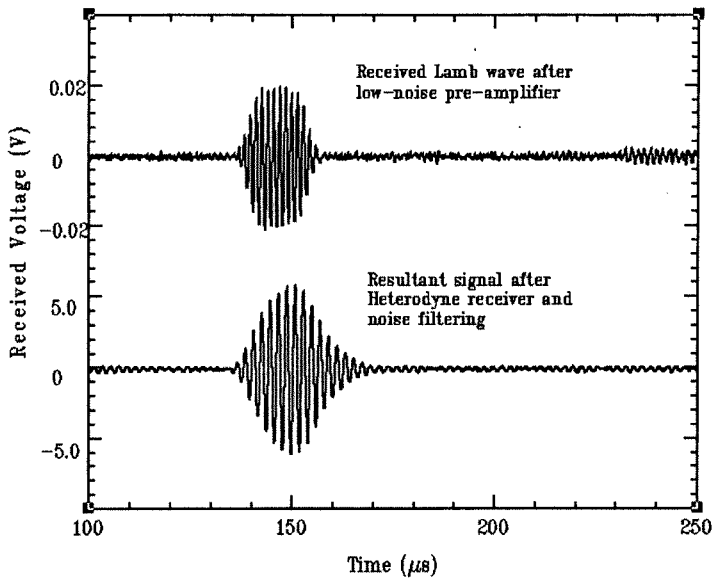

Figure 6.11 *Received Lamb wave mode generated in intact area of aluminium plate*

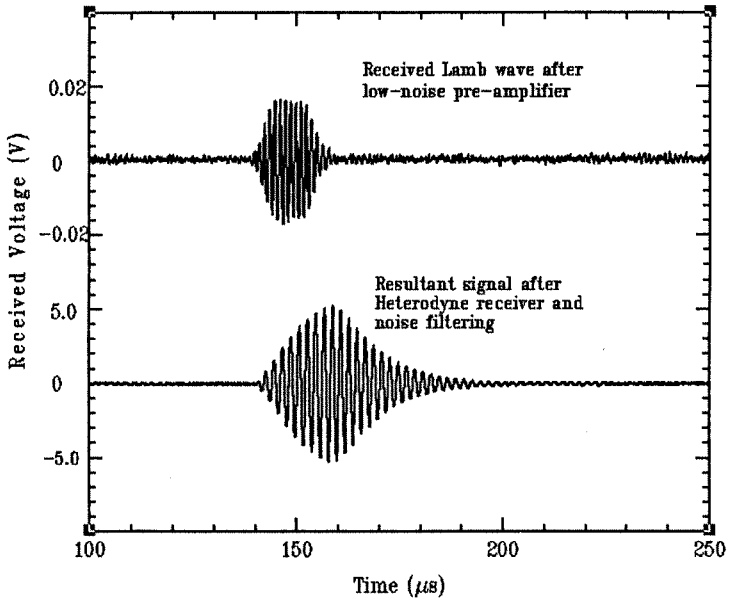

Figure 6.12 *Received Lamb wave mode generated in defective area of aluminium plate*

When Fourier transformation is applied to these signals, it can be shown that the heterodyned signals for both thicknesses of plates are identical at the pre-determined intermediate frequency of 500kHz, whereas the actual received frequencies for the intact and defect areas of the plate are 680kHz and 800kHz respectively. Figures 6.13 & 6.14 illustrate the difference in received and modulated signals in the frequency domain, noting that the pre-modulated receive signal has been scaled in order to appear at the same magnitude as that of the modulated signal. Consequently, by referring to Equation **2.39**, it is possible to determine the relative thickness of the plate and the

defect area as being 1.12mm and 0.95mm respectively, which shows good correlation with the actual values of 1.14mm and 0.95mm respectively. Note that the unmodulated signals in Figures 6.13 and 6.14 have been normalised for ease of comparison.

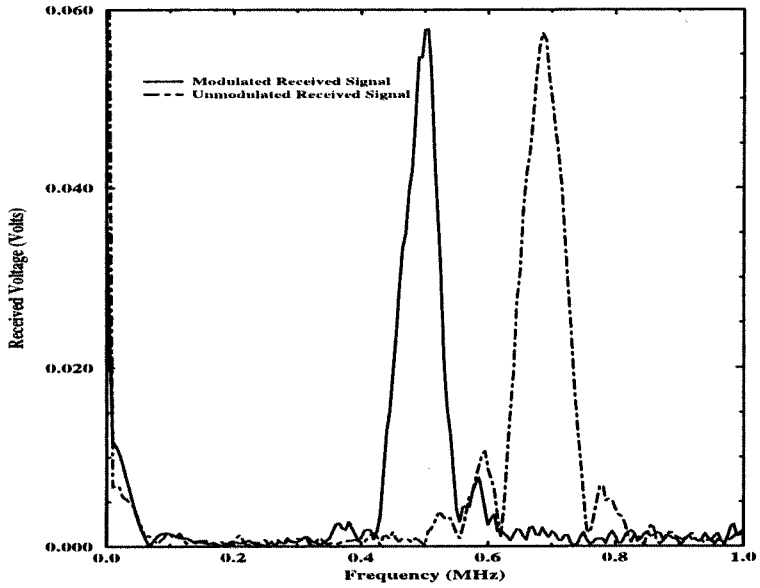

Figure 6.13 *Frequency domain representation of received signal over intact area of specimen plate illustrating heterodyne frequency shifting*

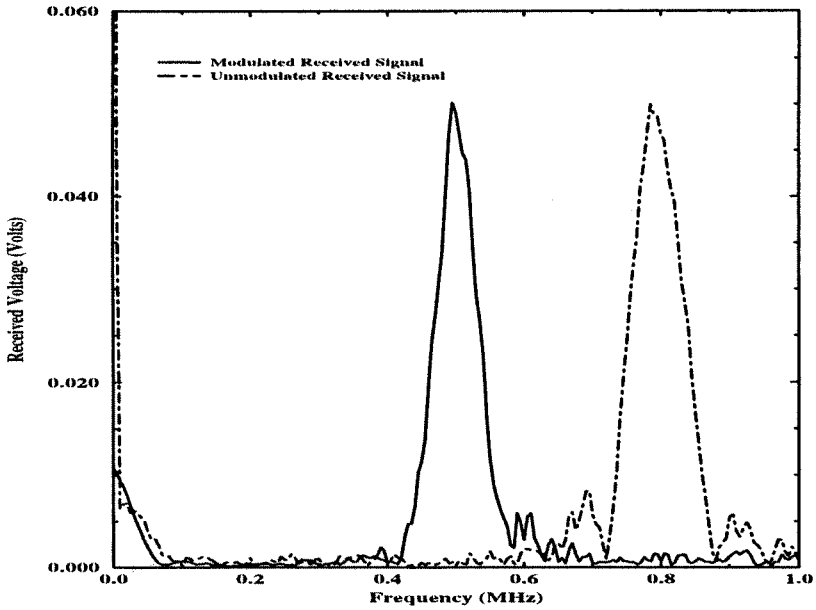

Figure 6.14 *Frequency domain representation of received signal over defective area of specimen plate illustrating heterodyne frequency shifting*

Therefore using the transducer pair described, at a given angle of 8.6°, it would be possible to scan samples ranging in thickness from ≈0.6mm to ≈2.5mm with the available bandwidth.

6.3 Minimum detectable defect size

In any system, it is essential to know the limitations of that design. In the case of an ultrasonic inspection system, the main criterion is obviously the detection of defects within the sample under test. Thus, it is of considerable interest to determine the accuracy by which the arrangement will detect different flaws. For example, it is futile to design/buy a scanner to look for defects of 3mm, if the system is incapable of resolving defects to that accuracy. In general, it is the acoustic radiation field of the transducer arrangement that will govern the accuracy of the system. If the transducers have a narrow beam profile or the transducers are focussed, the acoustic shadow (i.e. the area of plate insonified by the transducer) on the surface under inspection will be small. Therefore, since the transducers are only inspecting a small area, a defect within the plate will cause a more noticeable drop in the magnitude of the received signal.

However by referring to Figure 6.05, it is apparent from the divergent beam profile of these electrostatic transducers, that the output profile may be too diffuse for the detection of smaller defects. That is, the acoustic shadow will be too large for the drop in signal amplitude caused by the inclusion of a defect to be noticed. In order to determine the minimum defect detectability (MDD) of this scanning arrangement, two test plates were constructed, one with holes of various sizes and a second plate with holes of varying depths. The first calibration plate was manufactured from a 30cm square plate of 1.14mm thick aluminium with 18 holes ranging in size from 1mm∅ to 18mm∅ in diameter, in 1mm steps, as illustrated in Figure 6.15.

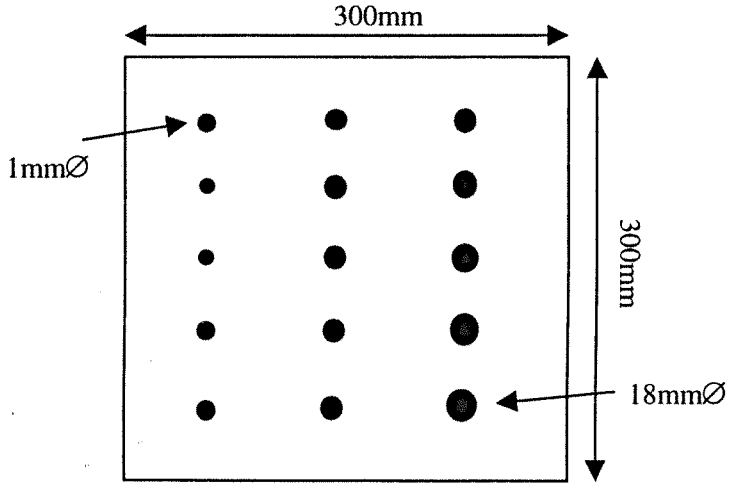

Figure 6.15 *Illustration of aluminium calibration plate*

The second plate, with similar dimensions as the first plate, had nine holes machined into the surface of the plate to varying depths. These holes were 12mm∅ in diameter, with between 10-90% of the plate thickness in 10% increments, these having been removed with a milling machine and illustrated in Figure 6.16. Using this plate, it will be possible to determine the amount of damage required for the scanner arrangements to detect the defect.

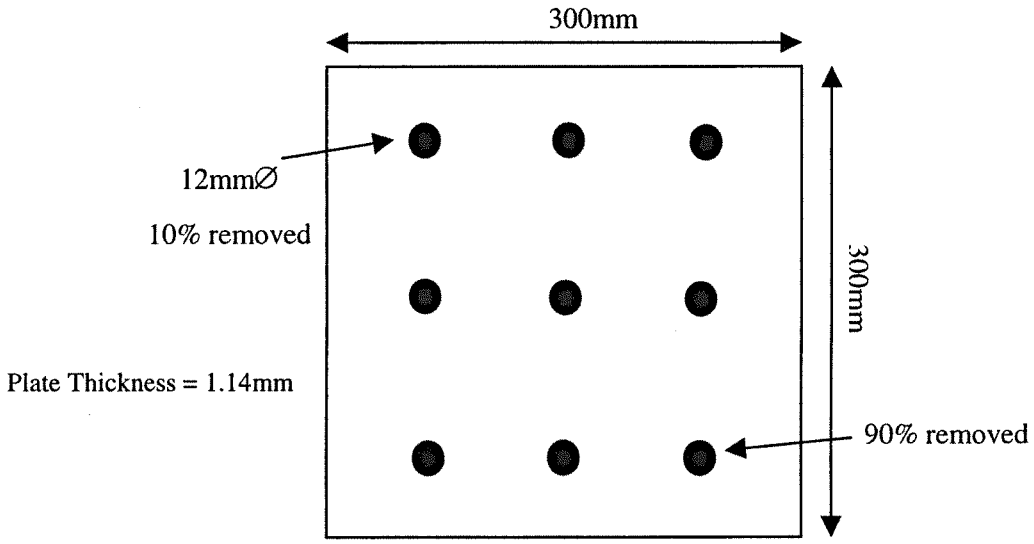

Figure 6.16 *Defect depth tolerance testing plate*

Since there are certain fluctuations in any scanning system due to such aspects as background noise and electronic noise, a protocol for the detection of defects has to be resolved. Therefore, by measuring the noise level of the scanner arrangement at rest, i.e. with the reception hardware activated but no received input signal, the *"noise-floor"* can be determined. For the receiver hardware in question, the noise-floor was found to be approximately 11mV (although this must be checked for each different configuration). In order to determine whether a defect has been found, the magnitude of the received signal should drop by at least this noise-floor level to prove that the drop is associated with the detection of the defect and not simply due to an anomaly in the received signal. In this instance, to be sure that a defect has been detected it was stipulated that the amplitude of the received signal should drop by at least twice this noise-floor level, to allow for any spurious signals above or below this mean noise level.

Figures 6.17 and 6.18 describe the resolution of the scanning arrangement utilising the 30mm∅ electrostatic transducers. The scanner was arranged as described in Figure 6.07 with the scanning head positioned separately over the various machined defects and the influence these exerted over the received signal was noted. Consequently, Figures 6.17 and 6.18 illustrates the degradation in the magnitude of the received signal as a percentage of the detected Lamb wave over an intact area of the test plate.

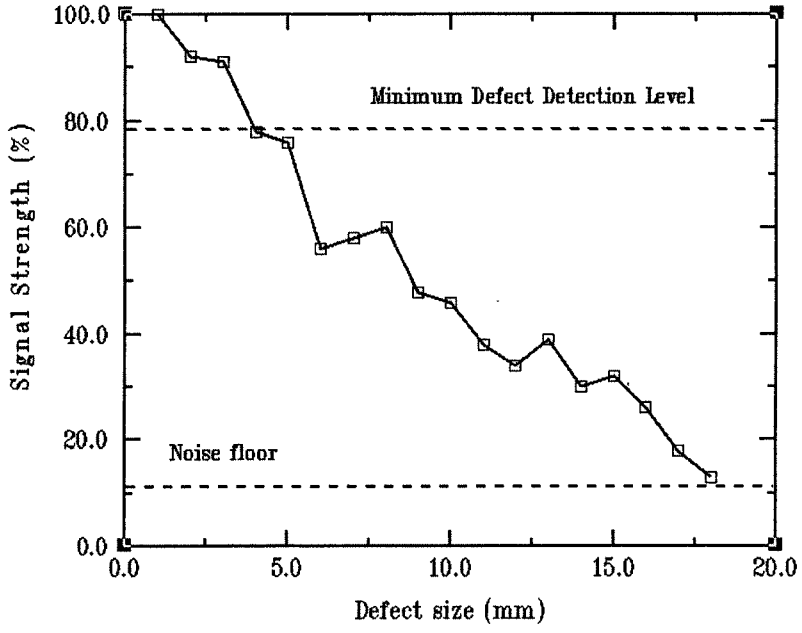

Figure 6.17 *Minimum detectable defect size using 30mm∅ electrostatic transducers*

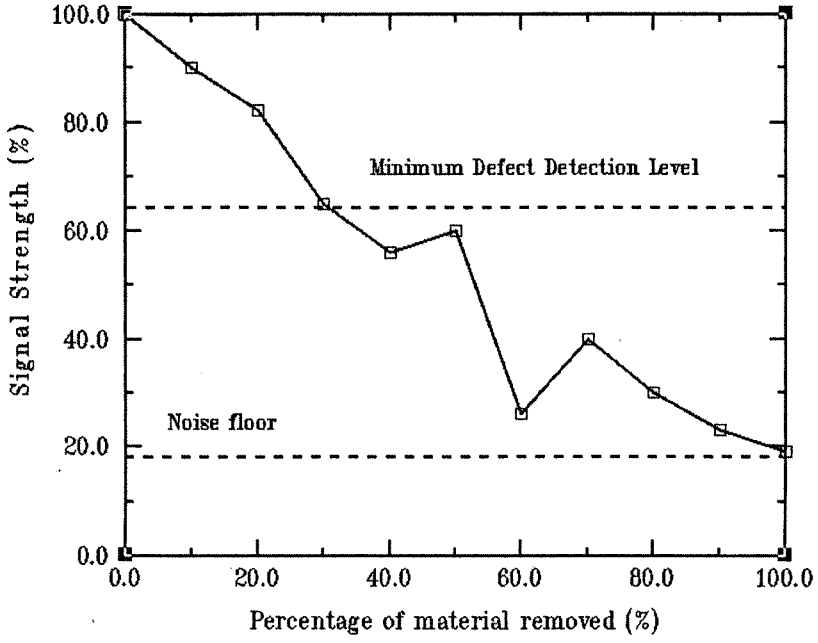

Figure 6.18 *Minimum detectable defect depth using 30mm∅ electrostatic transducers*

It was found that the prototype scanner with the 30mm∅ diameter electrostatic transducers was able to detect defects down to a size of approximately 4mm∅ from the drilled plate and ≈30% degradation on the milled plate. It is obvious from the MDD of this system and the overall size of the scanner head, that more compact focussed transducers are required to detect smaller, more precise defects (such as small particle impact damage).

6.4 Computer control of frequency adjustment

One of the original design requirements stipulated within the initial stages of the scanner development, was for the use of a computer software interface to control the frequency output of the transmitter stage and secondary modulating signal for the heterodyne amplifier. Computer software was developed for this purpose, using the HP-IB interface protocol to control the two HP33120A function generators through a LabWindows control environment.

However, although operational software was developed and tested successfully, an unforeseen problem arose with the application of this software to the HP33120 function generator. It was found that when the control information was passed to the function generators to alter the frequency, voltage, etc., the generator passed into a temporary reset status before changing to the new settings. During this mode in stasis, the function generator reverted to a 1volt, 1kHz continuous wave default setting for a brief period (typically <1 second). However, this short period in stasis was long enough to cause serious difficulties with the power amplifier, sometimes sending the amplifier into oscillation. Different means of solving this problem were attempted with limited degrees of success, optimisation of the code led to a reduction in the period of time spent in stasis, while other function generator coding commands led to resetting all the conditions simultaneously. Since no solution was found to overcome this problem, it was decided to forgo the use of computer control for the scanner and concentrate on producing a robust portable compact unit.

6.5 Improved electrostatic scanning arrangement

It has been shown that is possible to generate and detect Lamb waves within plates of differing thickness, by sweeping the transmission frequency to retune these elastic waves for the new thickness. Moreover, it is also apparent that the 30mm∅ diameter transducers used in the initial proof of concept phase were too large to resolve defects smaller than 4mm@600kHz in the calibration plate. In order to improve the spatial resolution of the electrostatic transducer arrangement, a pair of smaller electrostatic transducers was manufactured.

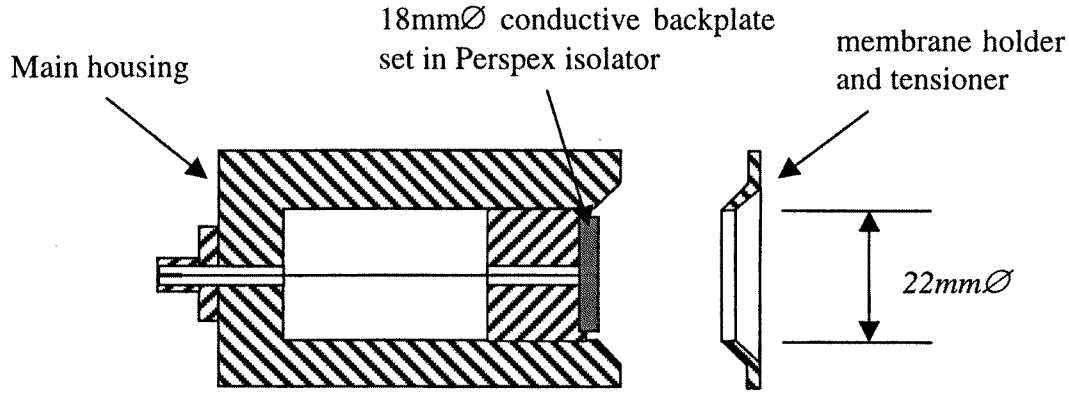

Figure 6.19 *Miniature electrostatic transducer*

The transducer illustrated in Figure 6.19 has a 18mm∅ brass conductive backplate with a slightly rougher finish and a 22mm∅ aperture ring that acts as a holder for the membrane and also applies a small tension across the Mylar, to remove wrinkles from the film. In this instance, a 3.5μm Mylar membrane was used to increase the robustness of the transducer, rather than the 2.5μm film used previously. This roughened backplate configuration differs slightly from that used by the original larger capacitive transducers due to the lack of sensitivity offered by the polished backplates. It was found, that as the diameter of the transducer was reduced, and therefore that too of the active area of the transducer, that the application of roughened backplates led to an improvement in transmitted power at the expense of transducer bandwidth. As a result, the frequency response (calculated using the previously described arrangement in Figure 6.02) was determined and is illustrated in Figure 6.20. By comparing this frequency response to that of the previous 30mm∅ electrostatics (Figure 6.03), it is apparent that the bandwidth of this device (~600kHz) is considerably less than that in the previous design (~1MHz).

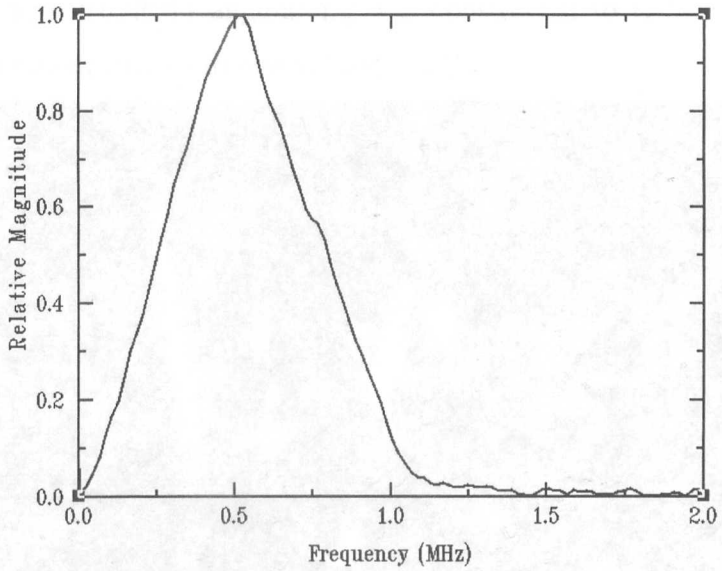

Figure 6.20 *Frequency response for miniature electrostatic transducers*

As before, the Strathclyde calibration facilities were utilised to determine the surface displacement and acoustic beam profiles of these smaller transducers. Figure 6.21 represents the front face vibration of the transducer and Figure 6.22, the beam profile.

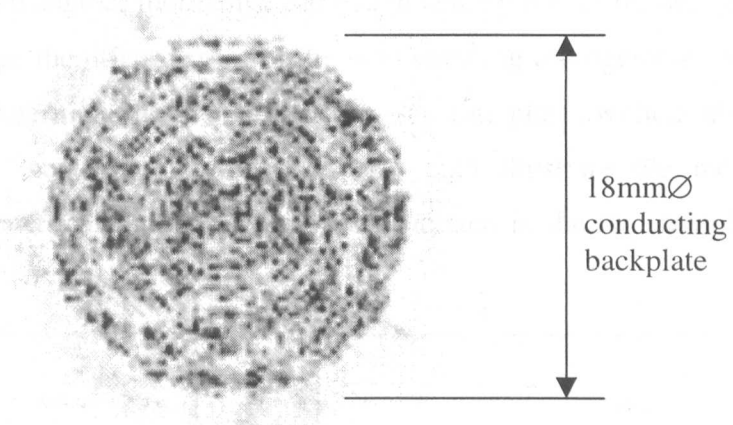

Figure 6.21 *Surface displacement of miniature electrostatic transducer*

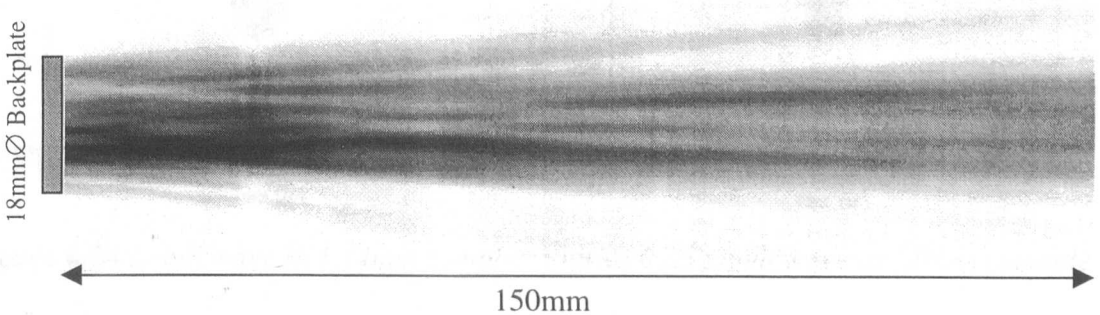

Figure 6.22 *Beam profile of miniature electrostatic transducer*

Additionally, a new handheld angular jig was constructed to reduce the size of the scanning head arrangement, as shown in Figure 6.23.

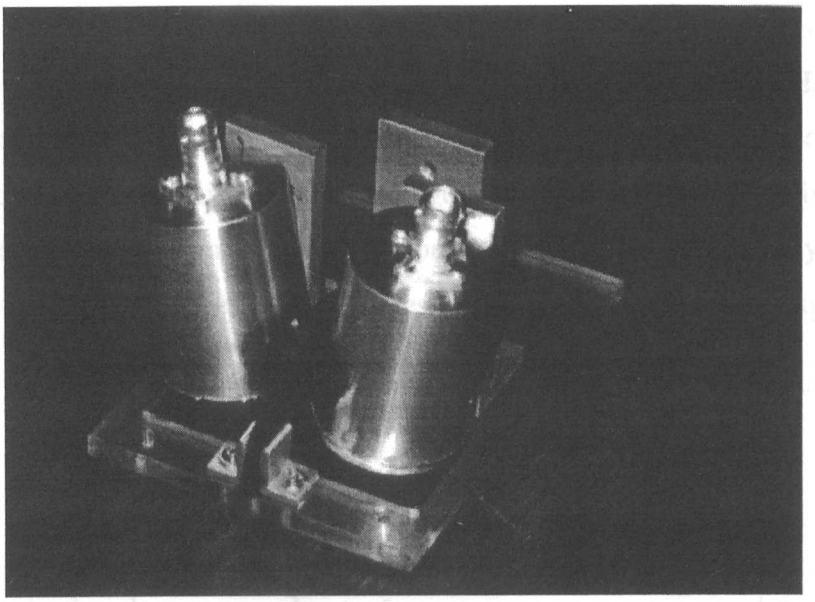

Figure 6.23 *Picture of miniaturised handheld scanner head*

The transducers described were mounted in the new handheld unit, consisting of a perspex base plate with two angular mountings and a high density rubber baffle. Testing was then repeated to gauge the effectiveness of the new scanning arrangement. Again, the scanner was used to determine the thickness of two separate plates without altering the transducer angle of incidence. Figures 6.24 and 6.25 illustrate the received responses from the asymmetrical Lamb wave modes generated in the two samples of differing thickness.

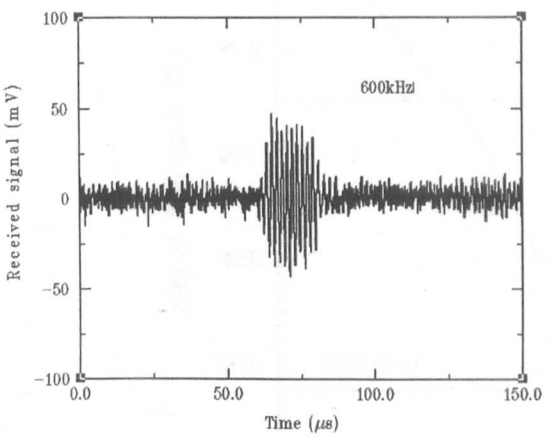

Figure 6.24 *Lamb wave in 1.14mm sample*

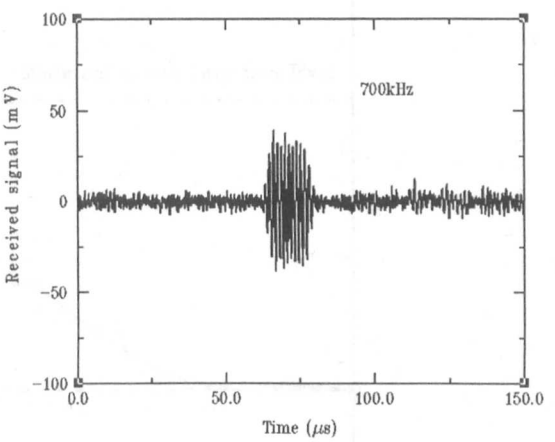

Figure 6.25 *Lamb wave in 1.01mm sample*

Using the calibration plates described in Section 6.3, the scanning system was re-evaluated using the miniature electrostatic transducers in the head assembly. The system was configured as shown in Figure 6.07, with an excitation voltage from the function generator of 300mV in the form of a 10cycle tone-burst at 600kHz, as before. The resultant signal was amplified using the current pre-amplifier and stored for analysis on disk. Note, in this scanning arrangement the noise floor level is lower than in the previous system, 11mV in comparison to 18mV. This is probably due to the lower bandwidth of the devices picking up less noise across the frequency spectrum.

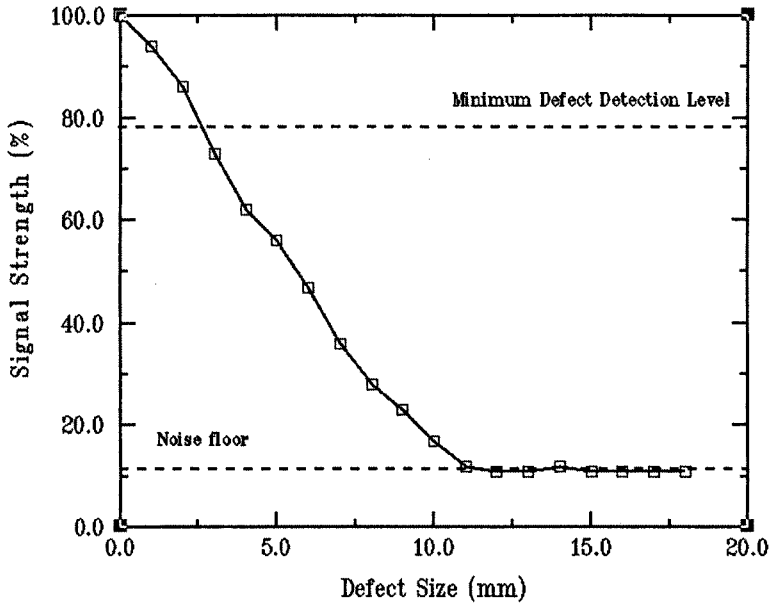

Figure 6.26 *Minimum detectable defect diameter for miniature electrostatics*

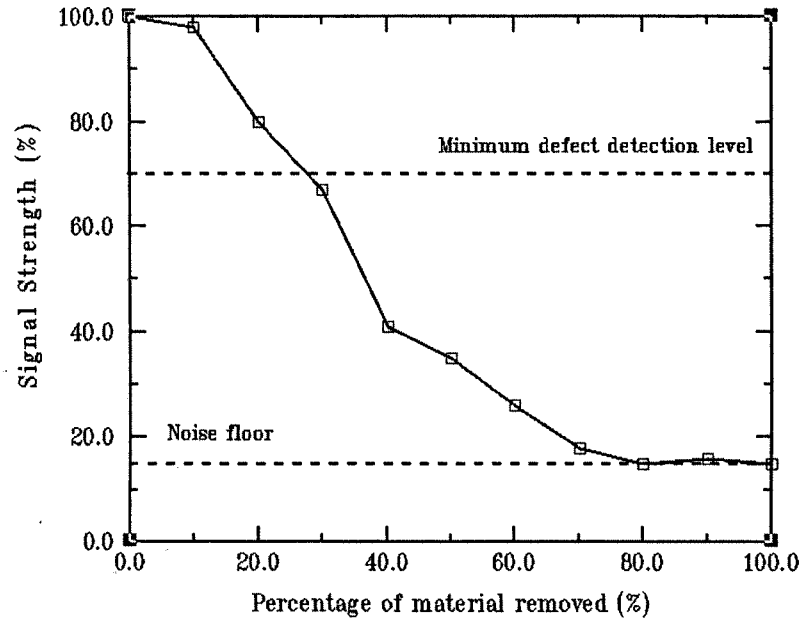

Figure 6.27 *Minimum detectable defect depth for miniature electrostatics*

Figure 6.26 illustrates the MDD diameter which the scanner can identify as approximately 2.5mm∅ and Figure 6.27 demonstrates the required percentage of degradation in plate thickness before a defect is realised as 25%. Thus, it is apparent that the reduction in diameter of the transducer head assembly has led to an increase in system resolution. By comparison of the two MDD graphs, for the 30mm∅ and 18mm∅ transducers, it is also apparent that the degradation in signal strength across the test range is higher in the case of the smaller transducers. This illustrates that the smaller transducers are insonifying a smaller area of the test plate and thus, smaller defects influence the magnitude of propagated Lamb wave to a higher degree.

6.6 Scanner utilising enhanced piezocomposites

Having proven that it is feasible to use an alteration in transmitted frequency to generate and detect Lamb waves in a range of different thicknesses, without changing the angle of incidence, the next requirement is to improve the robustness of the system. Additionally, it has been shown that the miniaturising of the scanning head assembly leads to a higher resolution of defect detection.

Thus, by completely replacing the electrostatic transducers used within the first two phases of the investigation with small wideband piezocomposites, it will be possible to reduce the complexity of the system by removing the additional expensive electronics required to bias the electrostatics and still maintain system resolution. Piezocomposites should also provide a more rugged design capable of standing mishandling and harsher working conditions than those tolerated by electrostatic devices. Typically, piezocomposites used in air-coupled operation are restricted to narrowband operation due the losses in sensitivity associated with the application of backing materials. However, by utilising the enhanced bandwidth composites discussed in the previous Chapter it should be possible to incorporate the necessary robustness, with the required frequency characteristics.

6.6.1 Composite transducer specifications

The conical composite transducers chosen for incorporation within the scanner arrangement were both of a 20mm∅ diameter with the specifications detailed in Table 6.01.

	Conical transducer 1 (TX1)	*Conical transducer 2 (TX2)*
Composite materials	PZT-5A/CY1301	PZT-5A/CY1301
Kerf width (mm)	0.25	0.25
Pillar width (mm)	0.6	0.6
Volume fraction (%)	50	50
Transducer width (mm∅)	20	20
Inner thickness (mm)	2.87	2.83
Outer thickness (mm)	2.01	1.77
Lowest f_e	560kHz	560kHz
Highest f_e	840kHz	1000kHz

Table 6.01 *Specifications for conical composites*

The operational impedance for each of these devices are illustrated in Figure 6.28 and 6.29. It is apparent from comparison of Figure 6.28 and 6.29 that there is a slight difference between the lowest electrical resonance for each transducer. This is so that the inner diameter electrical resonance of TX2 will coincide with the mechanical resonance of the inner diameter of TX1. Hence, TX2 will be configured as the transmitter and TX1 as the receiver within the head assembly.

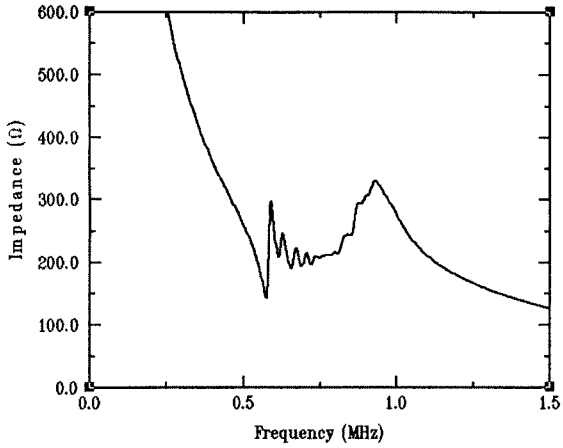

Figure 6.28 *Operational impedance of conical composite TX1*

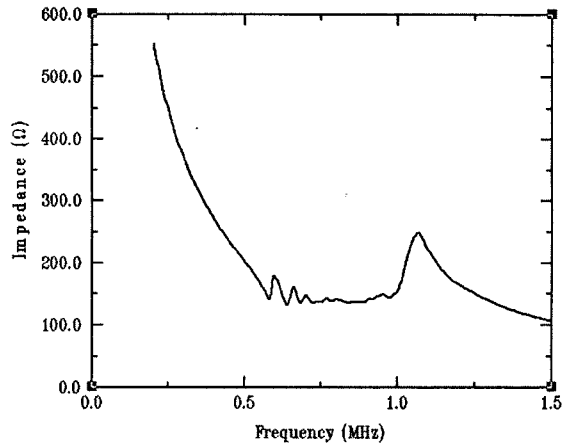

Figure 6.29 *Operational impedance of conical composite TX2*

Specialised matching layers developed and designed by Stephen Kelly [53] were then bonded to the front of both of these composites. These matching layers have been reported to give up to 20dB improvement in system sensitivity. These matching layers were not designed for operation at any specific resonant frequency, but rather, made as thin as possible to act purely as an acoustic impedance transformer. Figure 6.30 shows the operational impedance of the composite transducer, with the addition of this 0.17mm matching layer, where a slight smoothing of the impedance characteristics is evident.

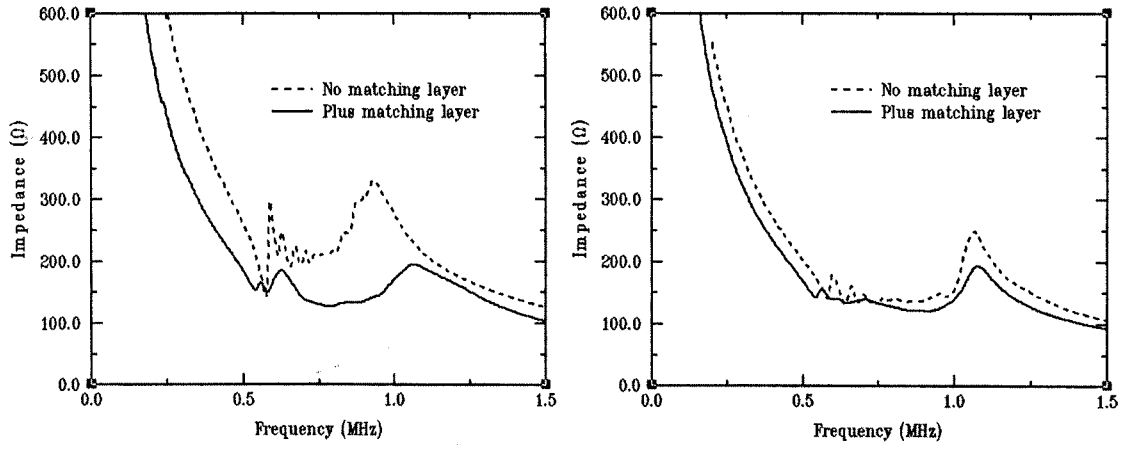

Figure 6.30 *Operational impedance of composites with additional matching layer*

Using the previously described arrangement for determining the frequency response (Figure 6.02), the bandwidth characteristic of the conical composite transducer pair was measured experimentally and is illustrated in Figure 6.31.

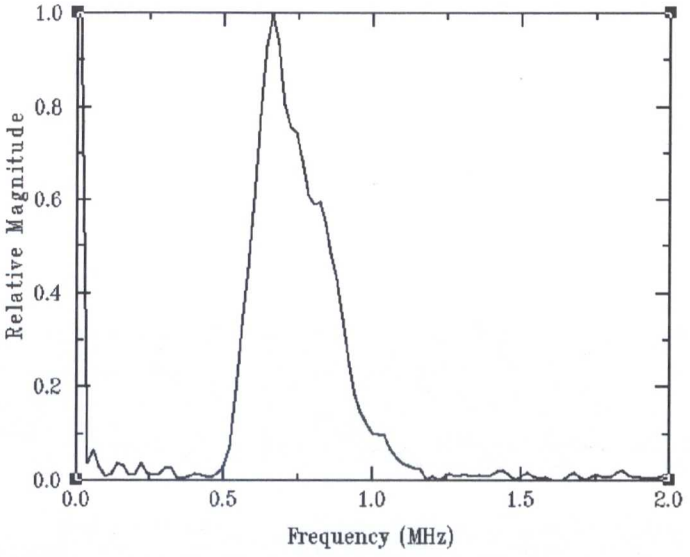

Figure 6.31 *Frequency response for conical composite transducers*

By examination of Figure 6.31, it is apparent that the 300kHz bandwidths of the conical composites, while significantly larger than those of conventional unbacked composites (typically ≈40kHz), are not as wideband as those previously shown for the electrostatics (1MHz). However, the piezocomposite pair does have comparable bandwidth characteristics to that of the miniature electrostatics described in Section 6.5.

These transducers were then examined using the Polytec laser interferometer and the beam profiling calibration equipment to determine their mode of operation. As with the work reported in Chapter 5, both transducers exhibited an initial central vibration, dispersing annularly with an increase in frequency. Figures 6.32 (a & b) illustrate experimentally, the effect for the conical transducer (TX1) at frequencies of 600kHz and 800kHz respectively.

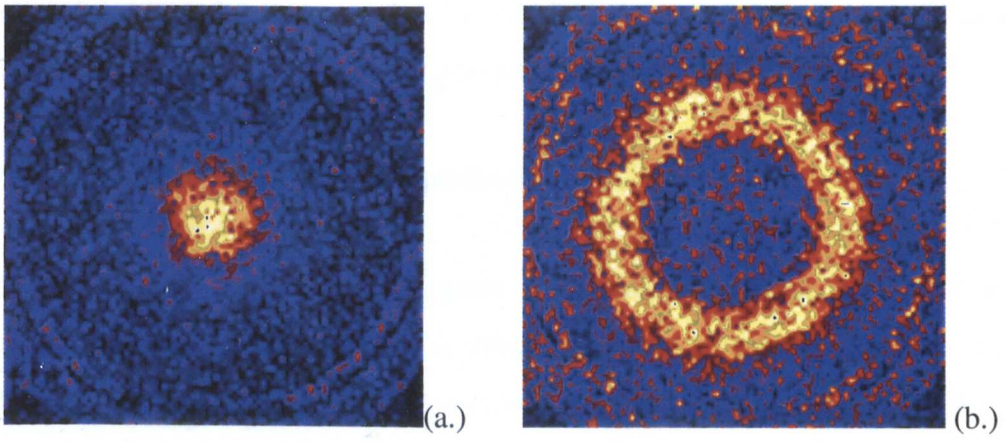
(a.) (b.)

Figure 6.32 *Surface displacements of cone TX1 at (a.) 600kHz and (b.) 800kHz*

The resultant beam profiles, again as in Chapter 5, demonstrated a narrow focussed acoustic radiation at the lower end of the electrical frequency range, shifting to a converging beam pattern synonymous with annular vibrating sources, focussing at a distance of ≈50mm. Again, Figures 6.33 (a & b) represent the beam patterns of the transducer (TX1) for corresponding frequencies.

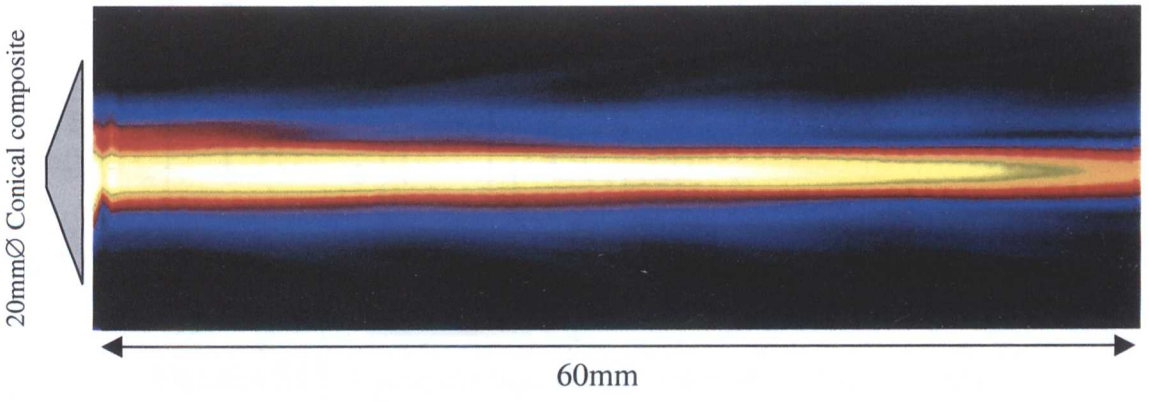

(a.) 600kHz

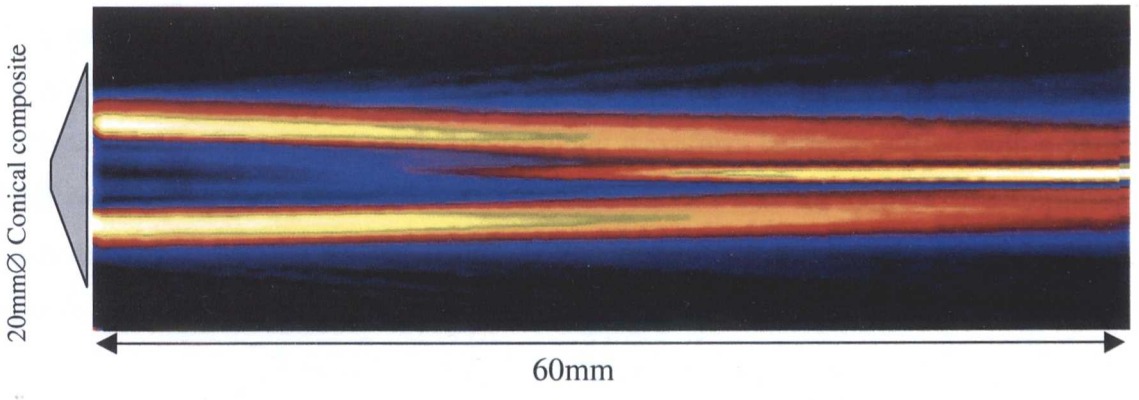

(b.) 800kHz

Figure 6.33 *Beam profiles of cone TX1 at (a.) 600kHz and (b.) 800kHz*

The composite transducers were then attached to the previously described handheld angular alignment unit and tested with a number of plates of different thickness.

6.6.2 Testing of wideband piezocomposite scanner

In accordance with the previous sequence of testing, the piezocomposite scanning system was initially tested on samples of differing thickness to satisfy the main criterion of thickness tuning capability. The conical transducers, mounted in the handheld

scanning head, were configured in the arrangement shown in Figure 6.34 for plate thickness testing.

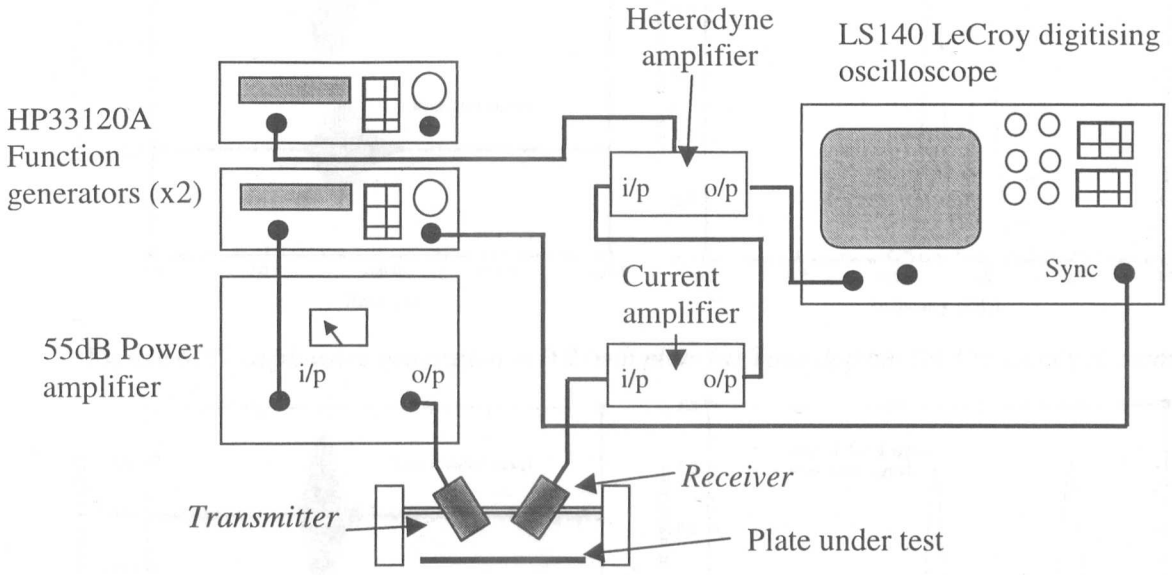

Figure 6.34 *Scanning arrangement for conical composite scanner*

The function generator was configured to output a 10 cycle tone-burst signal with a pulse repetition frequency of 100Hz and an amplitude of 300mV, as previously used with the electrostatic transducers. The resultant waveform being amplified with a 55dB ENI power amplifier. The reception hardware chosen was the current pre-amplifier, with the heterodyne receiver to determine the amplitude and frequency of the received signal, and data storage was again facilitated by the LeCroy oscilloscope.

As before, the conical transducer scanner was able to generate and detect the Lamb wave mode in the aluminium test plates. In this instance, a series of three thin aluminium shims of 0.21mm, 0.16mm and 0.095mm thickness were tested. Using the configuration detailed, the scanner was angularly aligned to generate the a_0 Lamb wave within the 0.21mm thick test piece at a frequency of 600kHz, shown in Figure 6.35(a) time domain and (b) frequency domain. Consequently, the 0.21mm shim was replaced by the 0.16mm plate (Figure 6.36) and the 0.095mm plate (Figure 6.37) and the a_0 mode was generated by re-tuning the frequency of operation to 780kHz and 920kHz respectively.

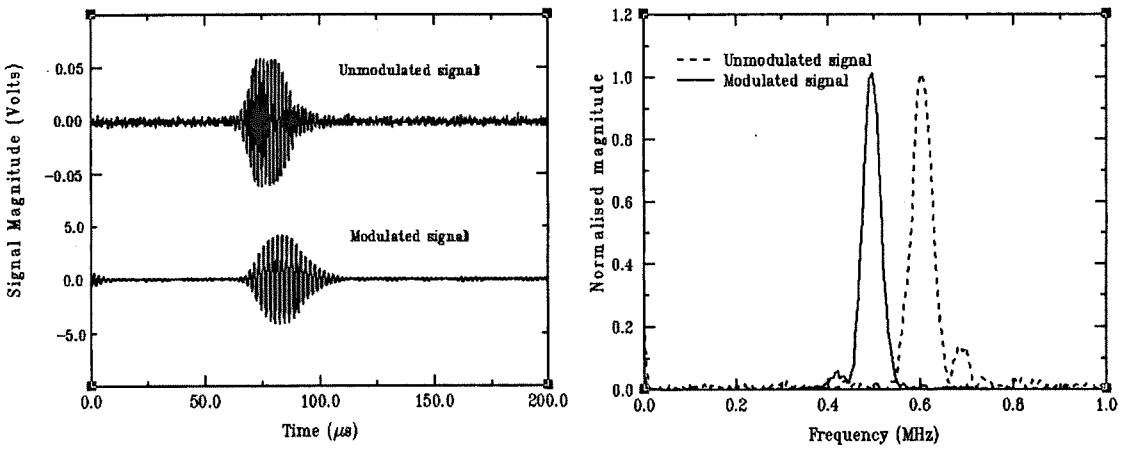

Figure 6.35 *Lamb wave generation in 0.21mm plate (a) Time domain (b) Frequency domain*

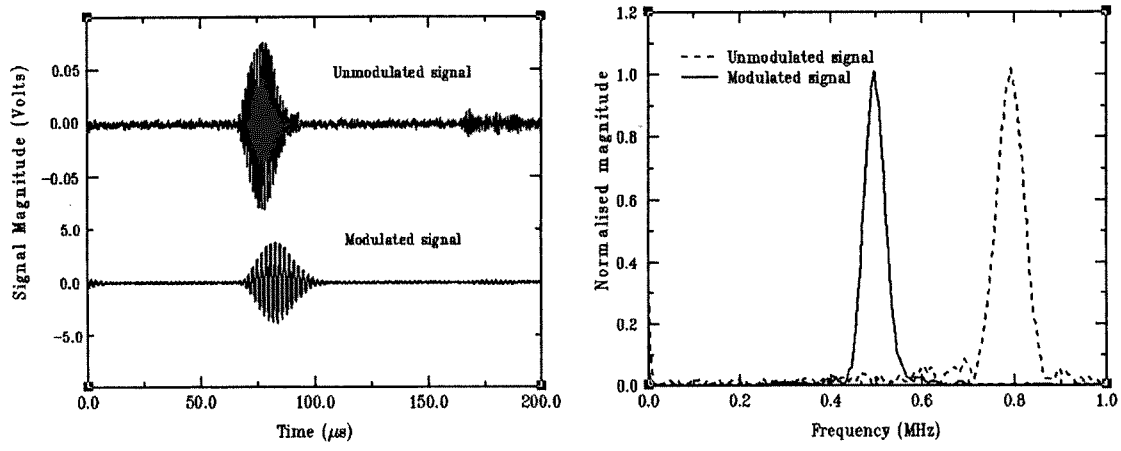

Figure 6.36 *Lamb wave generation in 0.16mm plate (a) Time domain (b) Frequency domain*

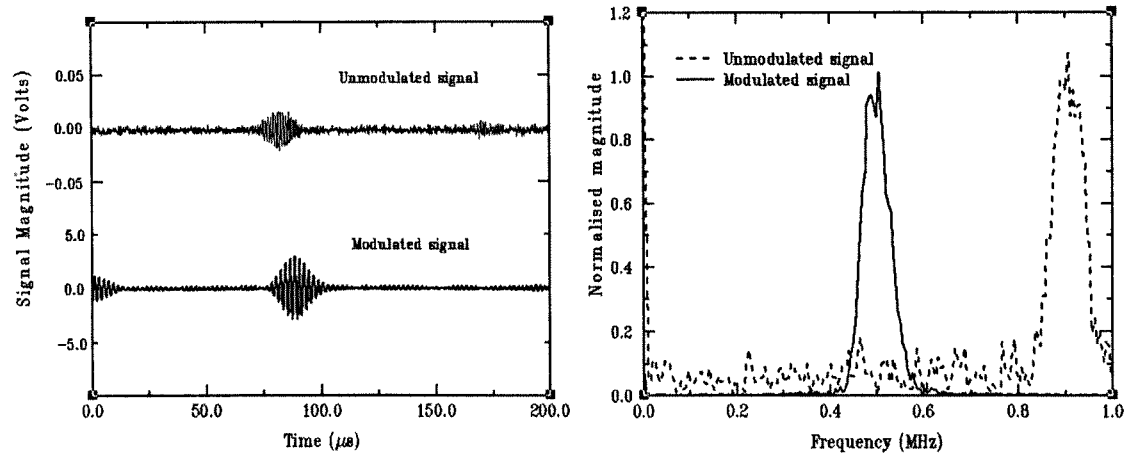

Figure 6.37 *Lamb wave generation in 0.095mm plate (a) Time domain (b) Frequency domain*

It is evident from the three preceding figures that, as with the electrostatic transducers, the conical composites are capable of operating over a range of thicknesses from a set angle of incidence.

In addition, by comparing the two differing transducer technologies, electrostatic and piezocomposite, it is possible to distinguish the relative sensitivities offered by each device. Figure 6.38 illustrates the received Lamb wave for a 1.14mm thick sample of aluminium for the three different transducer configurations.

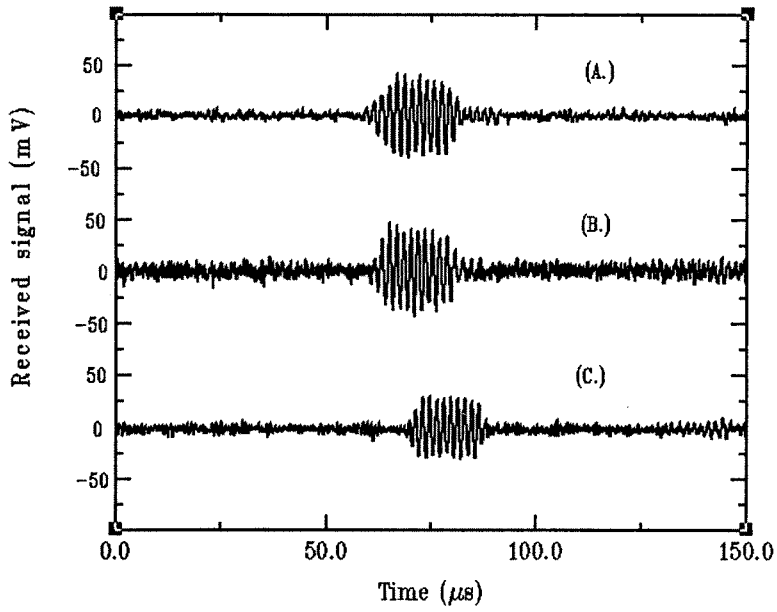

Figure 6.38 *Comparison of the composite and electrostatic transducer responses operating under similar conditions (A.) conical composites (B.) miniature electrostatics (C.) larger 30mm∅ electrostatic transducer*

From analysis of Figure 6.38, it is apparent that the composite transducers (Trace A.) are of comparable sensitivity to the miniature electrostatics (Trace B.) and an improvement over the wider bandwidth 30mm∅ electrostatics (Trace C.). Also apparent from Figure 6.38, it that the composite transducers have less noise interference than that of the electrostatics. By calculating the signal-to-noise ratio (SNR) for each of the transducers pairings, it was found that the SNR for both electrostatics configurations was ~14dB and approximately 18dB for the conical composites. It is possible to conclude that although the composite transducers still do not have the exceptional bandwidth characteristics of the electrostatic transducers (especially the original 30mm∅ transducers), there is an improvement in sensitivity offered by the composite pairing and overall robustness.

6.6.3 Defect detection using conical composites

Having illustrated the capability of the scanning system to tune to different thicknesses of test plates, the resolution of the defect detection within the scanner was then analysed using the calibration plates detailed in Section 6.3. Figure 6.39 illustrates the minimum detectable defect (MDD) size and Figure 6.40 represents the MDD depth for the composite transducers.

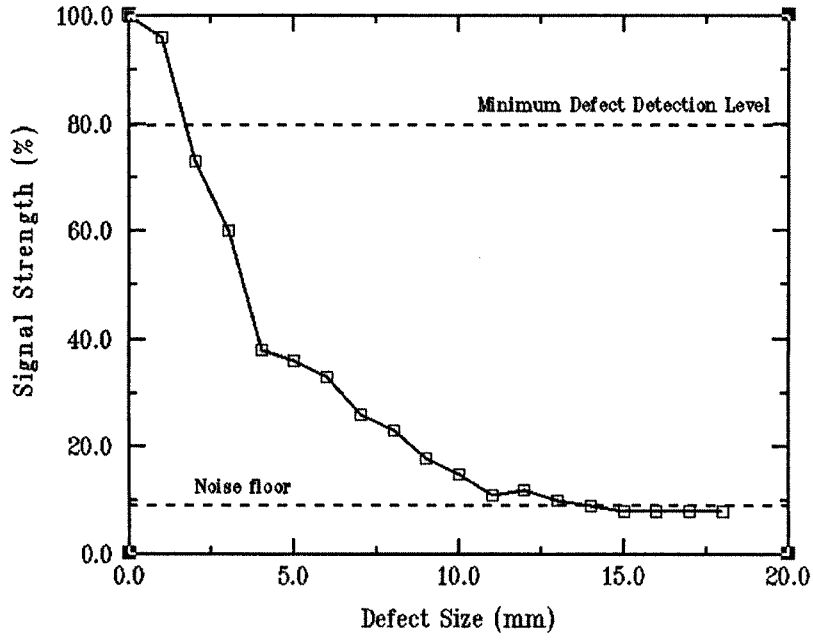

Figure 6.39 *MDD size*

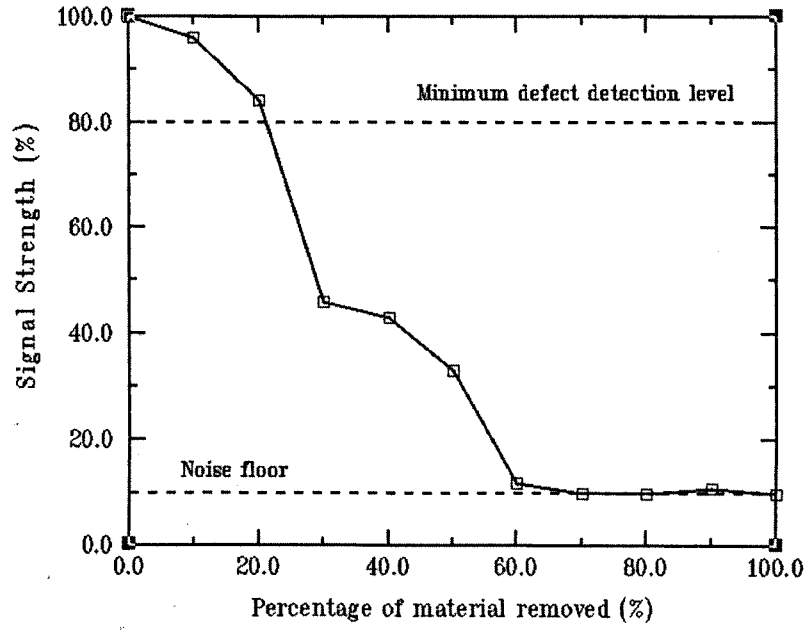

Figure 6.40 *MDD depth*

Figure 6.39 shows that the MDD size for the composite arrangement, is less than 2mm∅ diameter. This compares favourably to that of the system incorporating the miniature electrostatics and considerably better, than that of the original system using the large capacitive transducers. By comparing the MDD depth characteristics of the composite scanner head, in Figure 6.40, to that of the miniature electrostatic transducer in Figure 6.26, it is apparent that there is again good correlation between the capabilities of the two systems. In this instance, the composite transducers are capable of resolving defects in the plate, when a degradation in plate thickness of approximately 22% occurs. Comparing this to the defect depth resolution of the miniature electrostatics (≈28%) and the 30mm∅ electrostatics (≈30%), it is can be shown that the composite transducers offer greater resolution than that of the capacitive transducers. Again, it should be noted that the noise floor level associated with the conical composite scanning arrangement was lower than both of the previous systems. The noise level in this instance was 9-10mV in comparison to 11mV and 18mV of the miniature and large electrostatic transducers, respectively.

Comparison of the two scanning systems, electrostatic and piezocomposite, shows that both systems have the capability of generating and detecting Lamb waves within differing thicknesses of plate, without alteration of angular alignment. However, throughout the investigation of this multi-frequency scanning system, problems relating to the reliability of the electrostatic transducer technology were encountered. While these capacitive devices have excellent bandwidth characteristics, far in excess of that achievable with composite technology, their reduced sensitivity and fragility means that they are of limited use within an industrial environment. The conical composite system by comparison, has a considerably higher degree of operational robustness and, with the improved bandwidth offered by the conical geometry, a more practical solution for on-site inspection than the electrostatic technology.

6.7 Practical examples of NDT inspection

Now that the constraints of the conical composite scanner have been quantified, a series of tests to determine the applicability of the system to practical NDE/NDT situations will be examined. Firstly, testing was completed on a side panel from a Ford Transit

van in order to detect disbonds in lap joints between the outside skin of the panel and the inner support struts as illustrated in Figure 6.41 and 6.42. Figure 6.43 illustrates the portable Lamb wave scanner in operation over the defective region.

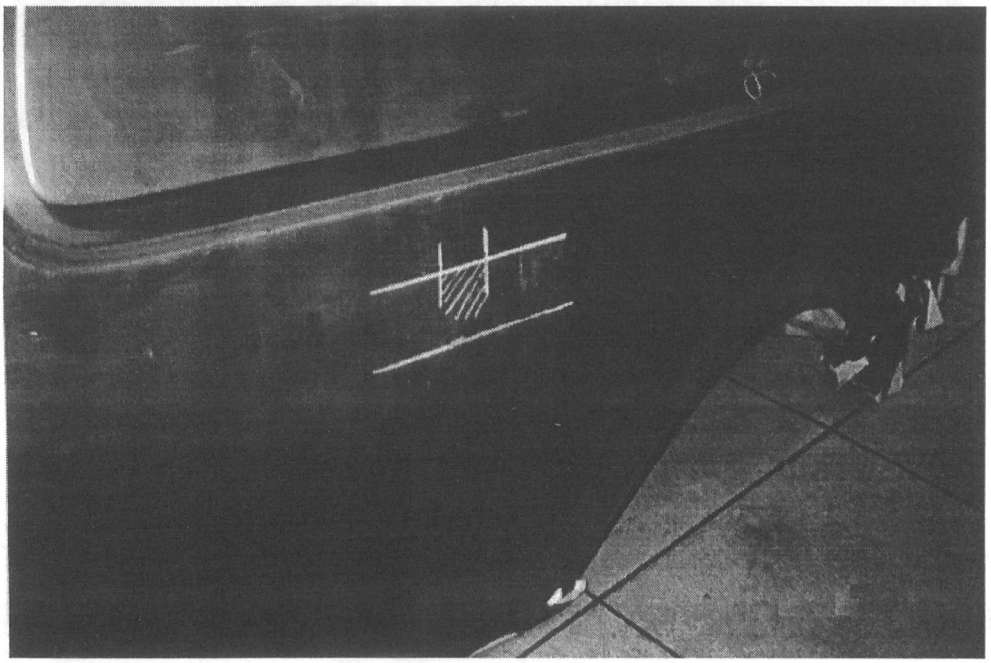

Figure 6.41 *Photograph of Ford Transit side panel with defect area highlighted*

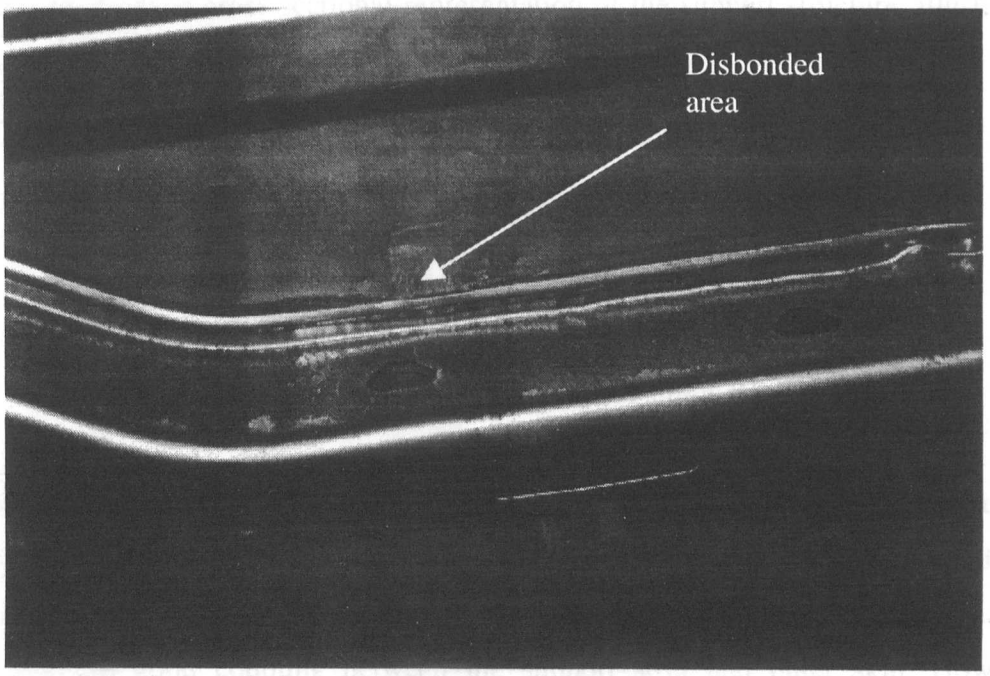

Figure 6.42 *Photograph of inner support strut to connect outer skin*

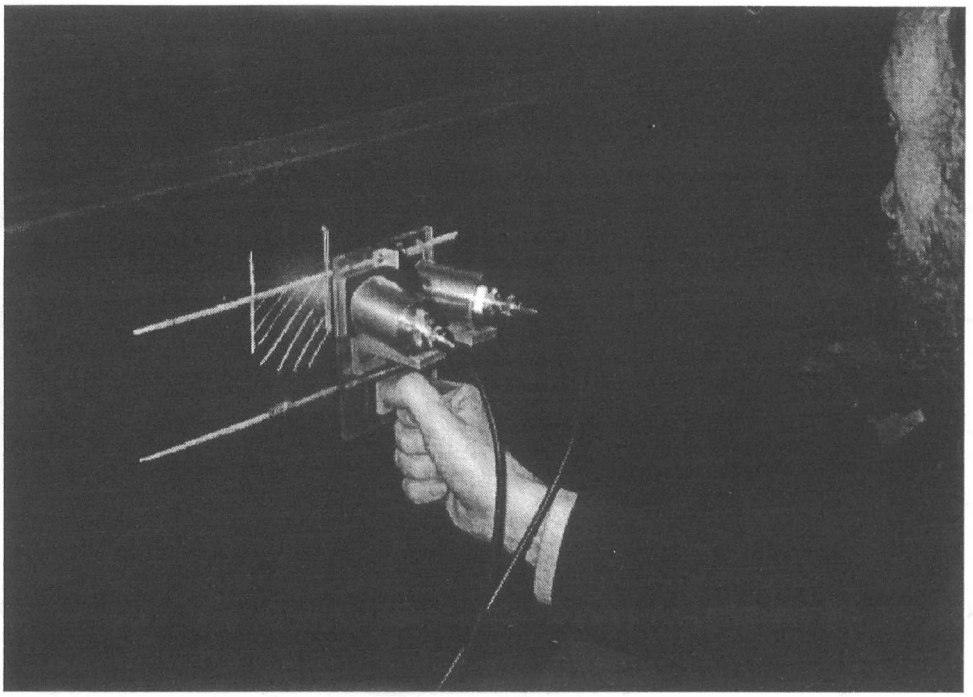

Figure 6.43 *Handheld conical piezocomposite scanner in operation*

This strengthening strut is bonded to the rolled steel outer skin of the vehicle by rubberised cement lap joints. In order to simulate a disbond occurring within the structure, the cement was parted from the outer skin of the side panel using a scalpel. Figure 6.44 shows a cross sectional representation of the support structure, illustrating the manufactured disbond.

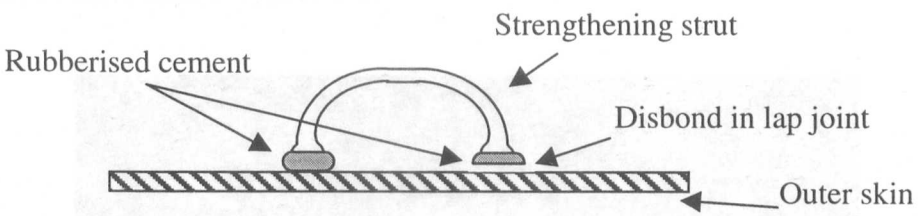

Figure 6.44 *Schematic of side panel support strut*

As can been seen in Figure 6.45, due to the highly attenuative nature of the rubberised cement, as the scanner is passed over an intact area of the Transit side panel bond line, the Lamb wave generated within the thin skin is reduced. This tells the operator that the bond line has good coupling between the support strut and outer skin. However, examination of Figure 6.46 illustrates the influence of a disbonded lap joint. Figure 6.46 shows that if the bondline between the outer skin and strengthener is broken, the Lamb wave is able to propagate in this region. Thus, if the magnitude of signal over the

bondline shows a considerable increase toward the level of that normally associated with the outer skin thickness, a defective region has been detected.

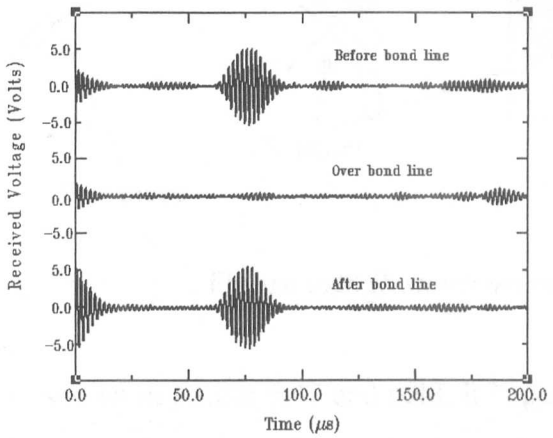

Figure 6.45 *Received responses over intact lap joint*

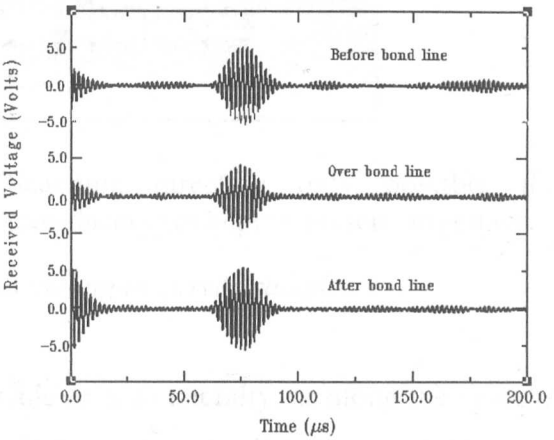

Figure 6.46 *Received response over defective lap joint*

Another point of interest within this section, was the ability of the scanning arrangement to generate and detect Lamb waves over the curved surface of the side panel. It was found that although the generation/detection of Lamb waves is dependent upon the angular alignment of the transducer pair, that the inspection of the curved sections of the side panel test piece was possible. The one condition being, that the direction of scanning was normal to the curvature of the surface, i.e. along the spine of the curve, as illustrated in Figure 6.47.

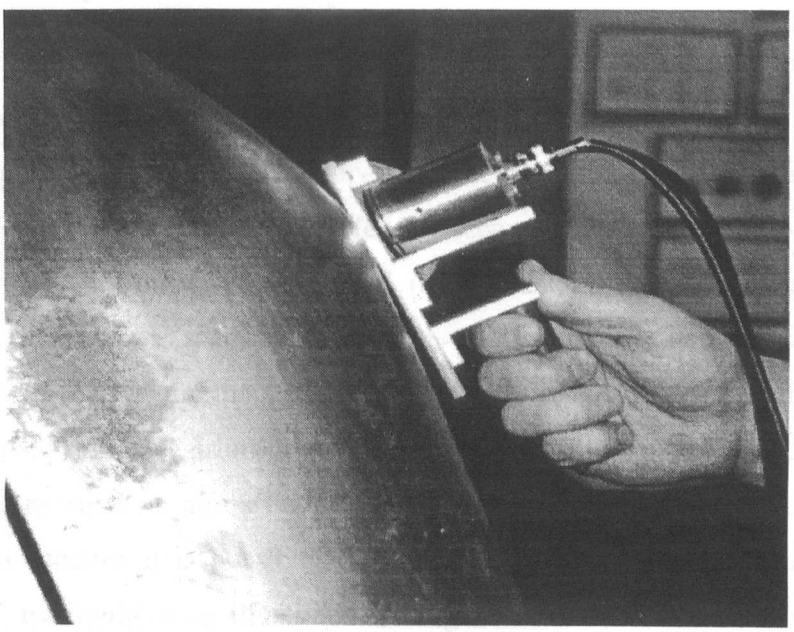

Figure 6.47 *Scanning of curved region of Transit side panel*

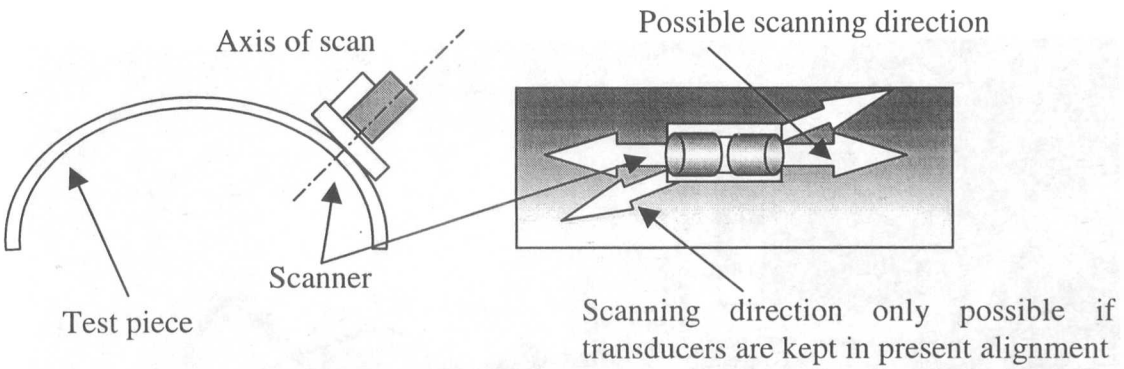

Figure 6.48 *Restrictions on scanning of curved samples*

As shown in Figure 6.47 and 6.48, it is possible to scan laterally, or along the spine of the curve. However, due to the base plate of the scanner head being rigid, diagonal scans can only be facilitated if the transducer alignment, or axis of scan is kept normal to the area of the curved sample under inspection. If the alignment of the transducers is altered such that the transducers are no longer normal to the curve, the scanner will be unable to efficiently generate Lamb waves within the sample. The degree by which the planar angular alignment influences the efficient generation of Lamb waves within curved surfaces was considered outwith the scope of this investigation. However, suggestions are made in Chapter 7 for possible further work that could be done to quantify the limitations in the inspection of non-planar geometries.

6.7.1 Integration to ANDSCAN® positional system

One of the increasing requirements of ultrasonic inspection is being able to represent the data in an understandable graphical format. The ANDSCAN® [28] system, is a commercial positioning system developed by the Defence Evaluation and Research Agency (DERA), formerly known as Defence Research Agency (DRA), to plot scanned data in a mapped format (C-scan) to aid in the visualisation of captured data. By plotting this data as a C-scan, it is possible to map large areas of plate and then distinguish defects from the mapped plot by variations in colour intensity. While the system described is meant primarily as a basic tool for the on-site inspection of large planar structures such as aircraft wings and automotive chassis, by incorporating a positional manipulator it is possible to generate C-scans of the inspected area. The ANDSCAN® manipulator is illustrated in Figure 6.49 with the conical composite scanning head assembly attached.

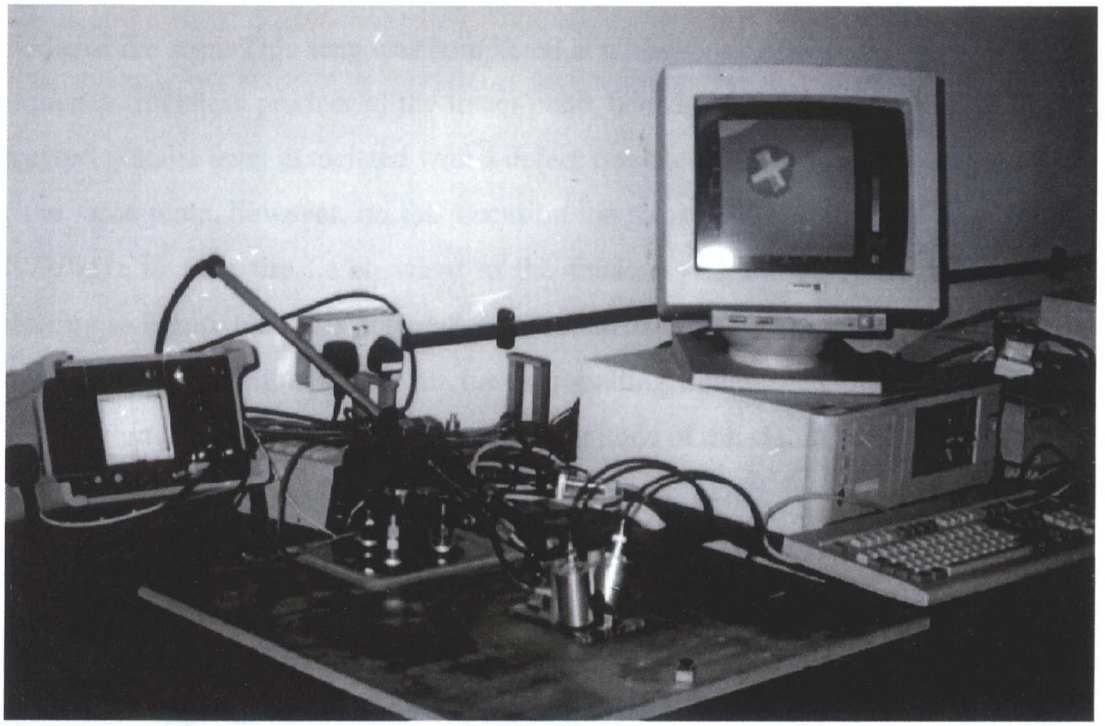

Figure 6.49 *Photograph of ANDSCAN® positional assembly*

Utilising this facility allows the graphical representation of the previously described sample defect plate. Namely the 1.14mm plate incorporating the 20x100mm slot defect, with a defect thickness of 0.95mm. Using the ANDSCAN® arm to record the positional data in conjunction with the signal strength of the detected Lamb wave, two scanned images were generated for the Lamb wave tuned to the normal thickness of the plate (1.14mm) and the defect thickness (0.95mm).

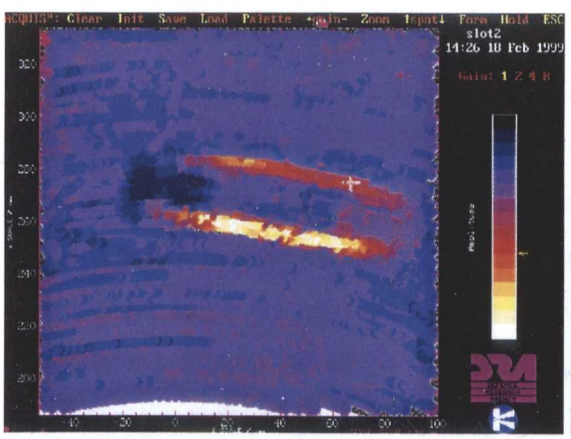

Figure 6.50 *C-scan of slot defect tuned to plate thickness*

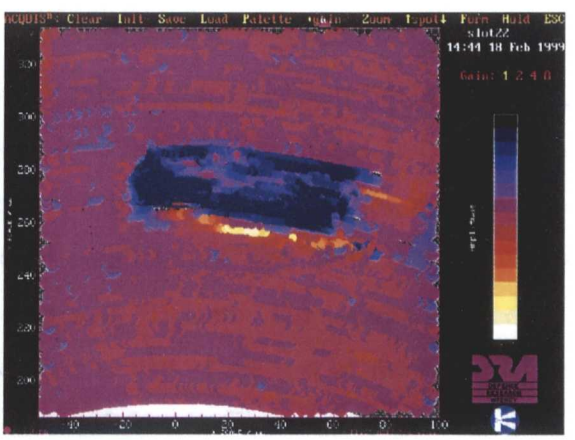

Figure 6.51 *C-scan of slot defect tuned to defect thickness*

Figure 6.50 illustrates the detection of the slot defect as the two bright regions in the middle of the scan. This scan was completed at a frequency of 600kHz, governed by the frequency-thickness product of the intact plate, hence the darker blue area signifies the received voltage level associated with a defect free area. Figure 6.51 illustrates a C-scan of the same plate, however, on this occasion the transmission frequency was increased to 720kHz to tune the Lamb wave to the thickness of the 0.95mm defect slot. By referring to Figure 6.51 it is apparent that the intensity of the signal over the defect area is now much larger than that over the surrounding undamaged plate. However, it is evident from the C-scan that although the magnitude of the signal is maximised over the defect, there is still quite a substantial amount of Lamb wave propagation in the 1.14mm plate thickness.

By examination of the previous C-scan image in Figure 6.50, two abnormalities are apparent. Firstly, that the scanner only definitively detects the edges of the machined slot as being defective and secondly, that there is a region of the plate (which should be defective) that returns the Lamb wave signal as a maximum. The reason for the edge detection could be due to the manufacture of the defect slot. By examination of the plate, it was found that slot had more material removed from the edge of the slot, see Figure 6.52.

Figure 6.52 *Cross section of slot defect*

This deeper groove round the outside of the defect was due to the manufacturing process with the grinding tool used. As the grinding tool used was only 3mm in diameter, it was not possible to machine the defect in one continuous motion, therefore the slot defect was constructed by a serious of parallel cuts. The outer cuts of which were found to be slightly deeper, by approximately 0.05mm. The resultant effect of which is to afford a greater variation in thickness to that of the rest of the defect. The second abnormality on the left-hand side of the defect in Figure 6.47 is more of a misnomer. This darker region, signifying a strong propagation of the Lamb wave may be due to direct line acoustic transmission leaking under the baffle or a problem with angular alignment of the ANDSCAN© manipulator. Presently, no definitive reason for this strong Lamb wave propagation can be given.

The capability of the conical composite scanning system to inspect damaged carbon fibre plates was investigated using the plate illustrated in Figure 6.54. The carbon fibre plate under examination, has dimensions of 300x300mm and four separate areas of impact damage, as represented in Figure 6.54. These defects were produced by striking the sample plate from differing heights to generate impacts of differing energy strengths, resulting impact damage of 10, 15, 20 and 30 joules. Using the testing arrangement described earlier in the Chapter (Figure 6.27) the carbon fibre plate was examined at a frequency of 600kHz and the C-scan shown in Figure 6.53 was generated.

Figure 6.53 *C-scan of damaged carbon fibre plate*

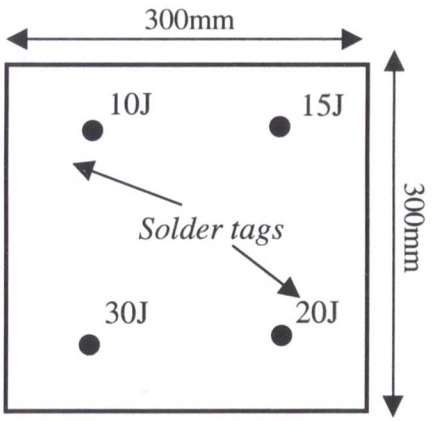

Figure 6.54 *Schematic of carbon fibre testplate*

In Figure 6.53, the lighter regions signify the areas of the plate damaged through the impact simulation process. Other defect regions of note are the double image above the 20J damage point and the lighter region below the 10J damage area. By referring to Figure 6.54 and 6.53 it is apparent that these defect regions are associated with the metal solder tags bonded to the carbon fibre.

6.8 Conclusions

This Chapter has shown the development of a novel ultrasonic Lamb wave scanner capable of inspecting differing thicknesses of planar test-pieces from a set angle of incidence. Traditional electrostatic technology was utilised to prove the theoretical supposition that an alteration in frequency could retune the frequency-thickness product of the system to that associated with the thickness of the plate under inspection.

Capactive devices of varying sizes were utilised to determine the influence on transducer size to the minimum detectable defect size and depth.

Secondly, a more robust scanning head arrangement was manufactured using the wideband composite transducers developed through the theoretical and experimental investigation completed in Chapter 5. This portable scanning system unit was tested on an array of test pieces of differing thicknesses, showing good comparison to that of the scanner using capacitive devices. Additionally, the operational restrictions i.e. minimum defect criteria of the composite arrangement was quantified and found to be superior to that of the capacitive designs.

Finally, examples have been given of the frequency agile scanner operating on a range of practical NDT test pieces. The scanner showed considerable flexibility in dealing with inspection of non-planar test pieces, and in association with existing NDT tools, i.e. ANDSCAN®. The use of this positional manipulator allowed the unit to map damage to carbon fibre and demonstrated the ability of the scanner to retune to different defect thicknesses.

Chapter 7

Conclusions and recommendations for future work

7.1 Concluding summary

With the increasing need for non-destructive testing in all aspects of modern industry, simple, robust scanning systems capable of multi-functional operation are required. This Thesis has presented the design and development of a novel frequency agile approach to ultrasonic Lamb wave inspection capable of defect detection and thickness characterisation. The frequency agility of the scanning system represents a simple method whereby the user of the operator need not be versed in Lamb wave theory to calibrate the scanner, but can merely re-tune the Lamb wave for differing thicknesses of plate by altering the frequency of operation.

Through theoretical analysis of the noise mechanisms inherent within a piezoelectric receiver system, it has been shown that careful consideration of many factors, including intrinsic transducer noise, electronic noise and bandwidth of operation is essential in low noise receiver design. One of the main contributors of noise within these systems is Thermal or Nyquist noise, namely the noise generated within the transducer itself. While this form of noise is unavoidable, as all transducers have resistive components, consideration of the influence of this noise must be made during the design of any proposed receiver electronics.

It has been shown that reduction in the system bandwidth, consequently leads to an increase in the available signal-to-noise ratio (SNR). While theoretically it is possible to achieve a SNR over 120dB with a 1Hz bandwidth, this is not achievable in a practical system. However, it has been illustrated that is possible to achieve a SNR of 35dB with a bandwidth 20kHz in a practically realisable system.

Consequently, an ultra-low noise electronic receiver was designed and manufactured using heterodyning principles to achieve a wide bandwidth system input with a narrowband output. This allows a sufficiently large operational bandwidth to encompass the range of frequencies required for a multi-frequency Lamb wave scanner. The resultant system offers high gain characteristics, approximately 103dB, and good frequency selectivity to reduce the overall system noise bandwidth to approximately 20kHz.

Through analytical and practical research, a method has been determined for introducing additional thickness mode resonances into piezocomposite transducers, by using standard machining techniques to introduce areas of differing thickness. The addition of separate thickness sections within the piezocomposite structure leads to an enhancement in the bandwidth of the transducers. Although disparity was found in the predicted resonant frequencies due to the inability of the modelling approach to correctly simulate depoling in the composite structure, good correlation was found in the mode and magnitude of displacement. Moreover, it was shown that as the frequency separation between the thickness sections was reduced below 80kHz, vibration in one thickness section was coupled into the adjacent thickness section, thereby increasing the area of displacement.

Subsequently, rather than utilising composites with multiple frequency steps, analysis of a conical composite transducer design illustrated the feasibility of an operational bandwidth in excess of 300kHz with a focussed emission profile, ideally suited to the proposed scanning system.

Utilising conventional electrostatic ultrasonic transducers, which offer wide bandwidth and good coupling to air, defect detection and characterisation was completed in order to prove the concept of Lamb wave tuning for differing thickness of plate from one angle of incidence. Without altering the angle of incidence, it was possible to generate the fundamental anti-symmetrical Lamb wave mode in a 1.14mm thick plate of aluminium at 680kHz at an incident angle of 8.6° and consequently detect and retune for the same Lamb wave mode for the defective area of plate (0.95mm thick) at 800kHz. Furthermore, experimental analysis showed that the minimum defect detectability of the prototype scanner was for a diameter of 4mm, or alternatively when 30% thinning had occurred in the original plate thickness.

Replacement of the electrostatic transducer pairing with the conical piezocomposite transducers increased the defect detection sensitivity of the Lamb wave scanner to below 2mm diameter, or plates with 20% thinning. The increase in this defect detection was made at a reduction in operational bandwidth (600kHz→300kHz), but with an

increased degree of robustness, making it considerably more attractive for use in an industrial environment.

Finally, defect detection testing was carried out on a range of practical test pieces. Disbonds between the thin outer skin and the strengthening struts were detected, over areas of curved geometry in large non-planar vehicle sections. Additionally, the scanner was combined with a commercial positioning system (ANDSCAN®) to produce C-scan images of defective plates of aluminium and carbon fibre.

In conclusion, using theoretical and experimental analysis, the following guidelines have been determined for air-coupled ultrasonic Lamb wave operation.

- SNR's of 35dB are possible for air-coupled operation with bandwidths restricted to 20kHz.

- Reducing the input impedance of the pre-amplifier arrangement (below 100Ω) increases the noise rejection of the system and eliminates the necessity of the receive circuitry to be closely positioned to the sensor.

- Using Heterodyning principles, it is possible to achieve high gain and good selectivity across a wide bandwidth with low noise characteristics.

- Additional thickness mode resonances can be incorporated into a single thickness piezocomposite by modifying the geometry of the transducer thickness dimensions.

- With wide bandwidth transducers, it is possible to generate Lamb waves in a variety of plate thicknesses, both metal and carbon fibre, from one angle of incidence by altering the transmission frequency instead of the angle.

7.2 Recommendations and suggestions for further work

One area of this research which requires more comprehensive investigation is the further development of the enhanced bandwidth piezocomposites. While the work undertaken for the completion of this Thesis led to the implementation of robust wide bandwidth composite devices, there is considerable scope for improvement and increased understanding of the mechanisms involved. Namely, a more detailed investigation into the microstructure interaction between steps of differing thickness should be implemented to determine the nature by which the steps convey vibration from one step to another. A fuller understanding of this will allow the designer to tailor devices in such a way as to increase or decrease the amount of sympathetic vibration generated in adjacent thickness sections.

Further study is also required into determining the optimum number of pillars under a given thickness section, or frequency gradient in a conical style transducer, to induce strong resonant behaviour in that section. Conventional composite arrays stipulate that between 4-6 pillars under any given electrode is prerequisite for adequate uniform displacement [100], however further analysis is required to determine the guidelines for this form of composite. However, initial studies with the saw tooth design described in Chapter 5, indicate that for composites with complex machined geometries, more pillars are required under the gradient to facilitate a higher degree of displacement and frequency coupling. This in turn requires smaller pillar geometries, which with the current facilities, are not feasible. Therefore, alternative solutions are required for fine scale composite manufacture, i.e. injection moulding of micro pillars or laser machining the ceramic. The inclusion of more pillars, in the case of the saw tooth design, should mean that stronger resonant behaviour will be supported in the concentric circles leading to a more uniform displacing transducer. Additionally, finer pillar structure in such devices may also facilitate the array patterning on the composites for beam steering.

Another important aspect of the FEA approach that requires investigation is the implementation of an accurate means by which to model the depoling of piezocomposites. As illustrated in Chapter 5, the depoling of composites and the consequent drop in the electromechanical coupling coefficient leads to disparities

between the modelled and experimental results. This requires practical investigation into how the depoling of the ceramic influences the material parameters and correlating this with modelled responses to fully characterise the transducer, whether in a composite structure or solid state ceramic transducer.

In addition to studies on the behaviour of the microstructure of the multi-frequency composite design, further work is required into the machined geometries. Chapters 5 and 6 illustrate the problem associated with beam spreading in the conical composite design as the frequency of operation was increased. Possible ways of preventing this may be to invert the geometry such that the transducer is concave rather than convex on the rear plane. Such a design would still incorporate a degree of beam spreading, however as the nature of most of the defects under inspection relates to plate thinning, when a defect is detected and the frequency is increased toward the central thickness section, the beam profile should become more collimated allowing for greater defect characterisation.

Furthermore, there is increasing interest in the biomedical industry in 2nd harmonic imaging [101], i.e. exciting a transducer at its resonant frequency and receiving at twice that frequency in a pulse-echo mode of operation, to reduce the amount of noise clutter from received signals due to diffraction and reflection. The new machined composite transducers could provide an alternative approach to conventional monolithic piezoceramic or piezocomposite transducers by incorporating differing thickness sections as illustrated in the 1/8th symmetry model in Figure 7.01.

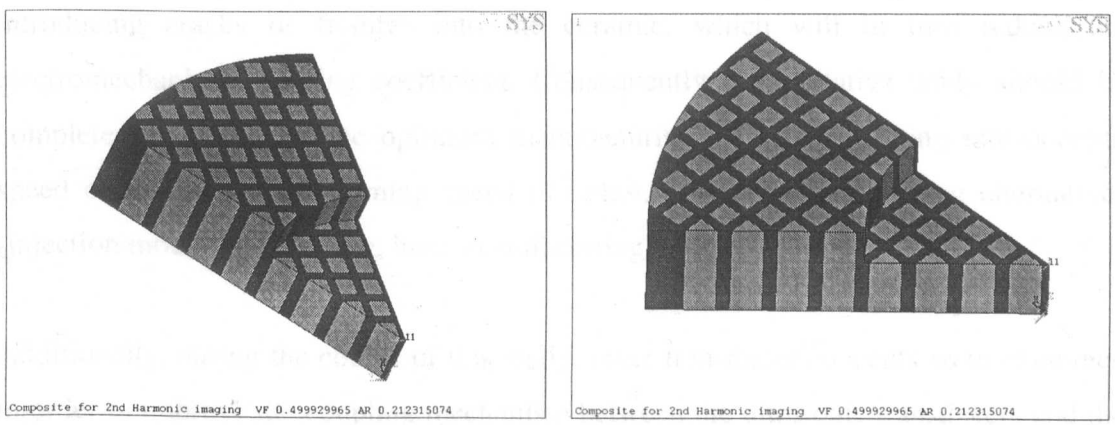

Figure 7.01 *Conceptual design for 2nd harmonic imaging composite transducer*

This form of transducer would theoretically provide the beam profile characteristics desired in 2nd harmonic imaging, with an annular source in the outer diameter thickness of the transducer producing a focussing effect in the far field. This may then be detected with the more collimated beam profile exhibited by the central section with its mechanical resonance matched to twice that of the outer diameter electrical resonance.
As previously highlighted, there was a degree of depoling exhibited in the machining of the multi-frequency composite transducers. In order to rectify this, it is recommended that an attempt should be made to re-pole the composites. Typically, poling is achieved by heating the ceramic until the Curie temperature of the ceramic has been reached and then allowing to cool, while applying a strong electric field across the poling direction. This has the effect of realigning the dipoles within the ceramic into the required domain. However, the Curie temperature of the ceramic is in excess of the glass transition temperature of the polymer filler, i.e. the temperature at which the polymer converts from a solid state to a more rubbery one. Therefore, further practical work is required to quantify the influence that this heating effect will have on the polymer in the composite structure and determine what advantages or disadvantages this has on the coupling coefficient. Research of this nature is currently underway at Strathclyde.

Further to this, practical investigation should be done to ascertain the effect of machining upon the piezoceramic, in order to determine the degree of depoling introduced by the machining process. Experimentation should be carried out on both solid ceramic and piezocomposite structures, with a focus on the effect of the machining tool on the surface of the transducer, i.e. if the machining process is introducing cracks or fissures into the ceramic, which will in turn reduce the electromechanical coupling coefficient. Consequently, a qualitative study should be completed to determine the optimum manufacturing techniques, taking into account speed of machining (i.e. turning speed of lathe), coolant and machining alternatives (injection moulding, grinding, laser manufacturing).

Additionally, during the course of this study, other transducer concepts were examined in order to improve the coupling mechanism between the ultrasonic transducers and the air medium. However, due to time constraints, some of these designs were unable to be investigated fully and would benefit from further analysis. For example, work by Babic [40] and Newnham et al. [41, 42, 43] on flextensional transducers and Schindel et al.

[64] on electrostatic transducers illustrates the advantages of coupling sound energy into a low acoustic impedance medium, such as air, via a secondary mechanism, i.e. a membrane. Such transducers operate on the principle that the induced motion in the membrane transfers the energy from the transducer into the air, thereby reducing some of the problems associated with the large acoustic impedance mismatch between the two media. Preliminary work was carried out to investigate the feasibility of this approach in composite structures with limited success. FEA was employed to predict the behaviour of 2-2 composites with high Poisson ratio polymer filler and membrane coupling to determine the magnitudes of displacement possible with such a design over conventional 2-2 composite transducers. It was found that the inclusion of the membrane to the composite led to a twofold increase in displacement magnitude over conventional transducers, however as the main thrust of the research at that instant was toward bandwidth enhancement, this line of investigation was terminated. It is recommended that further work is undertaken in the improvement of ultrasonic propagation from bulk solids to air by this method, both in experimental analysis and FEA prediction.

Finally, although the focus of the design process has been centred on the development of wideband piezocomposites for operation in air, these transducers would be equally suitable for operation in a water environment. Initial surface displacement and beam profile calibration of these transducers was carried out in a fluid medium and displayed good consistency with the results presented for operation in air. The advantages of such wideband composites in underwater operation is that the larger frequency range allows for differing degrees of resolution. For example, a stepped composite transducer could be excited at the its lowest frequency component for long range detection and then increased in frequency as the distance to target reduces, in order to gain higher resolution and therefore more information about the target. Subsequently, further investigation should be done regarding the suitability and efficiency of these non-uniform thickness composites for biomedical and underwater operation.

References

1. J.B. Hoyes, Q. Shan, R.J. Dewhurst, "A non-contact scanning system for laser ultrasonic defect imaging", Measurement science technology, No. 2, pp.628-634, 1991.
2. R.A. Banks, "An investigation into intrinsic noise within piezoelectric receive systems", M.Phil. Thesis, University of Strathclyde, Glasgow, UK, 1996.
3. R. Farlow & G. Hayward, "Real-time ultrasonic techniques suitable for implementing non-contact NDT systems employing piezoceramic composite transducers", Insight, Vol. 36, No. 12, December 1994.
4. R. Farlow, G. Hayward, "An automated ultrasonic NDT scanner employing advanced air-coupled 1-3 connectivity composite transducers", Insight, Vol. 38, No. 1, January, pp.41-50, 1996.
5. P. Cawley, "The detection of delaminations using flexural waves", NDT International, Vol. 23, No. 4, August, pp.207-213, 1990.
6. J. Blitz, "Fundamentals of Ultrasonics", Butterworths, London, 1963.
7. B. Jaffe, W.R. Cook & G. Jaffe, "Piezoelectric Ceramics", Academic Press, London, 1971.
8. J. Blitz, "Ultrasonics, Methods and applications", Butterworths, London, 1971.
9. J. Stor-Pellinen and M. Luukkala, "Paper roughness measurements using airborne ultrasound", Sensors and Actuators A – Physical", Vol. 49, 1995.
10. A.R. Selfridge, "Approximate material properties in isotropic materials", IEEE trans. on sonics and ultrasonics, Vol. SU-32, No. 3, May, pp.381-394, 1985.
11. J. Orear, "Fundamental Physics", John Wiley & sons, London, 1964.
12. L.M. Brekhovskikh, "Wave in layered media, Academic Press, 1960.
13. R. Farlow, "Boundary Model", University of Strathclyde, Glasgow.
14. I.A. Viktorov, "Rayleigh and Lamb waves: Physical theory and applications", Plenum Press, New York, 1967.
15. B. Pavlakovic, M. Lowe, "Disperse: User's manual", Imperial College, University of London, Non-Destructive Testing Laboratory.
16. D.A. Hutchins, "Ultrasonic generation by pulsed lasers", Physical Acoustics, Vol. 18, Academic Press, 1988.
17. D.A. Hutchins, W.M.D. Wright, G. Hayward, A. Gachagan, "Air-coupled piezoelectric detection of laser-generated ultrasound", IEEE trans. UFFC, Vol. 41, No. 6, November, 1994.
18. J.P. Monchalin, "Optical detection of ultrasound", IEEE Trans. UFFC, Vol. 33, No. 5, September, 1986.
19. J.W. Wagner, "Optical detection of ultrasound", Physical Acoustics, Vol. 19, Academic Press, 1990.

20. R.J. Dewhurst, R. He, Q. Shan, "Defect visualisation in carbon fiber composite using laser ultrasound", Materials evaluation, August, pp.935-940, 1993.
21. A.D.W. McKie, R.C. Addison Jnr., "Practical considerations for the rapid inspection of composite materials using laser-based ultrasound", Ultrasonics, Vol.32, No. 5, pp.333-345, 1994.
22. R.B. Thompson, "Physical principles of measurements with EMAT transducers", Physical Acoustics, Academic Press, Vol. 19, 1990.
23. B.W. Maxfield, A. Kuramoto, J.K. Hulbert, "Evaluating EMAT designs for selected applications", Materials Evaluation, No. 45, October, pp.1166-1183, 1987.
24. J. Krautkramer, H. Krautkramer, "Ultrasonic testing of materials, 4th Edition", Springer-Verlag, Berlin, 1989.
25. D.P. Jansen, D.A. Hutchins, "Lamb wave tomography", IEEE Ultrasonics Symposium, pp.1017-1020, 1990.
26. J. Blitz, G. Simpson, "Ultrasonic methods of non-destructive testing", Chapman & Hill, London, 1996.
27. S.J. Willsher, R.A. Smith, "Multi-element ultrasonic scanning of in-service airframes", Insight, Vol. 40, No. 3, March, pp.154-159, 1998.
28. R.A. Smith, "Evaluation and accuracy assessment of ANDSCAN – non-destructive portable scanner, Part 1. ANDSCAN hardware and software", Insight, Vol. 37, No. 5, pp.352-357, 1995.
29. C.M. Fortunko, M.C. Renken, A. Murray, "Examination of objects mode of wood using air-coupled ultrasound", IEEE Ultrasonics Symposium, pp.1099-1103, 1990.
30. A.J. Rogovsky, "Development and application of ultrasonic dry-contact and air-contact c-scan systems for non-destructive evaluation of aerospace composites", Material evaluation, December, pp.1491-1497, 1991
31. M.N. Jackson, "Simulation and control of thickness mode piezoelectric transducers", PhD Thesis, Glasgow, 1984.
32. S. Schiller, C-K. Hsieh, C-H. Chou, B.T. Khuri-Yakub, "Novel high frequency air transducers", Review of progress in quantitative non-destructive evaluation, Plenum Press, pp.795-798, 1990.
33. J. Stor-Pellinen, M. Oksanen, R. Vuohelainen, J. Rantala, J. Hartikainen, M. Luukkala, "Photoacoustic inspection of matching layers of ultrasonic air-coupled transducer", IEEE Ultrasonics Symposium, pp.665-668, 1989.

34. R. Gerlach, O. Kraus, J. Frieke, P. Eccardt, N. Kroemer, V. Magori, "Modified SiO_2 aerogels as acoustic impedance matching layers in ultrasonic devices", Journal of non-crystalline solids, pp.227-231, 1992.
35. J.D. Fox, B.T. Khuri-Yakub, G.S. Kino, "High frequency acoustic wave measurements in air", IEEE Ultrasonics Symposium, pp.581-584, 1983.
36. M. Tone, T. Yano, A. Fukumoto, "High frequency ultrasonic transducers operating in air", Japanese journal of applied physics, Vol. 23, No. 6, June, pp.L436-L438, 1984.
37. T. Yano, M. Tone, A. Fukumato, "Range finding and surface characterisation using high frequency air transducers", IEEE trans. UFFC, Vol. UFFC-34, No. 2, March, pp.232-236, 1987.
38. N.H. Fletcher, S. Thwaites, "Multi-horn matching plate for ultrasonic transducers", Ultrasonics, Vol. 30, No. 2, pp.67-75, 1992.
39. M.S. Seyed-Bolorforosh, "Novel integrated impedance matching layer", IEEE trans. UFFC, Vol. 42, No. 5, pp.809-881.
40. M. Babic, "A 200kHz ultrasonic transducer coupled to the air with a radiating membrane", IEEE trans. UFFC, Vol. 38, No. 3, pp.252-255, 1991.
41. Y. Sugawara, K. Onitsuko, S. Yoshikawa, Q. Xu, R.E. Newnham, K. Uchino, "Metal-ceramic composite transducers", Journal of American ceramic society, Vol. 75, No. 4, pp.996-998, 1991.
42. Q. Qu, S. Yoshikawa, J.R. Belsick, R.E. Newnham, "Piezoelectric composites with high sensitivity and high capacitance for use at high pressures", IEEE trans. UFFC, Vol. 38, No.6, pp.634-639, 1991.
43. J.F. Tressler, R.E. Newnham, "Doubly resonant cymbal-type transducers", IEEE trans. UFFC, Vol. 44, No. 5, September, pp.1175-1177, 1997.
44. H. Okada, M. Kurasawa, S. Ueha, M. Masadu, "New airborne ultrasonic transducer with high output sound pressure level", Japanese journal of applied physics, Vol. 33, pp.3040-3044, 1994.
45. H. Loertscher, B. Grandia, J. Strycek, W.A. Grandia, "Airscan transducers, technique and application", British Institute of Non-Destructive Testing conference, September, 1998.
46. T. Möckl, V. Magori, C. Eccardt, "Sandwich-layer transducer – A versatile design for ultrasonic transducers operating in air", Sensor and Actuators, A21-A23, pp.687-692, 1990.
47. W.A. Smith, "New opportunities in ultrasonic transducers emerging from innovations in piezoelectric materials", SPIE, Vol. 1733, 1990.

48. H.P. Savakus, K.A. Klicker, R.E. Newnham, "PZT-epoxy piezoelectric transducers: A simplified fabrication procedure", Materials research bulletin, 16, pp.677-680, 1981.
49. L.J. Bowen, R.L. Gentilman, H.T. Pham, D.F. Fiore, K.W. French, "Injection moulding fine scale piezoelectric composite transducers", IEEE Ultrasonics Symposium, pp.499-503, 1991.
50. A. Gachagan, "An evaluation of 1-3 connectivity composite transducers for air-coupled ultrasonic applications", Ph.D. Thesis, University of Strathclyde, Glasgow, 1996.
51. G. Hayward, A. Gachagan, "An evaluation of 1-3 connectivity composites transducer for air-coupled ultrasonic applications", J. Acoust. Soc. Amer., Vol. 99, No. 4, April, pp.2148-2157, 1996.
52. G. Hayward, Y. Gorfu, "An assessment of through air transmission for remote ultrasonic non-destructive testing", RAE Farnborough MOD contract 2065/058, 1988.
53. S.P. Kelly, R. Farlow, G. Hayward, "Applications of through-air ultrasound for rapid NDE scanning in the aerospace industry", IEEE trans. UFFC, Vol. 43, No. 4, July, pp.581-591, 1996.
54. S. Whiteley, G. Hayward, D. Reilly, "Thickness measurement using air-coupled ultrasound", Insight, Vol.39, No.11, pp.770-775, 1997.
55. W. Manthey, N. Kroemer, V. Magori, "Ultrasonic transducers and transducer arrays for applications in air", Measurement Science Technology, No. 3, pp.249-261, 1992.
56. W. Galbraith, "The development of a PVDF membrane hydrophone for use in air coupled transducer calibration", M.Phil. Thesis, Glasgow, 1997.
57. A. Gachagan, G. Hayward, S.P. Kelly, W. Galbraith, "Characterisation of air-coupled transducers", IEEE trans. UFFC, Vol. 43, No. 4, July, pp.678-689, 1996.
58. J.S. Schoewald, J.F. Martin, "PVF_2 transducers for acoustic ranging and imaging in air", IEEE Ultrasonic Symposium, pp.577-580, 1983.
59. H. Carr, C. Wykes, "Diagnostic measurements in capacitive transducers", Ultrasonics, Vol. 31, No. 1, pp.13-20, 1993.
60. W.S.H. Munro, C. Wykes, "Arrays for airborne 100kHz ultrasound", Ultrasonics, Vol. 32, No. 1, pp.57-64, 1994.
61. J. Hietanen, P. Mattila, J. Stor-Pellinen, F. Tsuzuki, H. Väätäjä, K. Sasaki, M. Luukkala, "Factors affecting the sensitivity of electrostatic ultrasonic transducers", Measurement Science Technology, No. 4, pp.1138-1142, 1993.
62. J. Hietanen, J. Stor-Pellinen, M. Luukkala, " A model for an electrostatic ultrasonic transducer with a grooved backplate", Measurement Science Technology, No. 3, pp.1095-1097, 1992.

63. P. Mattila, F. Tsuzuki, H. Väätäjä, K. Sasaki, "Electroacoustic model for electrostatic ultrasonic transducers with v-grooved backplates", IEEE trans. UFFC, Vol. 42, No. 1, January, pp.1-6, 1995.
64. D.W. Schindel, D.A. Hutchins, L. Zou, M. Sayer, "The design and characterisation of micromachined air-coupled capacitance transducers", IEEE trans. UFFC, Vol. 42, No. 1, January, pp.42-49, 1995.
65. A.G. Bashford, D.W. Schindel, D.A. Hutchins, W.M.D. Wright, "Field characterisation of an air-coupled micromachined ultrasonic capacitance transducer", J. Acoust. Soc. Amer., Vol. 101, No. 1, January, pp.315-322, 1997.
66. I. Ladabaum, B.T. Khuri-Yukab, D. Spoliansky, M.I. Haller, "Micromachined ultrasonic transducers (MUTs)", IEEE Ultrasonics Symposium, pp.501-504, 1995.
67. B.T. Khuri-Yukab, M.I. Haller, "A surface micromachined electrostatic ultrasonic air transducer", IEEE trans. UFFC, Vol. 43, No. 1, January, pp.1-6, 1996.
68. M. Luukkala, P. Meriläinen, "Metal plate testing using airborne ultrasound", Ultrasonics, September, pp.218-221, 1973.
69. D.A. Hutchins, W.M.D. Wright, D.W. Schindel, "Ultrasonic measurements in polymeric materials using air-coupled capacitance transducers", J. Acoust. Soc. Amer., Vol. 96, No. 3, September, pp.1634-1642, 1994.
70. D.W Schindel, D.A. Hutchins, "Through-thickness characterisation of solids by wideband air-coupled ultrasound", Ultrasonics, Vol. 33, No. 1, pp.11-17, 1995.
71. W. Wright, D. Hutchins, D. Jansen, D. Schindel, "Air-coupled Lamb wave tomography", IEEE trans. UFFC, Vol. 44, No. 1, January, pp.53-59, 1997.
72. I. Ladabaum, X.C. Jin, B.T. Khuri-Yukab, "Air coupled through transmission of aluminium and other recent results using MUTs", IEEE Ultrasonics Symposium, pp.983-986, 1997.
73. P. Horowitz, W. Hill, "The Art of Electronics", Cambridge University Press, 2nd Edition.
74. J.B. Johnson, "Thermal agitation of electricity in conductors", Physical Review, Vol. 32, July, pp.97-109, 1928.
75. H. Nyquist, "Thermal agitation of electric charge in conductors", Physical Review, Vol. 32, July, pp.110-113, 1928.
76. G. Hayward, "Time and frequency domain modelling of the piezoelectric transducer", Ph.D. Thesis, University of Strathclyde, Glasgow, UK, 1981.
77. D.G. Smith, J. Dunlop, "Telecommunications Engineering" Van Nostrand Reinhold Ltd.
78. C.D. Motchenbacher, J.A. Connelly, "Low Noise Electronics System Design", John Wiley & Sons Inc., 1993.

79. G. Hayward, C.J. MacLeod, T.S. Durrani, "A systems model of thickness mode piezoelectric transducers", J. Acoust. Soc. Amer., Vol. 79, No. 2, pp.369-382, 1984.
80. D.W. Schindel, D.S. Forsyth, D.A. Hutchins, A. Fahr, "Air-coupled ultrasonic NDE of bonded aluminium lap joints", Ultrasonics, Vol. 35, No. 1, pp.1-6, 1997.
81. A.F. Arbel, "Comparison between the noise performance of current-mode and voltage-mode amplifiers", Analog Integrated Circuits and Signal Processing, Vol. 7., pp221-242, 1995.
82. T. Kalthoff, T. Wang, R.M. Stitt, "Classical op-amp or current-feedback op-amp?", Burr-Brown Application Note. March 1991.
83. L. Magram, A.F. Arbel, "Current mode feedback amplifier employing a transistorised feedback network", in Proceedings ISCAS, 1994.
84. ANSYS, Swanson Analysis Systems Inc., Houston, PA, USA.
85. C. Pasquier, "A beam profile simulation programme: XBEAM", User manual, University of Strathclyde, Glasgow, 1998.
86. I.C. Zienkiewicz, R.L. Taylor, "The finite element method", 4th Edition.
87. J.T. Bennett, "Development of a finite element modelling system for piezocomposite transducers", Ph.D. Thesis, University of Strathclyde, Glasgow, 1995.
88. P. Reynolds, "Analysis and design of piezocomposite ultrasonic transducers using finite element technique and surface displacement profiles", Ph.D. Thesis, University of Strathclyde, Glasgow, 1999.
89. Pv-Wave, Visual Numerics, Houston, Texas, USA, 1998.
90. G. Benny, G. Hayward, R. Chapman, "Beam profile measurements and simulations for ultrasonic transducers operating in air", Submitted to Journal of Acoustical Society of America, submitted 1999.
91. R. Lerch, W. Friedrich, "Field patterns of ultrasonic transducers in attenuating media", Proceedings IEEE Ultrasonic Symposium, pp.677-682, 1985.
92. J.A. Hossack, "Modelling techniques for 1-3 composite transducers", Ph.D Thesis, University of Strathclyde, Glasgow, 1988.
93. T.R. Gururaja, W.A. Schulze, R.E. Newham, L.E. Cross, B.A. Auld, Y.J. Yang, "Piezoelectric composite materials for ultrasonic transducer applications Part 1: Resonant modes of vibration of PZT rod-polymer composites", IEEE transactions on Sonics and Ultrasonics, Vol. SU-32, pp.481-498, July 1985.
94. T.R. Gururaja, W.A. Schulze, R.E. Newham, L.E. Cross, "Piezoelectric composite materials for ultrasonic transducer applications Part 2: Evaluation of ultrasonics medical

applications", IEEE transactions on Sonics and Ultrasonics, Vol. SU-32, pp.499-513, July 1985.

95. B.A. Auld, Y.J. Yang, "Acoustic wave vibrations in periodic composite plates", IEEE Symposium Proceedings, Dallas, pp.528-532, 1984.
96. B.A. Auld. "Waves and vibrations in periodic composite plates", Materials science and engineering, Vol. A122, pp.65-70, 1989.
97. G. Kossoff, "The effects of backing and matching on the performance of piezoelectric ceramic transducers", IEEE transactions on Sonics and Ultrasonics, Vol. Su-13, No. 1, pp.20-30, 1966.
98. C.S. Desilets, J.D. Fraser, G.S. Kino, "The design of efficient broad-band piezoelectric transducers", IEEE transactions on Sonics and Ultrasonics, Vol. SU-25, No. 3, pp.115-125, 1978.
99. Ferroperm A/S, Piezoceramics Division, Hejreskovvej 6, DK-3490 Kvistgård, Denmark.
100. J. Hyslop, G. Hayward, "An experimental and theoretical investigation into the fluid-loaded performance of 1-3 piezocomposite transducer array structures: with specific regard to device surface displacement and beam profile", IEEE Ultrasonics Symposium Proceedings, Vol. 2, pp.907-910, 1997.
101. T.R. Gururaja, A. Shurland, J. Chen, "Medical ultrasonic transducers with switchable frequency bands centred about f_0 and $2f_0$", IEEE Ultrasonics Symposium Proceedings, Vol. 2, pp.1659-1661, 1997.
102. L. Bowen, T.R. Gururaja, "High frequency electromechanical properties of piezoelectric ceramic/polymer composites in broadband applications", Journal of Applied Physics, Vol. 51, No. 11, pp.5661-5666, 1980.
103. L. Germain, J.D.N. Cheeke, "Electronic B-scan imaging using a wedge transducer", IEEE Ultrasonics Symposium Proceedings, Vol. 2, pp.1025-1028, 1990.
104. L. Germain, J.D.N. Cheeke, "Electronic scanning in acoustic microscopy using a wedge transducer", IEEE Acoustical Imaging, Vol. 18, Plenum Publishing, New York, 1990.

Appendix A.

Amplifier specifications

AD797, Ultralow Distortion, Ultralow Noise Op Amp

FEATURES

Low Noise 0.9 nV/√Hz typ (1.2 nV/√Hz max) Input Voltage Noise at 1 kHz

50 nV p-p Input Voltage Noise, 0.1 Hz to 10 Hz

Low Distortion

−120 dB Total Harmonic Distortion at 20 kHz

Excellent AC Characteristics

800 ns Settling Time to 16 Bits (10 V Step)

110 MHz Gain Bandwidth (G = 1000)

8 MHz Bandwidth (G = 10)

280 kHz Full Power Bandwidth at 20 V p-p

20 V/μs Slew Rate

Excellent DC Precision

80 μV max Input Offset Voltage

1.0 μV/°C V_{OS} Drift

Specified for ±5 V and ±15 V Power Supplies

High Output Drive Current of 50 mA

APPLICATIONS

Professional Audio Preamplifiers

IR, CCD, and Sonar Imaging Systems

Spectrum Analyzers

Ultrasound Preamplifiers

Seismic Detectors

ADC/DAC Buffers

Full technical specifications can be found in Analog Devices reference manual, Rev A, pp.2-271-pp.2.276, 1992.

AD811 High Performance Video Op Amp

FEATURES

High Speed

- 140 MHz Bandwidth (3 dB, G = +1)
- 120 MHz Bandwidth (3 dB, G = +2)
- 35 MHz Bandwidth (0.1 dB, G = +2)
- 2500 V/ms Slew Rate
- 25 ns Settling Time to 0.1% (For a 2 V Step)
- 65 ns Settling Time to 0.01% (For a 10 V Step)

Excellent Video Performance (R_L =150 V)

- 0.01% Differential Gain, 0.01° Differential Phase
- Voltage Noise of 1.9 nV/√Hz

Low Distortion: THD = –74 dB @ 10 MHz

Excellent DC Precision

- 3 mV max Input Offset Voltage

Flexible Operation

- Specified for ±5 V and ±15 V Operation
- ±2.3 V Output Swing into a 75Ω Load (V_S = ±5 V)

APPLICATIONS

- Video Crosspoint Switchers, Multimedia Broadcast Systems
- HDTV Compatible Systems
- Video Line Drivers, Distribution Amplifiers
- ADC/DAC Buffers
- DC Restoration Circuits
- Medical—Ultrasound, PET, Gamma and Counter Applications

Full technical specifications can be found in Analogue Devices reference manual, Rev. A, pp.2-281-pp.2-294), 1992.

MC1496B Balanced modulator/demodulator

These devices were designed for use where the output voltage is a product of an input voltage (signal) and a switching function (carrier). Typical applications include suppressed carrier and amplitude modulation, synchronous detection, FM detection, phase detection, and chopper applications. See Motorola Application Note AN531 for additional design information.

- Excellent Carrier Suppression –65 dB typ @ 0.5 MHz
  –50 dB typ @ 10 MHz
- Adjustable Gain and Signal Handling
- Balanced Inputs and Outputs
- High Common Mode Rejection –85 dB typical

For additional technical specifications, refer to the MC1496B data sheet supplied by Motorola website (www.motorola.com)– mc1496ref4f.pdf

Appendix B.

Calibration facilities

B.1 Calibration Tools

Of increasing importance in the manufacture of piezoelectric devices of all natures, is the ability to accurately measure all the characteristics of said device. Of vital importance, is the capability to quantify the mode of vibration within the transducer and the acoustic output pattern, or beam-profile. These describe, firstly, the way in which the transducer is vibrating, allowing the designer to distinguish any areas of the transducer that are inactive or vibrating in an unexpected manner. Secondly, the ability to beam profile transducers allows the designer to visualise the angular output pattern and intensity of the device. Within the Laboratories in the University of Strathclyde, two systems have been installed which allow the characterisation of transducers both in air and water. These scanners utilise some of the latest hardware to examine and store information on transducer surface vibration and pressure output beam profiles.

B.2 Surface displacement scanning

The laser vibrometer utilised within analysis phase of this Thesis, was a Polytec OFV302 Helium-Neon laser with a Polytec OFV2700 vibrometer controller. This laser scanner operates as a heterodyne interferometer, by determining the phase difference between the path lengths of the interferometer signal output and that of a reference beam. Using this method, the displacement resolution of the system can be measured into the sub-nanometer displacement range. This laser is mounted upon a fixed level surface, while the transducer under examination is affixed to a Physik Instrumente X-Y positional system. Said positioning system has two 200mm micro-positioning axes, controlled by a Physik Instrumente C-842 DC motor controller. These positioning and scanning elements are controlled via a Lab-Windows environment, which captures data from a Sonotek data acquisition card and controls the axes positioner via the C-842 pc card. The basic configuration is shown in Figure B.01

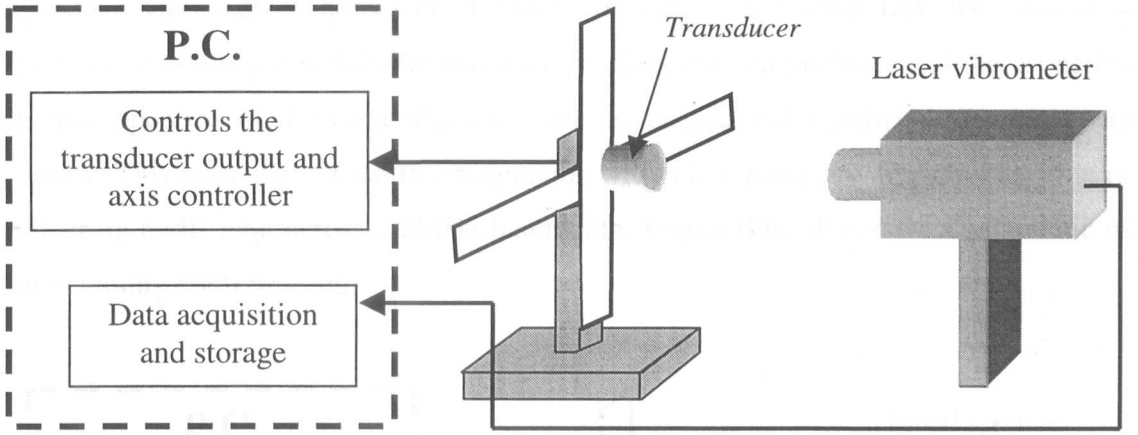

Figure B.01 *Surface displacement scanning arrangement*

The transducer to be characterised is then placed on the dual axis scanning arrangement and the surface displacement profile captured within the software package, rendering displacement information as illustrated in Figure B.02.

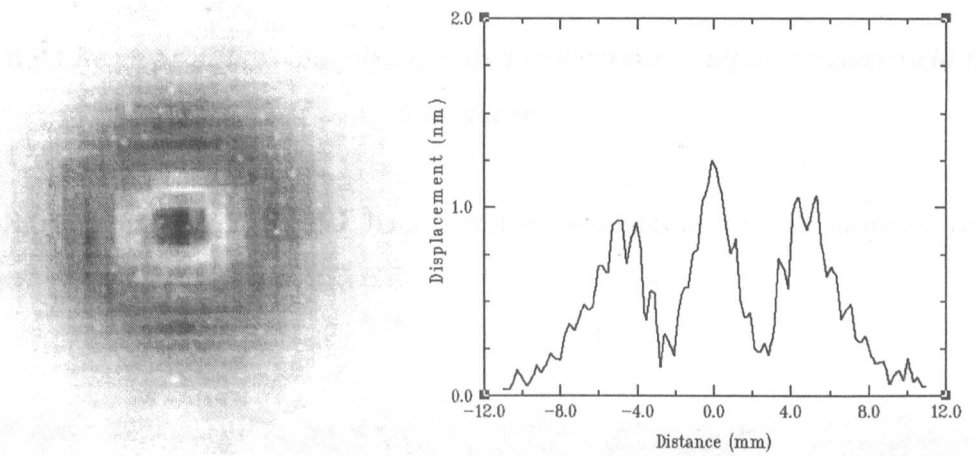

Figure B.02 *Sample displacement information from laser vibrometer*

B.3 Acoustic beam profile scanning

The beam profile of a given transducer is determined using a similar arrangement to that described previously. In this instance, the transducer under examination is affixed, as before, to another Physik Instrumente X-Y positional system while the receiving hydrophone is mounted on a positioning axis capable of scanning 1000mm in the z-direction. The three axes of the beam profiler are controlled by a Physik Instrumente C-560 stepping controller motor. These positioning and scanning elements are again

controlled via a Lab-Windows environment via the RS-232 serial link. The receiving hydrophone employed within the scanning arrangement is a pinducer and has an active circular aperture of 1.35mm diameter and an operational bandwidth from d.c. to 10MHz. This pinducer is used in combination with a low noise pre-amplifier capable of delivering 66dB gain across a 2MHz bandwidth. Figure B.03 illustrates a schematic of this scanning configuration.

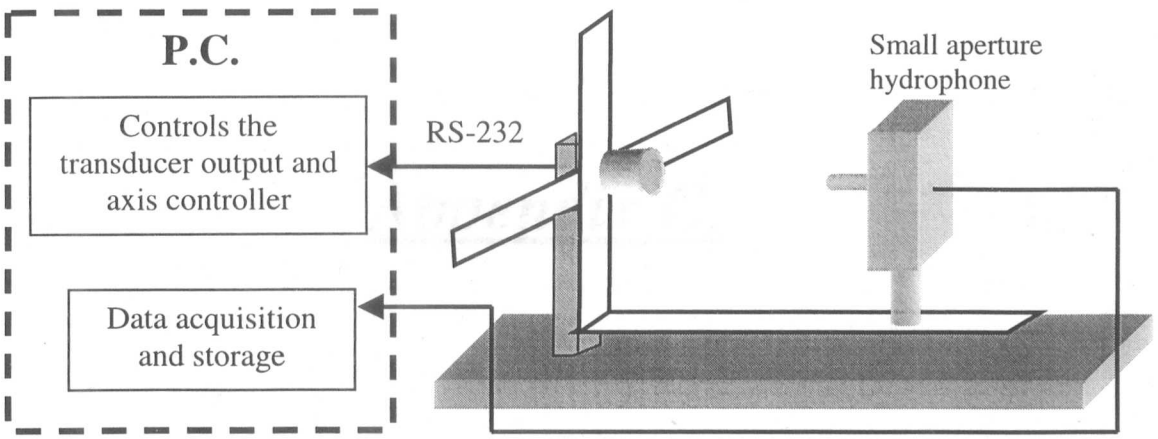

Figure B.03 *Beam profiling configuration used to determine output pressure field from transducer*

Figure B.04 illustrates a typical beam profile attained using the aforementioned hardware.

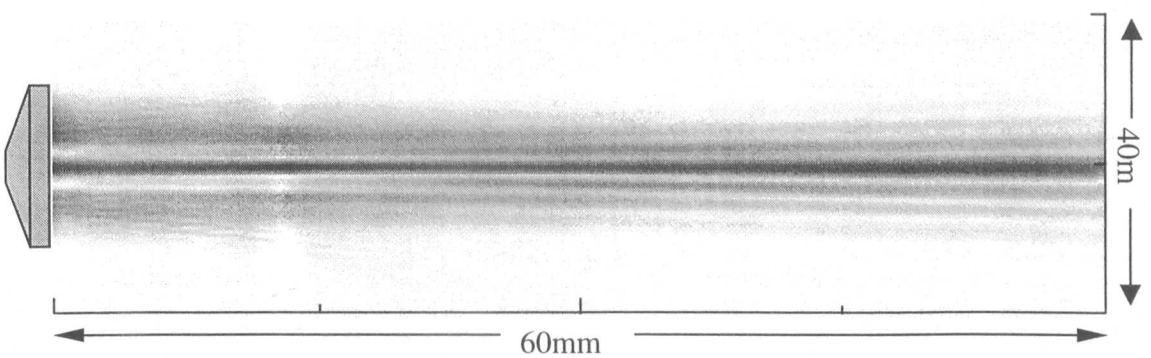

Figure B.04 *Beam profile of conical composite transducer as determined using the experimental apparatus*

Appendix C.

Material parameters

Ceramic material

	PZT-5A	PZT-5H
Stiffness (10^{10} Pa)		
C_{11}^E	14.7	14.0
C_{12}^E	10.4	9.55
C_{13}^E	9.39	8.98
C_{33}^E	11.3	11.1
C_{44}^E	2.3	1.85
C_{66}^E	2.15	2.21
Piezoelectric stress (Cm^{-1})		
e_{13}	-3.33	-4.23
e_{33}	15.7	21.3
e_{15}	11.6	13.4
Relative permitivitty		
ε_{11}^S	1130	1340
ε_{33}^S	870	1230
Density (kgm^{-1})		
ρ	7700	7450

Polymer materials

Ciba-Geigy polymers	Hard-set	Soft-set
Polymer mix	CY1301/1300	CY208/HY956
Youngs Modulus (10^9Pa)	4.0293	1.9992
Shear Modulus (10^9 Pa)	1.4608	0.7177
Poisson's ratio	0.3791	0.3928
Density (kgm^{-1})	1140	1150
Relative permittivity	4	3
Longitudinal velocity (ms^{-1})	2565	1880
Shear velocity (ms^{-1})	1132	790